AN IMAGING SURVEY OF LATE-TYPE GALAXIES: LOCAL BENCHMARKS OF GALAXY EVOLUTION

by

Violet Taylor

A Dissertation Presented in Partial Fulfillment
of the Requirements for the Degree
Doctor of Philosophy

ARIZONA STATE UNIVERSITY
December 2005

AN IMAGING SURVEY OF LATE-TYPE GALAXIES:
LOCAL BENCHMARKS OF GALAXY EVOLUTION
by
Violet Taylor

has been approved
November 2005

APPROVED:

_____, Chair

_____

_____

_____

_____
Supervisory Committee

ACCEPTED:

_____
Department Chair

_____
Dean, Division of Graduate Studies

ABSTRACT

The majority of galaxies observed at high redshift display structures and morphologies resembling those of nearby ($z \sim 0$) irregular, peculiar and merging galaxies. To better understand galaxy assembly and evolution, the properties of such nearby galaxies must be compared with distant ones in the rest-frame ultraviolet (UV), where the highest resolution and deepest observations of high-redshift galaxies were taken. To evaluate the possible dependence of galaxy structure and morphology on rest-frame wavelength, it is necessary to study the nearby galaxies in redder bands as well. For this purpose, a panchromatic imaging survey was conducted in the far-UV through the near-infrared of 199 nearby, mostly late-type, irregular, peculiar, and merging galaxies.

An analysis is presented here of the color gradients, and the wavelength-dependent quantitative morphology of this sample. Whereas ellipticals and early- to mid-type spiral galaxies tend to become bluer at larger radial distances from their centers, most late-type spiral, irregular, and merging galaxies become increasingly redder at larger radii. This may indicate that late-type galaxies have a significant halo or thick disk of older stars, while their inner regions are dominated by younger, UV-bright stars. This result is consistent with recent numerical models of hierarchical galaxy assembly.

Galaxy morphology is also quantitatively analyzed, as parametrized with measurements of concentration index, asymmetry, and clumpiness (CAS) parameters. These CAS parameters depend on both galaxy type and the wavelength of observation, and can be used to measure the "morphological k-correction", i.e., the change in appearance of a galaxy with rest-frame wavelength. Whereas early-type galaxies (E–S0) appear the same at all wavelengths longward of the Balmer break, there is a significant wavelength-dependence of the CAS parameters for galaxies of types later than S0, which generally become less concentrated and more asymmetric and clumpy toward shorter wavelengths. Also, as a merger progresses from pre-merger via major merger to merger remnant stages, it evolves through the CAS parameter space, becoming first less concentrated and more asymmetric and clumpy, and then returning towards the locus of normal galaxies. The final merger products are, on average, much more concentrated than normal spiral galaxies.

For my mother, who has always encouraged me to reach for the stars.

ACKNOWLEDGMENTS

First I would like to extend special thanks to my advisor, Rogier Windhorst, who has been an inspiration, as well as a strong driving force for the completion of my graduate studies at ASU. I am also very grateful for the support and advice of Stephen Odewahn and Rolf Jansen, who offered me their computing skills and astronomical knowledge, as well as alot of their precious time. Also, I thank everyone else in our research group (past and present) who has given me support and advice during my time here. These people are: Seth Cohen, Luis Echevarria, Michael Corbin, Claudia Chiarenza, Kazuyuki Tamura, Hao-Jing Yan, Nimish Hathi, Russell Ryan, and Amber Straughn.

Special thanks to John Hibbard, Richard de Grijs, and Chris Conselice for their helpful contribution to my research. I also thank my committee members for helping me through this process. They are: Rogier Windhorst, Rolf Jansen, David Burstein, John Hibbard, Jeff Drucker, and Stephen Odewahn.

I am eternally grateful to my mother, Terry Taylor, for all of her support during my graduate career and throughout my life. Without her encouragement and inspirational example, none of this would have been possible. Also, thank you to my brother and sister, Basil Wellington and Summer Taylor, for always being there for me and offering me their encouragement. I also give special thanks to Jason Mager, whose support the past few years has been invaluable.

I wish to thank the staff of Steward Observatory and the Vatican Advanced Technology Telescope for all of their help and support on this project. I especially thank Richard Boyle, Matt Nelson, and Chris Corbally for offering so much of their time and expertise during the VATT observing runs. On behalf of all MGIO observers, I wish to thank the Tucson and Safford city councils for passing strict low pressure sodium light ordinances, which make a noticeable difference in the sky brightness at Mt. Graham.

I also thank the many people that trekked up the mountain to helped me on my observing runs at the VATT. These are (in chronological order): Claudia Chiarenza, Thomas McGrath, Luis Echevarria, Hu Zhan, Seth Cohen, Stephen Odewahn, Richard de Grijs, Corey Bartley, Joe Baker, Jason Mager, and Kazuyuki Tamura. Without you, the long nights at the telescope would have been more difficult.

This research is based on observations with the Vatican Advanced Technology Telescope (VATT): the Alice P. Lennon Telescope and the Thomas J. Bannan Astrophysics Facility. It is also based on observations made with the NASA/ESA Hubble Space Telescope, obtained at the Space Telescope Science Institute, which is operated by the Association of Universities for Research in Astronomy, Inc., under NASA contract NAS 5-26555. These observations are associated with programs #8645, 9124, and 9824. This research is also based on observations made with the NASA Goddard Space Flight Center Galaxy Evolution Explorer (GALEX) under program #036.

This research was partially funded by NASA grants GO-8645.01-A, GO-9124.01-A and GO-9824.01-A, awarded by STScI, which is operated by AURA for NASA under contract NAS 5-26555. Additional funding was provided by GALEX grant #GALEXGI04-0000-0036, and the NASA Space Grant Graduate Fellowship at ASU.

TABLE OF CONTENTS

LIST OF TABLES

LIST OF FIGURES

Figure Page

CHAPTER 1

INTRODUCTION

1.1. Nearby Galaxies as Local Benchmarks for Galaxy Evolution

Technological advances such as space-based telescopes like the *Hubble Space Telescope* (*HST*) have expanded our view of the Universe to higher redshifts than ever before, giving us the opportunity to look back in time to the earliest stages of galaxy formation and evolution, to determine the mechanisms of galaxy assembly and how galaxies evolved into what we observe in the present-day Universe. The vast majority of galaxies in the Hubble Deep Fields (HDF's) appear to have characteristics resembling local irregular and peculiar/merging galaxies (e.g., Driver et al. 1995, 1998; Glazebrook et al. 1995; Abraham et al. 1996; Odewahn et al. 1996; Ellis 1997), although it is difficult to distinguish these classes at lower linear spatial resolution. Size-luminosity evolution studies show that, at the same luminosity, high redshift galaxies are more compact and less massive than nearby galaxies, as measured in both the UV and optical rest-frames (Giavalisco et al. 1996; Lowenthal et al. 1997; Ferguson et al. 2004; Trujillo et al. 2004). These authors show that high redshift galaxies are inherently different from nearby luminous galaxies, regardless of band-pass shifting effects. Therefore, the resemblance of high redshift galaxies to nearby lower-luminosity irregular and peculiar/merging galaxies may be real, and studying the stellar population distributions of nearby irregular and peculiar/merging galaxies can provide further understanding of high redshift galaxies. Furthermore, the larger fraction of merging galaxies at high redshift suggests that there was an evolution in the number of merging and interacting galaxies throughout the history of the Universe, which supports models of hierarchical galaxy formation (e.g., White 1979; White & Frenk 1991; Cole et al. 1994; Kauffmann et al. 1997; Roukema et al. 1997; Baugh et al. 1998). To reveal how galaxies assemble and evolve over time, it is therefore essential to conduct detailed comparisons of galaxies as a function of redshift.

Since the optical and near-infrared (IR) light of high redshift galaxies observed with *HST* was emitted in the rest-frame far- to mid-UV, an understanding of the fundamental UV properties of galaxies in general is crucial to our understanding of high redshift galaxies, particularly since galaxies can look substantially different at shorter wavelengths than at longer ones (e.g., Bohlin et al. 1991; Hill et al. 1992; Kuchinski et al. 2000, 2001; Marcum et al. 2001; Windhorst et al. 2002). Due to significant atmospheric extinction and the

poor response of most older thick CCD detectors below the Balmer break, large studies of the near-UV properties of galaxies, especially of the fainter irregular galaxies which seem to be analogs of the majority of high redshift galaxies, have not been feasible until the recent advent of large-format UV sensitive detectors in space, such as on the balloon-born FOCA telescope (Milliard et al. 1992), and sounding rocket and Astro/UIT flights (Bohlin et al. 1991; Hill et al. 1992; Kuchinski et al. 2000; Marcum et al. 2001), and with the *HST*/WFPC2 (Windhorst et al. 2002). The overall UV properties of galaxies in general, and of faint late-type galaxies in particular, is still rather poorly understood.

To address these issues we have obtained images of 199 nearby, mostly late-type, irregular, peculiar, and merging galaxies, with various combinations of filters for each galaxy in the far-UV through the near-IR. Wavelengths longer than the UV are necessary to properly sample a large range of stellar populations, and to effectively evaluate the dependence of galaxy structure on rest-frame wavelength. In this dissertation we therefore examine several morphological and structural parameters of this dataset as a function of wavelength, as described in Chapters 1.2–1.3. Furthermore, we compare our results to those at high redshift, and discuss possible implications for high redshift studies and our understanding of galaxy assembly and evolution.

1.2. Color Gradients

Radial color gradients can provide an indication of stellar population or metallicity distribution differences between the inner and outer regions of a galaxy (as modulated by dust), and can constrain certain mechanisms for how a galaxy assembled and subsequently evolved to its present state (Tinsley & Larson 1978; de Jong 1996). There have been several studies of the optical color gradients of sizable samples of nearby field galaxies. These include (but are not limited to) color gradients of early-type galaxies measured by Vader et al. (1988) from 35 elliptical and early-type spirals in $(B-R)$, by Franx et al. (1989) from 17 ellipticals in $(U-R)$ and $(B-R)$, by Peletier et al. (1990) from 39 ellipticals in $(U-R)$ and $(B-R)$, and by Tamura & Ohta (2003) from 51 rich galaxy cluster E and S0 galaxies in $(B-R)$. All four of these relatively large samples found that ellipticals either become bluer with radius or are constant in color, with color gradients that are generally interpreted as metallicity gradients.

Large studies of later-type galaxy color gradients were conducted by several other authors, such as Balcells & Peletier (1994), who measured color gradients from the bulges of 45 early-type spirals in *UBVRI*. De Jong (1996) determined the color gradients of 86 face-on spiral galaxies in *BVRIHK*, and Tully et al. (1996) did so for 79 galaxies in the Ursa Major cluster. Jansen et al. (2000) determined $(U-B)$ and $(B-R)$ color differences between the inner and outer regions of a sample of 196 galaxies of all Hubble types. Bell & de Jong (2000) found stellar population and metallicity gradients for their 121 spiral galaxies, and MacArthur et al. (2004) analyzed color gradients and stellar population and metallicity gradients for these plus 51 other galaxies, including some irregular galaxies.

All of these studies confirm the earlier finding (e.g., Sandage 1972; Persson et al. 1979) that spiral galaxies tend to get bluer with increasing radius. These color gradients were found to be mainly caused by stellar population gradients (de Jong 1996; Bell & de Jong 2000; MacArthur et al. 2004). However, Tully et al. (1996) and Jansen et al. (2000) find that low-luminosity ($M_B > -17$ mag), often late-type/irregular galaxies are equally likely to become bluer or redder outward. Since there is no plausible galaxy formation theory that predicts positive metallicity gradients (Vader et al. 1988), these redder outer parts are most likely due to stellar age effects or dust. Jansen et al. (2000) find that the low-luminosity galaxies that are bluer in their central regions tend to have strong central Hα emission, supporting the hypothesis that the color gradients in these galaxies are due to a few star-forming regions dominating the local colors. In more luminous massive galaxies, a single star-forming region cannot dominate the azimuthally averaged colors and, hence, the observed color gradients reflect either systematically younger populations or systematically less extinction by dust at larger distances from the center. The presence of a bulge is likely to enhance such color gradients.

Most of these previous color gradient studies have focused on earlier galaxy types (elliptical and spiral), with only a small number of irregulars included. We compliment these studies with the addition of our large sample of late-type, irregular, and merging/peculiar galaxies. The mid and near-UV data in our sample is particularly useful for color gradient analysis: because the UV is more sensitive to changes in age and metallicity, color gradients will be more apparent. This combined with the near-IR data in our sample provides a more significant color gradient due to the long base-line in wavelength coverage.

1.3. CAS Parameters

One method for examining the role of mergers in galaxy evolution is to compare and characterize galaxies by their morphological structure. Extensive work has gone into improving on the traditional Hubble sequence, which does not distinguish between the large variety of galaxies that fall into the catch-all irregular class (e.g. irregular, peculiar and merging galaxies). It is of particular importance, especially at high redshift, to find a method that quantifies the morphologies of both normal and irregular/peculiar galaxies. Hubble typing is also a somewhat subjective method of classification that requires visual inspection of each individual galaxy. With the advent of large deep sky surveys that produce images of hundreds to thousands of galaxies at a time, it is most desirable to develop an automated method of objectively classifying galaxies using a system that quantitatively describes the physical properties that shape their light distributions, independent of rest-frame wavelength.

One of the parameters developed for use in automated galaxy classification is the concentration index (C) (Abraham et al. 1994, 1996). This parameter measures how centrally concentrated the light distribution is within a galaxy, which is a tracer of the disk-to-bulge ratio, effective (or half-light) radius, and the stellar population distribution. Abraham et al. (1994, 1996) show that classifications using this parameter are less dependent on high

spatial resolution than Hubble typing, and thus are more robust at high redshift and in poor ground-based seeing conditions. Schade et al. (1995) introduced the rotational asymmetry index (A) to describe the degree of peculiarity and asymmetry in the light-distribution of galaxies imaged with HST at redshifts of z $\sim$ 0.5-1.2. This parameter is particularly useful in identifying merging and strongly interacting galaxies, which tend to have high asymmetries. Another parameter was introduced by Isserstedt & Schindler (1986) as a ratio of the smoothly distributed light distribution to the clumped light distribution. This clumpiness index (S) compares the amount of light in star-forming clusters and associations to the light in a more diffuse older disk population, which correlates with hydrogen recombination lines (Hα) (Takamiya 1999), and gives an indication of the recent star-formation activity within the galaxy.

Other authors proposed improved methods of measuring these concentration, asymmetry, and clumpiness (CAS) parameters, making them less sensitive to choice of center, surface-brightness cut-offs, signal-to-noise, and resolution effects (e.g. Bershady et al. 2000; Conselice et al. 2000; Lotz et al. 2004). The CAS parameters were found to correlate with each-other, as well as other fundamental parameters such as galaxy color, luminosity, size, surface brightness, and star formation rate (Isserstedt & Schindler 1986; Abraham et al. 1996; Takamiya 1999; Bershady et al. 2000; Corbin et al. 2001). Galaxy types are separated-out within parameter spaces involving color, surface brightness, and various combinations of the CAS parameters, providing a method of galaxy classification that is relatively robust over a large range of redshifts (Bershady et al. 2000; Conselice et al. 2000, 2003a; Conselice 2003b).

Since galaxies can look substantially different at shorter wavelengths than at longer ones (e.g., Bohlin et al. 1991; Hill et al. 1992; Kuchinski et al. 2000, 2001; Marcum et al. 2001; Windhorst et al. 2002) the morphological k-correction may be significant, and CAS measurements for low and high redshift galaxies may not be directly comparable. For example, Schade et al. (1995) found that their galaxies (z = 0.5–1.2) looked more irregular in their B images (rest-frame UV) than at longer wavelengths, which may affect the asymmetry index measurement in that pass-band. Jansen (2000) noted a similar systematic shift from U to R for galaxies in the Nearby Field Galaxy Survey. We also observe this effect when comparing HST/WFPC2 UV and near-infrared (IR) images available for a subset of our galaxies as presented in Windhorst et al (2002). To address this problem, in this work we quantitatively analyze how the CAS parameters vary as a function of wavelength and morphological type for our sample of 199 objects.

1.4. Outline of This Work

The results of this work are organized as follows. In Chapter 2[1], we present the results of the color gradient analysis of our dataset, along with a comparison of our results to those of other authors at both low and high redshifts. We also discuss the possible

[1]Originally published as: Taylor, V.A., Jansen, R.A., Windhorst, R.A., Odewahn, S.C., & Hibbard, J.E. 2005, The Astrophysical Journal, Vol. 630, pp.784–803

implications of these results on galaxy assembly and evolution theories. In Chapter 3, we present the results of the CAS parameter analysis of our dataset, including the relationship of these parameters with galaxy color, galaxy type, and rest-frame wavelength. We discuss the implications of these results on the morphological k-correction, and offer a possible evolutionary scenario of mergers through the CAS parameter space. In Chapter 4[2], we present measurements of the data quality of our ground-based images through a study of the observing conditions at the site from which they were obtained, the Vatican Advanced Technology Telescope (VATT) at Mt. Graham International Observatory (MGIO). We present seeing and sky surface brightness measurements obtained from our images and discuss their trends. In Chapter 5, we present concluding remarks on the color gradient and CAS parameter studies.

[2]Originally published as: Taylor, V.A., Jansen, R.A., & Windhorst, R.A., 2004, Publications of the Astronomical Society of the Pacific, Vol. 116, pp.762–777

CHAPTER 2

RADIAL COLOR GRADIENTS OF LATE-TYPE GALAXIES

2.1. Overview of Chapter 2.

In order to address the deficit of published color gradient studies for a large, homogeneous sample of irregular, peculiar, and merging galaxies across a large range of optical wavelengths, we present measurements of radial color gradients for a sample of 142 mostly late-type spiral, irregular, and peculiar (interacting or merging) nearby galaxies observed in $UBVR$ at the Vatican Advanced Technology Telescope (VATT). We also analyze the color gradients of six nearby galaxies observed by HST with NICMOS in the near-IR (H) and with WFPC2 in the mid-UV (F300W) and red (F814W). We confirm that nearby elliptical and early- to mid-type spiral galaxies show either no or only small color gradients, becoming slightly bluer with radius. In contrast, we find that late-type spiral, irregular, peculiar, and merging galaxies become on average redder with increasing distance from the center. The scatter in radial color gradient trends increases toward later Hubble type.

We discuss these datasets in Section 2 and describe the data analysis in Section 3. In Section 4 we discuss our results, complementing the findings of previous studies and increasing the database of color gradients to include a larger sample of irregular and peculiar/merging galaxies. In Section 5 we compare our results to those of the high-redshift universe, and discuss possible implications on galaxy formation and evolution.

2.2. Data Acquisition and Reduction

2.2.1. *Sample Selection*

We selected 82 galaxies from the RC3 (de Vaucouleurs et al. 1991) with (1) types later than or equal to Sd (de Vaucouleurs type $7 \leqq \mathrm{T} \leqq 10$), (2) sizes small enough to comfortably fit within the $\sim 6.4'$ FOV of the VATT imager (to ensure accurate subtraction of the sky background), and (3) B-band surface brightness[1] brighter than $\mu_B = 25$ mag arcsec^{-2}, to ensure efficient imaging at the VATT and with *HST*. The median diameter of the galaxies in this sample is $\sim 1.4'$, and the median surface brightness is ~ 23.0 mag arcsec^{-2}. We supplemented this sample with 23 galaxies from the list of Hibbard & Vacca (1997), which

[1] RC3 total B-band magnitude per unit area within the RC3 25 mag arcsec^{-2} B-band isophote.

contains UGC galaxies classified as peculiar or interacting. We imposed the same size and surface brightness criteria while excluding galaxies already imaged by John Hibbard and collaborators. Lastly, for comparison we included 13 earlier type galaxies (T < 7) and 24 peculiar or unclassified galaxies that were observed for other projects. The total sample therefore contains 142 galaxies, most of which are irregular or peculiar/merging.

Figure 1 shows the resulting Hubble type distribution of our galaxy sample. It shows both the distribution of types from the RC3 and from our own visual classifications, which are the average of the values assigned to each galaxy by three different observers (V.A.T., S.C.O., S.H.C.)[2] experienced with classifying galaxies. A type of T $= -9$ was assigned to the rare cases where no classification could be determined. Because mergers may play an important role in galaxy evolution via hierarchical galaxy formation models, a type of T $= 14$ was assigned to those galaxies that appeared to be interacting, or in the stages of a merger or post-merger. This extra class was created so that galaxies under the special condition of interactions and mergers could be treated separately. The bottom panel of Figure 1 compares our classifications to those of the RC3, which for the most part agree. Differences between our classifications and those of the RC3 are partially due to galaxies that were unclassified in the RC3 being classifiable from our CCD images. Additionally, our classifiers classified several RC3 irregular types as late-type spirals. This misclassification in the RC3 is also evident in the *HST* images of Windhorst et al. (2002), and is due to the difficulty of accurately classifying these small, faint galaxies with the photographic plates used for the RC3. These plates had lower spatial resolution, signal-to-noise, and dynamic range than our VATT CCD and *HST* images, such that faint spiral structure may have been missed.

Since most of our sample was chosen from the RC3, biases that are inherent in the RC3 itself will also exist in our own sample. We can test for the consistency of our sample with respect to the RC3 through a comparison between the samples of several quantities. Figure 2 compares the (a) 25 mag arcsec^{-2} B-band isophotal diameter, (b) axis ratio (b/a), (c) total B-band magnitude (B_T), and (d) total ($B-V$) color distributions of the RC3 to the measurements for our sample. Only galaxies with diameters less than the $\sim 6'$ FOV of the VATT CCD are included in Figure 2a. This does not affect the shape of the distribution, since only $\lesssim 1\%$ of the galaxies in the RC3 have diameters larger than $6'$. Our diameter distribution closely resembles that of the RC3. Figure 2b shows that our sample is underrepresented in very flat galaxies, which is to be expected from the deficit of early- to mid-type spiral galaxies in our sample, which are more likely to appear flat when viewed edge-on. Our sample also peaks at a slightly fainter B_T magnitude and a much bluer $(B-V)_T$ color than the RC3 (Figure 2c and 2d, respectively). This is also to be expected with a late-type galaxy-selected sample, because later-type galaxies are on average fainter and bluer than earlier-type galaxies.

The high resolution of *HST* images allows us to resolve individual stars or associations, which provides further, more detailed information about the distribution of metallicity

[2]Violet A. Taylor, Stephen C. Odewahn, and Seth H. Cohen; Arizona State University

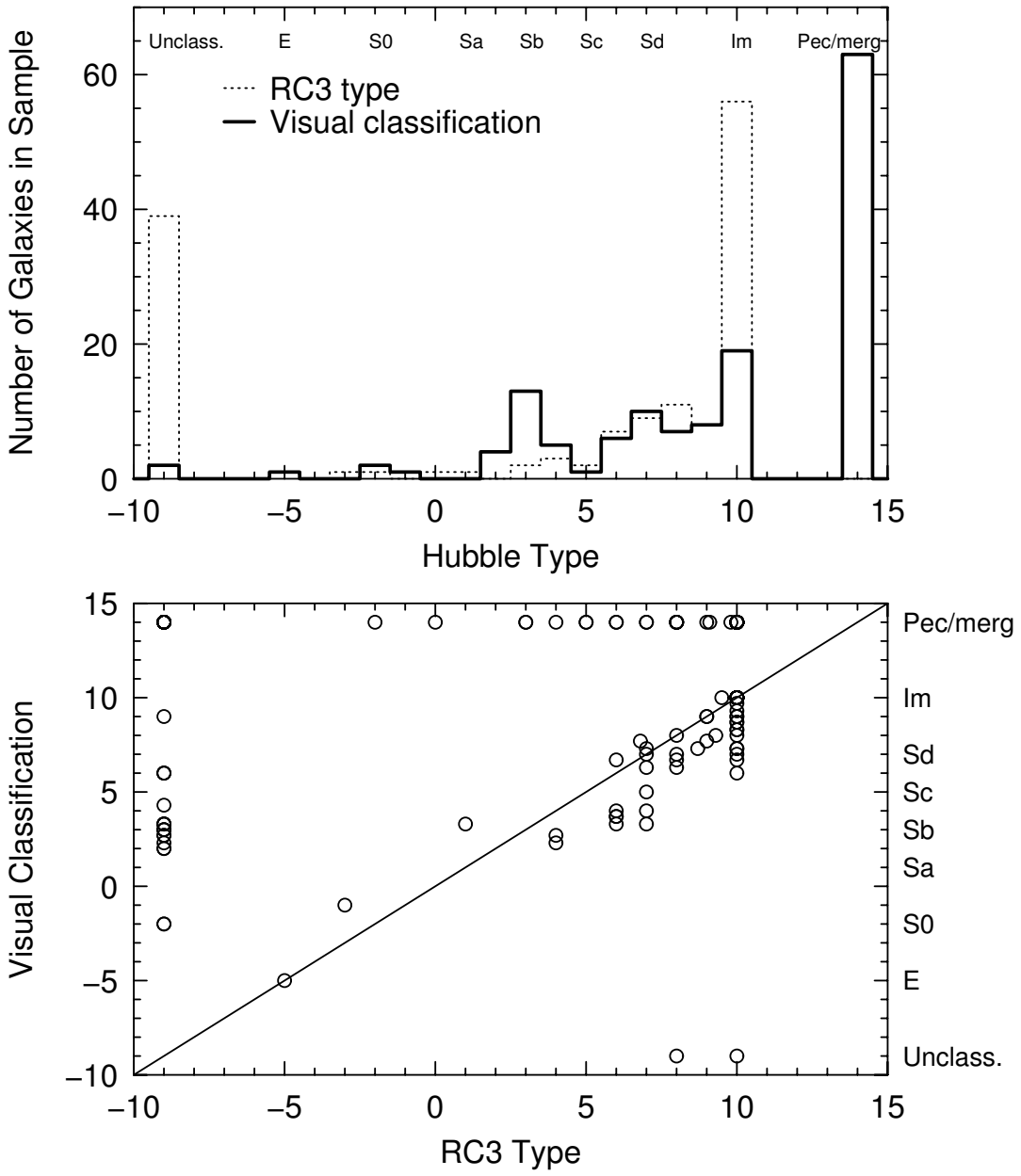

Figure 1 **Top panel:** Distribution of morphological type in our sample of 142 galaxies, using classifications as listed in the RC3 (*dotted*) and as determined from our VATT *R*-filter images (*solid*). A numeric type T=−9 indicates that no type was given in the RC3, or that it appeared unclassifiable by all of our classifiers. A type of T = 14 indicates that our classifiers determined that the object was a strongly interacting galaxy pair, galaxies in the process of merging, or a likely merger remnant. Our sample concentrates on late-type, irregular, and peculiar/merging galaxies. **Bottom panel:** Comparison of RC3 types to our visual classifications. Several RC3 irregular type galaxies were classified by our classifiers as late-type spirals, which may be due to faint spiral structure not being visible in the photographic plates used to classify these small, faint galaxies for the RC3.

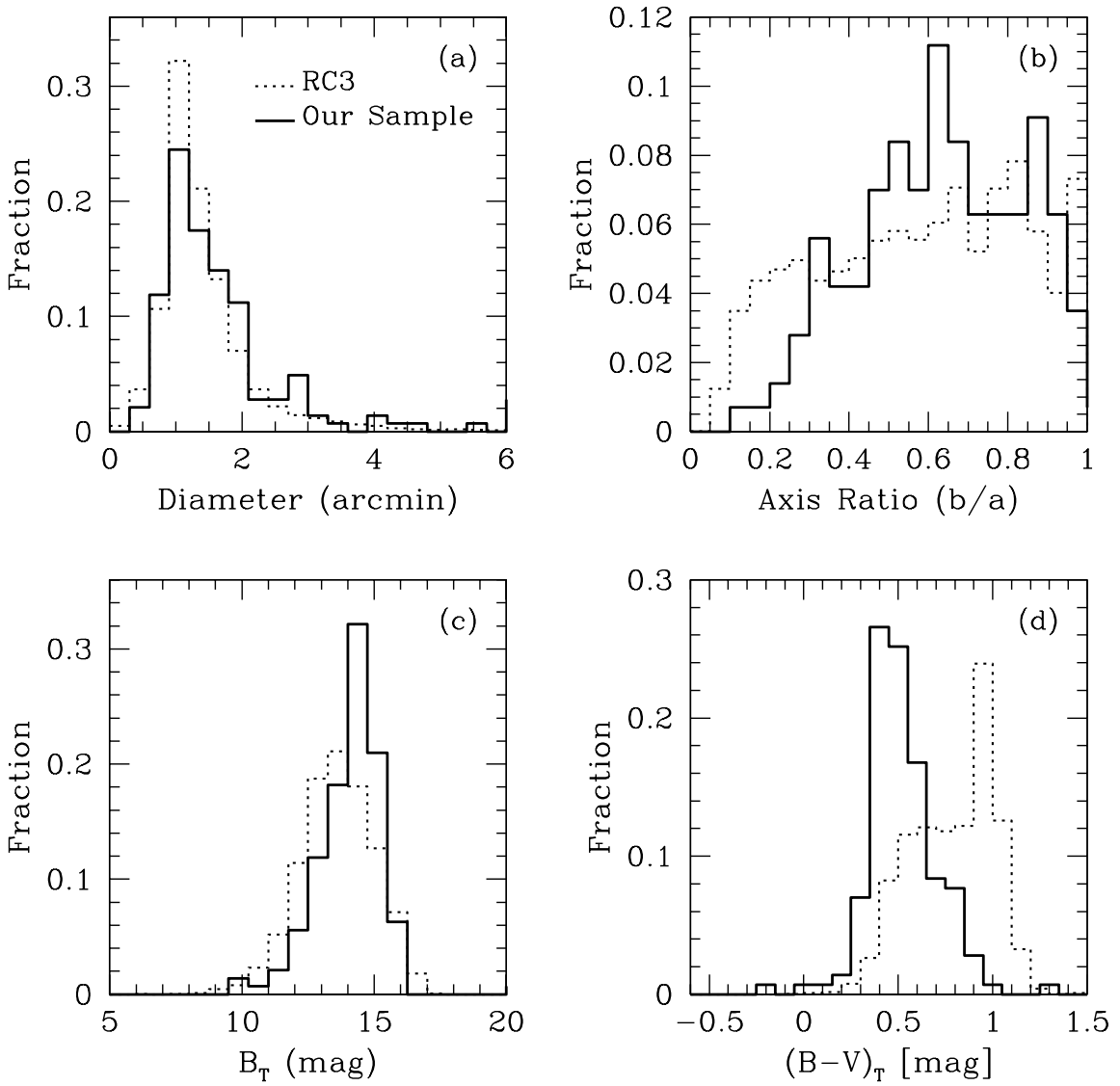

Figure 2 Distribution of the (a) 25 mag arcsec^{-2} B-band isophotal diameter, (b) axis ratio (b/a), (c) total B-band magnitude (B_T), and (d) total $(B-V)_T$ color of all galaxies in our sample (*solid*) compared to that in the RC3 (*dotted*). The diameter distribution of the galaxies in our sample is similar to that of the RC3. Our sample is underrepresented in very flat galaxies, which is expected from the selection effects of our particular sample, since late-type galaxies will not be as flat as earlier-type spiral galaxies when viewed edge-on. Our sample peaks at a slightly fainter B_T magnitude than the RC3, which is dominated by more luminous early-type galaxies. The bluer $(B-V)$ color in our sample is the direct result of our selection of UV-bright, late-type galaxies.

and stellar populations within a galaxy. The addition of H-band *HST* images removes some of the dust degeneracy in a color analysis, considerably improving stellar population measurements over optical colors alone (Cardiel et al. 2003). Therefore, we include an analysis of six galaxies observed with *HST* NICMOS, which are part of a larger sample of 136 galaxies observed in the mid-UV (F300W) and near-IR (F814W) by WFPC2 (Windhorst et al. 2002; Eskridge et al. 2003; de Grijs et al. 2003), which overlaps significantly with our VATT sample. The entire *HST* data-set will be analyzed in more detail in Chapter 3. The *HST* sample was chosen to include galaxies that were predicted to be UV bright and small enough for most of the galaxy to fit within the WFPC2 FOV.

2.2.2. *Observations*

We obtained our ground-based observations at the VATT at Mt. Graham International Observatory (MGIO, AZ) with the 2k×2k Direct Imager because of its high sensitivity in the near-UV, which is critical for our ultimate science goals. The effective quantum efficiency in U is ∼40%, which includes transmission loss through the atmosphere combined with the ∼75% transmission of the CCD and the ∼67% transmission of the filter.[3] We binned the CCD images 2×2 upon read-out, giving a pixel scale of ∼0.375 arcsec pixel^{-1}. The typical seeing at the VATT is well sampled by this pixel scale. The detector read-noise is 5.7 e^- and the gain is 1.9 e^- ADU^{-1}. Typical exposure times used for the galaxies in our sample were 2×600 s in U, 2×300 s in B, 2×240 s in V, and 2×180 s in R for galaxies with average total surface brightness brighter than $\mu_B = 24.0$ mag arcsec^{-2}, and twice these exposure times for lower surface brightness galaxies. The long exposure times in U and B relative to V and R were chosen to overcome the lower sensitivity and higher atmospheric extinction in these pass-bands, such that colors within the galaxies can be reliably measured at larger radii before the low surface brightness U and B light is lost within the sky noise. Observations were spread over 9 runs between April 1999 and April 2002. Photometric nights were defined as those with magnitudes measured for a particular standard star varying no more than 3% throughout the night. During photometric nights, short photometric exposures were taken of galaxies that were observed during non-photometric conditions.

Table 1 contains a list of all 142 galaxies for which we obtained a full set of calibrated observations in $UBVR$. The full table is available only in the electronic edition. Each galaxy is assigned an internal ID number (column 1), which we will use for brevity throughout the remainder of this chapter when referring to a particular galaxy. The average sky background level in each image was determined by taking the median of the median pixel values in 13 120×120 pixel regions along the image border that were relatively devoid of objects. Thus, we minimize contamination by light from the galaxy, which is usually centered within each image. Taking the median values also helps to reject stars, background galaxies, and cosmic rays. Sky gradients have little effect on these sky measurements since, after flat fielding, the sky background in each image on scales of ∼6′ is flat to better than 1%, and typically to ∼0.5% in each of the filters. These sky-values were used in the reduction process, but local

[3] http://clavius.as.arizona.edu/vo/R1024/vattinst.html

and global sky-values were recalculated in a more sophisticated way where appropriate, as described in sections below. Table 1 lists these sky background levels (column 11) and corresponding sky surface brightnesses (column 13) and seeing estimates (column 14) determined from the median stellar FWHM (full width at half max) in each image, using the method described in Chapter 4, where the sky surface brightness and seeing trends in these VATT data are analyzed in more detail.

The near-IR *HST* NICMOS H-band data, summarized in Table 2, were taken as part of Cycle 12 SNAP-shot program #9824 (P.I.: R. Windhorst), using NIC3 in the near-IR (F160W, $\lambda_c = 15,500$Å, or 1.55 μm). Three 500 s exposures were taken of each galaxy. Since NIC3 has a small FOV of $51.2''$, we dithered by about 45 pixels between the three observations to include more of the galaxy in the final mosaic and to facilitate bad pixel removal. The NIC3 detector has a pixel scale of $\sim$0.20 arcsec pixel^{-1}. The *HST*/WFPC2 mid-UV (F300W, $\lambda_c = 2992$Å) and I (F814W, $\lambda_c = 8002$Å) data (see Table 2) were taken as part of Cycle 9 GO program #8645 (Windhorst et al. 2002) or Cycle 10 SNAP-shot program #9124 (P.I.: R. Windhorst; Jansen et al. 2005, in preparation). We combined the two separate exposures per filter and the images of all four WFPC2 cameras into a single mosaic. Individual exposures in the mid-UV F300W filter were typically 300–1000 s, while we exposed 40–130 s in I. For the Cycle 9 data, the two individual exposures per filter were dithered by $\sim$4 pixels to facilitate rejection of bad pixels. The pixel scale in the combined WFPC2 images is $\sim$0.0996 arcsec pix^{-1}.

2.2.3. *VATT Data Reduction and Calibration*

The median dark signal (column 2) and dark rates (column 4) measured in six dark images taken in April 2001 are listed in Table 3. Because these exposures were taken during the day when some sunlight may have leaked onto the detector, they represent an upper limit of the actual dark current, which may be even smaller. There is an average dark current of 7.54 ± 0.21 ADU hr^{-1}, which results in a worst case scenario (column 5) of 2.51 ± 0.07 ADU in our longest exposure of 1200 seconds in the U-band, and which is very small compared to the median U sky of 492 ± 12 ADU. If dark current is neglected, this leads to a possible average error in the absolute sky determinations of 0.51% in U, 0.16% in B, 0.08% in V, and 0.05% in R (which only matters when finding the absolute sky surface brightnesses, and will not affect the galaxy photometry, even to second order). Much larger errors can be introduced through various other uncertainties in the photometry, and subtracting a dark image will only introduce another source of noise without any benefit to the large-scale galaxy surface photometry. Therefore, we did not subtract a dark image or a, likely overestimated, constant dark level from the images.

All images were zero subtracted, flat fielded, and calibrated with Landolt standard stars (Landolt 1992) using standard methods in IRAF.[4] The photometric zero-point for all

[4]IRAF is distributed by the National Optical Astronomy Observatories, which are operated by the Association of Universities for Research in Astronomy, Inc., under cooperative agreement with the National Science Foundation.

Table 1. Observed VATT Galaxy List.

ID#	Galaxy	RA	DEC	T_{RC3}	T	Filter	N_{exp}	T_{exp}	*Secz*	Sky	σ_{sky}	μ_{sky}	Seeing	σ_{seeing}	Obs. date	Phot?
(1)	(2)	(3)	(4)	(5)	(6)	(7)	(8)	(9)	(10)	(11)	(12)	(13)	(14)	(15)	(16)	(17)
001	UGC00156	$00^h16^m46^s.30$	$+12°21'13''.1$	10.0	9.3	U	2.0	1200.0	1.068	624.654	2.498	20.98	1.554	0.089	1999 Dec 07	n
...	...	...	...	...	...	B	2.0	600.0	1.073	971.057	3.935	21.67	1.470	0.115	1999 Dec 07	n
...	...	...	...	...	...	V	2.0	480.0	1.079	1666.022	13.948	20.65	1.403	0.044	1999 Dec 07	n
...	...	...	...	...	...	R	2.0	360.0	1.069	2230.095	17.548	20.00	1.963	0.153	1999 Dec 08	n
002	UGC00404	$00^h39^m19^s.17$	$+13°06'40''.3$	8.0	14.0	U	2.0	1200.0	1.108	654.128	5.195	20.99	1.965	0.119	1999 Dec 07	n
...	...	...	...	...	...	B	2.0	600.0	1.114	1024.339	18.580	21.53	1.680	0.163	1999 Dec 07	n
...	...	...	...	...	...	V	2.0	480.0	1.121	1762.469	18.790	20.73	1.374	0.103	1999 Dec 07	n
...	...	...	...	...	...	R	3.0	360.0	1.064	2195.478	41.374	20.06	2.021	0.186	1999 Dec 08	n
003	UGC00512	$00^h50^m02^s.59$	$+07°54'55''.3$	8.0	14.0	U	2.0	1200.0	1.342	740.667	4.676	20.78	1.845	0.077	1999 Dec 07	n
...	...	...	...	...	...	B	2.0	600.0	1.355	1211.626	6.261	21.15	1.813	0.056	1999 Dec 07	n
...	...	...	...	...	...	V	2.0	480.0	1.369	2221.780	23.531	20.54	1.691	0.045	1999 Dec 07	n
...	...	...	...	...	...	R	2.0	360.0	1.103	2380.214	16.848	19.94	1.926	0.133	1999 Dec 08	n
004	UGC00644	$01^h03^m16^s.65$	$+14°02'01''.6$	-9.0	14.0	U	2.0	600.0	1.436	328.397	2.273	20.88	1.905	0.175	1999 Dec 05	n
...	...	...	...	...	...	B	2.0	300.0	1.441	549.109	5.125	21.46	2.017	0.103	1999 Dec 05	n
...	...	...	...	...	...	V	2.0	240.0	1.446	961.138	13.536	20.56	1.742	0.047	1999 Dec 05	n
...	...	...	...	...	...	R	2.0	180.0	1.056	993.174	10.910	20.05	1.354	0.102	1999 Dec 06	n
005	UGC00749	$01^h11^m30^s.28$	$+01°19'10''.9$	8.0	14.0	U	2.0	600.0	1.186	313.720	1.674	20.98	2.239	0.215	1999 Dec 08	n
...	...	...	...	...	...	B	2.0	300.0	1.188	509.273	6.873	21.83	2.257	0.200	1999 Dec 08	n
...	...	...	...	...	...	V	2.0	240.0	1.190	901.062	11.823	20.61	2.130	0.176	1999 Dec 08	n
...	...	...	...	...	...	R	2.0	180.0	1.173	1032.213	17.354	19.89	1.266	0.153	1999 Dec 06	n
006	UGC00849	$01^h19^m23^s.03$	$+12°26'57''.4$	8.0	14.0	U	2.0	1200.0	1.173	555.018	3.437	21.16	2.398	0.625	1999 Dec 05	n
...	...	...	...	...	...	B	2.0	600.0	1.180	941.693	7.004	21.71	2.122	0.065	1999 Dec 05	n
...	...	...	...	...	...	V	2.0	480.0	1.189	1617.641	14.125	20.81	1.879	0.040	1999 Dec 05	n
...	...	...	...	...	...	R	2.0	360.0	1.075	1885.133	17.085	19.97	1.425	0.188	1999 Dec 06	n
007	UGC01104	$01^h32^m43^s.47$	$+18°19'01''.4$	10.0	10.0	U	2.0	600.0	1.080	321.698	1.520	20.20	1.860	0.167	2002 Jan 18	n
...	...	...	...	...	...	B	2.0	300.0	1.077	632.436	2.407	20.73	2.092	0.375	2002 Jan 18	n
...	...	...	...	...	...	V	2.0	240.0	1.077	1019.565	4.676	19.81	1.879	0.144	2002 Jan 18	n
...	...	...	...	...	...	R	2.0	180.0	1.076	1320.217	14.134	19.44	1.819	0.148	2002 Jan 18	n
008	UGC01133	$01^h35^m00^s.85$	$+04°23'11''.8$	10.0	14.0	U	2.0	1200.0	1.167	572.971	3.850	20.95	1.729	0.104	1999 Dec 04	n
...	...	...	...	...	...	B	2.0	600.0	1.174	941.990	8.528	21.59	1.729	0.154	1999 Dec 04	n
...	...	...	...	...	...	V	2.0	480.0	1.181	1618.724	14.945	20.76	1.521	0.201	1999 Dec 04	n
...	...	...	...	...	...	R	2.0	360.0	1.156	2233.333	25.213	19.42	1.118	0.048	1999 Dec 06	n
009	UGC01219	$01^h44^m20^s.13$	$+17°28'42''.9$	-9.0	3.0	U	2.0	600.0	1.068	184.311	0.804	21.27	1.447	0.169	2002 Jan 15	n
...	...	...	...	...	...	B	2.0	300.0	1.065	357.344	1.232	21.63	1.824	0.183	2002 Jan 15	n
...	...	...	...	...	...	V	2.0	240.0	1.064	542.139	1.726	20.94	1.744	0.276	2002 Jan 15	n
...	...	...	...	...	...	R	2.0	180.0	1.063	718.337	1.929	20.14	1.665	0.212	2002 Jan 15	n
010	UGC01240	$01^h46^m19^s.56$	$+04°15'52''.5$	8.0	14.0	U	2.0	600.0	1.273	290.342	2.543	21.11	1.991	0.117	1999 Dec 04	n
...	...	...	...	...	...	B	2.0	300.0	1.275	465.680	5.036	21.69	1.901	0.137	1999 Dec 04	n
...	...	...	...	...	...	V	2.0	240.0	1.278	823.495	8.784	20.75	2.070	0.041	1999 Dec 04	n
...	...	...	...	...	...	R	2.0	180.0	1.167	1215.579	14.472	18.73	1.211	0.076	1999 Dec 06	n

Table 1—Continued

ID#	Galaxy	RA	DEC	T_{RC3}	T	Filter	N_{exp}	T_{exp}	*Secz*	Sky	σ_{sky}	μ_{sky}	Seeing	σ_{seeing}	Obs. date	Phot?
(1)	(2)	(3)	(4)	(5)	(6)	(7)	(8)	(9)	(10)	(11)	(12)	(13)	(14)	(15)	(16)	(17)
011	UGC01449	$01^h58^m04^s.15$	$+03°05'57''.2$	9.1	14.0	U	2.0	600.0	1.223	339.404	1.532	20.81	2.261	0.123	1999 Dec 08	n
...	...	...	...	...	...	B	2.0	300.0	1.225	505.730	3.034	21.56	2.040	0.116	1999 Dec 08	n
...	...	...	...	...	...	V	2.0	240.0	1.228	890.307	4.748	20.65	1.852	0.094	1999 Dec 08	n
...	...	...	...	...	...	R	2.0	180.0	1.228	988.962	5.977	20.17	2.010	0.050	1999 Dec 08	n
012	UGC01753	$02^h16^m34^s.98$	$+28°12'16''.1$	10.0	8.7	U	2.0	600.0	1.135	204.143	1.471	21.02	2.046	0.129	2002 Jan 18	n
...	...	...	...	...	...	B	2.0	300.0	1.130	453.015	2.767	21.01	1.747	0.086	2002 Jan 18	n
...	...	...	...	...	...	V	2.0	240.0	1.110	635.966	3.046	20.82	1.764	0.121	2002 Jan 18	n
...	...	...	...	...	...	R	2.0	180.0	1.092	970.427	5.011	19.74	1.877	0.100	2002 Jan 18	n
013	NGC0959	$02^h32^m23^s.45$	$+35°29'20''.1$	8.0	7.0	U	2.0	600.0	1.126	206.496	1.338	21.30	1.260	0.087	2002 Jan 15	n
...	...	...	...	...	...	B	2.0	300.0	1.121	362.814	1.793	21.86	1.421	0.114	2002 Jan 15	n
...	...	...	...	...	...	V	2.0	240.0	1.120	565.639	1.972	21.10	1.226	0.083	2002 Jan 15	n
...	...	...	...	...	...	R	2.0	180.0	1.120	662.323	2.855	20.45	1.127	0.077	2002 Jan 15	n
014	NGC1156	$02^h59^m41^s.41$	$+25°13'37''.5$	10.0	10.0	U	2.0	600.0	1.247	220.250	1.488	21.19	1.717	0.166	2002 Jan 15	n
...	...	...	...	...	...	B	2.0	300.0	1.242	383.013	2.387	21.78	1.507	0.112	2002 Jan 15	n
...	...	...	...	...	...	V	2.0	240.0	1.240	606.287	3.019	20.97	1.408	0.106	2002 Jan 15	n
...	...	...	...	...	...	R	2.0	180.0	1.240	685.015	3.247	20.45	1.159	0.136	2002 Jan 15	n
015	NGC1614	$04^h33^m59^s.20$	$-08°35'56''.3$	5.0	14.0	U	2.0	600.0	1.813	235.943	1.170	21.77	1.472	0.040	2001 Feb 21	y
...	...	...	...	...	...	B	2.0	300.0	1.825	349.783	1.700	22.32	1.440	0.116	2001 Feb 21	y
...	...	...	...	...	...	V	2.0	240.0	1.836	644.434	2.542	21.20	1.466	0.054	2001 Feb 21	y
...	...	...	...	...	...	R	2.0	180.0	1.828	864.038	2.737	20.44	1.268	0.077	2001 Feb 21	y
016	UGC03690	$07^h09^m10^s.37$	$+53°24'59''.8$	10.0	14.0	U	2.0	1198.5	1.149	629.734	1.757	21.35	1.657	0.094	2002 Jan 20	y
...	...	...	...	...	...	B	2.0	600.0	1.153	1053.816	2.274	21.69	1.729	0.117	2002 Jan 20	y
...	...	...	...	...	...	V	2.0	480.0	1.157	1185.539	3.133	21.19	1.511	0.125	2002 Jan 20	y
...	...	...	...	...	...	R	2.0	360.0	1.163	1338.578	4.339	20.58	1.511	0.134	2002 Jan 20	y
017	UGC03748	$07^h15^m26^s.12$	$+65°26'18''.7$	10.0	-9.0	U	2.0	1200.0	1.417	487.021	2.116	21.20	3.152	0.175	1999 Dec 03	n
...	...	...	...	...	...	B	2.0	600.0	1.423	770.766	3.977	21.91	3.497	0.133	1999 Dec 03	n
...	...	...	...	...	...	V	2.0	480.0	1.433	1423.927	5.591	20.91	3.302	0.101	1999 Dec 03	n
...	...	...	...	...	...	R	2.0	360.0	1.519	2613.264	3.722	19.12	1.748	0.088	1999 Dec 06	n
018	UGC03860	$07^h28^m19^s.58$	$+40°46'22''.6$	10.0	10.0	U	2.0	600.0	1.012	181.589	1.311	21.26	1.429	0.083	2002 Jan 15	n
...	...	...	...	...	...	B	2.0	300.0	1.013	319.321	2.270	21.87	1.509	0.079	2002 Jan 15	n
...	...	...	...	...	...	V	2.0	240.0	1.015	485.106	2.525	21.13	1.260	0.062	2002 Jan 15	n
...	...	...	...	...	...	R	2.0	180.0	1.016	600.979	3.041	20.40	1.361	0.078	2002 Jan 15	n
019	NGC2415	$07^h36^m45^s.09$	$+35°14'38''.7$	10.0	14.0	U	2.0	600.0	1.402	227.671	2.843	21.04	1.875	0.062	2002 Jan 15	n
...	...	...	...	...	...	B	2.0	300.0	1.402	417.237	8.044	21.66	1.421	0.075	2002 Jan 15	n
...	...	...	...	...	...	V	2.0	240.0	1.402	708.451	7.444	20.82	1.309	0.054	2002 Jan 15	n
...	...	...	...	...	...	R	2.0	180.0	1.403	830.432	6.830	20.25	1.178	0.035	2002 Jan 15	n
020	UGC04079	$07^h55^m07^s.13$	$+55°42'31''.6$	-9.0	14.0	U	2.0	600.0	1.091	166.868	0.785	21.50	1.710	0.118	2002 Jan 15	n
...	...	...	...	...	...	B	2.0	300.0	1.089	281.507	0.747	22.04	1.624	0.188	2002 Jan 15	n
...	...	...	...	...	...	V	2.0	240.0	1.089	450.462	0.953	21.22	1.551	0.138	2002 Jan 15	n
...	...	...	...	...	...	R	2.0	180.0	1.088	516.975	1.680	20.68	1.472	0.133	2002 Jan 15	n

Table 1—Continued

ID#	Galaxy	RA	DEC	T_{RC3}	T	Filter	N_{exp}	T_{exp}	*Secz*	Sky	σ_{sky}	μ_{sky}	Seeing	σ_{seeing}	Obs. date	Phot?
(1)	(2)	(3)	(4)	(5)	(6)	(7)	(8)	(9)	(10)	(11)	(12)	(13)	(14)	(15)	(16)	(17)
021	UGC04095	$07^h56^m50\overset{s}{.}08$	$+66°36'24\overset{''}{.}5$	-9.0	6.0	U	2.0	600.0	1.431	364.682	3.887	20.75	2.027	0.281	1999 Dec 07	n
...	...	...	...	...	...	B	2.0	300.0	1.432	521.820	9.412	21.55	2.089	0.105	1999 Dec 07	n
...	...	...	...	...	...	V	2.0	240.0	1.434	1014.471	12.342	20.49	2.143	0.075	1999 Dec 07	n
...	...	...	...	...	...	R	2.0	180.0	1.392	1540.121	3.811	17.96	2.004	0.370	1999 Dec 06	n
022	UGC04098	$07^h57^m18\overset{s}{.}19$	$+66°26'09\overset{''}{.}1$	-9.0	3.3	U	2.0	600.0	1.311	358.919	1.430	20.82	2.291	0.046	1999 Dec 07	n
...	...	...	...	...	...	B	2.0	300.0	1.312	495.082	2.402	21.61	2.096	0.066	1999 Dec 07	n
...	...	...	...	...	...	V	2.0	240.0	1.313	939.261	2.878	20.61	2.089	0.045	1999 Dec 07	n
...	...	...	...	...	...	R	2.0	180.0	1.258	1153.630	3.914	19.16	1.914	0.131	1999 Dec 06	n
023	UGC04182	$08^h03^m47\overset{s}{.}95$	$+61°20'11\overset{''}{.}5$	-9.0	14.0	U	2.0	600.0	1.314	284.701	1.504	21.54	3.060	0.195	1999 Apr 10	y
...	...	...	...	...	...	B	2.0	240.0	1.242	359.972	2.580	21.91	3.163	0.143	1999 Apr 10	y
...	...	...	...	...	...	V	2.0	300.0	1.314	974.568	3.181	20.86	2.426	0.153	1999 Apr 10	y
...	...	...	...	...	...	R	2.0	180.0	1.228	825.406	2.657	20.33	2.363	0.176	1999 Apr 10	y
024	UGC04261	$08^h11^m01\overset{s}{.}71$	$+36°50'42\overset{''}{.}2$	-9.0	14.0	U	2.0	600.0	1.314	259.699	1.620	20.63	2.021	0.146	2001 Apr 23	n
...	...	...	...	...	...	B	2.0	300.0	1.308	404.186	3.168	21.67	1.719	0.113	2001 Apr 23	n
...	...	...	...	...	...	V	2.0	240.0	1.300	660.957	4.048	20.87	1.665	0.080	2001 Apr 23	n
...	...	...	...	...	...	R	2.0	180.0	1.287	707.307	4.301	20.38	1.523	0.053	2001 Apr 23	n
025	UGC04434	$08^h28^m54\overset{s}{.}30$	$+34°39'04\overset{''}{.}9$	-9.0	14.0	U	2.0	600.0	1.084	192.047	1.267	21.30	1.669	0.037	2002 Jan 15	n
...	...	...	...	...	...	B	2.0	300.0	1.082	350.859	1.463	21.40	1.455	0.051	2002 Jan 15	n
...	...	...	...	...	...	V	2.0	240.0	1.081	573.295	1.973	20.78	1.305	0.096	2002 Jan 15	n
...	...	...	...	...	...	R	2.0	180.0	1.081	660.757	2.177	20.31	1.312	0.053	2002 Jan 15	n
026	UGC04438	$08^h29^m58\overset{s}{.}87$	$+52°41'51\overset{''}{.}3$	-9.0	2.3	U	2.0	600.0	1.085	363.133	1.424	20.88	2.539	0.093	1999 Dec 05	n
...	...	...	...	...	...	B	2.0	300.0	1.087	480.172	2.697	21.70	2.312	0.238	1999 Dec 05	n
...	...	...	...	...	...	V	3.0	240.0	1.095	848.198	2.500	20.77	2.235	0.182	1999 Dec 05	n
...	...	...	...	...	...	R	2.0	180.0	1.779	1525.236	4.209	18.89	2.479	0.098	1999 Dec 06	n
027	UGC04459	$08^h34^m07\overset{s}{.}45$	$+66°10'16\overset{''}{.}7$	10.0	14.0	U	2.0	1200.0	1.379	517.183	2.802	21.07	3.696	0.466	1999 Dec 03	n
...	...	...	...	...	...	B	2.0	600.0	1.389	790.396	5.447	21.80	3.457	0.177	1999 Dec 03	n
...	...	...	...	...	...	V	2.0	480.0	1.394	1466.967	7.893	20.86	3.090	0.117	1999 Dec 03	n
...	...	...	...	...	...	R	2.0	360.0	1.632	3213.135	6.504	18.22	1.688	0.125	1999 Dec 06	n
028	UGC04483	$08^h37^m09\overset{s}{.}12$	$+69°47'29\overset{''}{.}9$	10.0	10.0	U	2.0	1200.0	1.270	281.017	5.376	21.64	3.062	0.224	2000 Feb 02	n
...	...	...	...	...	...	B	2.0	600.0	1.262	474.299	18.238	22.38	2.807	0.199	2000 Feb 02	n
...	...	...	...	...	...	V	2.0	480.0	1.259	802.895	21.161	21.55	2.572	0.192	2000 Feb 02	n
...	...	...	...	...	...	R	2.0	360.0	1.257	1198.050	18.881	20.65	2.704	0.229	2000 Feb 02	n
029	NGC2623	$08^h38^m26\overset{s}{.}40$	$+25°44'24\overset{''}{.}0$	-9.0	14.0	U	2.0	600.0	1.025	239.674	0.671	21.96	1.116	0.062	2001 Feb 22	y
...	...	...	...	...	...	B	2.0	300.0	1.026	337.566	1.350	22.85	1.207	0.087	2001 Feb 22	y
...	...	...	...	...	...	V	2.0	240.0	1.028	528.212	1.807	21.71	1.035	0.080	2001 Feb 22	y
...	...	...	...	...	...	R	2.0	180.0	1.029	554.752	2.120	21.27	1.102	0.158	2001 Feb 22	y
030	UGC04564	$08^h45^m20\overset{s}{.}48$	$+55°06'35\overset{''}{.}3$	-9.0	14.0	U	2.0	600.0	1.203	360.672	0.822	20.81	2.160	0.080	1999 Dec 07	n
...	...	...	...	...	...	B	2.0	300.0	1.205	479.048	1.477	21.65	2.122	0.053	1999 Dec 07	n
...	...	...	...	...	...	V	3.0	240.0	1.222	905.259	3.510	20.70	1.954	0.033	1999 Dec 07	n
...	...	...	...	...	...	R	2.0	180.0	1.183	990.611	1.623	19.71	1.822	0.178	1999 Dec 06	n

Table 1—Continued

ID#	Galaxy	RA	DEC	T_{RC3}	T	Filter	N_{exp}	T_{exp}	*Secz*	Sky	σ_{sky}	μ_{sky}	Seeing	σ_{seeing}	Obs. date	Phot?
(1)	(2)	(3)	(4)	(5)	(6)	(7)	(8)	(9)	(10)	(11)	(12)	(13)	(14)	(15)	(16)	(17)
031	UGC04671	$08^h56^m41^s.58$	$+52°06'11''.8$	-9.0	3.0	U	2.0	600.0	1.074	367.812	3.786	20.97	1.999	0.108	1999 Dec 07	n
...	...	...	...	...	...	B	2.0	300.0	1.075	460.707	8.283	21.74	2.031	0.073	1999 Dec 07	n
...	...	...	...	...	...	V	2.0	240.0	1.076	831.935	10.508	20.75	1.875	0.082	1999 Dec 07	n
...	...	...	...	...	...	R	2.0	180.0	1.159	975.560	7.265	19.64	1.770	0.151	1999 Dec 06	n
032	UGC04687	$08^h58^m50^s.83$	$+66°27'33''.9$	-9.0	-2.0	U	2.0	600.0	1.211	268.983	2.184	21.13	4.494	0.206	1999 Dec 04	n
...	...	...	...	...	...	B	2.0	300.0	1.211	404.296	3.893	21.84	4.534	0.286	1999 Dec 04	n
...	...	...	...	...	...	V	2.0	240.0	1.217	759.594	5.976	20.85	4.044	0.298	1999 Dec 04	n
...	...	...	...	...	...	R	2.0	180.0	1.658	1552.999	2.678	18.39	1.558	0.129	1999 Dec 06	n
033	NGC2719	$09^h00^m19^s.51$	$+35°43'59''.5$	10.0	14.0	U	2.0	600.0	1.092	175.991	1.068	21.65	2.017	0.120	2001 Apr 25	n
...	...	...	...	...	...	B	2.0	300.0	1.094	312.943	1.442	22.00	1.905	0.065	2001 Apr 25	n
...	...	...	...	...	...	V	2.0	240.0	1.095	496.662	1.662	21.17	1.808	0.102	2001 Apr 25	n
...	...	...	...	...	...	R	2.0	180.0	1.096	654.322	2.954	20.46	1.721	0.146	2001 Apr 25	n
034	UGC04722	$09^h00^m21^s.87$	$+25°37'32''.1$	8.0	14.0	U	2.0	600.0	1.262	318.702	1.774	21.04	2.287	0.075	1999 Dec 09	n
...	...	...	...	...	...	B	2.0	300.0	1.268	475.698	3.152	21.66	2.040	0.328	1999 Dec 09	n
...	...	...	...	...	...	V	2.0	240.0	1.273	832.398	4.133	20.72	1.916	0.118	1999 Dec 09	n
...	...	...	...	...	...	R	2.0	180.0	1.279	932.807	4.383	20.21	1.808	0.103	1999 Dec 09	n
035	UGC04739	$09^h03^m47^s.80$	$+69°29'08''.1$	-9.0	6.0	U	2.0	1200.0	1.273	513.032	2.395	21.73	1.851	0.079	1999 Apr 11	y
...	...	...	...	...	...	B	2.0	480.0	1.278	679.353	2.745	21.99	1.806	0.063	1999 Apr 11	y
...	...	...	...	...	...	V	2.0	600.0	1.275	1887.073	6.831	20.97	1.654	0.056	1999 Apr 11	y
...	...	...	...	...	...	R	2.0	360.0	1.281	1688.865	5.481	20.30	1.466	0.055	1999 Apr 11	y
036	NGC2742A	$09^h09^m56^s.11$	$+62°14'18''.7$	3.0	14.0	U	2.0	600.0	1.154	269.824	1.611	21.19	3.413	0.142	1999 Dec 04	n
...	...	...	...	...	...	B	2.0	300.0	1.155	424.292	4.069	21.80	2.989	0.307	1999 Dec 04	n
...	...	...	...	...	...	V	3.0	240.0	1.153	717.828	4.015	20.91	2.899	0.205	1999 Dec 04	n
...	...	...	...	...	...	R	2.0	180.0	1.634	1435.684	3.568	18.80	1.665	0.092	1999 Dec 06	n
037	NGC2785	$09^h15^m14^s.37$	$+40°54'50''.4$	10.0	14.0	U	2.0	1200.0	1.135	636.031	2.109	21.02	3.997	0.239	1999 Dec 03	n
...	...	...	...	...	...	B	2.0	600.0	1.142	911.188	4.369	21.73	4.009	0.222	1999 Dec 03	n
...	...	...	...	...	...	V	2.0	480.0	1.149	1589.880	5.606	20.79	3.769	0.281	1999 Dec 03	n
...	...	...	...	...	...	R	2.0	180.0	1.137	859.751	2.894	20.15	1.995	0.156	1999 Dec 06	n
038	UGC04879	$09^h16^m00^s.23$	$+52°50'28''.6$	10.0	10.0	U	2.0	1200.0	1.119	653.132	4.856	20.99	2.445	0.062	1999 Dec 08	n
...	...	...	...	...	...	B	2.0	600.0	1.069	897.233	10.355	21.79	2.563	0.129	1999 Dec 08	n
...	...	...	...	...	...	V	4.0	480.0	1.070	1616.875	17.760	20.82	2.282	0.094	1999 Dec 08	n
...	...	...	...	...	...	R	2.0	360.0	1.084	1660.204	5.067	20.05	1.759	0.233	1999 Dec 06	n
039	UGC04998	$09^h25^m07^s.47$	$+68°23'05''.8$	10.0	8.7	U	2.0	1200.0	1.421	715.036	1.686	20.78	1.843	0.159	1999 Dec 05	n
...	...	...	...	...	...	B	2.0	600.0	1.426	974.227	4.360	21.63	1.854	0.083	1999 Dec 05	n
...	...	...	...	...	...	V	3.0	480.0	1.467	1769.534	7.337	20.67	1.714	0.098	1999 Dec 05	n
...	...	...	...	...	...	R	2.0	360.0	1.231	1675.636	13.493	20.07	1.363	0.092	1999 Dec 06	n
040	UGC05101	$09^h35^m55^s.74$	$+61°21'24''.8$	-9.0	14.0	U	4.0	300.0	1.223	122.528	0.729	21.85	1.946	0.056	2000 May 01	y
...	...	...	...	...	...	B	1.0	300.0	1.203	322.119	2.017	22.38	1.973	0.110	2000 May 01	y
...	...	...	...	...	...	V	1.0	240.0	1.197	558.859	2.363	21.33	2.029	0.092	2000 May 01	y
...	...	...	...	...	...	R	1.0	180.0	1.192	705.519	4.060	20.58	2.062	0.114	2000 May 01	y

Table 1—Continued

ID#	Galaxy	RA	DEC	T_{RC3}	T	Filter	N_{exp}	T_{exp}	*Secz*	Sky	σ_{sky}	μ_{sky}	Seeing	σ_{seeing}	Obs. date	Phot?
(1)	(2)	(3)	(4)	(5)	(6)	(7)	(8)	(9)	(10)	(11)	(12)	(13)	(14)	(15)	(16)	(17)
041	NGC2922	$09^h36^m50^s.75$	$+37°41'33''.5$	10.0	7.3	U	2.0	600.0	1.166	376.825	0.728	20.87	2.036	0.080	1999 Dec 07	n
...	...	...	...	...	...	B	2.0	300.0	1.168	505.578	1.290	21.61	2.010	0.100	1999 Dec 07	n
...	...	...	...	...	...	V	2.0	240.0	1.171	917.406	5.797	20.63	1.961	0.109	1999 Dec 07	n
...	...	...	...	...	...	R	2.0	180.0	1.129	893.686	6.128	20.24	2.224	0.068	1999 Dec 08	n
042	UGC05119	$09^h37^m14^s.23$	$+38°05'26''.9$	-9.0	-2.0	U	2.0	600.0	1.009	170.401	0.766	21.38	1.586	0.060	2002 Jan 15	n
...	...	...	...	...	...	B	2.0	300.0	1.007	292.996	0.774	22.00	1.386	0.033	2002 Jan 15	n
...	...	...	...	...	...	V	2.0	240.0	1.006	504.532	0.991	20.94	1.301	0.029	2002 Jan 15	n
...	...	...	...	...	...	R	2.0	180.0	1.006	558.073	1.583	20.64	1.260	0.023	2002 Jan 15	n
043	UGC05189	$09^h42^m56^s.73$	$+09°28'26''.3$	10.0	14.0	U	2.0	1200.0	1.123	388.362	2.488	21.88	1.941	0.048	2002 Jan 19	y
...	...	...	...	...	...	B	2.0	600.0	1.113	654.066	4.427	22.26	1.761	0.032	2002 Jan 19	y
...	...	...	...	...	...	V	2.0	480.0	1.110	1061.656	6.233	21.29	1.669	0.074	2002 Jan 19	y
...	...	...	...	...	...	R	2.0	360.0	1.109	1288.333	7.336	20.61	1.609	0.046	2002 Jan 19	y
044	NGC2909	$09^h44^m06^s.19$	$+65°58'27''.5$	-9.0	4.3	U	2.0	600.0	1.220	474.384	2.530	20.53	2.902	0.142	1999 Dec 04	n
...	...	...	...	...	...	B	2.0	300.0	1.215	532.452	4.590	21.54	2.880	0.146	1999 Dec 04	n
...	...	...	...	...	...	V	2.0	240.0	1.212	872.864	5.359	20.69	2.820	0.132	1999 Dec 04	n
...	...	...	...	...	...	R	2.0	180.0	1.233	901.210	10.874	20.22	2.104	0.087	1999 Dec 08	n
045	UGC05272	$09^h50^m20^s.20$	$+31°29'29''.5$	10.0	10.0	U	2.0	1200.0	1.074	603.292	1.305	21.15	2.925	0.090	1999 Dec 09	n
...	...	...	...	...	...	B	2.0	600.0	1.079	861.442	3.873	21.92	2.753	0.113	1999 Dec 09	n
...	...	...	...	...	...	V	2.0	480.0	1.085	1492.754	6.671	20.93	2.764	0.175	1999 Dec 09	n
...	...	...	...	...	...	R	2.0	360.0	1.097	1655.885	6.446	20.37	2.186	0.143	1999 Dec 09	n
046	UGC05340	$09^h56^m47^s.11$	$+28°49'19''.4$	10.0	14.0	U	2.0	1200.0	1.215	485.846	1.992	21.75	1.575	0.157	2000 May 03	y
...	...	...	...	...	...	B	2.0	600.0	1.223	736.526	2.400	22.19	1.822	0.243	2000 May 03	y
...	...	...	...	...	...	V	2.0	480.0	1.233	1267.182	4.919	21.11	1.470	0.179	2000 May 03	y
...	...	...	...	...	...	R	2.0	360.0	1.243	1453.217	5.633	20.44	1.609	0.368	2000 May 03	y
047	NGC3079	$10^h01^m58^s.00$	$+55°39'26''.1$	7.0	6.3	U	2.0	600.0	1.156	186.850	6.405	21.39	2.565	0.126	2001 Apr 25	n
...	...	...	...	...	...	B	2.0	300.0	1.157	298.914	16.504	21.87	2.179	0.059	2001 Apr 25	n
...	...	...	...	...	...	V	2.0	240.0	1.159	527.690	21.708	20.72	2.036	0.069	2001 Apr 25	n
...	...	...	...	...	...	R	2.0	180.0	1.159	668.062	24.014	19.87	2.106	0.084	2001 Apr 25	n
048	NGC3104	$10^h03^m56^s.94$	$+40°44'58''.6$	10.0	9.0	U	2.0	1200.0	1.225	502.617	2.942	21.71	1.703	0.095	2000 May 03	y
...	...	...	...	...	...	B	2.0	600.0	1.616	803.925	2.621	22.10	1.749	0.124	2000 May 03	y
...	...	...	...	...	...	V	2.0	480.0	1.605	1493.326	5.509	20.93	1.631	0.061	2000 May 03	y
...	...	...	...	...	...	R	2.0	360.0	1.600	1664.207	6.862	20.29	1.477	0.097	2000 May 03	y
049	UGC05423	$10^h05^m35^s.79$	$+70°21'20''.1$	10.0	10.0	U	2.0	600.0	1.424	194.911	0.424	21.88	1.950	0.060	2002 Jan 20	y
...	...	...	...	...	...	B	2.0	300.0	1.425	332.047	1.188	22.19	1.984	0.088	2002 Jan 20	y
...	...	...	...	...	...	V	2.0	240.0	1.426	531.815	1.581	21.31	1.740	0.114	2002 Jan 20	y
...	...	...	...	...	...	R	2.0	180.0	1.426	680.292	2.352	20.56	1.808	0.104	2002 Jan 20	y
050	UGC05485	$10^h11^m20^s.65$	$+65°16'48''.5$	-9.0	14.0	U	2.0	1200.0	1.518	331.112	3.058	21.55	1.965	0.187	2000 Feb 05	n
...	...	...	...	...	...	B	2.0	600.0	1.510	581.862	8.191	22.16	1.866	0.202	2000 Feb 05	n
...	...	...	...	...	...	V	2.0	480.0	1.508	974.717	11.965	21.30	1.931	0.250	2000 Feb 05	n
...	...	...	...	...	...	R	2.0	360.0	1.236	1185.642	6.212	20.81	1.594	0.233	2000 May 04	y

Table 1—Continued

ID#	Galaxy	RA	DEC	T_{RC3}	T	Filter	N_{exp}	T_{exp}	*Secz*	Sky	σ_{sky}	μ_{sky}	Seeing	σ_{seeing}	Obs. date	Phot?
(1)	(2)	(3)	(4)	(5)	(6)	(7)	(8)	(9)	(10)	(11)	(12)	(13)	(14)	(15)	(16)	(17)
051	UGC05626	$10^h24^m24^s.19$	$+57°22'59''.1$	10.0	7.0	U	2.0	1200.0	1.417	298.979	1.151	22.30	2.012	0.127	2000 Feb 04	y
...	...	...	...	...	...	B	2.0	600.0	1.427	541.206	1.562	22.49	1.875	0.077	2000 Feb 04	y
...	...	...	...	...	...	V	2.0	480.0	1.436	938.815	2.313	21.51	1.822	0.053	2000 Feb 04	y
...	...	...	...	...	...	R	2.0	360.0	1.444	1359.675	4.717	20.60	1.787	0.045	2000 Feb 04	y
052	NGC3239	$10^h25^m04^s.76$	$+17°08'58''.3$	10.0	14.0	U	2.0	600.0	1.108	223.409	0.981	21.83	1.935	0.136	2001 Feb 21	y
...	...	...	...	...	...	B	2.0	300.0	1.110	337.756	2.361	22.36	2.087	0.263	2001 Feb 21	y
...	...	...	...	...	...	V	2.0	240.0	1.112	525.775	2.833	21.42	1.777	0.215	2001 Feb 21	y
...	...	...	...	...	...	R	2.0	180.0	1.115	585.241	3.293	20.86	1.744	0.169	2001 Feb 21	y
053	NGC3274	$10^h32^m17^s.03$	$+27°39'58''.0$	6.8	7.7	U	2.0	600.0	1.272	176.425	0.560	22.12	1.785	0.170	2000 Feb 04	y
...	...	...	...	...	...	B	2.0	300.0	1.267	309.696	0.944	22.35	1.811	0.157	2000 Feb 04	y
...	...	...	...	...	...	V	2.0	240.0	1.264	500.679	2.740	21.44	1.494	0.144	2000 Feb 04	y
...	...	...	...	...	...	R	2.0	180.0	1.263	658.541	4.914	20.63	1.260	0.063	2000 Feb 04	y
054	NGC3264	$10^h32^m23^s.77$	$+56°04'43''.3$	8.0	6.7	U	2.0	600.0	1.104	328.716	0.847	20.59	1.463	0.181	2001 Feb 23	n
...	...	...	...	...	...	B	2.0	300.0	1.106	389.431	3.358	21.49	1.710	0.140	2001 Feb 23	n
...	...	...	...	...	...	V	2.0	240.0	1.118	663.656	2.025	20.73	1.427	0.052	2001 Feb 23	n
...	...	...	...	...	...	R	2.0	180.0	1.115	574.785	2.478	20.66	1.384	0.139	2001 Feb 23	n
055	UGC05846	$10^h44^m26^s.24$	$+60°22'06''.3$	10.0	9.7	U	2.0	1200.0	1.142	380.006	2.610	20.94	1.646	0.063	2002 Apr 13	n
...	...	...	...	...	...	B	2.0	600.0	1.145	602.121	3.115	21.63	1.763	0.239	2002 Apr 13	n
...	...	...	...	...	...	V	2.0	480.0	1.148	1070.958	4.352	20.69	1.571	0.324	2002 Apr 13	n
...	...	...	...	...	...	R	2.0	360.0	1.152	1380.591	9.519	20.11	1.603	0.075	2002 Apr 13	n
056	NGC3353	$10^h45^m22^s.53$	$+55°57'32''.9$	3.0	14.0	U	2.0	600.0	1.121	158.825	1.152	20.59	1.601	0.059	2002 Apr 10	n
...	...	...	...	...	...	B	2.0	300.0	1.119	271.508	1.225	21.60	1.684	0.067	2002 Apr 10	n
...	...	...	...	...	...	V	2.0	240.0	1.119	463.406	1.093	20.96	1.504	0.061	2002 Apr 10	n
...	...	...	...	...	...	R	2.0	180.0	1.118	646.405	2.186	20.25	1.519	0.075	2002 Apr 10	n
057	UGC05883	$10^h47^m15^s.41$	$+54°02'11''.1$	10.0	6.7	U	2.0	600.0	1.075	262.713	0.962	21.08	1.652	0.107	1999 Apr 12	n
...	...	...	...	...	...	B	2.0	480.0	1.081	655.473	2.659	21.16	1.669	0.216	1999 Apr 12	n
...	...	...	...	...	...	V	2.0	600.0	1.078	1805.453	7.951	20.66	1.477	0.091	1999 Apr 12	n
...	...	...	...	...	...	R	2.0	360.0	1.085	1836.133	7.110	19.34	1.477	0.117	1999 Apr 12	n
058	UGC05989	$10^h52^m30^s.00$	$+19°48'00''.1$	10.0	14.0	U	2.0	600.0	1.155	279.841	0.847	21.61	1.519	0.227	2000 May 04	y
...	...	...	...	...	...	B	2.0	300.0	1.157	372.795	0.957	22.21	1.744	0.217	2000 May 04	y
...	...	...	...	...	...	V	2.0	240.0	1.159	614.743	1.708	21.18	1.693	0.243	2000 May 04	y
...	...	...	...	...	...	R	2.0	180.0	1.160	636.610	1.609	20.73	1.802	0.306	2000 May 04	y
059	NGC3445	$10^h54^m41^s.17$	$+56°59'33''.2$	9.0	14.0	U	2.0	600.0	1.173	203.952	2.026	21.27	3.030	0.152	2001 Apr 25	n
...	...	...	...	...	...	B	2.0	300.0	1.174	295.469	2.901	22.02	2.651	0.165	2001 Apr 25	n
...	...	...	...	...	...	V	2.0	240.0	1.176	511.182	2.373	21.03	2.698	0.145	2001 Apr 25	n
...	...	...	...	...	...	R	2.0	180.0	1.177	655.177	3.849	20.03	2.574	0.159	2001 Apr 25	n
060	MCG6-24-47	$11^h05^m09^s.97$	$+38°03'57''.0$	-9.0	6.0	U	2.0	600.0	1.032	158.376	0.935	22.25	2.430	0.075	2000 Feb 03	y
...	...	...	...	...	...	B	2.0	300.0	1.030	265.703	1.628	22.66	2.649	0.124	2000 Feb 03	y
...	...	...	...	...	...	V	2.0	240.0	1.029	422.204	2.391	21.63	2.423	0.105	2000 Feb 03	y
...	...	...	...	...	...	R	2.0	180.0	1.186	542.515	3.110	20.84	2.452	0.067	2000 Feb 04	y

Table 1—Continued

ID#	Galaxy	RA	DEC	T_{RC3}	T	Filter	N_{exp}	T_{exp}	*Secz*	Sky	σ_{sky}	μ_{sky}	Seeing	σ_{seeing}	Obs. date	Phot?
(1)	(2)	(3)	(4)	(5)	(6)	(7)	(8)	(9)	(10)	(11)	(12)	(13)	(14)	(15)	(16)	(17)
061	NGC3543	$11^h10^m58^s.26$	$+61°21'21''.3$	-9.0	14.0	U	2.0	600.0	1.468	169.465	0.742	21.42	1.759	0.102	2000 Feb 05	n
...	...	...	...	...	...	B	2.0	300.0	1.465	286.271	1.065	22.15	1.894	0.169	2000 Feb 05	n
...	...	...	...	...	...	V	2.0	240.0	1.475	466.624	1.486	21.35	1.637	0.109	2000 Feb 05	n
...	...	...	...	...	...	R	2.0	180.0	1.143	606.555	2.084	20.74	1.444	0.043	2000 May 05	y
062	UGC06249	$11^h13^m18^s.57$	$+59°55'02''.0$	6.0	3.3	U	4.0	300.0	1.167	116.796	0.778	21.86	2.730	0.159	2000 Apr 30	y
...	...	...	...	...	...	B	2.0	300.0	1.168	306.266	1.842	22.39	2.618	0.151	2000 Apr 30	y
...	...	...	...	...	...	V	2.0	240.0	1.169	520.540	3.188	21.37	2.325	0.175	2000 Apr 30	y
...	...	...	...	...	...	R	2.0	180.0	1.138	560.167	4.652	20.82	2.348	0.141	2000 Apr 30	y
063	UGC06258	$11^h13^m47^s.03$	$+21°31'31''.4$	10.0	14.0	U	2.0	1200.0	1.347	546.855	2.132	21.63	1.905	0.250	2000 May 04	y
...	...	...	...	...	...	B	2.0	600.0	1.331	734.212	1.490	22.22	1.796	0.214	2000 May 04	y
...	...	...	...	...	...	V	2.0	480.0	1.485	1263.369	3.346	21.15	1.532	0.213	2000 May 04	y
...	...	...	...	...	...	R	2.0	360.0	1.497	1539.269	3.749	20.53	1.425	0.121	2000 May 04	y
064	UGC06315	$11^h18^m15^s.59$	$+53°45'37''.2$	-9.0	2.7	U	2.0	600.0	1.163	250.782	3.588	20.56	1.342	0.078	2000 May 08	n
...	...	...	...	...	...	B	2.0	300.0	1.243	471.181	4.046	21.03	1.286	0.076	2000 May 08	n
...	...	...	...	...	...	V	2.0	240.0	1.253	734.343	2.113	20.25	1.185	0.079	2000 May 08	n
...	...	...	...	...	...	R	2.0	180.0	1.309	1050.258	5.067	19.17	1.273	0.074	2000 May 08	n
065	NGC3664	$11^h24^m23^s.90$	$+03°18'49''.5$	9.0	9.0	U	2.0	600.0	1.168	205.260	1.485	21.25	2.505	0.102	2001 Apr 24	n
...	...	...	...	...	...	B	2.0	300.0	1.165	324.635	2.918	21.92	2.707	0.101	2001 Apr 24	n
...	...	...	...	...	...	V	2.0	240.0	1.164	560.190	2.570	21.05	2.447	0.105	2001 Apr 24	n
...	...	...	...	...	...	R	2.0	180.0	1.163	751.700	2.835	20.31	2.396	0.104	2001 Apr 24	n
066	UGC06447	$11^h26^m42^s.47$	$+59°09'26''.3$	-9.0	14.0	U	2.0	600.0	1.180	300.835	1.181	21.55	1.976	0.223	1999 Apr 11	y
...	...	...	...	...	...	B	2.0	240.0	1.156	333.841	1.185	22.01	1.899	0.086	1999 Apr 11	y
...	...	...	...	...	...	V	2.0	300.0	1.181	929.936	2.811	20.99	1.834	0.206	1999 Apr 11	y
...	...	...	...	...	...	R	2.0	180.0	1.148	654.068	2.068	20.58	1.723	0.072	1999 Apr 11	y
067	UGC06527	$11^h32^m37^s.59$	$+52°56'53''.4$	0.0	14.0	U	2.0	1200.0	1.083	284.599	4.486	22.60	2.385	0.252	2000 Feb 02	y
...	...	...	...	...	...	B	2.0	600.0	1.078	488.145	10.898	22.88	2.497	0.192	2000 Feb 02	y
...	...	...	...	...	...	V	2.0	480.0	1.077	845.806	12.754	21.76	2.342	0.137	2000 Feb 02	y
...	...	...	...	...	...	R	2.0	360.0	1.212	1068.198	14.653	20.86	2.483	0.110	2000 Feb 04	y
068	UGC06541	$11^h33^m37^s.56$	$+49°14'33''.2$	10.0	10.0	U	2.0	600.0	1.135	238.910	1.546	21.20	2.034	0.190	2001 Apr 23	n
...	...	...	...	...	...	B	2.0	300.0	1.133	297.360	1.664	22.07	2.021	0.119	2001 Apr 23	n
...	...	...	...	...	...	V	2.0	240.0	1.132	524.433	1.925	21.15	1.942	0.130	2001 Apr 23	n
...	...	...	...	...	...	R	3.0	200.0	1.130	658.220	3.307	20.59	1.933	0.139	2001 Apr 23	n
069	NGC3729	$11^h33^m48^s.69$	$+53°07'12''.9$	1.0	3.3	U	2.0	600.0	1.071	142.714	1.074	22.60	2.241	0.034	2000 Feb 02	y
...	...	...	...	...	...	B	2.0	300.0	1.070	238.849	1.130	22.91	2.152	0.136	2000 Feb 02	y
...	...	...	...	...	...	V	2.0	240.0	1.069	423.724	1.564	21.76	1.838	0.082	2000 Feb 02	y
...	...	...	...	...	...	R	2.0	180.0	1.168	505.958	1.369	20.92	2.186	0.096	2000 Feb 04	y
070	NGC3738	$11^h35^m50^s.46$	$+54°30'53''.9$	10.0	10.0	U	2.0	600.0	1.077	386.281	2.807	20.75	2.147	0.091	2000 May 09	n
...	...	...	...	...	...	B	2.0	300.0	1.078	626.284	4.204	21.33	1.723	0.134	2000 May 09	n
...	...	...	...	...	...	V	2.0	240.0	1.079	694.912	3.878	20.97	1.553	0.046	2000 May 09	n
...	...	...	...	...	...	R	2.0	180.0	1.080	815.257	5.660	20.29	1.354	0.083	2000 May 09	n

Table 1—Continued

ID#	Galaxy	RA	DEC	T_{RC3}	T	Filter	N_{exp}	T_{exp}	*Secz*	Sky	σ_{sky}	μ_{sky}	Seeing	σ_{seeing}	Obs. date	Phot?
(1)	(2)	(3)	(4)	(5)	(6)	(7)	(8)	(9)	(10)	(11)	(12)	(13)	(14)	(15)	(16)	(17)
071	NGC3741	$11^h36^m06^s.39$	$+45°16'59''.5$	10.0	10.0	U	2.0	1200.0	1.028	366.606	1.344	22.05	1.596	0.095	2001 Feb 21	y
...	...	...	...	...	...	B	2.0	600.0	1.031	495.333	2.345	22.69	1.770	0.120	2001 Feb 21	y
...	...	...	...	...	...	V	2.0	480.0	1.035	810.901	4.193	21.70	1.549	0.105	2001 Feb 21	y
...	...	...	...	...	...	R	2.0	360.0	1.039	911.263	4.560	21.13	1.468	0.131	2001 Feb 21	y
072	UGC06697	$11^h43^m46^s.78$	$+19°58'20''.9$	10.0	14.0	U	2.0	600.0	1.035	176.934	2.213	22.13	2.363	0.211	2000 Feb 03	y
...	...	...	...	...	...	B	2.0	300.0	1.032	291.333	7.736	22.56	2.436	0.290	2000 Feb 03	y
...	...	...	...	...	...	V	3.0	240.0	1.043	471.886	15.703	21.55	2.299	0.329	2000 Feb 02	y
...	...	...	...	...	...	R	2.0	180.0	1.162	549.618	28.515	20.83	2.426	0.151	2000 Feb 04	y
073	MCG3-30-71	$11^h44^m03^s.76$	$+19°47'06''.0$	-9.0	3.3	U	2.0	600.0	1.045	150.293	1.182	22.31	2.370	0.013	2000 Feb 03	y
...	...	...	...	...	...	B	2.0	300.0	1.043	267.313	2.957	22.65	2.318	0.078	2000 Feb 03	y
...	...	...	...	...	...	V	2.0	240.0	1.042	450.414	4.836	21.56	2.259	0.078	2000 Feb 03	y
...	...	...	...	...	...	R	2.0	180.0	1.120	545.984	3.790	20.84	2.134	0.073	2000 Feb 04	y
074	NGC3846A	$11^h44^m21^s.21$	$+55°02'40''.7$	9.3	8.0	U	2.0	1200.0	1.098	371.482	2.546	22.15	1.639	0.149	2000 May 05	y
...	...	...	...	...	...	B	2.0	600.0	1.102	511.997	2.136	22.68	1.774	0.131	2000 May 05	y
...	...	...	...	...	...	V	2.0	480.0	1.105	845.204	2.592	21.63	1.549	0.132	2000 May 05	y
...	...	...	...	...	...	R	2.0	360.0	1.109	1082.229	3.950	20.86	1.485	0.121	2000 May 05	y
075	NGC3860	$11^h44^m49^s.20$	$+19°47'42''.0$	-9.0	2.7	U	2.0	600.0	1.036	175.529	0.856	21.08	1.489	0.198	2000 Feb 05	n
...	...	...	...	...	...	B	2.0	300.0	1.035	300.505	2.478	21.56	1.732	0.376	2000 Feb 05	n
...	...	...	...	...	...	V	2.0	240.0	1.034	499.927	2.888	20.85	1.594	0.385	2000 Feb 05	n
...	...	...	...	...	...	R	2.0	180.0	1.166	551.373	2.530	21.28	2.364	0.112	2000 May 07	y
076	NGC3913	$11^h50^m38^s.96$	$+55°20'47''.0$	7.0	3.3	U	2.0	600.0	1.191	205.665	1.085	21.81	1.384	0.062	2002 Apr 12	y
...	...	...	...	...	...	B	2.0	300.0	1.189	301.179	1.045	22.32	1.395	0.082	2002 Apr 12	y
...	...	...	...	...	...	V	2.0	240.0	1.188	524.073	1.718	21.30	1.230	0.032	2002 Apr 12	y
...	...	...	...	...	...	R	2.0	180.0	1.188	681.842	3.979	20.65	1.252	0.060	2002 Apr 12	y
077	UGC06816	$11^h50^m46^s.86$	$+56°27'59''.3$	10.0	14.0	U	2.0	1200.0	1.232	353.019	2.129	22.21	1.986	0.135	2000 May 05	y
...	...	...	...	...	...	B	2.0	600.0	1.238	529.630	2.155	22.65	2.201	0.257	2000 May 05	y
...	...	...	...	...	...	V	2.0	480.0	1.242	878.062	2.806	21.59	2.124	0.530	2000 May 05	y
...	...	...	...	...	...	R	2.0	360.0	1.247	1100.967	4.161	20.84	2.186	0.231	2000 May 05	y
078	NGC3952	$11^h53^m39^s.20$	$-04°00'40''.6$	9.8	14.0	U	2.0	600.0	1.309	235.413	1.346	21.04	2.376	0.110	2001 Apr 24	n
...	...	...	...	...	...	B	2.0	300.0	1.305	354.630	2.044	21.74	2.464	0.051	2001 Apr 24	n
...	...	...	...	...	...	V	3.0	200.0	1.306	556.756	2.552	20.81	2.051	0.059	2001 Apr 24	n
...	...	...	...	...	...	R	2.0	180.0	1.299	859.655	4.061	20.15	2.122	0.051	2001 Apr 24	n
079	UGC07019	$12^h02^m31^s.22$	$+62°25'04''.0$	10.0	7.3	U	2.0	1200.0	1.291	321.610	1.397	22.08	1.628	0.127	2002 Jan 20	y
...	...	...	...	...	...	B	2.0	600.0	1.295	480.326	0.836	22.54	1.524	0.139	2002 Jan 20	y
...	...	...	...	...	...	V	2.0	480.0	1.299	843.720	1.266	21.56	1.361	0.105	2002 Jan 20	y
...	...	...	...	...	...	R	2.0	360.0	1.304	1321.933	4.502	20.59	1.281	0.173	2002 Jan 20	y
080	NGC4068	$12^h04^m02^s.40$	$+52°34'55''.2$	10.0	10.0	U	2.0	1200.0	1.066	399.772	2.251	20.74	1.899	0.255	2000 May 06	n
...	...	...	...	...	...	B	2.0	600.0	1.069	667.496	2.721	20.92	2.021	0.236	2000 May 06	n
...	...	...	...	...	...	V	2.0	480.0	1.074	1115.945	3.339	20.59	1.646	0.105	2000 May 06	n
...	...	...	...	...	...	R	2.0	360.0	1.078	1370.574	4.617	20.16	1.954	0.335	2000 May 06	n

Table 1—Continued

ID#	Galaxy	RA	DEC	T_{RC3}	T	Filter	N_{exp}	T_{exp}	*Secz*	Sky	σ_{sky}	μ_{sky}	Seeing	σ_{seeing}	Obs. date	Phot?
(1)	(2)	(3)	(4)	(5)	(6)	(7)	(8)	(9)	(10)	(11)	(12)	(13)	(14)	(15)	(16)	(17)
081	NGC4234	$12^h17^m07^s.78$	$+03°40'35''.6$	8.7	7.3	U	2.0	600.0	1.279	240.212	1.258	21.03	2.543	0.041	2001 Apr 24	n
...	...	...	...	...	...	B	2.0	300.0	1.281	354.443	1.693	21.80	2.308	0.152	2001 Apr 24	n
...	...	...	...	...	...	V	2.0	240.0	1.280	638.015	2.372	20.89	1.931	0.066	2001 Apr 24	n
...	...	...	...	...	...	R	2.0	180.0	1.279	786.425	3.240	20.22	2.218	0.119	2001 Apr 24	n
082	UGC07321	$12^h17^m34^s.80$	$+22°32'51''.2$	7.0	7.0	U	2.0	600.0	1.018	199.498	0.678	21.85	1.749	0.236	2002 Apr 12	y
...	...	...	...	...	...	B	2.0	300.0	1.018	304.571	0.988	22.31	1.742	0.264	2002 Apr 12	y
...	...	...	...	...	...	V	2.0	240.0	1.017	493.615	1.282	21.36	1.403	0.145	2002 Apr 12	y
...	...	...	...	...	...	R	2.0	180.0	1.017	555.483	1.300	20.87	1.564	0.283	2002 Apr 12	y
083	NGC4278	$12^h20^m06^s.85$	$+29°16'18''.6$	-5.0	-5.0	U	2.0	300.0	1.087	111.688	1.566	21.72	1.286	0.254	2002 Apr 12	y
...	...	...	...	...	...	B	2.0	180.0	1.086	197.049	5.168	22.23	1.425	0.112	2002 Apr 12	y
...	...	...	...	...	...	V	2.0	120.0	1.085	281.049	6.056	21.22	1.342	0.108	2002 Apr 12	y
...	...	...	...	...	...	R	2.0	120.0	1.085	436.711	8.978	20.70	1.283	0.093	2002 Apr 12	y
084	NGC4299	$12^h21^m41^s.87$	$+11°29'29''.7$	8.0	8.0	U	2.0	600.0	1.146	202.728	1.092	21.83	1.207	0.040	2002 Apr 12	y
...	...	...	...	...	...	B	2.0	300.0	1.143	310.341	1.616	22.29	1.196	0.053	2002 Apr 12	y
...	...	...	...	...	...	V	2.0	240.0	1.142	503.543	1.858	21.34	1.039	0.058	2002 Apr 12	y
...	...	...	...	...	...	R	2.0	180.0	1.143	521.146	2.465	20.94	1.056	0.050	2002 Apr 12	y
085	NGC4449	$12^h28^m15^s.67$	$+44°06'15''.5$	10.0	8.0	U	2.0	600.0	1.129	250.501	21.552	21.19	3.131	0.094	2001 Apr 23	n
...	...	...	...	...	...	B	2.0	300.0	1.127	302.393	30.157	22.06	3.375	0.266	2001 Apr 23	n
...	...	...	...	...	...	V	2.0	240.0	1.126	529.671	35.671	21.13	3.075	0.111	2001 Apr 23	n
...	...	...	...	...	...	R	2.0	180.0	1.125	602.618	36.794	20.57	3.637	0.185	2001 Apr 23	n
086	NGC4476	$12^h29^m59^s.71$	$+12°20'48''.3$	-3.0	-1.0	U	2.0	300.0	1.116	124.264	0.555	20.87	1.342	0.116	2002 Apr 12	n
...	...	...	...	...	...	B	2.0	180.0	1.115	214.880	0.963	21.71	1.477	0.165	2002 Apr 12	n
...	...	...	...	...	...	V	2.0	120.0	1.115	298.082	0.628	20.93	1.234	0.170	2002 Apr 12	n
...	...	...	...	...	...	R	2.0	120.0	1.114	433.911	1.824	20.43	1.239	0.165	2002 Apr 12	n
087	NGC4490	$12^h30^m31^s.71$	$+41°38'26''.4$	7.0	14.0	U	2.0	600.0	1.031	195.007	9.088	21.26	2.303	0.542	2002 Apr 13	n
...	...	...	...	...	...	B	2.0	300.0	1.029	267.944	21.047	22.14	2.171	0.584	2002 Apr 13	n
...	...	...	...	...	...	V	2.0	240.0	1.028	437.308	24.766	21.26	1.553	0.289	2002 Apr 13	n
...	...	...	...	...	...	R	2.0	180.0	1.028	474.816	24.591	20.72	1.519	0.274	2002 Apr 13	n
088	NGC4485	$12^h30^m35^s.45$	$+41°39'56''.4$	7.0	14.0	U	2.0	600.0	1.048	246.646	21.131	21.93	1.774	0.392	2001 Feb 22	y
...	...	...	...	...	...	B	2.0	300.0	1.050	300.923	53.882	22.97	1.118	0.459	2001 Feb 22	y
...	...	...	...	...	...	V	2.0	240.0	1.051	510.764	54.480	21.75	1.148	0.408	2001 Feb 22	y
...	...	...	...	...	...	R	2.0	180.0	1.052	601.213	49.419	21.18	1.305	0.338	2001 Feb 22	y
089	NGC4519	$12^h33^m30^s.36$	$+08°39'26''.4$	7.0	5.0	U	2.0	600.0	1.099	267.525	0.843	21.07	1.793	0.202	2001 Feb 23	n
...	...	...	...	...	...	B	2.0	300.0	1.100	347.345	1.079	21.87	1.849	0.263	2001 Feb 23	n
...	...	...	...	...	...	V	2.0	240.0	1.102	612.320	1.269	20.86	1.567	0.093	2001 Feb 23	n
...	...	...	...	...	...	R	2.0	180.0	1.104	605.040	1.434	20.53	1.538	0.252	2001 Feb 23	n
090	NGC4532	$12^h34^m19^s.39$	$+06°28'39''.7$	10.0	14.0	U	2.0	600.0	1.253	174.530	0.850	21.51	1.695	0.087	2000 May 07	n
...	...	...	...	...	...	B	2.0	300.0	1.256	292.820	1.921	22.15	1.704	0.114	2000 May 07	n
...	...	...	...	...	...	V	2.0	240.0	1.259	486.446	2.874	21.30	1.663	0.133	2000 May 07	n
...	...	...	...	...	...	R	2.0	180.0	1.262	614.196	2.988	20.56	1.566	0.082	2000 May 07	n

Table 1—Continued

ID#	Galaxy	RA	DEC	T_{RC3}	T	Filter	N_{exp}	T_{exp}	*Secz*	Sky	σ_{sky}	μ_{sky}	Seeing	σ_{seeing}	Obs. date	Phot?
(1)	(2)	(3)	(4)	(5)	(6)	(7)	(8)	(9)	(10)	(11)	(12)	(13)	(14)	(15)	(16)	(17)
091	UGC07816	$12^h38^m55^s.49$	$+38°05'53''.4$	-9.0	14.0	U	2.0	1200.0	1.372	479.854	2.372	21.76	1.997	0.179	2000 May 03	y
...	...	...	...	...	...	B	2.0	600.0	1.383	636.264	2.598	22.35	2.040	0.182	2000 May 03	y
...	...	...	...	...	...	V	2.0	480.0	1.396	1158.109	4.159	21.21	2.021	0.169	2000 May 03	y
...	...	...	...	...	...	R	2.0	360.0	1.410	1385.228	4.880	20.49	2.243	0.217	2000 May 03	y
092	NGC4618	$12^h41^m32^s.00$	$+41°08'59''.1$	9.0	7.7	U	2.0	600.0	1.265	209.586	1.198	21.79	1.474	0.292	2002 Apr 12	y
...	...	...	...	...	...	B	2.0	300.0	1.258	299.082	1.637	22.33	1.307	0.097	2002 Apr 12	y
...	...	...	...	...	...	V	2.0	240.0	1.257	520.018	2.181	21.30	1.196	0.142	2002 Apr 12	y
...	...	...	...	...	...	R	2.0	180.0	1.256	532.833	3.096	20.92	1.178	0.214	2002 Apr 12	y
093	IC3687	$12^h42^m14^s.62$	$+38°29'57''.5$	10.0	8.3	U	2.0	600.0	1.502	243.855	1.089	21.63	1.470	0.061	2002 Apr 12	y
...	...	...	...	...	...	B	2.0	300.0	1.495	331.376	1.171	22.22	1.273	0.122	2002 Apr 12	y
...	...	...	...	...	...	V	2.0	240.0	1.492	576.767	1.510	21.19	1.258	0.060	2002 Apr 12	y
...	...	...	...	...	...	R	2.0	180.0	1.491	638.467	2.049	20.72	1.271	0.057	2002 Apr 12	y
094	NGC4644	$12^h42^m50^s.43$	$+55°08'34''.7$	-9.0	14.0	U	2.0	600.0	1.100	924.960	3.842	19.26	1.689	0.295	2002 Jan 19	n
...	...	...	...	...	...	B	2.0	300.0	1.098	563.084	2.657	21.09	1.684	0.070	2002 Jan 19	n
...	...	...	...	...	...	V	2.0	240.0	1.098	526.893	2.016	20.98	1.466	0.066	2002 Jan 19	n
...	...	...	...	...	...	R	2.0	180.0	1.097	667.103	3.311	20.35	1.416	0.044	2002 Jan 19	n
095	NGC4639	$12^h42^m53^s.15$	$+13°15'17''.7$	4.0	2.7	U	2.0	600.0	1.062	244.337	1.018	21.85	2.188	0.336	2000 May 01	y
...	...	...	...	...	...	B	2.0	300.0	1.064	338.886	2.151	22.32	2.422	0.074	2000 May 01	y
...	...	...	...	...	...	V	2.0	240.0	1.063	593.703	2.695	21.27	2.199	0.103	2000 May 01	y
...	...	...	...	...	...	R	2.0	180.0	1.063	663.896	2.612	20.65	2.280	0.168	2000 May 01	y
096	UGC07905	$12^h43^m51^s.12$	$+54°54'13''.6$	-9.0	14.0	U	2.0	600.0	1.114	212.117	1.382	20.45	1.301	0.045	2002 Apr 13	n
...	...	...	...	...	...	B	2.0	300.0	1.112	305.957	1.668	21.63	1.172	0.065	2002 Apr 13	n
...	...	...	...	...	...	V	2.0	240.0	1.114	541.212	2.097	20.56	1.033	0.039	2002 Apr 13	n
...	...	...	...	...	...	R	2.0	180.0	1.112	609.548	4.279	20.04	0.949	0.037	2002 Apr 13	n
097	UGC08091	$12^h58^m41^s.78$	$+14°12'58''.6$	10.0	10.0	U	2.0	600.0	1.159	199.499	0.760	21.85	1.236	0.160	2002 Apr 12	y
...	...	...	...	...	...	B	2.0	300.0	1.155	297.637	0.898	22.34	1.189	0.055	2002 Apr 12	y
...	...	...	...	...	...	V	2.0	240.0	1.154	481.126	1.173	21.39	1.035	0.059	2002 Apr 12	y
...	...	...	...	...	...	R	2.0	180.0	1.153	525.698	1.417	20.93	1.059	0.088	2002 Apr 12	y
098	UGC08107	$12^h59^m39^s.06$	$+53°20'27''.3$	10.0	14.0	U	2.0	600.0	1.138	269.187	2.068	21.01	1.661	0.099	1999 Apr 11	n
...	...	...	...	...	...	B	2.0	240.0	1.140	308.654	2.432	21.67	1.757	0.112	1999 Apr 11	n
...	...	...	...	...	...	V	2.0	300.0	1.139	811.626	4.388	20.91	1.541	0.106	1999 Apr 11	n
...	...	...	...	...	...	R	2.0	180.0	1.141	680.870	3.419	20.21	1.626	0.129	1999 Apr 11	n
099	UGC08201	$13^h06^m27^s.32$	$+67°42'45''.6$	10.0	10.0	U	2.0	600.0	1.224	166.051	0.816	22.15	2.070	0.071	2001 Feb 21	y
...	...	...	...	...	...	B	2.0	300.0	1.225	223.452	0.903	22.80	2.042	0.199	2001 Feb 21	y
...	...	...	...	...	...	V	2.0	240.0	1.226	378.875	1.536	21.77	1.796	0.124	2001 Feb 21	y
...	...	...	...	...	...	R	2.0	180.0	1.227	503.801	2.088	21.02	1.954	0.141	2001 Feb 21	y
100	UGC08320	$13^h14^m27^s.47$	$+45°55'36''.3$	10.0	10.0	U	2.0	600.0	1.035	174.234	0.668	22.10	1.549	0.255	2001 Feb 21	y
...	...	...	...	...	...	B	2.0	300.0	1.036	227.621	1.283	22.78	1.723	0.109	2001 Feb 21	y
...	...	...	...	...	...	V	2.0	240.0	1.037	373.440	1.830	21.79	1.628	0.336	2001 Feb 21	y
...	...	...	...	...	...	R	2.0	180.0	1.038	448.188	2.251	21.15	1.433	0.152	2001 Feb 21	y

Table 1—Continued

ID#	Galaxy	RA	DEC	T_{RC3}	T	Filter	N_{exp}	T_{exp}	*Secz*	Sky	σ_{sky}	μ_{sky}	Seeing	σ_{seeing}	Obs. date	Phot?
(1)	(2)	(3)	(4)	(5)	(6)	(7)	(8)	(9)	(10)	(11)	(12)	(13)	(14)	(15)	(16)	(17)
101	UGC08323	$13^h14^m49\overset{s}{.}73$	$+34°52'52\overset{''}{.}6$	10.0	14.0	U	2.0	600.0	1.022	194.816	0.870	20.96	1.356	0.077	2002 Apr 13	n
...	...	...	...	...	...	B	2.0	300.0	1.020	279.878	0.730	21.76	1.384	0.064	2002 Apr 13	n
...	...	...	...	...	...	V	2.0	240.0	1.019	487.984	1.025	20.81	1.234	0.146	2002 Apr 13	n
...	...	...	...	...	...	R	2.0	180.0	1.019	554.841	2.908	20.13	1.211	0.054	2002 Apr 13	n
102	NGC5147	$13^h26^m18\overset{s}{.}62$	$+02°05'09\overset{''}{.}5$	8.0	6.3	U	2.0	600.0	1.403	227.384	1.335	21.78	2.355	0.150	2001 May 26	y
...	...	...	...	...	...	B	2.0	300.0	1.405	333.876	0.974	22.21	2.059	0.112	2001 May 26	y
...	...	...	...	...	...	V	2.0	240.0	1.411	545.655	1.725	21.20	1.941	0.117	2001 May 26	y
...	...	...	...	...	...	R	2.0	180.0	1.415	590.350	2.522	20.72	1.684	0.046	2001 May 26	y
103	UGC08508	$13^h30^m42\overset{s}{.}31$	$+54°55'03\overset{''}{.}7$	10.0	8.3	U	2.0	1200.0	1.105	362.469	2.179	22.26	1.665	0.106	2000 May 07	y
...	...	...	...	...	...	B	2.0	600.0	1.109	541.323	3.054	22.88	1.830	0.349	2000 May 07	y
...	...	...	...	...	...	V	2.0	480.0	1.114	829.660	3.240	21.90	1.607	0.085	2000 May 07	y
...	...	...	...	...	...	R	2.0	360.0	1.118	1057.788	5.655	21.33	1.650	0.170	2000 May 07	y
104	UGC08507	$13^h31^m00\overset{s}{.}05$	$+19°27'30\overset{''}{.}4$	10.0	14.0	U	2.0	1200.0	1.234	409.002	1.899	20.99	2.059	0.273	2000 May 06	n
...	...	...	...	...	...	B	2.0	600.0	1.194	589.254	4.914	22.07	2.149	0.135	2000 May 06	n
...	...	...	...	...	...	V	2.0	480.0	1.068	945.773	4.843	21.27	2.119	0.165	2000 May 06	n
...	...	...	...	...	...	R	2.0	360.0	1.060	1137.347	3.241	20.66	2.303	0.232	2000 May 06	n
105	UGCA363	$13^h33^m37\overset{s}{.}21$	$+60°23'40\overset{''}{.}8$	10.0	14.0	U	2.0	1200.0	1.184	471.286	2.653	21.74	2.184	0.143	1999 Apr 10	y
...	...	...	...	...	...	B	2.0	480.0	1.191	712.682	2.913	21.92	2.475	0.381	1999 Apr 10	y
...	...	...	...	...	...	V	2.0	600.0	1.187	1647.099	6.878	21.04	2.004	0.117	1999 Apr 10	y
...	...	...	...	...	...	R	2.0	360.0	1.194	1463.029	5.118	20.46	2.224	0.182	1999 Apr 10	y
106	NGC5253	$13^h39^m54\overset{s}{.}84$	$-31°38'34\overset{''}{.}7$	10.0	14.0	U	5.0	300.0	2.307	142.917	0.759	21.65	3.184	0.109	2000 Apr 30	y
...	...	...	...	...	...	B	2.0	300.0	2.304	429.989	4.308	22.06	2.535	0.076	2000 May 01	y
...	...	...	...	...	...	V	2.0	240.0	2.308	852.021	4.632	20.86	2.434	0.080	2000 Apr 30	y
...	...	...	...	...	...	R	2.0	180.0	2.314	991.910	5.504	20.21	2.325	0.083	2000 Apr 30	y
107	UGC08708	$13^h46^m51\overset{s}{.}33$	$+07°24'05\overset{''}{.}4$	10.0	14.0	U	2.0	1200.0	1.444	483.314	2.346	21.77	2.006	0.152	2000 May 04	y
...	...	...	...	...	...	B	2.0	600.0	1.470	682.511	2.300	22.30	1.989	0.147	2000 May 04	y
...	...	...	...	...	...	V	2.0	480.0	1.489	1193.334	3.119	21.21	1.845	0.187	2000 May 04	y
...	...	...	...	...	...	R	2.0	360.0	1.510	1495.251	3.368	20.56	1.875	0.285	2000 May 04	y
108	UGC08823	$13^h53^m11\overset{s}{.}38$	$+69°18'11\overset{''}{.}9$	-2.0	14.0	U	4.0	300.0	1.333	89.809	1.069	22.15	3.114	0.182	2000 Apr 30	y
...	...	...	...	...	...	B	2.0	300.0	1.316	260.974	4.512	22.57	2.976	0.189	2000 Apr 30	y
...	...	...	...	...	...	V	2.0	240.0	1.317	466.885	4.517	21.49	2.599	0.137	2000 Apr 30	y
...	...	...	...	...	...	R	2.0	180.0	1.317	605.399	4.493	20.74	2.602	0.119	2000 Apr 30	y
109	HolmbergIV	$13^h54^m44\overset{s}{.}34$	$+53°53'55\overset{''}{.}3$	9.5	10.0	U	3.0	600.0	1.157	272.372	1.100	20.92	1.762	0.229	1999 Apr 12	n
...	...	...	...	...	...	B	2.0	480.0	1.157	587.635	4.440	21.85	1.811	0.128	1999 Apr 12	n
...	...	...	...	...	...	V	2.0	600.0	1.149	1558.823	8.279	20.96	1.661	0.104	1999 Apr 12	n
...	...	...	...	...	...	R	2.0	360.0	1.165	1277.631	6.133	20.49	1.684	0.152	1999 Apr 12	n
110	NGC5372	$13^h54^m45\overset{s}{.}08$	$+58°39'11\overset{''}{.}0$	-9.0	9.0	U	2.0	600.0	1.158	238.111	0.592	21.73	4.508	0.993	1999 Apr 10	y
...	...	...	...	...	...	B	2.0	240.0	1.189	297.399	2.315	22.11	4.485	1.601	1999 Apr 10	y
...	...	...	...	...	...	V	2.0	300.0	1.159	773.535	4.767	21.11	3.540	0.204	1999 Apr 10	y
...	...	...	...	...	...	R	2.0	180.0	1.201	712.367	5.041	20.49	3.443	0.169	1999 Apr 10	y

Table 1—Continued

ID#	Galaxy	RA	DEC	T_{RC3}	T	Filter	N_{exp}	T_{exp}	*Secz*	Sky	σ_{sky}	μ_{sky}	Seeing	σ_{seeing}	Obs. date	Phot?
(1)	(2)	(3)	(4)	(5)	(6)	(7)	(8)	(9)	(10)	(11)	(12)	(13)	(14)	(15)	(16)	(17)
111	UGC08849	$13^h56^m01^s.41$	$+17°30'22''.1$	-9.0	14.0	U	2.0	600.0	1.475	182.169	1.469	20.84	1.804	0.420	2001 Apr 25	n
...	...	...	...	...	...	B	2.0	300.0	1.483	311.255	2.477	21.41	3.285	0.667	2001 Apr 25	n
...	...	...	...	...	...	V	2.0	240.0	1.489	575.233	3.501	20.44	2.876	0.077	2001 Apr 25	n
...	...	...	...	...	...	R	2.0	180.0	1.494	719.492	4.349	19.98	2.747	0.226	2001 Apr 25	n
112	PGC049633	$13^h57^m09^s.86$	$+34°31'44''.9$	-9.0	3.0	U	2.0	600.0	1.149	166.830	1.034	21.59	1.759	0.157	2000 May 08	n
...	...	...	...	...	...	B	2.0	300.0	1.150	246.027	2.110	22.28	1.821	0.174	2000 May 08	n
...	...	...	...	...	...	V	2.0	240.0	1.152	433.915	2.184	21.20	1.721	0.168	2000 May 08	n
...	...	...	...	...	...	R	2.0	180.0	1.152	579.939	2.457	20.20	1.719	0.179	2000 May 08	n
113	NGC5477	$14^h05^m33^s.27$	$+54°28'00''.0$	9.0	9.0	U	2.0	600.0	1.279	197.405	1.654	21.83	1.886	0.167	2001 May 25	y
...	...	...	...	...	...	B	2.0	300.0	1.279	265.308	1.058	22.45	1.710	0.200	2001 May 25	y
...	...	...	...	...	...	V	2.0	240.0	1.274	438.191	1.632	21.51	1.702	0.065	2001 May 25	y
...	...	...	...	...	...	R	2.0	180.0	1.276	531.222	3.118	20.82	1.493	0.073	2001 May 25	y
114	ESO446-G44	$14^h17^m49^s.66$	$-31°21'04''.8$	6.0	6.7	U	2.0	600.0	2.286	398.652	1.549	21.28	2.396	0.083	2000 May 09	y
...	...	...	...	...	...	B	2.0	300.0	2.291	758.289	2.451	21.42	2.303	0.079	2000 May 09	y
...	...	...	...	...	...	V	2.0	240.0	2.297	1023.587	3.225	20.69	2.175	0.107	2000 May 09	y
...	...	...	...	...	...	R	2.0	180.0	2.304	1033.682	3.081	20.14	2.111	0.098	2000 May 09	y
115	NGC5591	$14^h22^m33^s.53$	$+13°43'22''.1$	-9.0	14.0	U	2.0	600.0	1.097	201.871	0.733	21.20	2.218	0.085	2000 May 06	n
...	...	...	...	...	...	B	2.0	300.0	1.099	304.210	1.417	21.86	2.173	0.124	2000 May 06	n
...	...	...	...	...	...	V	2.0	240.0	1.100	521.792	2.392	21.03	1.744	0.152	2000 May 06	n
...	...	...	...	...	...	R	2.0	180.0	1.102	661.503	3.268	20.14	1.785	0.163	2000 May 06	n
116	NGC5608	$14^h23^m18^s.73$	$+41°47'00''.3$	10.0	9.0	U	2.0	1200.0	1.386	404.985	2.580	21.13	2.289	0.199	2000 May 06	n
...	...	...	...	...	...	B	2.0	600.0	1.398	590.436	2.605	21.98	2.244	0.331	2000 May 06	n
...	...	...	...	...	...	V	2.0	480.0	1.410	1081.079	4.266	21.07	1.980	0.127	2000 May 06	n
...	...	...	...	...	...	R	2.0	360.0	1.421	1481.592	5.634	20.33	1.888	0.159	2000 May 06	n
117	UGC09240	$14^h24^m49^s.88$	$+44°32'08''.8$	10.0	10.0	U	2.0	600.0	1.219	199.820	1.660	21.44	1.999	0.222	2001 Apr 23	n
...	...	...	...	...	...	B	2.0	300.0	1.158	266.382	3.418	22.19	4.292	0.423	2001 Apr 23	n
...	...	...	...	...	...	V	2.0	240.0	1.149	474.156	3.945	21.25	3.986	0.262	2001 Apr 23	n
...	...	...	...	...	...	R	2.0	180.0	1.149	562.391	4.291	20.61	3.744	0.432	2001 Apr 23	n
118	NGC5667	$14^h30^m18^s.74$	$+59°29'09''.4$	6.0	14.0	U	2.0	600.0	1.195	202.383	1.663	22.06	2.325	0.230	2000 May 05	y
...	...	...	...	...	...	B	2.0	300.0	1.196	271.914	2.010	22.62	2.434	0.236	2000 May 05	y
...	...	...	...	...	...	V	2.0	240.0	1.197	464.742	2.594	21.52	2.370	0.244	2000 May 05	y
...	...	...	...	...	...	R	2.0	180.0	1.198	533.241	3.430	20.87	2.415	0.242	2000 May 05	y
119	NGC5668	$14^h33^m26^s.64$	$+04°26'23''.0$	7.0	4.0	U	2.0	600.0	1.147	211.549	2.953	21.21	2.415	0.175	2001 Apr 24	n
...	...	...	...	...	...	B	2.0	300.0	1.144	313.175	6.743	21.99	2.130	0.135	2001 Apr 24	n
...	...	...	...	...	...	V	2.0	240.0	1.143	531.391	6.657	21.11	2.121	0.134	2001 Apr 24	n
...	...	...	...	...	...	R	2.0	180.0	1.142	621.477	6.445	20.51	2.196	0.130	2001 Apr 24	n
120	UGC09638	$14^h58^m03^s.21$	$+58°52'51''.5$	10.0	6.0	U	2.0	1200.0	1.160	340.766	2.065	22.33	1.532	0.375	2000 May 07	y
...	...	...	...	...	...	B	2.0	600.0	1.163	449.932	3.031	23.08	1.440	0.078	2000 May 07	y
...	...	...	...	...	...	V	2.0	480.0	1.167	760.220	3.177	22.00	1.279	0.153	2000 May 07	y
...	...	...	...	...	...	R	2.0	360.0	1.171	1004.412	4.676	21.38	1.356	0.100	2000 May 07	y

Table 1—Continued

ID#	Galaxy	RA	DEC	T_{RC3}	T	Filter	N_{exp}	T_{exp}	*Secz*	Sky	σ_{sky}	μ_{sky}	Seeing	σ_{seeing}	Obs. date	Phot?
(1)	(2)	(3)	(4)	(5)	(6)	(7)	(8)	(9)	(10)	(11)	(12)	(13)	(14)	(15)	(16)	(17)
121	UGC09855	$15^h25^m00^s.32$	$+66°14'21''.3$	10.0	14.0	U	2.0	600.0	1.234	212.335	0.675	21.86	2.764	0.063	1999 Apr 10	y
...	...	...	...	...	...	B	2.0	240.0	1.255	263.620	0.677	22.25	2.904	0.129	1999 Apr 10	y
...	...	...	...	...	...	V	2.0	300.0	1.234	724.498	2.565	21.18	2.588	0.235	1999 Apr 10	y
...	...	...	...	...	...	R	2.0	180.0	1.264	698.631	2.550	20.51	2.655	0.129	1999 Apr 10	y
122	UGC09899	$15^h31^m56^s.35$	$+68°14'24''.1$	6.0	3.7	U	2.0	600.0	1.283	367.333	1.387	20.74	1.611	0.122	1999 Apr 11	n
...	...	...	...	...	...	B	2.0	240.0	1.263	461.649	1.673	21.27	1.575	0.189	1999 Apr 11	n
...	...	...	...	...	...	V	2.0	300.0	1.284	1061.450	3.357	20.62	1.384	0.133	1999 Apr 11	n
...	...	...	...	...	...	R	2.0	180.0	1.256	823.484	2.992	20.19	1.395	0.065	1999 Apr 11	n
123	UGC09913	$15^h34^m56^s.33$	$+23°29'33''.8$	-9.0	14.0	U	2.0	600.0	1.148	180.564	1.153	22.01	1.678	0.077	2001 May 23	y
...	...	...	...	...	...	B	2.0	300.0	1.150	250.460	1.251	22.50	1.586	0.073	2001 May 23	y
...	...	...	...	...	...	V	2.0	240.0	1.152	387.846	1.774	21.64	1.496	0.071	2001 May 23	y
...	...	...	...	...	...	R	2.0	180.0	1.155	390.485	1.994	21.13	1.373	0.068	2001 May 23	y
124	NGC5994-6	$15^h46^m58^s.09$	$+17°54'42''.2$	-9.0	14.0	U	2.0	600.0	1.066	172.264	1.390	22.07	1.534	0.087	2001 May 23	y
...	...	...	...	...	...	B	2.0	300.0	1.067	246.130	3.594	22.52	1.470	0.169	2001 May 23	y
...	...	...	...	...	...	V	2.0	240.0	1.069	387.470	4.246	21.64	1.341	0.068	2001 May 23	y
...	...	...	...	...	...	R	2.0	180.0	1.070	406.607	5.724	21.09	1.294	0.091	2001 May 23	y
125	UGC10043	$15^h48^m41^s.79$	$+21°51'31''.9$	4.0	2.3	U	2.0	1800.0	1.048	606.302	2.733	22.14	1.485	0.305	2001 Feb 22	y
...	...	...	...	...	...	B	2.0	1200.0	1.158	1141.141	4.763	23.03	1.206	0.168	2001 Feb 22	y
...	...	...	...	...	...	V	2.0	900.0	1.167	2051.166	7.973	21.68	1.093	0.240	2001 Feb 22	y
...	...	...	...	...	...	R	2.0	600.0	1.331	2551.404	10.731	20.92	1.221	0.155	2001 Feb 22	y
126	UGC10061	$15^h51^m15^s.74$	$+16°21'16''.9$	10.0	10.0	U	2.0	1200.0	1.256	450.626	2.388	21.84	2.183	0.199	2000 May 04	y
...	...	...	...	...	...	B	2.0	600.0	1.266	988.705	4.238	21.90	2.070	0.254	2000 May 04	y
...	...	...	...	...	...	V	2.0	480.0	1.278	1905.436	5.835	20.70	1.986	0.229	2000 May 04	y
...	...	...	...	...	...	R	2.0	360.0	1.290	3198.856	10.155	19.73	2.046	0.245	2000 May 04	y
127	NGC6052	$16^h05^m11^s.54$	$+20°32'05''.9$	5.0	14.0	U	2.0	600.0	1.041	177.508	1.630	21.44	2.753	0.181	2001 Apr 24	n
...	...	...	...	...	...	B	2.0	300.0	1.038	253.712	2.982	22.23	2.606	0.329	2001 Apr 24	n
...	...	...	...	...	...	V	2.0	240.0	1.037	424.146	3.320	21.37	2.670	0.131	2001 Apr 24	n
...	...	...	...	...	...	R	2.0	180.0	1.037	503.132	3.639	20.76	2.295	0.137	2001 Apr 24	n
128	UGC10279	$16^h11^m51^s.93$	$+60°34'40''.2$	-9.0	14.0	U	4.0	300.0	1.145	87.138	0.489	22.18	3.019	0.248	2000 Apr 30	y
...	...	...	...	...	...	B	2.0	300.0	1.146	241.103	1.414	22.65	2.977	0.271	2000 Apr 30	y
...	...	...	...	...	...	V	2.0	240.0	1.148	416.169	1.840	21.62	2.933	0.332	2000 Apr 30	y
...	...	...	...	...	...	R	2.0	180.0	1.150	555.305	2.632	20.83	2.977	0.167	2000 Apr 30	y
129	UGC10315	$16^h15^m42^s.63$	$+68°22'56''.2$	-9.0	2.0	U	2.0	600.0	1.244	238.526	1.672	21.23	1.517	0.134	2000 May 02	n
...	...	...	...	...	...	B	1.0	300.0	1.252	277.219	1.649	22.11	1.534	0.340	2000 May 02	n
...	...	...	...	...	...	V	1.0	240.0	1.256	486.124	2.088	21.23	1.222	0.083	2000 May 02	n
...	...	...	...	...	...	R	1.0	180.0	1.259	623.727	3.915	20.55	1.249	0.146	2000 May 02	n
130	NGC6104	$16^h16^m29^s.13$	$+35°42'51''.9$	-9.0	3.3	U	2.0	600.0	1.150	178.088	1.341	21.94	1.984	0.180	2001 May 25	y
...	...	...	...	...	...	B	2.0	300.0	1.152	263.021	1.085	22.45	2.066	0.142	2001 May 25	y
...	...	...	...	...	...	V	2.0	240.0	1.154	420.684	1.949	21.56	1.886	0.083	2001 May 25	y
...	...	...	...	...	...	R	2.0	180.0	1.156	478.996	3.115	20.93	1.751	0.102	2001 May 25	y

Table 1—Continued

ID#	Galaxy	RA	DEC	T_{RC3}	T	Filter	N_{exp}	T_{exp}	*Secz*	Sky	σ_{sky}	μ_{sky}	Seeing	σ_{seeing}	Obs. date	Phot?
(1)	(2)	(3)	(4)	(5)	(6)	(7)	(8)	(9)	(10)	(11)	(12)	(13)	(14)	(15)	(16)	(17)
131	UGC10334	$16^h17^m13^s.68$	$+63°51'09''.6$	10.0	14.0	U	2.0	600.0	1.206	662.335	2.115	20.08	1.733	0.135	1999 Apr 12	n
...	...	...	...	...	...	B	2.0	360.0	1.206	6002.481	19.070	18.59	1.669	0.094	1999 Apr 12	n
...	...	...	...	...	...	V	2.0	450.0	1.207	2665.166	8.548	19.82	1.493	0.101	1999 Apr 12	n
...	...	...	...	...	...	R	2.0	270.0	1.207	4362.851	8.393	18.50	1.524	0.099	1999 Apr 12	n
132	UGC10351	$16^h21^m28^s.16$	$+28°38'17''.5$	8.0	-9.0	U	2.0	600.0	1.035	166.849	1.358	21.50	4.538	0.210	2001 Apr 24	n
...	...	...	...	...	...	B	2.0	300.0	1.043	267.763	2.007	22.20	4.538	0.312	2001 Apr 23	n
...	...	...	...	...	...	V	2.0	240.0	1.039	469.465	3.253	21.28	4.492	0.248	2001 Apr 23	n
...	...	...	...	...	...	R	2.0	180.0	1.038	573.329	4.031	20.61	3.862	0.451	2001 Apr 23	n
133	UGC10445	$16^h33^m48^s.35$	$+28°58'52''.1$	6.0	4.0	U	2.0	600.0	1.049	175.161	1.253	21.43	4.569	0.320	2001 Apr 24	n
...	...	...	...	...	...	B	2.0	300.0	1.068	559.644	2.302	21.40	3.461	0.312	2001 Apr 23	n
...	...	...	...	...	...	V	2.0	240.0	1.067	534.420	2.376	21.15	3.371	0.198	2001 Apr 23	n
...	...	...	...	...	...	R	2.0	180.0	1.067	633.775	3.290	20.51	3.285	0.289	2001 Apr 23	n
134	NGC6202	$16^h43^m22^s.31$	$+61°58'15''.2$	-9.0	2.0	U	2.0	600.0	1.146	400.491	1.905	21.17	2.460	0.224	1999 Apr 10	y
...	...	...	...	...	...	B	2.0	240.0	1.147	497.535	1.542	21.56	2.370	0.162	1999 Apr 10	y
...	...	...	...	...	...	V	2.0	300.0	1.147	1078.615	3.387	20.75	2.113	0.214	1999 Apr 10	y
...	...	...	...	...	...	R	2.0	180.0	1.149	812.615	2.884	20.34	2.332	0.208	1999 Apr 10	y
135	NGC6238	$16^h47^m12^s.46$	$+62°08'41''.4$	-9.0	14.0	U	2.0	600.0	1.566	163.383	0.784	22.21	2.816	0.221	2000 Feb 04	y
...	...	...	...	...	...	B	2.0	240.0	1.164	766.798	2.819	20.80	1.721	0.187	1999 Apr 11	n
...	...	...	...	...	...	V	2.0	300.0	1.171	4150.571	14.959	18.52	1.416	0.071	1999 Apr 11	n
...	...	...	...	...	...	R	2.0	180.0	1.167	1337.476	4.753	19.71	2.003	0.146	1999 Apr 10	n
136	UGC10670	$17^h01^m26^s.92$	$+63°42'14''.7$	-9.0	3.3	U	2.0	600.0	1.184	146.919	1.348	21.49	1.359	0.059	2000 May 07	n
...	...	...	...	...	...	B	2.0	300.0	1.185	218.292	1.742	22.44	1.380	0.094	2000 May 07	n
...	...	...	...	...	...	V	2.0	240.0	1.186	362.642	1.842	21.58	1.234	0.065	2000 May 07	n
...	...	...	...	...	...	R	2.0	180.0	1.187	535.383	3.466	20.72	1.249	0.091	2000 May 07	n
137	UGC10770	$17^h13^m08^s.44$	$+59°20'19''.9$	10.0	14.0	U	2.0	600.0	1.130	248.807	1.532	21.84	1.592	0.102	2000 May 05	y
...	...	...	...	...	...	B	2.0	300.0	1.130	308.267	1.513	22.48	1.650	0.121	2000 May 05	y
...	...	...	...	...	...	V	2.0	240.0	1.131	521.684	1.865	21.40	1.496	0.124	2000 May 05	y
...	...	...	...	...	...	R	2.0	180.0	1.132	542.648	2.916	20.86	1.515	0.124	2000 May 05	y
138	NGC6365A	$17^h22^m45^s.63$	$+62°09'23''.4$	6.0	3.7	U	4.0	300.0	1.158	96.502	1.039	22.07	2.856	0.111	2000 Apr 30	y
...	...	...	...	...	...	B	2.0	300.0	1.159	291.029	4.265	22.45	2.918	0.131	2000 Apr 30	y
...	...	...	...	...	...	V	2.0	240.0	1.160	460.378	4.519	21.51	2.666	0.155	2000 Apr 30	y
...	...	...	...	...	...	R	2.0	180.0	1.161	554.718	5.136	20.83	2.724	0.171	2000 Apr 30	y
139	NGC6690	$18^h34^m45^s.88$	$+70°31'06''.9$	7.0	7.3	U	2.0	600.0	1.266	188.008	1.633	21.97	2.025	0.056	2001 May 23	y
...	...	...	...	...	...	B	2.0	300.0	1.268	260.743	2.476	22.45	1.875	0.062	2001 May 23	y
...	...	...	...	...	...	V	2.0	240.0	1.269	399.453	4.093	21.61	1.558	0.073	2001 May 23	y
...	...	...	...	...	...	R	2.0	180.0	1.270	428.589	4.521	21.03	1.671	0.091	2001 May 23	y
140	NGC6789	$19^h16^m40^s.89$	$+63°58'05''.6$	10.0	10.0	U	2.0	600.0	1.674	281.583	2.372	20.97	2.130	0.095	1999 Dec 05	n
...	...	...	...	...	...	B	2.0	300.0	1.676	426.491	4.058	21.72	1.980	0.038	1999 Dec 05	n
...	...	...	...	...	...	V	2.0	240.0	1.586	799.420	7.891	20.80	1.828	0.059	1999 Dec 05	n
...	...	...	...	...	...	R	2.0	180.0	1.657	1343.917	13.913	19.21	1.399	0.100	1999 Dec 06	n

Table 1—Continued

ID#	Galaxy	RA	DEC	T_{RC3}	T	Filter	N_{exp}	T_{exp}	*Secz*	Sky	σ_{sky}	μ_{sky}	Seeing	σ_{seeing}	Obs. date	Phot?
(1)	(2)	(3)	(4)	(5)	(6)	(7)	(8)	(9)	(10)	(11)	(12)	(13)	(14)	(15)	(16)	(17)
141	NGC7320	$22^h36^m01^s.57$	$+33°57'32''.8$	4.0	14.0	U	2.0	600.0	1.284	247.574	1.609	21.69	2.083	0.060	2001 May 26	y
...	...	...	...	...	...	B	2.0	300.0	1.286	378.572	4.573	22.08	2.003	0.081	2001 May 26	y
...	...	...	...	...	...	V	2.0	240.0	1.265	550.454	3.997	21.27	1.920	0.081	2001 May 25	y
...	...	...	...	...	...	R	2.0	180.0	1.265	618.115	4.615	20.65	2.036	0.089	2001 May 25	y
142	NGC7732	$23^h41^m33^s.03$	$+03°43'26''.7$	6.0	14.0	U	2.0	1200.0	1.241	594.946	3.040	21.00	2.186	0.212	1999 Dec 05	n
...	...	...	...	...	...	B	2.0	600.0	1.250	984.463	5.205	21.57	2.334	0.132	1999 Dec 05	n
...	...	...	...	...	...	V	2.0	480.0	1.259	1736.645	16.955	20.61	2.201	0.135	1999 Dec 05	n
...	...	...	...	...	...	R	2.0	360.0	1.187	2194.672	21.050	19.74	1.159	0.117	1999 Dec 06	n

Note. — **Columns:** (1) ID number assigned to this galaxy, (2) galaxy name, (3) Right Ascension (J2000), (4) Declination (J2000), (5) RC3 classification, (6) visual classification, (7) filter, (8) number of images used in each stack, (9) average exposure time of those images (s), (10) average airmass (sec z), (11) median sky in ADU, (12) uncertainty on a single pixel measurement of the sky, (13) sky surface brightness in magarcsec^{-2}, (14) average stellar FWHM ("seeing") (arcsec), (15) uncertainty on the seeing, (16) observation date of the first deep image combined into the final stack, and (17) whether the individual deep images were photometric: if no (n), then the deep images were calibrated with shorter photometric exposures.

Table 2. *HST* NICMOS and WFPC2 dataset.

galaxy	RA	DEC	T_{RC3}	r_{outer}	δ_1	σ_{δ_1}	δ_2	σ_{δ_2}	δ_3	σ_{δ_3}
NGC1311	$03^h20^m06\overset{s}{.}66$	-52°11′12″.5	9.0	39.44	0.97	0.05	1.42	0.04	0.64	0.03
ESO418-G008	$03^h31^m30\overset{s}{.}58$	-30°12′46″.6	8.0	22.94	-1.05	0.04	-1.26	0.03	-0.26	0.03
NGC1679	$04^h49^m55\overset{s}{.}31$	-31°58′05″.5	9.5	33.61	-0.50	0.03	-0.85	0.03	-0.25	0.02
NGC2551	$08^h24^m50\overset{s}{.}16$	+73°24′43″.0	0.2	28.56	-2.39	0.03	-2.88	0.03	-0.50	0.01
NGC3516	$11^h06^m47\overset{s}{.}48$	+72°34′06″.7	-2.0	25.22	-0.35	0.06	-0.60	0.06	-0.25	0.02
NGC6789	$19^h16^m41\overset{s}{.}93$	+63°58′20″.8	10.0	23.51	2.09	0.08	1.87	0.07	-0.32	0.03

Note. — The six galaxies for which we have *HST* NICMOS F160W and WFPC2 F300W and F814W images. **Columns:** Galaxy name, Right Ascension (J2000), Declination (J2000), RC3 classification, the outer annulus radius used in the surface brightness profiles (r_{outer}) in arcseconds, and the three color profile slopes and their errors (from the linear-least-squares fit) in units of Δmag per r_{outer}, where δ_1 is the slope in (F300W–F814W), δ_2 is the slope in (F300W–F160W), and δ_3 is the slope in (F814W–F160W).

Table 3. Dark current measurements.

T_{exp}	⟨Dark⟩	σ_{dark}	hr^{-1}	$(1200s)^{-1}$
240	0.546	3.36	8.18	2.73
240	0.525	3.40	7.87	2.62
300	0.611	3.54	7.34	2.45
300	0.624	3.42	7.49	2.50
600	1.131	3.83	6.79	2.26
600	1.261	4.08	7.57	2.52

Note. — **Columns:** Exposure time (s) of the dark image, total median dark current (ADU) in the image, standard deviation on the median dark current, dark current rate (ADU hr^{-1}), and the dark current (ADU $1200s^{-1}$) corresponding to our longest object exposures of 1200 s taken in the *U*-band. Most exposures are much shorter, down to 180 seconds. It was determined that this dark current is negligible and unnecessary to subtract from object images.

images is accurate to within $\sim 3\%$. The VATT, at present, does not offer a reliable way of taking dome flats, so only twilight sky-flat fields were used. We were usually able to obtain at least 3–4 good evening sky-flats per filter per night, and at least another 3–4 morning sky-flats, which sufficed to remove all traces of high frequency structure. After flat-fielding, at most a 1% gradient in the sky background remained across the entire image. Differences in illumination of the detector between the twilight and night sky, which depend at least in part on the position of the telescope relative to the Sun and Moon, appear to be the cause. Because this gradient is less than 1% across the entire image, and because most of our galaxies are $\sim 1'$ in size and centered in the exposure, galaxy photometry will be only slightly affected by this gradient, especially when compared to other larger sources of uncertainty. A 1% error in the sky corresponds on average to 27.0, 27.5, 26.5, and 26.0 mag arcsec^{-2} in U, B, V, and R, respectively (as calculated from the average sky brightnesses presented in Chapter 4), which is fainter than the level at which our surface brightness profiles are reliably determined, and therefore should have little effect on our results. Therefore, sky-gradient corrections were not applied.

Individual galaxy images were combined on a per filter basis with integer pixel shifts. This is sufficient for our purposes because the seeing is oversampled (with 4 to 5 pixels per FWHM, on average), and because this analysis focuses on large scale radial trends. We also normalized the images to an exposure time of 1 second, airmass of 1, and zero-point of 25 mag arcsec^{-2}, for convenience. To verify the consistency of our photometry, we present a plot of the difference between our measured total B-band magnitudes and those from the RC3 vs. our measured total B-band magnitudes in Figure 3. Our values agree with those of the RC3 within an average of 0.2 magnitudes, which is comparable to the total magnitude errors quoted in the RC3. There is no significant systematic trend with total B-band magnitude, which shows that our photometry is consistently accurate for the full range of galaxy brightnesses.

Cosmic rays were removed using an IRAF script by Rhoads (2000), which rejects cosmic rays based on filtering out the point spread function (PSF) minus a user-scaled delta function, and rejecting any objects below a defined threshold to remove those objects that are much sharper than the PSF, and therefore cannot be real objects. The input parameters were modified by hand on a galaxy-per-galaxy basis to avoid erroneously rejecting pieces of the target galaxy. Any remaining cosmic rays were masked manually and interpolated over.

The images were astrometrically calibrated using LMORPHO (Odewahn et al. 2002), which calculates approximate astrometric solutions from user-interactive comparisons of several stars in the target image to the same stars in a DSS[5] image of the same region. It then refines the solutions by comparing all objects found with SExtractor (Bertin & Arnouts 1996) in the target image to accurate positions for all objects in this region listed in the USNO A2.0 catalog (Monet et al. 1996).

[5]The Digitized Sky Surveys were produced at the Space Telescope Science Institute under U.S. Government grant NAG W-2166. The images of these surveys are based on photographic data obtained using the Oschin Schmidt Telescope on Palomar Mountain and the UK Schmidt Telescope. The plates were processed into the present compressed digital form with the permission of these institutions.

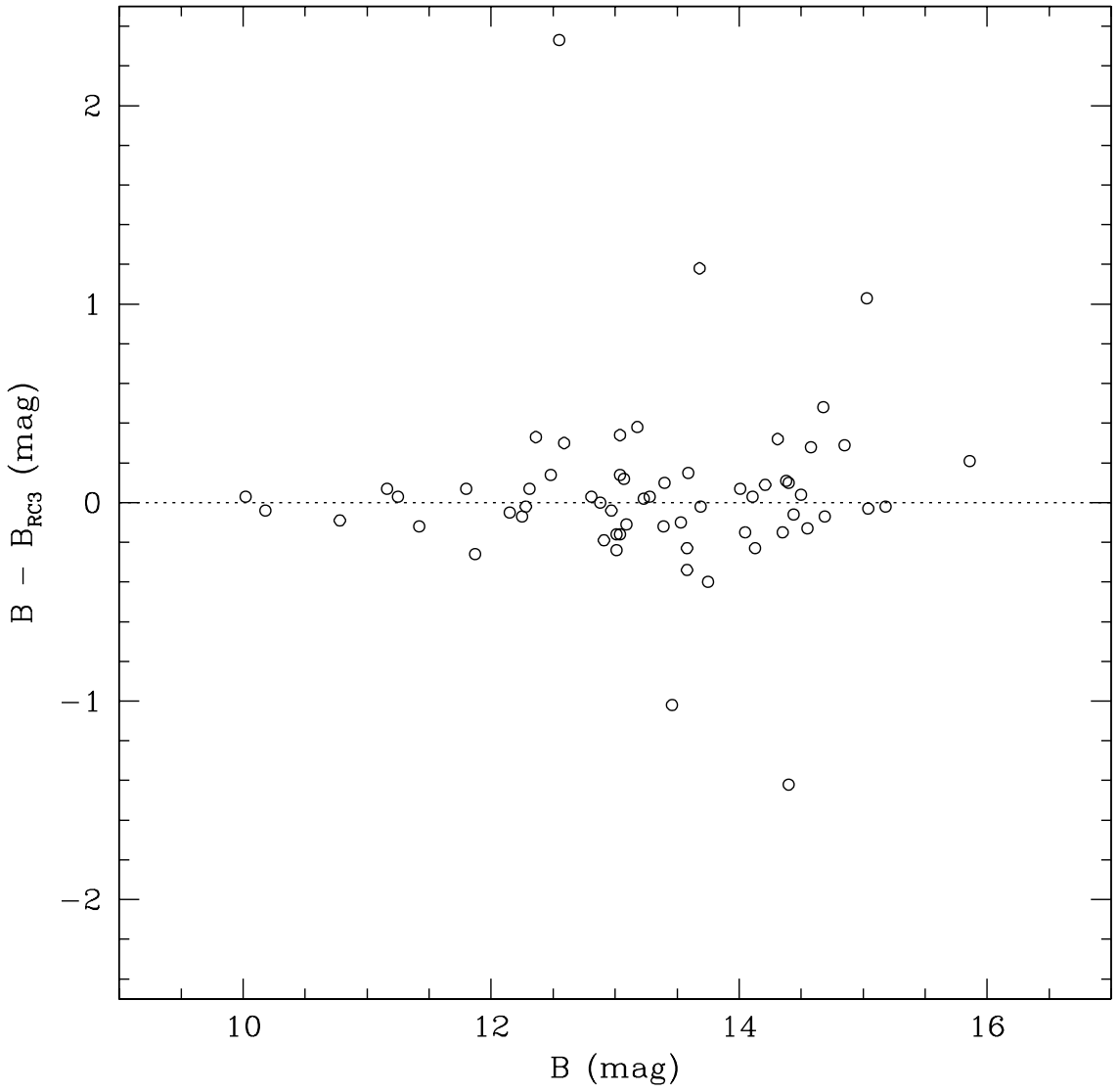

Figure 3 Comparison of our calibrated total B-band magnitudes to those listed in the RC3, for verifying the consistency of our photometry. Our measured magnitudes tend to agree with those of the RC3 within an average of about 0.2 magnitudes, which is generally comparable to the total magnitude errors quoted in the RC3. There is no significant systematic trend with B-band magnitude, which shows that our photometry is consistently accurate for all galaxy brightnesses.

In order to obtain matched aperture photometry so that galaxy properties in different pass-bands can be directly compared to one another, the images in each filter were all registered with LMORPHO to the V-band, which was chosen as the reference pass-band because it typically has high signal-to-noise and few saturated stars. The SExtractor object lists were compared between filters to find linear shifts, and the images were shifted accordingly.

Finally, non-target objects were replaced with a local sky value ("patched") using LMORPHO, which uses positions from the object list created by SExtractor, and a user defined threshold value to patch out a large enough area to remove most of the light from each unrelated neighboring object. Each image was reviewed interactively to remove the target galaxy from the patch list, and to add any objects that SExtractor missed. In the case of interacting galaxies, the target was treated separately and the companion galaxy patched out unless there was no clear way to distinguish the galaxies, in which case they were treated as one. The patched area was replaced with an average value for the local sky that LMORPHO determined through an iterative sky-mapping procedure, which rejects objects above a certain signal-to-noise threshold level.

2.2.4. HST *Data Reduction and Calibration*

Combined images of the *HST* WFPC2 mid-UV F300W and near-IR F814W observations were obtained as type B associations from the Space Telescope Science Institute (STSCI) data archive.[6] The associations were then mosaiced using `WMOSAIC` within the `STSDAS` package in IRAF.

The individual *HST* NIC3 F160W images were combined with `CALNICB` within the `STSDAS` package in IRAF, using shifts found semi-automatically with `IMCENTROID`. We used the VEGA zero point of 21.901 mag arcsec^{-2} for the NICMOS data, calculated from the calibration data presented on the NICMOS website at STSCI.[7] Some bad pixels that were not removed with the pipeline bad pixel mask were removed by hand.

The WFPC2 images were registered to the NICMOS images by manually finding the coordinates of stars in common between images in each field, and by using these in `GEOMAP` and `GEOTRAN` in IRAF to apply the proper transformations. Non-target sources in all images were patched within LMORPHO to an average local sky-value using the same method as with the VATT data. We adopted the Holtzmann et al. (1995) zero points for each WFPC2 image.

2.3. Data Analysis

2.3.1. *Surface Brightness Profiles*

Surface brightness profiles were calculated with LMORPHO for each galaxy within 12 equally spaced elliptical annuli, starting from the galaxy center. Parameters such as

[6] http://archive.stsci.edu/hst/wfpc2/index.html
[7] http://www.stsci.edu/hst/nicmos/performance/photometry/postncs_keywords.html

galaxy center, annulus radius, axis ratio, and position angle were chosen to match the shape of the outer isophotes, and were fixed in the R-band for the VATT data, and the NICMOS F160W band for the *HST* data. These were then applied to all other pass-bands in order to achieve matched aperture photometry that could be directly and consistently translated into a color profile. The random error was calculated for the surface brightnesses with the formula:

$$\sigma = \sqrt{\frac{\sigma_{sky}^2}{N} + \frac{\langle F \rangle + \langle sky \rangle}{N}} \tag{2.1}$$

where $\langle F \rangle$ is the measured average flux per pixel above sky within the annulus, and N is the number of pixels in the annulus. This does not include systematic errors due to small sky-subtraction errors, which can result in significant errors in the galaxy surface brightnesses as calculated at large radii, making the last few points in the surface brightness profiles less reliable than the inner points. Because the FOV in the VATT images ($6.4'$) is much larger than the size of most of the galaxies (diameter $\sim 1'$), and because the fields tend to be un-crowded at high Galactic and Ecliptic latitudes, we expect few objects to contaminate the VATT sky determinations. Errors due to the small ($\lesssim 1\%$) gradients in the sky tend to drop out in the ellipse fitting, as long as the background shows no higher order structure. The *HST* NICMOS data, however, have a much smaller FOV ($51.2''$). Therefore, it is much more difficult to obtain sky-values in the *HST* images that are not contaminated by the galaxy, and as such the points in the outer part of the *HST* profiles are less reliable than those in the VATT profiles. These larger uncertainties in the outer profile points are accounted for when determining color gradients, as described in Section 3.2, such that they will have minimal impact on the accuracy of our final results.

Figure 4 shows a comparison of our VATT surface brightness profiles in UBR to those of Jansen et al. (2000), for the 6 galaxies in common between our samples. For this comparison, our major axis radii, r, were converted to *elliptical* or *equivalent* radii, $r_{ell} = r\sqrt{b/a}$. The solid curves represent an estimate of the average 1-σ error found by adding our errors in quadrature with those of Jansen et al. (2000). For the most part, both our profiles agree within the uncertainties, with a few slightly deviant points that can be attributed to various differences in the way that the two profiles were created. Jansen et al. (2000) applied a color term correction to each annulus separately, while we applied a single color term to the entire galaxy, based on its overall average color. The color term correction is small and difficult to measure accurately without a large number of standard stars of all colors taken throughout each observing night (which would sacrifice significant galaxy observing time). Therefore, errors introduced by using the average color of a galaxy to determine an average color term will be small compared to the errors inherent in measuring the small color term correction, and will therefore have little effect on our results. In extreme cases, this will cause the profiles to vary only slightly, if the galaxy color is a significant function of radius. Larger deviations in color gradient measurements are introduced by different choices of the galaxy center, and its axis ratio and position angle, which is especially an issue for galaxies with irregular or peculiar morphologies. For these

morphologies, the choice of center is somewhat subjective, and the brightest peak often does not coincide with the center of the outer parts or disk. That center, and the shape and orientation of the isophotes, can vary significantly with radius. This effect can lead to vast differences in the choice of axis ratio and position angle, depending on how the observer chose to define them. In our case, these parameters were calculated automatically by LMORPHO, then inspected manually, with a few values tweaked to change the center, ellipticities, and position angles from the brightest un-centered peak to the center and shape of the outer disk. The choice of these parameters has the largest effect on the inner parts of the profiles, where a change in adopted axis ratio and orientation may result in different structures within the galaxy being sampled. The outer parts of the profile will be more dominated by sky subtraction errors. No attempt was made to correct for choice of the galaxy center, axis ratio, or position angle for this comparison.

Our profiles generally agree with those of Jansen et al. (2000) within a few tenths of a magnitude, which is similar to the differences they found in comparing their profiles with several other independent observers. The galaxy with the largest disagreement between our and Jansen et al.'s (2000) profiles is NGC3913, which is an asymmetric spiral galaxy. This asymmetry makes the choice of position angle and axis ratio particularly important, such that small changes in either could have a significant effect on the surface brightness profile. Here, Jansen et al. (2000) used an axis ratio (b/a) of 0.9333 and a position angle (PA) (East of North) of 165°, compared to our b/a of 0.967 and PA of 38.4°, which could account for the relatively large discrepancy in our surface brightness profiles.

2.3.2. *Color Profiles and Radial Color Gradients*

Radial color profiles were calculated from the surface brightness profiles. The errors on the color profiles were calculated by adding the independent errors of the surface brightnesses profiles for each of the two filters (see eq.[1]), converted to units of mag arcsec^{-2}, in quadrature. Using units of mag arcsec^{-2} is adequate, since the error on the flux, σ, will be small, and the error on the magnitude, σ_μ, is related to the error on the log of the flux, $\sigma_{log(f)}$ by:

$$\sigma_\mu = 2.5\ \sigma_{log(f)} = 1.0857\ \frac{\sigma}{f} \approx \frac{\sigma}{f}. \tag{2.2}$$

To measure the extent to which the VATT color profiles are becoming redder or bluer with increasing radius (color "gradient", or "slope"), we applied a linear-least-squares fit to the color profiles outside of the half-light, or *effective*, radius, r_e (as calculated from the R-band surface brightness profile), for the outer disk components, and separately applied a fit inside of r_e for the inner parts, which may be more affected by a bulge component, if present. Points where the measured average flux per pixel was smaller than 0.5 σ_{sky} were not included in the fit in order to ignore values that have large uncertainties due to low signal-to-noise. To obtain more reliable color gradients, we weighted the points on the color profile by their errors. All radii were normalized to the effective radius in order to allow comparison of galaxies with various sizes. Therefore, our adopted units for the color

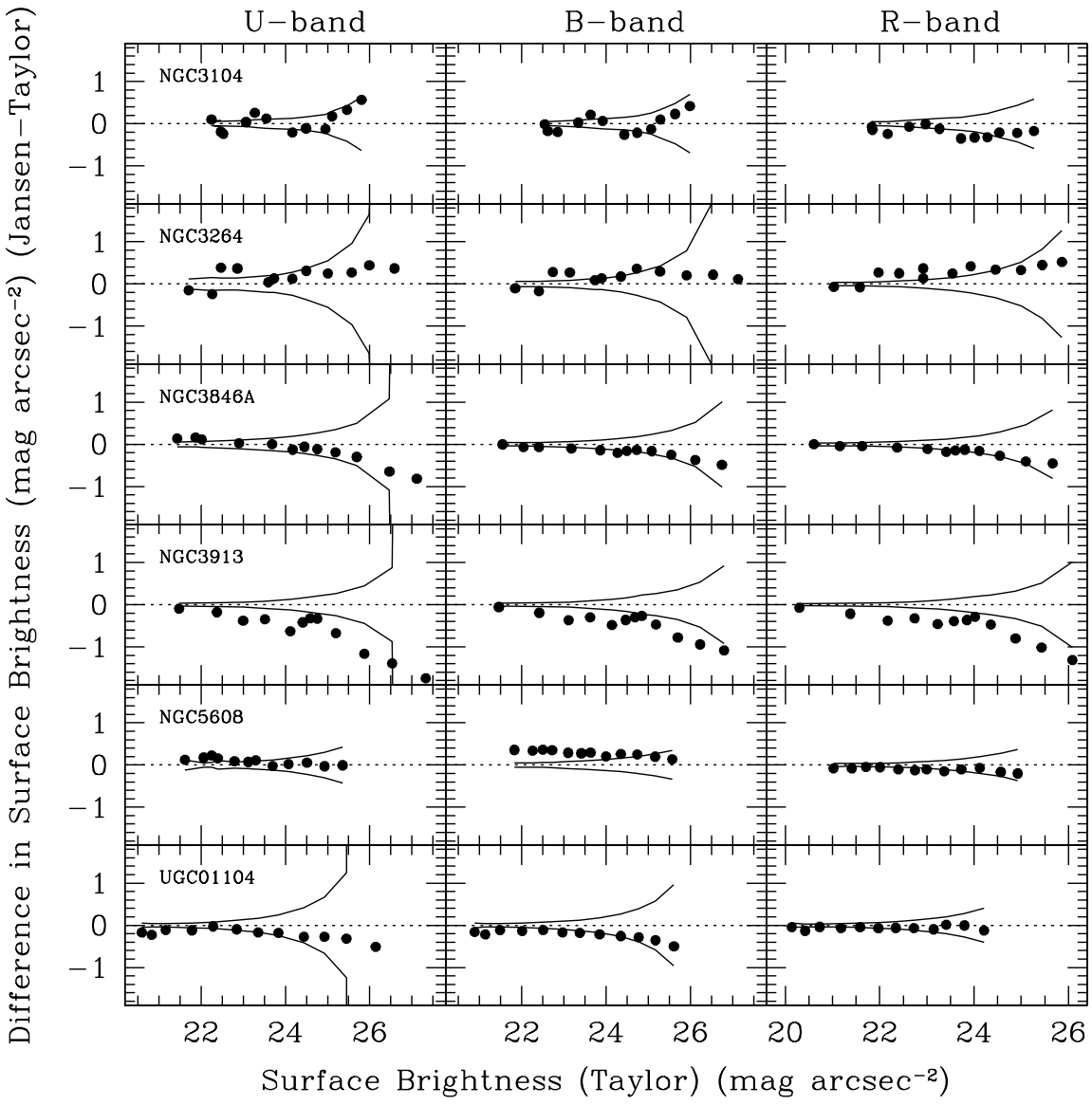

Figure 4 The difference in surface brightnesses ($\Delta\mu$) at particular radii as a function of surface brightness μ for six galaxies previously observed by Jansen et al. (2000). The difference is in the sense (Jansen et al. minus our profile), and the abscissa reflects our measurements of μ. As an aid in distinguishing significant differences, the solid curves indicate 1-σ deviations, computed as the quadratic sum of the errors in the individual profiles. Deviations from zero in the inner parts of the galaxies result most frequently from a different choice of center, position angle and/or axis ratio, causing different morphological structures to be sampled. Deviations in the outer parts are dominated by sky-subtraction uncertainties. For the most part, both profiles agree to within the uncertainties — typically a few tenths of a magnitude. The galaxy showing the poorest agreement, NGC3913, is asymmetric with significant spiral structure, causing differences in assumed shape and orientation to have a large impact. The position angles adopted here and in Jansen et al. differ by over 50°, which could account for the relatively large discrepancies.

profile slopes are the change in color (Δmag) per unit effective radius (r_e), where a positive slope indicates that a galaxy is getting redder with increasing radius from its center, and a negative slope indicates that it becomes bluer outward. If there were fewer than three good points in the inner or outer region of a galaxy, no slope was calculated for that region. Table 4 lists the outer color slopes (gradients) measured for all 142 galaxies (columns 16–19), as well as some other measured quantities such as effective radius (in both angular (column 3) and linear (column 4) units), total apparent and absolute B magnitudes (columns 7 and 8), average B surface brightness within r_e (column 12), and total (columns 9–11) and effective $(U-B)$, $(B-V)$, and $(V-R)$ colors (columns 13–15), where the effective color is defined as the average color within r_e. Figure 5 consists of a total of 13 pages, with all of the VATT surface brightness and color profiles and their fits.

Due to the small FOV of the *HST* images and the low signal-to-noise at low surface brightness levels, the outer-most parts of the galaxies are not necessarily detectable in the *HST* images, and it is thus not feasible to measure r_e from their surface brightness profiles. Therefore, we measured all *HST* color gradients across the entire galaxy profile, such that the units for the slopes are change in color (Δmag) per r_{outer}, where r_{outer} is the radius of the outer-most annulus used in the surface brightness profile (which was defined to go out far enough to include most of the light visible in the F160W image). When the signal-to-noise ratio was too low to reliably determine a surface brightness in an annulus, a surface brightness was not calculated for that annulus and not included in the color slope calculation. The remaining points were weighted by their errors, except for the inner-most point of NGC3516, which was eliminated from the fit because the galaxy's center is saturated in the WFPC2 images. The color gradients measured from the *HST* F300W, I and H surface brightness profiles are listed in Table 2.

Table 4. VATT Measured Galaxy Parameters.

ID#	D_{24}	$r_e('')$	$r_e(kpc)$	b/a	V_{GSR}	B_T	$B_T(abs)$	$(U-B)_T$	$(B-V)_T$	$(V-R)_T$	$\mu_e(B)$	$(U-B)_e$	$(B-V)_e$	$(V-R)_e$	$\delta(U-R)/r_e$	$\delta(U-B)/r_e$	$\delta(B-V)/r_e$	$\delta(V-R)/r_e$
(1)	(2)	(3)	(4)	(5)	(6)	(7)	(8)	(9)	(10)	(11)	(12)	(13)	(14)	(15)	(16)	(17)	(18)	(19)
001	95.61	26.88	2.33	0.540	1267.	14.580	-16.678	-0.083	0.576	0.394	23.150	-0.083	0.691	0.379	0.180	0.125	-0.112	0.157
...	...	...	...	...	...	0.024	0.064	0.037	0.032	0.029	0.027	0.043	0.037	0.034	0.159	0.171	0.118	0.105
002	51.13	14.90	10.93	0.460	10742.	15.836	-20.063	0.050	0.362	0.374	22.895	-0.179	0.405	0.374	0.251	0.364	-0.074	-0.048
...	...	...	...	...	...	0.041	0.071	0.064	0.057	0.055	0.047	0.072	0.066	0.066	0.251	0.266	0.202	0.189
003	45.74	10.60	3.98	0.770	5496.	14.966	-19.478	0.065	-0.004	0.640	21.986	0.065	0.185	0.636	-0.174	0.039	-0.476	0.323
...	...	...	...	...	...	0.024	0.064	0.038	0.036	0.034	0.031	0.047	0.048	0.048	0.084	0.088	0.105	0.100
004	58.99	10.85	-99.99	0.420	-9999.	15.382	99.999	0.063	0.662	0.652	21.836	0.158	0.760	0.780	0.395	0.079	-0.072	0.444
...	...	...	...	...	...	0.023	9.999	0.038	0.030	0.023	0.036	0.055	0.050	0.049	0.119	0.136	0.073	0.053
005	85.13	12.65	5.94	0.280	6882.	14.560	-20.372	-0.678	0.653	0.285	20.949	-0.790	0.765	0.441	-0.050	0.048	-0.035	-0.054
...	...	...	...	...	...	0.013	0.061	0.017	0.017	0.016	0.031	0.045	0.045	0.047	0.025	0.027	0.029	0.027
006	58.12	11.49	11.31	0.620	14410.	14.805	-21.732	-0.081	0.572	0.532	21.686	-0.072	0.677	0.532	-0.083	0.093	-0.109	-0.068
...	...	...	...	...	...	0.019	0.062	0.029	0.025	0.022	0.028	0.040	0.039	0.039	0.046	0.052	0.046	0.038
007	72.83	13.39	0.71	0.610	775.	14.507	-15.683	-0.153	0.533	0.448	21.393	-0.333	0.413	0.364	0.569	0.298	0.188	0.120
...	...	...	...	...	...	0.019	0.062	0.028	0.026	0.023	0.029	0.042	0.040	0.038	0.089	0.098	0.067	0.059
008	26.98	14.53	2.02	0.920	2031.	14.684	-17.598	-0.432	0.077	-1.138	22.973	-0.310	0.204	-0.690	-99.990	-0.134	-0.202	-99.990
...	...	...	...	...	...	0.081	0.100	0.113	0.126	0.233	0.051	0.070	0.082	0.256	9.999	0.660	0.697	9.999
009	81.79	10.43	3.35	0.530	4708.	13.718	-20.390	0.178	0.709	0.592	20.871	0.488	1.102	0.957	-0.157	-0.050	-0.063	-0.042
...	...	...	...	...	...	0.009	0.060	0.015	0.011	0.009	0.022	0.030	0.034	0.039	0.016	0.018	0.014	0.010
010	67.98	11.07	1.41	0.300	1862.	15.102	-16.992	-0.324	0.401	0.173	21.136	-0.203	0.401	0.301	-0.495	-0.262	-0.033	-0.205
...	...	...	...	...	...	0.019	0.062	0.026	0.026	0.032	0.037	0.051	0.053	0.059	0.203	0.170	0.163	0.198
011	67.27	14.44	5.51	0.800	5590.	13.841	-20.640	-0.190	0.487	0.355	21.463	-0.264	0.543	0.373	-0.057	0.201	-0.071	-0.178
...	...	...	...	...	...	0.010	0.060	0.014	0.013	0.012	0.019	0.028	0.027	0.027	0.050	0.055	0.047	0.046
012	71.56	13.21	2.79	0.400	3098.	15.380	-17.819	-0.258	0.559	0.425	21.983	-0.258	0.559	0.425	0.292	0.045	0.131	0.112
...	...	...	...	...	...	0.030	0.066	0.039	0.037	0.030	0.039	0.052	0.051	0.047	0.218	0.253	0.235	0.196
013	123.57	26.01	1.27	0.740	715.	13.068	-16.947	-0.082	0.588	0.452	21.833	-0.082	0.593	0.470	0.482	0.254	0.163	0.048
...	...	...	...	...	...	0.013	0.061	0.021	0.017	0.015	0.016	0.024	0.021	0.020	0.066	0.074	0.048	0.035
014	179.40	37.02	1.14	0.850	452.	12.248	-16.771	-0.131	0.618	0.469	21.763	-0.348	0.535	0.408	0.135	0.094	0.089	0.029

Table 4—Continued

ID#	D_{24}	$r_e('')$	$r_e(kpc)$	b/a	V_{GSR}	B_T	$B_T(abs)$	$(U–B)_T$	$(B–V)_T$	$(V–R)_T$	$\mu_e(B)$	$(U–B)_e$	$(B–V)_e$	$(V–R)_e$	$\delta(U–R)/r_e$	$\delta(U–B)/r_e$	$\delta(B–V)/r_e$	$\delta(V–R)/r_e$
(1)	(2)	(3)	(4)	(5)	(6)	(7)	(8)	(9)	(10)	(11)	(12)	(13)	(14)	(15)	(16)	(17)	(18)	(19)
...	...	...	...	...	...	0.010	0.060	0.015	0.013	0.010	0.011	0.016	0.015	0.014	0.047	0.054	0.032	0.027
015	80.11	7.52	2.40	0.850	4681.	13.527	-20.568	-0.018	0.637	0.677	20.085	-0.178	0.637	1.038	0.163	0.075	0.055	0.018
...	...	...	...	...	...	0.008	0.060	0.012	0.010	0.008	0.028	0.041	0.039	0.043	0.014	0.016	0.012	0.010
016	40.69	18.85	4.12	0.780	3200.	15.857	-17.412	-0.072	0.547	0.308	23.952	-0.166	0.443	0.407	-0.370	-0.140	-0.026	-0.236
...	...	...	...	...	...	0.061	0.084	0.090	0.077	0.066	0.064	0.093	0.082	0.072	0.666	0.766	0.334	0.368
017	63.28	12.00	-99.99	0.310	-9999.	15.859	99.999	-0.194	0.524	0.264	22.091	-0.194	0.639	0.264	-0.268	-0.092	-0.067	-0.107
...	...	...	...	...	...	0.039	9.999	0.060	0.051	0.055	0.040	0.059	0.057	0.066	0.784	0.779	0.624	0.629
018	68.94	21.89	0.53	0.590	356.	15.036	-13.465	-0.322	0.458	0.341	23.189	-0.354	0.468	0.363	-0.230	-0.278	0.019	0.025
...	...	...	...	...	...	0.028	0.065	0.040	0.038	0.035	0.031	0.044	0.043	0.042	0.335	0.356	0.249	0.233
019	76.02	10.32	2.65	0.690	3764.	12.805	-20.817	-0.294	0.413	0.414	19.528	-0.375	0.333	0.558	0.176	0.116	0.042	0.013
...	...	...	...	...	...	0.005	0.060	0.006	0.006	0.005	0.026	0.037	0.036	0.036	0.011	0.013	0.012	0.011
020	71.52	8.76	3.71	0.580	6195.	14.049	-20.655	0.045	0.535	0.425	19.638	-0.160	0.117	0.318	0.113	0.101	0.011	0.017
...	...	...	...	...	...	0.012	0.061	0.018	0.015	0.013	0.043	0.064	0.056	0.049	0.022	0.024	0.018	0.016
021	64.50	9.48	2.70	0.500	4178.	14.470	-19.379	0.009	0.714	0.484	20.740	-0.083	0.806	0.538	-0.235	-0.011	-0.065	-0.149
...	...	...	...	...	...	0.012	0.061	0.018	0.015	0.015	0.033	0.048	0.047	0.049	0.070	0.068	0.053	0.055
022	73.24	11.03	3.77	0.640	5010.	14.252	-19.991	-0.057	0.580	0.508	21.252	-0.057	0.716	0.651	-0.103	0.024	-0.053	-0.065
...	...	...	...	...	...	0.012	0.061	0.019	0.015	0.014	0.024	0.036	0.035	0.037	0.082	0.088	0.063	0.052
023	58.32	10.08	-99.99	0.560	-9999.	14.870	99.999	-0.322	0.482	0.369	21.310	-0.155	0.541	0.369	-0.145	-0.104	-0.043	0.000
...	...	...	...	...	...	0.017	9.999	0.022	0.023	0.021	0.031	0.043	0.045	0.045	0.043	0.047	0.046	0.042
024	56.75	7.69	3.33	0.620	6347.	14.562	-20.195	-0.592	0.407	0.353	20.465	-0.862	0.407	0.353	0.051	0.093	-0.006	-0.041
...	...	...	...	...	...	0.015	0.061	0.019	0.020	0.018	0.038	0.057	0.054	0.054	0.032	0.036	0.035	0.032
025	79.42	9.37	4.00	0.380	6256.	14.706	-20.019	-0.048	0.530	0.426	20.290	-0.560	0.313	0.426	0.004	0.039	-0.013	-0.020
...	...	...	...	...	...	0.016	0.062	0.022	0.021	0.017	0.044	0.070	0.059	0.056	0.042	0.049	0.045	0.037
026	105.03	9.81	2.90	0.900	4322.	13.643	-20.279	-0.067	0.582	0.488	20.623	0.070	0.725	0.488	-0.052	0.075	-0.033	-0.084
...	...	...	...	...	...	0.011	0.060	0.017	0.014	0.013	0.023	0.033	0.034	0.035	0.056	0.059	0.049	0.044
027	127.10	24.45	0.19	0.760	114.	13.462	-12.566	-0.484	0.329	0.814	22.494	-0.484	0.329	1.210	-99.990	0.736	0.184	-99.990
...	...	...	...	...	...	0.026	0.065	0.033	0.040	0.285	0.014	0.019	0.020	0.024	9.999	0.434	0.537	9.999

Table 4—Continued

ID#	D_{24}	$r_e('')$	$r_e(kpc)$	b/a	V_{GSR}	B_T	$B_T(abs)$	$(U-B)_T$	$(B-V)_T$	$(V-R)_T$	$\mu_e(B)$	$(U-B)_e$	$(B-V)_e$	$(V-R)_e$	$\delta(U-R)/r_e$	$\delta(U-B)/r_e$	$\delta(B-V)/r_e$	$\delta(V-R)/r_e$
(1)	(2)	(3)	(4)	(5)	(6)	(7)	(8)	(9)	(10)	(11)	(12)	(13)	(14)	(15)	(16)	(17)	(18)	(19)
028	61.40	19.36	-99.99	0.490	-9999.	15.070	99.999	-0.510	0.199	0.288	22.766	-0.678	0.153	0.377	0.521	0.396	0.071	0.040
...	...	...	...	...	...	0.020	9.999	0.026	0.031	0.034	0.025	0.034	0.038	0.042	0.123	0.100	0.108	0.125
029	79.43	11.16	4.16	0.500	5464.	14.306	-20.125	0.125	0.750	0.471	21.161	0.261	1.126	0.471	-0.057	-0.020	-0.022	0.000
...	...	...	...	...	...	0.011	0.060	0.018	0.014	0.011	0.025	0.035	0.038	0.041	0.025	0.028	0.020	0.016
030	70.29	9.76	-99.99	0.290	-9999.	15.234	99.999	0.308	0.844	0.628	21.062	0.444	0.919	0.785	-0.130	-0.047	-0.046	-0.040
...	...	...	...	...	...	0.018	9.999	0.035	0.022	0.016	0.041	0.061	0.058	0.060	0.072	0.080	0.050	0.036
031	86.39	9.20	2.60	0.910	4138.	13.587	-20.241	0.061	0.573	0.516	20.569	-0.211	0.845	0.516	0.052	0.036	-0.006	0.017
...	...	...	...	...	...	0.010	0.060	0.016	0.013	0.012	0.023	0.035	0.035	0.037	0.023	0.025	0.020	0.018
032	68.03	5.34	1.35	0.960	3694.	14.065	-19.516	0.282	0.865	0.472	19.868	0.065	0.865	0.689	0.072	0.052	0.032	-0.026
...	...	...	...	...	...	0.010	0.060	0.017	0.012	0.011	0.039	0.059	0.055	0.058	0.030	0.031	0.022	0.020
033	84.57	13.99	2.99	0.240	3135.	14.415	-18.810	-0.167	0.414	0.312	20.542	-0.263	0.321	0.360	0.172	0.156	0.015	0.008
...	...	...	...	...	...	0.011	0.060	0.015	0.015	0.014	0.034	0.049	0.047	0.047	0.028	0.030	0.028	0.026
034	96.45	23.13	2.73	0.250	1728.	14.794	-17.137	-0.226	0.340	0.205	22.152	-0.155	0.389	0.205	0.044	0.007	0.076	-0.040
...	...	...	...	...	...	0.019	0.062	0.027	0.027	0.028	0.026	0.037	0.038	0.039	0.091	0.088	0.088	0.090
035	43.33	6.17	-99.99	0.650	-9999.	15.180	99.999	-0.090	0.573	0.453	20.322	-0.106	0.239	0.453	0.275	0.131	0.082	0.051
...	...	...	...	...	...	0.020	9.999	0.028	0.027	0.024	0.053	0.075	0.070	0.065	0.041	0.046	0.041	0.035
036	171.54	16.28	8.54	0.400	7682.	13.473	-21.698	0.782	0.751	0.480	20.851	0.901	0.906	0.647	-0.102	0.008	-0.011	-0.095
...	...	...	...	...	...	0.010	0.060	0.018	0.013	0.011	0.020	0.030	0.029	0.031	0.047	0.050	0.033	0.029
037	121.03	21.73	4.05	0.330	2732.	14.347	-18.579	0.273	0.969	0.665	22.292	0.434	1.230	0.874	-0.276	-0.117	-0.051	-0.120
...	...	...	...	...	...	0.015	0.061	0.030	0.018	0.012	0.021	0.037	0.028	0.027	0.068	0.076	0.040	0.026
038	114.71	33.07	1.45	0.740	643.	13.681	-16.104	-0.077	0.583	0.272	22.897	-0.276	0.460	0.348	0.057	0.086	-0.001	-0.099
...	...	...	...	...	...	0.027	0.065	0.044	0.037	0.037	0.029	0.045	0.040	0.040	0.213	0.212	0.111	0.147
039	93.40	24.13	-99.99	0.630	-9999.	14.778	99.999	0.219	0.623	0.700	23.148	0.202	0.666	0.623	0.439	0.323	-0.153	0.215
...	...	...	...	...	...	0.027	9.999	0.051	0.035	0.028	0.030	0.059	0.040	0.034	0.267	0.296	0.136	0.107
040	53.87	7.46	6.12	0.620	12022.	15.401	-20.743	0.398	0.795	0.734	21.547	0.465	0.988	0.850	-0.024	-0.012	-0.004	0.001
...	...	...	...	...	...	0.019	0.062	0.036	0.024	0.018	0.036	0.054	0.052	0.054	0.064	0.071	0.042	0.033
041	96.48	18.31	5.44	0.360	4350.	14.156	-19.780	-0.019	0.514	0.483	21.523	-0.019	0.623	0.544	0.235	0.139	-0.034	0.141

Table 4—Continued

ID#	D_{24}	$r_e('')$	$r_e(kpc)$	b/a	V_{GSR}	B_T	$B_T(abs)$	$(U-B)_T$	$(B-V)_T$	$(V-R)_T$	$\mu_e(B)$	$(U-B)_e$	$(B-V)_e$	$(V-R)_e$	$\delta(U-R)/r_e$	$\delta(U-B)/r_e$	$\delta(B-V)/r_e$	$\delta(V-R)/r_e$
(1)	(2)	(3)	(4)	(5)	(6)	(7)	(8)	(9)	(10)	(11)	(12)	(13)	(14)	(15)	(16)	(17)	(18)	(19)
...	...	...	...	...	...	0.012	0.061	0.019	0.016	0.014	0.022	0.032	0.031	0.031	0.048	0.054	0.039	0.033
042	50.62	2.49	1.01	0.920	5968.	14.330	-20.293	0.300	0.911	0.524	18.397	0.767	1.148	0.471	-0.007	-0.015	0.004	0.004
...	...	...	...	...	...	0.013	0.061	0.023	0.016	0.011	0.085	0.110	0.127	0.132	0.013	0.015	0.010	0.007
043	107.71	59.89	12.51	0.570	3058.	13.904	-19.267	-0.408	0.385	0.331	24.254	-0.237	0.451	0.346	-0.935	-0.698	0.004	-0.247
...	...	...	...	...	...	0.030	0.066	0.040	0.045	0.048	0.046	0.061	0.067	0.069	0.601	0.575	0.605	0.630
044	41.62	5.23	-99.99	0.810	-9999.	14.303	99.999	-0.171	0.503	0.482	19.630	-0.235	0.457	0.499	0.394	0.262	0.085	0.050
...	...	...	...	...	...	0.011	9.999	0.016	0.014	0.012	0.049	0.070	0.068	0.067	0.025	0.029	0.023	0.019
045	78.62	27.54	0.90	0.610	480.	14.497	-14.653	-0.387	0.404	0.224	23.151	-0.416	0.408	0.218	0.255	0.246	0.070	-0.054
...	...	...	...	...	...	0.038	0.070	0.053	0.056	0.059	0.043	0.061	0.064	0.068	0.241	0.231	0.246	0.255
046	67.99	24.12	0.75	0.640	454.	14.689	-14.340	-0.440	0.192	0.301	22.949	-0.317	0.110	0.222	-0.915	-0.380	-0.238	-0.160
...	...	...	...	...	...	0.037	0.069	0.048	0.062	0.071	0.039	0.052	0.067	0.079	0.373	0.243	0.305	0.440
047	411.86	61.69	4.98	0.270	1182.	11.416	-19.691	0.127	0.712	0.507	21.281	0.268	0.811	0.751	-0.109	0.056	-0.016	-0.088
...	...	...	...	...	...	0.012	0.061	0.019	0.015	0.014	0.011	0.018	0.015	0.014	0.067	0.074	0.030	0.031
048	149.82	43.11	1.80	0.630	612.	13.163	-16.514	-0.258	0.383	0.328	22.912	-0.372	0.421	0.375	0.281	0.191	0.077	0.011
...	...	...	...	...	...	0.010	0.060	0.014	0.015	0.016	0.012	0.016	0.017	0.018	0.042	0.040	0.045	0.047
049	63.36	18.07	0.56	0.780	454.	15.155	-13.874	-0.111	0.613	0.476	23.003	-0.309	0.487	0.442	0.680	0.347	0.189	0.027
...	...	...	...	...	...	0.026	0.065	0.037	0.035	0.031	0.028	0.040	0.038	0.036	0.172	0.186	0.110	0.098
050	65.62	12.90	-99.99	0.390	-9999.	15.052	99.999	-0.178	0.548	0.438	21.730	-0.186	0.677	0.463	-0.259	-0.132	-0.050	-0.070
...	...	...	...	...	...	0.018	9.999	0.027	0.024	0.021	0.029	0.042	0.042	0.042	0.047	0.054	0.046	0.039
051	74.74	22.12	-99.99	0.350	-9999.	15.001	99.999	-0.326	0.296	0.228	22.616	-0.435	0.334	0.228	0.010	0.103	-0.024	-0.077
...	...	...	...	...	...	0.017	9.999	0.023	0.025	0.028	0.023	0.032	0.035	0.039	0.087	0.077	0.088	0.097
052	253.16	53.30	2.42	0.660	666.	11.795	-18.066	-0.302	0.393	0.367	21.978	-0.394	0.347	0.421	0.151	0.079	0.053	0.032
...	...	...	...	...	...	0.010	0.060	0.014	0.015	0.014	0.010	0.014	0.015	0.015	0.046	0.045	0.040	0.040
053	106.64	19.30	0.65	0.610	491.	13.226	-15.973	-0.318	0.384	0.343	21.157	-0.230	0.431	0.343	-0.175	-0.036	-0.066	-0.060
...	...	...	...	...	...	0.007	0.060	0.009	0.009	0.009	0.015	0.021	0.022	0.022	0.016	0.016	0.018	0.017
054	134.30	35.68	2.45	0.480	1005.	13.678	-17.077	-0.233	0.516	0.330	22.581	-0.245	0.436	0.355	-0.117	-0.099	-0.025	-0.047
...	...	...	...	...	...	0.028	0.065	0.044	0.038	0.032	0.029	0.045	0.039	0.034	0.233	0.260	0.153	0.131

Table 4—Continued

ID#	D_{24}	$r_e('')$	$r_e(kpc)$	b/a	V_{GSR}	B_T	$B_T(abs)$	$(U-B)_T$	$(B-V)_T$	$(V-R)_T$	$\mu_e(B)$	$(U-B)_e$	$(B-V)_e$	$(V-R)_e$	$\delta(U-R)/r_e$	$\delta(U-B)/r_e$	$\delta(B-V)/r_e$	$\delta(V-R)/r_e$
(1)	(2)	(3)	(4)	(5)	(6)	(7)	(8)	(9)	(10)	(11)	(12)	(13)	(14)	(15)	(16)	(17)	(18)	(19)
055	47.64	30.61	2.30	0.810	1100.	15.175	-15.776	-0.488	0.529	0.253	24.306	-0.270	0.548	0.171	-0.282	-0.316	-0.045	0.075
...	...	...	...	...	...	0.050	0.077	0.069	0.070	0.069	0.056	0.078	0.077	0.078	0.580	0.587	0.548	0.539
056	82.50	7.93	0.55	0.720	1009.	13.014	-17.749	-0.367	0.319	0.309	19.040	-0.422	0.212	0.309	0.193	0.059	0.084	0.040
...	...	...	...	...	...	0.006	0.060	0.008	0.008	0.008	0.035	0.051	0.049	0.048	0.012	0.012	0.011	0.010
057	56.44	11.88	0.67	0.810	825.	14.985	-15.341	-0.624	0.354	0.292	22.244	-0.510	0.354	0.413	-0.183	-0.087	-0.020	-0.074
...	...	...	...	...	...	0.031	0.067	0.039	0.040	0.042	0.032	0.040	0.044	0.047	0.333	0.327	0.324	0.330
058	93.34	18.42	1.33	0.390	1056.	14.262	-16.600	-0.310	0.438	0.370	21.529	-0.410	0.497	0.281	0.486	0.244	0.170	0.095
...	...	...	...	...	...	0.012	0.061	0.016	0.016	0.015	0.022	0.031	0.031	0.031	0.043	0.047	0.036	0.033
059	98.82	18.32	2.62	0.870	2092.	13.036	-19.311	-0.405	0.371	0.383	21.285	-0.326	0.412	0.435	0.248	0.159	0.025	0.060
...	...	...	...	...	...	0.006	0.060	0.008	0.009	0.009	0.014	0.019	0.019	0.020	0.020	0.020	0.021	0.020
060	52.80	10.33	-99.99	0.530	-9999.	15.523	99.999	-0.018	0.793	0.367	21.963	0.042	0.859	0.367	0.071	0.138	0.007	-0.074
...	...	...	...	...	...	0.019	9.999	0.028	0.024	0.019	0.032	0.046	0.045	0.045	0.092	0.107	0.087	0.066
061	89.23	16.10	-99.99	0.300	-9999.	14.856	99.999	0.002	0.718	0.509	21.514	0.023	0.656	0.509	0.097	0.114	0.029	-0.061
...	...	...	...	...	...	0.017	9.999	0.028	0.021	0.016	0.028	0.041	0.039	0.038	0.052	0.061	0.041	0.031
062	82.89	21.66	1.69	0.860	1142.	14.188	-16.844	-0.148	0.492	0.370	22.930	-0.082	0.726	0.370	-0.154	-0.030	-0.052	-0.062
...	...	...	...	...	...	0.014	0.061	0.021	0.019	0.017	0.017	0.025	0.024	0.023	0.069	0.076	0.067	0.059
063	96.76	28.95	2.76	0.310	1398.	15.055	-16.416	-0.128	0.461	0.428	23.136	-0.115	0.565	0.376	-0.053	-0.006	-0.062	0.012
...	...	...	...	...	...	0.042	0.072	0.064	0.061	0.060	0.049	0.075	0.070	0.068	0.279	0.289	0.272	0.261
064	37.75	5.78	-99.99	0.520	-9999.	15.706	99.999	-0.144	0.618	0.460	20.919	-0.202	0.647	0.552	0.395	0.234	0.153	0.017
...	...	...	...	...	...	0.023	9.999	0.033	0.029	0.025	0.055	0.078	0.077	0.078	0.094	0.107	0.099	0.084
065	119.29	32.66	2.83	0.970	1267.	13.044	-18.214	-0.301	0.346	0.287	22.574	-0.301	0.346	0.287	0.910	0.775	0.143	0.006
...	...	...	...	...	...	0.008	0.060	0.012	0.012	0.012	0.011	0.016	0.016	0.017	0.155	0.153	0.112	0.158
066	54.86	5.28	0.46	0.710	1284.	14.354	-16.933	-0.308	0.611	0.513	19.426	-0.251	0.449	0.513	0.072	0.005	0.039	0.026
...	...	...	...	...	...	0.012	0.061	0.016	0.015	0.012	0.054	0.076	0.074	0.071	0.016	0.020	0.019	0.015
067	97.36	19.87	11.10	0.450	8180.	14.400	-20.907	0.244	0.935	0.529	21.991	0.364	0.963	0.475	-0.316	-0.115	-0.012	-0.217
...	...	...	...	...	...	0.011	0.060	0.017	0.013	0.009	0.019	0.028	0.026	0.026	0.095	0.110	0.066	0.049
068	82.39	20.25	0.42	0.530	302.	14.440	-13.704	-0.289	0.449	0.275	22.034	-0.391	0.382	0.101	0.510	0.241	0.123	0.075

Table 4—Continued

ID#	D_{24}	$r_e('')$	$r_e(kpc)$	b/a	V_{GSR}	B_T	$B_T(abs)$	$(U-B)_T$	$(B-V)_T$	$(V-R)_T$	$\mu_e(B)$	$(U-B)_e$	$(B-V)_e$	$(V-R)_e$	$\delta(U-R)/r_e$	$\delta(U-B)/r_e$	$\delta(B-V)/r_e$	$\delta(V-R)/r_e$
(1)	(2)	(3)	(4)	(5)	(6)	(7)	(8)	(9)	(10)	(11)	(12)	(13)	(14)	(15)	(16)	(17)	(18)	(19)
...	...	...	...	...	...	0.015	0.061	0.022	0.021	0.021	0.021	0.030	0.029	0.029	0.078	0.080	0.059	0.057
069	166.13	29.40	2.19	0.780	1089.	12.356	-18.573	0.127	0.791	0.544	21.463	0.127	0.833	0.544	0.157	0.111	0.031	-0.030
...	...	...	...	...	...	0.007	0.060	0.010	0.008	0.007	0.010	0.014	0.014	0.013	0.021	0.024	0.016	0.013
070	186.43	28.87	0.59	0.840	299.	11.871	-16.251	-0.084	0.424	0.491	20.398	-0.497	0.115	0.221	0.280	0.117	0.079	0.030
...	...	...	...	...	...	0.009	0.060	0.014	0.012	0.010	0.012	0.019	0.016	0.014	0.031	0.034	0.024	0.020
071	67.76	18.75	0.32	0.930	249.	14.402	-13.323	-0.465	0.379	0.359	22.266	-0.898	0.162	0.162	0.238	0.065	0.078	0.079
...	...	...	...	...	...	0.015	0.061	0.021	0.022	0.022	0.018	0.027	0.025	0.025	0.057	0.058	0.046	0.045
072	92.79	16.15	7.36	0.430	6678.	14.108	-20.759	-0.339	0.454	0.451	21.541	-0.339	0.582	0.639	-0.111	-0.011	-0.049	-0.034
...	...	...	...	...	...	0.010	0.060	0.014	0.014	0.013	0.020	0.028	0.029	0.030	0.024	0.026	0.026	0.025
073	47.11	9.60	3.20	0.480	4886.	15.670	-18.518	-0.183	0.457	0.373	21.725	-0.280	0.404	0.373	0.195	0.142	0.057	-0.011
...	...	...	...	...	...	0.021	0.063	0.030	0.030	0.028	0.037	0.054	0.053	0.052	0.062	0.065	0.061	0.061
074	110.03	23.44	2.43	0.690	1518.	13.701	-17.949	-0.131	0.499	0.392	22.127	-0.232	0.438	0.439	0.350	0.264	0.070	0.019
...	...	...	...	...	...	0.017	0.062	0.024	0.024	0.023	0.018	0.026	0.025	0.025	0.061	0.062	0.048	0.052
075	83.79	11.51	6.66	0.630	8470.	14.241	-21.142	0.038	0.800	0.634	21.206	0.140	0.911	0.692	-0.007	-0.079	0.035	0.040
...	...	...	...	...	...	0.015	0.061	0.025	0.018	0.012	0.025	0.035	0.035	0.035	0.040	0.047	0.028	0.018
076	103.95	25.45	1.79	0.970	1032.	13.010	-17.802	0.224	0.505	0.375	22.239	0.278	0.745	0.375	0.042	0.049	-0.023	-0.007
...	...	...	...	...	...	0.018	0.062	0.028	0.025	0.023	0.014	0.025	0.020	0.019	0.076	0.081	0.052	0.048
077	75.03	23.38	1.55	0.930	970.	14.206	-16.472	-0.300	0.319	0.304	23.136	-0.176	0.433	0.362	0.094	0.175	-0.025	-0.041
...	...	...	...	...	...	0.014	0.061	0.019	0.021	0.022	0.016	0.023	0.024	0.026	0.090	0.087	0.091	0.094
078	111.85	17.90	1.78	0.420	1453.	13.392	-18.163	-0.176	0.374	0.318	20.597	-0.413	0.200	0.381	0.311	0.179	0.064	0.065
...	...	...	...	...	...	0.007	0.060	0.011	0.010	0.010	0.021	0.032	0.029	0.028	0.022	0.022	0.020	0.020
079	71.32	21.56	2.38	0.560	1616.	15.051	-16.735	-0.165	0.514	0.395	23.137	-0.165	0.524	0.440	0.249	0.198	0.054	0.035
...	...	...	...	...	...	0.021	0.063	0.030	0.029	0.028	0.025	0.036	0.035	0.035	0.103	0.105	0.078	0.084
080	147.49	44.47	0.86	0.620	283.	13.148	-14.855	-0.289	0.418	0.311	22.850	-0.302	0.453	0.265	-0.170	-0.271	0.072	0.008
...	...	...	...	...	...	0.027	0.065	0.035	0.034	0.029	0.032	0.042	0.041	0.035	0.299	0.357	0.218	0.181
081	95.63	18.23	2.42	0.880	1946.	13.398	-18.791	-0.113	0.514	0.497	21.470	-0.189	0.461	0.463	0.519	0.306	0.143	0.065
...	...	...	...	...	...	0.008	0.060	0.013	0.011	0.010	0.015	0.022	0.021	0.021	0.034	0.038	0.026	0.023

Table 4—Continued

ID#	D_{24}	$r_e('')$	$r_e(kpc)$	b/a	V_{GSR}	B_T	$B_T(abs)$	$(U-B)_T$	$(B-V)_T$	$(V-R)_T$	$\mu_e(B)$	$(U-B)_e$	$(B-V)_e$	$(V-R)_e$	$\delta(U-R)/r_e$	$\delta(U-B)/r_e$	$\delta(B-V)/r_e$	$\delta(V-R)/r_e$
(1)	(2)	(3)	(4)	(5)	(6)	(7)	(8)	(9)	(10)	(11)	(12)	(13)	(14)	(15)	(16)	(17)	(18)	(19)
082	271.55	60.51	1.59	0.120	384.	13.750	-14.915	-0.090	0.560	0.436	22.458	-0.090	0.609	0.494	-0.108	-0.025	-0.041	-0.016
...	...	...	...	...	...	0.026	0.064	0.039	0.034	0.030	0.029	0.044	0.040	0.035	0.167	0.189	0.112	0.096
083	239.56	16.72	0.74	0.860	647.	11.163	-18.635	0.466	0.949	0.583	19.187	0.696	1.133	0.478	-0.054	-0.024	-0.020	-0.005
...	...	...	...	...	...	0.007	0.060	0.014	0.008	0.006	0.014	0.020	0.021	0.021	0.013	0.015	0.007	0.005
084	111.51	22.55	0.26	0.930	171.	12.884	-14.025	-0.312	0.412	0.362	21.466	-0.353	0.318	0.358	0.853	0.495	0.223	0.129
...	...	...	...	...	...	0.005	0.060	0.007	0.008	0.007	0.012	0.017	0.016	0.016	0.022	0.024	0.025	0.023
085	363.90	54.16	0.94	0.630	255.	10.020	-17.756	-0.303	0.383	0.359	19.998	-0.255	0.290	0.270	-0.099	-0.133	0.008	0.034
...	...	...	...	...	...	0.003	0.060	0.004	0.004	0.004	0.006	0.009	0.008	0.008	0.008	0.008	0.007	0.007
086	118.67	10.53	1.35	0.760	1873.	12.968	-19.138	0.170	0.765	0.510	19.775	0.170	0.765	0.510	-0.026	-0.019	0.005	-0.010
...	...	...	...	...	...	0.007	0.060	0.013	0.009	0.007	0.025	0.035	0.035	0.035	0.016	0.018	0.010	0.008
087	390.10	59.27	2.53	0.530	625.	10.184	-19.539	-0.252	0.459	0.380	20.395	-0.170	0.434	0.448	0.231	0.165	0.052	0.016
...	...	...	...	...	...	0.003	0.060	0.004	0.004	0.003	0.006	0.008	0.008	0.008	0.008	0.008	0.007	0.007
088	115.28	21.96	0.81	0.870	542.	12.550	-16.864	-0.347	0.369	0.245	21.045	-0.181	0.283	0.276	-0.117	-0.172	0.050	0.032
...	...	...	...	...	...	0.006	0.060	0.009	0.009	0.010	0.012	0.017	0.017	0.017	0.020	0.019	0.018	0.019
089	139.38	29.67	2.34	0.860	1157.	12.484	-18.576	-0.157	0.481	0.393	22.000	-0.055	0.706	0.494	-0.103	-0.043	-0.012	-0.047
...	...	...	...	...	...	0.011	0.060	0.017	0.015	0.014	0.012	0.019	0.018	0.017	0.039	0.043	0.031	0.027
090	174.73	28.47	3.77	0.490	1938.	12.283	-19.897	-0.414	0.364	0.464	20.750	-0.550	0.438	0.367	0.514	0.263	0.133	0.100
...	...	...	...	...	...	0.007	0.060	0.009	0.010	0.009	0.012	0.018	0.018	0.018	0.019	0.020	0.019	0.018
091	33.89	4.62	-99.99	0.590	-9999.	15.646	99.999	-0.290	0.421	0.333	20.389	-0.290	0.421	0.333	-0.058	-0.035	-0.033	-0.002
...	...	...	...	...	...	0.025	9.999	0.035	0.035	0.035	0.063	0.090	0.090	0.090	0.043	0.042	0.044	0.044
092	251.52	48.11	1.94	0.870	592.	11.250	-18.355	-0.162	0.475	0.406	21.514	-0.133	0.514	0.379	0.148	0.114	0.071	0.028
...	...	...	...	...	...	0.004	0.060	0.006	0.006	0.005	0.006	0.009	0.009	0.009	0.017	0.018	0.015	0.013
093	106.17	38.68	1.05	0.780	399.	13.695	-15.054	-0.312	0.355	0.340	23.407	-0.333	0.485	0.261	-99.990	-99.990	0.120	0.026
...	...	...	...	...	...	0.026	0.065	0.037	0.040	0.040	0.029	0.041	0.043	0.044	9.999	9.999	0.378	0.372
094	86.35	13.90	4.61	0.330	4856.	14.680	-19.495	0.418	0.837	0.545	21.384	0.076	0.994	0.588	0.109	0.151	0.019	-0.043
...	...	...	...	...	...	0.021	0.063	0.056	0.024	0.015	0.030	0.061	0.041	0.041	0.185	0.197	0.040	0.024
095	158.65	21.88	1.44	0.700	963.	12.312	-18.350	0.080	0.713	0.524	21.119	0.318	1.003	0.735	-0.164	-0.068	-0.074	-0.024

Table 4—Continued

ID#	D_{24}	$r_e('')$	$r_e(kpc)$	b/a	V_{GSR}	B_T	$B_T(abs)$	$(U-B)_T$	$(B-V)_T$	$(V-R)_T$	$\mu_e(B)$	$(U-B)_e$	$(B-V)_e$	$(V-R)_e$	$\delta(U-R)/r_e$	$\delta(U-B)/r_e$	$\delta(B-V)/r_e$	$\delta(V-R)/r_e$
(1)	(2)	(3)	(4)	(5)	(6)	(7)	(8)	(9)	(10)	(11)	(12)	(13)	(14)	(15)	(16)	(17)	(18)	(19)
...	...	...	...	...	...	0.008	0.060	0.013	0.010	0.009	0.011	0.016	0.016	0.017	0.016	0.018	0.013	0.011
096	36.92	4.25	1.46	0.680	5026.	14.729	-19.521	-0.427	0.588	0.360	19.430	-0.713	0.487	0.445	0.188	0.117	0.056	0.011
...	...	...	...	...	...	0.013	0.061	0.018	0.017	0.015	0.064	0.097	0.089	0.089	0.026	0.030	0.026	0.022
097	78.10	23.00	0.29	0.610	183.	14.549	-12.507	-0.474	0.327	0.320	22.814	-0.474	0.327	0.320	1.074	0.421	0.351	0.298
...	...	...	...	...	...	0.017	0.062	0.021	0.025	0.025	0.020	0.027	0.029	0.030	0.175	0.176	0.203	0.202
098	141.62	21.15	-99.99	0.400	-9999.	13.711	99.999	0.608	0.681	0.541	21.533	0.788	0.878	0.541	-0.125	0.011	-0.066	-0.072
...	...	...	...	...	...	0.014	9.999	0.025	0.017	0.012	0.017	0.030	0.025	0.025	0.052	0.059	0.039	0.028
099	146.93	60.56	0.70	0.620	169.	13.177	-13.706	-0.191	0.357	0.323	23.431	-0.288	0.284	0.266	-99.990	-99.990	0.266	0.167
...	...	...	...	...	...	0.016	0.061	0.023	0.024	0.027	0.018	0.027	0.028	0.032	9.999	9.999	0.179	0.342
100	183.12	60.55	1.12	0.530	272.	13.037	-14.880	-0.192	0.415	0.380	23.105	-0.274	0.368	0.281	0.477	0.227	0.146	0.110
...	...	...	...	...	...	0.014	0.061	0.020	0.020	0.020	0.015	0.023	0.023	0.023	0.214	0.199	0.082	0.107
101	66.26	15.57	0.95	0.750	893.	14.580	-15.918	-0.439	0.463	0.307	22.113	-0.486	0.363	0.299	0.603	0.394	0.149	0.021
...	...	...	...	...	...	0.016	0.062	0.022	0.023	0.023	0.023	0.032	0.033	0.033	0.105	0.106	0.084	0.084
102	116.03	23.52	1.68	0.880	1044.	12.586	-18.251	-0.229	0.450	0.406	21.427	-0.125	0.466	0.520	0.364	0.274	0.097	-0.006
...	...	...	...	...	...	0.005	0.060	0.007	0.007	0.006	0.010	0.014	0.015	0.015	0.016	0.018	0.016	0.014
103	91.04	27.52	0.32	0.670	171.	14.128	-12.781	-0.252	0.455	0.306	22.734	-0.252	0.281	0.330	0.461	0.257	0.192	-0.001
...	...	...	...	...	...	0.012	0.061	0.017	0.016	0.016	0.014	0.021	0.021	0.021	0.052	0.054	0.044	0.046
104	98.39	25.24	1.73	0.550	1004.	14.123	-16.629	-0.286	0.501	0.396	22.492	-0.284	0.556	0.355	1.118	0.617	0.266	0.147
...	...	...	...	...	...	0.013	0.061	0.019	0.017	0.015	0.017	0.026	0.024	0.023	0.141	0.154	0.057	0.051
105	40.99	14.20	2.12	0.680	2190.	15.345	-17.101	-0.178	-0.178	0.323	22.691	-0.042	-0.228	0.383	-0.057	-0.004	-0.042	-0.011
...	...	...	...	...	...	0.044	0.073	0.059	0.061	0.059	0.032	0.044	0.058	0.068	0.298	0.312	0.324	0.311
106	335.82	31.90	0.59	0.460	271.	10.777	-17.132	-0.305	0.497	0.319	19.085	-1.273	0.497	-0.042	0.250	0.139	0.049	0.044
...	...	...	...	...	...	0.003	0.060	0.004	0.004	0.004	0.013	0.023	0.018	0.016	0.006	0.007	0.006	0.006
107	62.67	11.76	5.58	0.500	6946.	14.884	-20.068	-0.075	0.480	0.217	21.447	-0.075	0.480	0.187	0.013	0.065	-0.032	-0.020
...	...	...	...	...	...	0.019	0.062	0.028	0.026	0.025	0.029	0.042	0.042	0.042	0.051	0.054	0.048	0.045
108	54.37	2.69	1.71	0.690	9323.	13.763	-21.828	-0.761	0.491	0.452	16.770	-1.025	0.034	0.177	0.370	0.224	0.099	0.011
...	...	...	...	...	...	0.008	0.060	0.010	0.010	0.009	0.135	0.203	0.175	0.148	0.007	0.008	0.007	0.006

Table 4—Continued

ID#	D_{24}	$r_e('')$	$r_e(kpc)$	b/a	V_{GSR}	B_T	$B_T(abs)$	$(U-B)_T$	$(B-V)_T$	$(V-R)_T$	$\mu_e(B)$	$(U-B)_e$	$(B-V)_e$	$(V-R)_e$	$\delta(U-R)/r_e$	$\delta(U-B)/r_e$	$\delta(B-V)/r_e$	$\delta(V-R)/r_e$
(1)	(2)	(3)	(4)	(5)	(6)	(7)	(8)	(9)	(10)	(11)	(12)	(13)	(14)	(15)	(16)	(17)	(18)	(19)
109	175.65	66.11	1.17	0.360	259.	13.579	-14.231	-0.284	0.446	0.415	23.418	-0.381	0.364	0.351	-99.990	-99.990	0.172	0.043
...	...	...	...	...	...	0.030	0.066	0.045	0.042	0.039	0.033	0.050	0.047	0.045	9.999	9.999	0.312	0.295
110	55.50	8.51	1.08	0.660	1863.	13.898	-18.197	-0.209	0.525	0.439	20.122	-0.344	0.558	0.439	0.087	0.060	0.020	-0.004
...	...	...	...	...	...	0.008	0.060	0.011	0.011	0.009	0.032	0.047	0.046	0.047	0.019	0.022	0.020	0.017
111	38.06	6.83	-99.99	0.720	-9999.	15.804	99.999	-0.097	0.613	0.389	21.821	-0.026	0.677	0.534	-0.076	-0.028	0.045	-0.094
...	...	...	...	...	...	0.031	9.999	0.047	0.041	0.035	0.044	0.065	0.061	0.061	0.106	0.119	0.101	0.084
112	49.07	9.58	-99.99	0.520	-9999.	15.556	99.999	0.042	0.736	0.464	21.982	0.120	0.892	0.544	-0.236	-0.035	-0.065	-0.131
...	...	...	...	...	...	0.021	9.999	0.034	0.027	0.022	0.034	0.051	0.048	0.049	0.081	0.082	0.064	0.057
113	87.11	23.59	0.68	0.750	425.	14.134	-14.752	-0.353	0.393	0.325	22.641	-0.426	0.367	0.314	0.394	0.225	0.113	0.050
...	...	...	...	...	...	0.012	0.061	0.017	0.018	0.017	0.016	0.022	0.023	0.023	0.069	0.067	0.062	0.063
114	171.53	31.80	-99.99	0.150	-9999.	14.520	99.999	0.166	0.785	0.549	22.054	0.163	0.738	0.685	-0.579	-0.329	0.017	-0.036
...	...	...	...	...	...	0.029	9.999	0.045	0.035	0.025	0.037	0.058	0.047	0.038	0.377	0.456	0.182	0.102
115	72.49	16.20	8.50	0.710	7688.	14.454	-20.719	-0.038	0.569	0.454	21.974	-0.153	0.483	0.391	0.235	0.196	0.053	0.000
...	...	...	...	...	...	0.017	0.062	0.026	0.022	0.020	0.022	0.033	0.030	0.029	0.094	0.101	0.061	0.061
116	105.88	26.23	1.36	0.650	762.	13.716	-16.437	-0.273	0.360	0.316	22.384	-0.202	0.360	0.365	0.058	0.087	-0.011	-0.018
...	...	...	...	...	...	0.011	0.060	0.016	0.016	0.016	0.015	0.022	0.021	0.022	0.053	0.054	0.051	0.051
117	119.86	29.99	0.53	0.900	259.	13.280	-14.530	-0.240	0.457	0.337	22.476	-0.380	0.383	0.344	0.441	0.260	0.155	-0.001
...	...	...	...	...	...	0.009	0.060	0.012	0.012	0.012	0.011	0.017	0.016	0.016	0.055	0.056	0.048	0.047
118	113.51	20.27	2.96	0.490	2141.	13.365	-19.032	-0.269	0.416	0.393	21.312	-0.256	0.568	0.435	0.273	0.185	0.064	0.036
...	...	...	...	...	...	0.007	0.060	0.009	0.009	0.009	0.015	0.021	0.022	0.023	0.018	0.019	0.018	0.017
119	166.56	32.47	3.51	0.970	1581.	12.147	-19.591	-0.293	0.436	0.403	21.760	-0.126	0.479	0.457	-0.068	-0.026	-0.015	-0.017
...	...	...	...	...	...	0.008	0.060	0.012	0.012	0.011	0.010	0.015	0.014	0.014	0.035	0.037	0.026	0.027
120	67.32	20.72	3.42	0.670	2419.	14.867	-17.795	-0.257	0.415	0.335	23.153	-0.144	0.447	0.449	0.048	0.056	-0.002	-0.007
...	...	...	...	...	...	0.017	0.062	0.025	0.024	0.023	0.019	0.029	0.028	0.029	0.078	0.082	0.077	0.072
121	67.90	18.34	4.56	0.540	3644.	14.487	-19.065	-0.354	0.300	0.238	22.138	-0.474	0.420	0.129	0.099	0.111	-0.049	0.014
...	...	...	...	...	...	0.013	0.061	0.018	0.020	0.021	0.020	0.029	0.030	0.032	0.068	0.063	0.061	0.075
122	68.83	13.34	6.11	0.780	6709.	13.907	-20.970	-0.136	0.404	0.406	21.402	-0.028	0.518	0.438	0.041	0.100	-0.015	-0.027

Table 4—Continued

ID#	D_{24}	$r_e('')$	$r_e(kpc)$	b/a	V_{GSR}	B_T	$B_T(abs)$	$(U-B)_T$	$(B-V)_T$	$(V-R)_T$	$\mu_e(B)$	$(U-B)_e$	$(B-V)_e$	$(V-R)_e$	$\delta(U-R)/r_e$	$\delta(U-B)/r_e$	$\delta(B-V)/r_e$	$\delta(V-R)/r_e$
(1)	(2)	(3)	(4)	(5)	(6)	(7)	(8)	(9)	(10)	(11)	(12)	(13)	(14)	(15)	(16)	(17)	(18)	(19)
...	...	...	...	...	...	0.012	0.061	0.017	0.016	0.014	0.021	0.029	0.029	0.029	0.041	0.046	0.035	0.030
123	87.70	13.87	5.24	0.820	5531.	14.011	-20.447	0.330	0.824	0.716	21.930	0.349	0.898	1.073	0.005	-0.028	0.045	0.008
...	...	...	...	...	...	0.011	0.060	0.020	0.014	0.010	0.017	0.026	0.023	0.024	0.039	0.045	0.023	0.017
124	106.16	16.33	3.76	0.690	3375.	13.086	-20.299	-0.275	0.419	0.409	20.804	-0.527	0.419	0.472	0.101	0.121	0.004	-0.029
...	...	...	...	...	...	0.006	0.060	0.008	0.008	0.007	0.017	0.025	0.023	0.024	0.012	0.014	0.013	0.012
125	120.62	27.64	4.25	0.230	2254.	14.919	-17.589	0.100	0.734	0.515	22.782	0.199	0.963	0.544	-0.265	-0.048	-0.133	-0.060
...	...	...	...	...	...	0.027	0.065	0.051	0.037	0.033	0.030	0.056	0.041	0.038	0.162	0.174	0.104	0.088
126	27.72	34.99	5.19	0.830	2171.	15.034	-17.393	0.018	0.303	0.091	24.705	0.072	0.367	0.187	-99.990	-99.990	-99.990	-99.990
...	...	...	...	...	...	0.095	0.111	0.134	0.148	0.180	0.108	0.158	0.174	0.228	9.999	9.999	9.999	9.999
127	58.48	9.40	3.09	0.760	4820.	13.592	-20.567	-0.448	0.417	0.398	20.180	-0.328	0.297	0.545	0.124	0.116	0.020	0.001
...	...	...	...	...	...	0.007	0.060	0.009	0.009	0.008	0.028	0.038	0.038	0.038	0.015	0.017	0.017	0.015
128	51.39	13.44	-99.99	0.870	-9999.	14.694	99.999	-0.292	0.388	0.322	22.202	-0.419	0.396	0.338	0.200	0.118	0.085	0.025
...	...	...	...	...	...	0.014	9.999	0.018	0.019	0.019	0.021	0.030	0.030	0.031	0.089	0.091	0.063	0.074
129	57.77	9.20	4.67	0.810	7435.	14.253	-20.847	0.058	0.553	0.457	20.935	0.089	0.596	0.513	0.053	0.093	0.017	-0.041
...	...	...	...	...	...	0.011	0.060	0.018	0.014	0.012	0.027	0.039	0.038	0.039	0.030	0.034	0.024	0.021
130	64.24	11.95	6.96	0.850	8526.	14.331	-21.066	0.097	0.711	0.505	21.687	0.083	0.837	0.532	0.537	0.272	0.167	0.064
...	...	...	...	...	...	0.012	0.061	0.019	0.015	0.012	0.021	0.030	0.030	0.030	0.040	0.047	0.032	0.023
131	85.56	19.00	4.29	0.460	3307.	14.850	-18.491	-1.353	1.325	-0.436	22.394	-1.118	1.325	-0.436	-0.244	-0.331	0.186	-0.097
...	...	...	...	...	...	0.076	0.096	0.082	0.081	0.044	0.081	0.084	0.084	0.047	0.324	0.603	0.588	0.296
132	62.21	13.10	0.92	0.590	1025.	15.021	-15.776	-0.237	0.509	0.445	21.941	-0.396	0.456	0.412	0.100	-0.008	0.050	0.055
...	...	...	...	...	...	0.018	0.062	0.026	0.024	0.022	0.027	0.040	0.038	0.037	0.065	0.072	0.062	0.055
133	114.24	26.23	1.97	0.800	1102.	13.466	-17.489	-0.457	0.396	0.433	22.559	-0.431	0.576	0.501	-0.025	-0.104	-0.001	0.076
...	...	...	...	...	...	0.022	0.063	0.027	0.027	0.022	0.027	0.033	0.034	0.028	0.085	0.104	0.099	0.077
134	63.66	10.15	-99.99	0.620	-9999.	14.329	99.999	0.072	0.755	0.535	21.029	0.086	0.907	0.577	0.141	0.097	0.062	-0.020
...	...	...	...	...	...	0.013	9.999	0.019	0.015	0.011	0.027	0.039	0.039	0.040	0.035	0.041	0.029	0.021
135	45.44	8.32	-99.99	0.590	-9999.	14.790	99.999	-0.343	0.317	0.445	20.955	-0.192	0.500	0.405	-0.117	-0.162	-0.236	0.310
...	...	...	...	...	...	0.018	9.999	0.020	0.034	0.033	0.036	0.048	0.059	0.059	0.039	0.047	0.096	0.089

Table 4—Continued

ID#	D_{24}	$r_e('')$	$r_e(kpc)$	b/a	V_{GSR}	B_T	$B_T(abs)$	$(U–B)_T$	$(B–V)_T$	$(V–R)_T$	$\mu_e(B)$	$(U–B)_e$	$(B–V)_e$	$(V–R)_e$	$\delta(U–R)/r_e$	$\delta(U–B)/r_e$	$\delta(B–V)/r_e$	$\delta(V–R)/r_e$
(1)	(2)	(3)	(4)	(5)	(6)	(7)	(8)	(9)	(10)	(11)	(12)	(13)	(14)	(15)	(16)	(17)	(18)	(19)
136	60.62	11.59	-99.99	0.940	-9999.	14.284	99.999	-0.331	0.560	0.492	21.696	-0.345	0.694	0.524	0.105	0.094	0.008	0.001
...	...	...	...	...	...	0.012	9.999	0.017	0.015	0.013	0.020	0.029	0.029	0.030	0.028	0.032	0.028	0.025
137	110.53	27.38	2.43	0.300	1301.	14.318	-16.997	-0.350	0.367	0.342	22.091	-0.458	0.308	0.301	0.117	0.069	0.038	0.026
...	...	...	...	...	...	0.012	0.061	0.016	0.017	0.017	0.018	0.026	0.027	0.027	0.047	0.048	0.046	0.045
138	60.26	11.37	6.29	0.890	8100.	14.774	-20.512	0.038	0.619	0.476	22.527	0.229	1.082	0.620	-0.347	-0.094	-0.163	-0.090
...	...	...	...	...	...	0.017	0.062	0.026	0.022	0.018	0.021	0.032	0.031	0.032	0.050	0.056	0.041	0.034
139	198.64	43.53	2.06	0.450	693.	12.913	-17.034	-0.032	0.637	0.504	22.379	-0.032	0.759	0.528	0.153	0.142	0.003	0.006
...	...	...	...	...	...	0.013	0.061	0.019	0.016	0.013	0.013	0.020	0.018	0.016	0.057	0.065	0.036	0.029
140	75.45	16.18	-99.99	0.950	-9999.	14.087	99.999	0.063	0.543	0.371	21.969	-0.193	0.443	0.371	0.024	0.122	0.009	-0.123
...	...	...	...	...	...	0.013	9.999	0.022	0.018	0.020	0.019	0.029	0.026	0.028	0.080	0.075	0.049	0.059
141	111.98	25.82	1.75	0.560	990.	13.584	-17.138	-0.030	0.622	0.449	22.199	-0.055	0.699	0.564	0.219	0.144	0.140	0.043
...	...	...	...	...	...	0.009	0.060	0.014	0.012	0.010	0.014	0.020	0.019	0.018	0.057	0.066	0.031	0.025
142	101.58	23.64	4.94	0.340	3059.	14.375	-18.797	-0.141	0.479	0.499	22.071	-0.141	0.544	0.440	0.095	0.135	-0.126	0.083
...	...	...	...	...	...	0.016	0.061	0.024	0.022	0.020	0.022	0.032	0.031	0.031	0.062	0.068	0.063	0.057

Note. — **Columns:** (1) Galaxy ID number assigned in table 1, (2) *R*-band 24th magnitude isophotal diameter in arcseconds, (3) R-band effective radius within which half of the light is contained in arcseconds, (4) r_e in kpc using $H_o = 71$ km s^{-1} Mpc^{-1}, (5) axis ratio, (6) RC3 galactic standard of rest velocity in km sec^{-1}, (7) total *B*-band apparent magnitude derived from extrapolating the surface brightness profile to infinity, (8) total absolute *B*-band magnitude, average total colors for (9) $(U-B)_T$, (10) $(B-V)_T$, and (11) $(V-R)_T$, (12) *B*-band surface brightness within r_e, average colors within r_e for (13) $(U-B)_e$, (14) $(B-V)_e$, and (15) $(V-R)_e$, and color gradients outside of r_e (measured by finding the slope of the linear fit to the color profile for all good points outside of r_e) in units of Δmag per r_e for (16) $(U-R)$, (17) $(U-B)$, (18) $(B-V)$, and (19) $(V-R)$. A negative slope indicates the galaxy becomes bluer with increasing radius, and a positive slope indicates that it is gets redder outward. The second line for each galaxy lists errors for some quantities. The B_T error was derived from the total signal-to-noise in the largest aperture measured. $B_T(abs)$ errors also include the uncertainty on H_o from WMAP measurements. Errors on the total and effective colors, $(X-Y)_T$ and $(X-Y)_e$, are the quadratic sum of the respective total X and Y magnitude errors. The $\mu_e(B)$ error is the accidental error derived from EQ. 1. The errors on the color gradients were determined from the scatter of the fits.

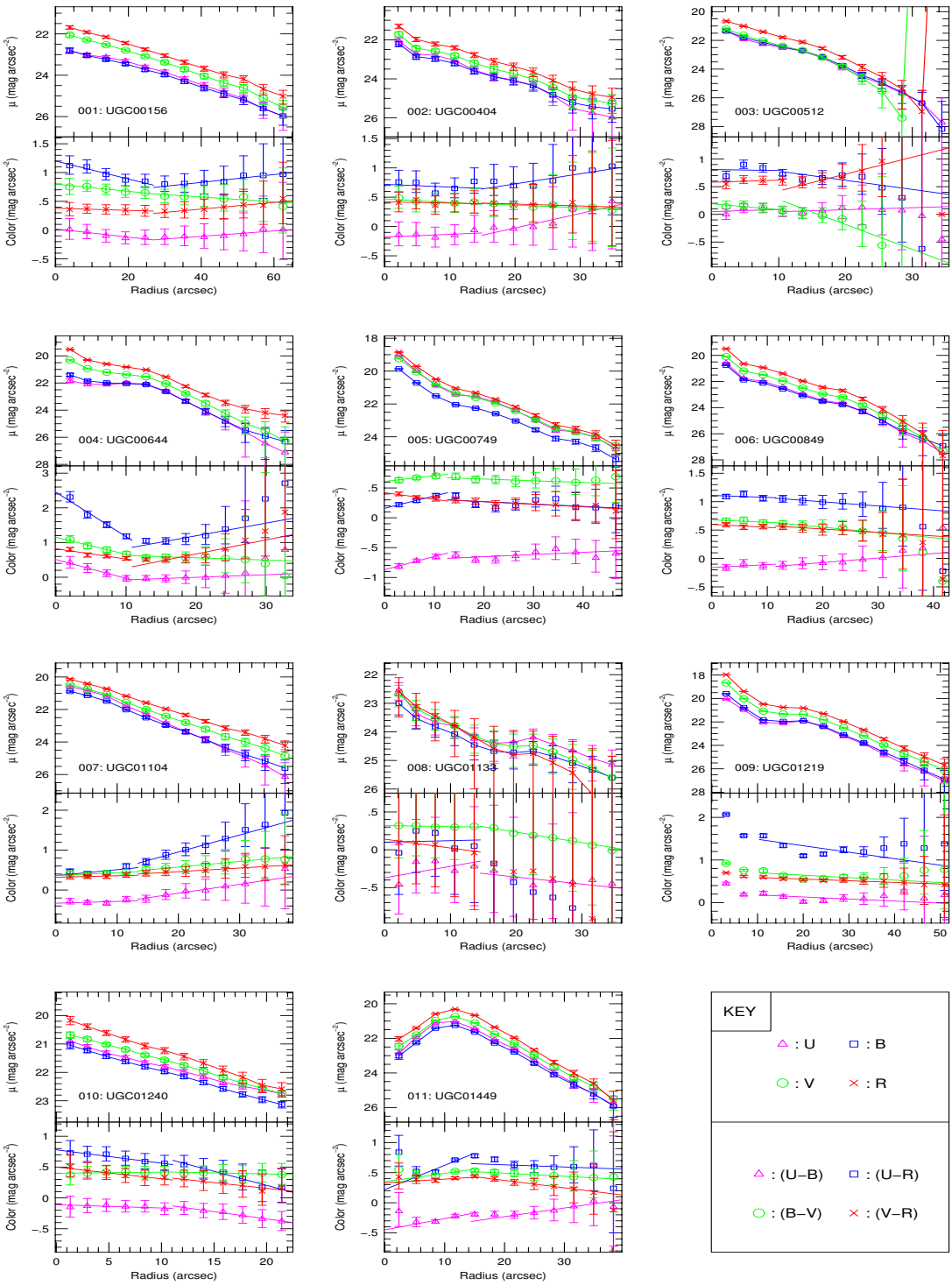
001: UGC00156
002: UGC00404
003: UGC00512
004: UGC00644
005: UGC00749
006: UGC00849
007: UGC01104
008: UGC01133
009: UGC01219
010: UGC01240
011: UGC01449
μ (mag arcsec^{-2})
Color (mag arcsec^{-2})
Radius (arcsec)
KEY
△ : U
□ : B
○ : V
× : R
△ : (U–B)
□ : (U–R)
○ : (B–V)
× : (V–R)

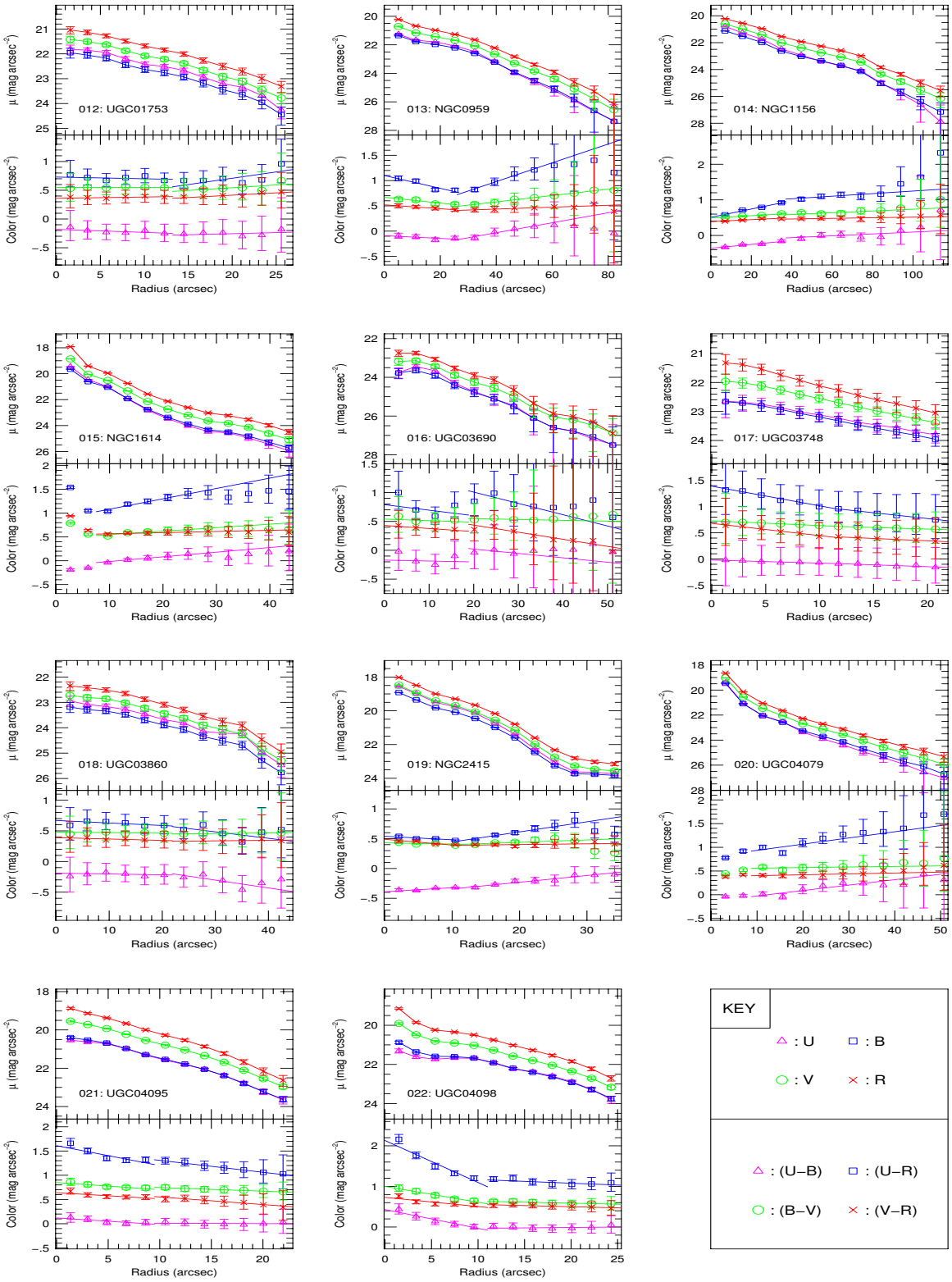
012: UGC01753
013: NGC0959
014: NGC1156
015: NGC1614
016: UGC03690
017: UGC03748
018: UGC03860
019: NGC2415
020: UGC04079
021: UGC04095
022: UGC04098
μ (mag arcsec⁻²)
Color (mag arcsec⁻²)
Radius (arcsec)
KEY
△ : U
□ : B
○ : V
× : R
△ : (U–B)
□ : (U–R)
○ : (B–V)
× : (V–R)

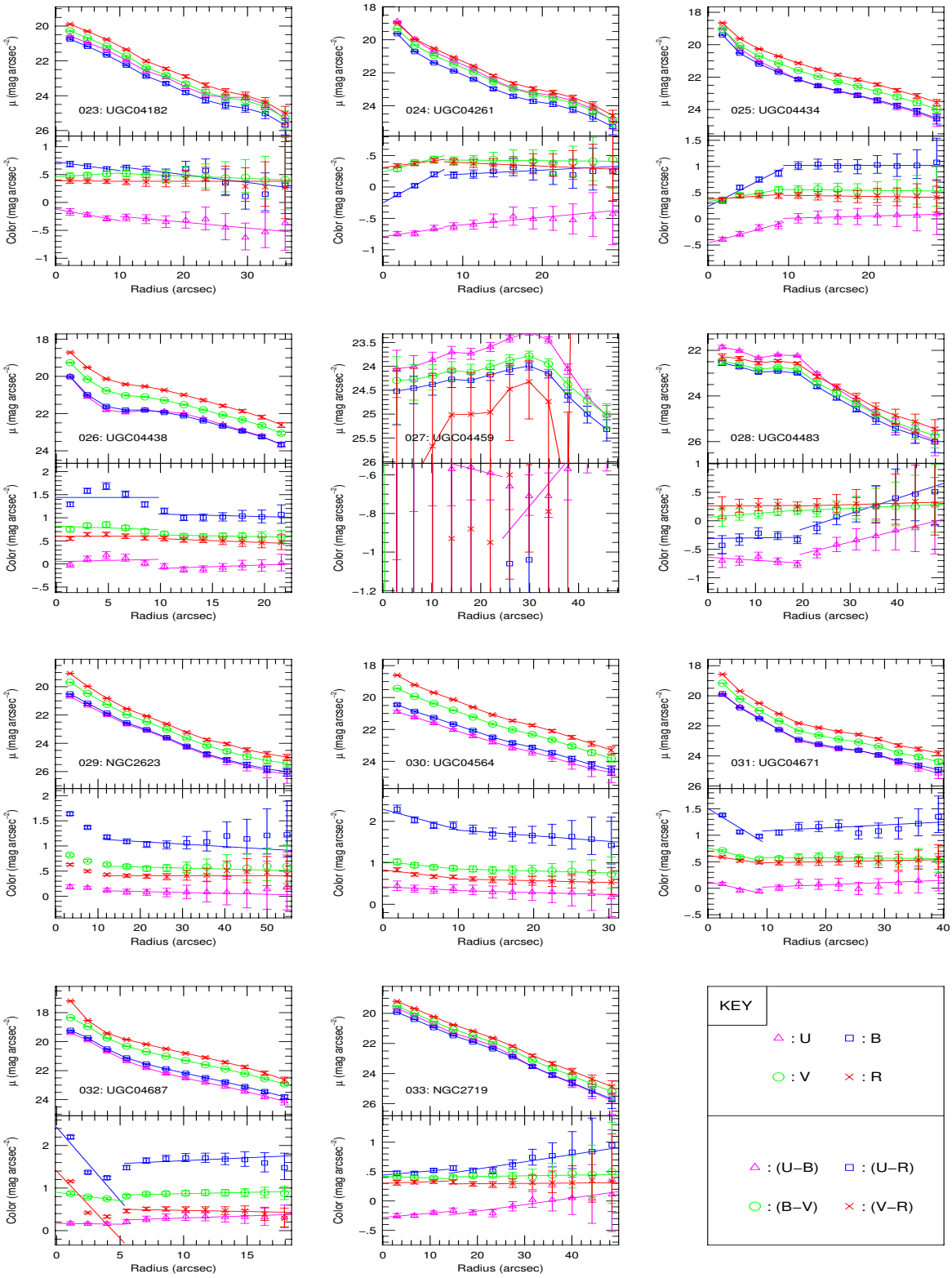
023: UGC04182
024: UGC04261
025: UGC04434
026: UGC04438
027: UGC04459
028: UGC04483
029: NGC2623
030: UGC04564
031: UGC04671
032: UGC04687
033: NGC2719
μ (mag arcsec⁻²)
Color (mag arcsec⁻²)
Radius (arcsec)
KEY
△ : U
□ : B
○ : V
× : R
△ : (U−B)
□ : (U−R)
○ : (B−V)
× : (V−R)

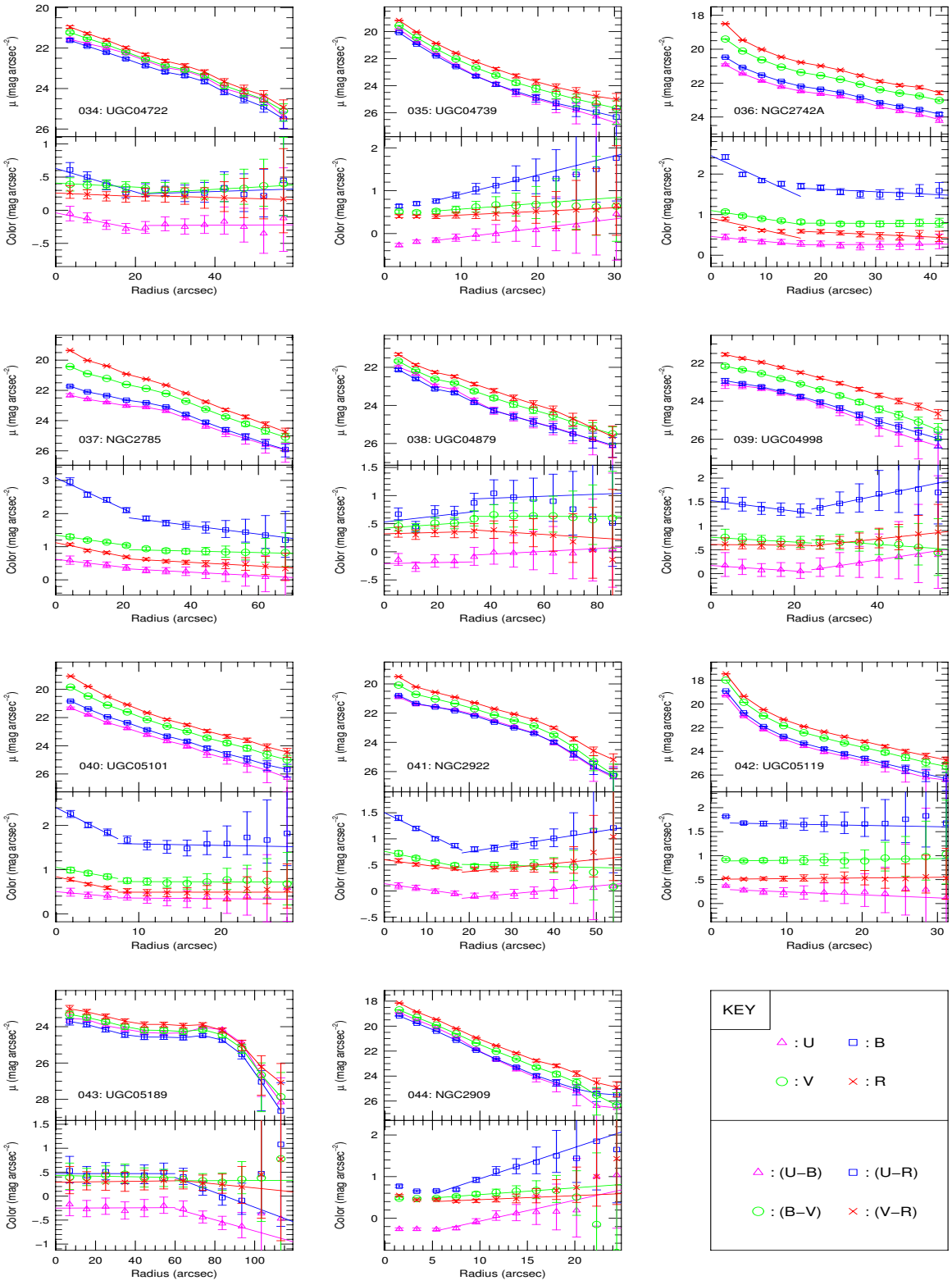
034: UGC04722
035: UGC04739
036: NGC2742A
037: NGC2785
038: UGC04879
039: UGC04998
040: UGC05101
041: NGC2922
042: UGC05119
043: UGC05189
044: NGC2909
μ (mag arcsec^{-2})
Color (mag arcsec^{-2})
Radius (arcsec)
KEY
△ : U
□ : B
○ : V
× : R
△ : (U−B)
□ : (U−R)
○ : (B−V)
× : (V−R)

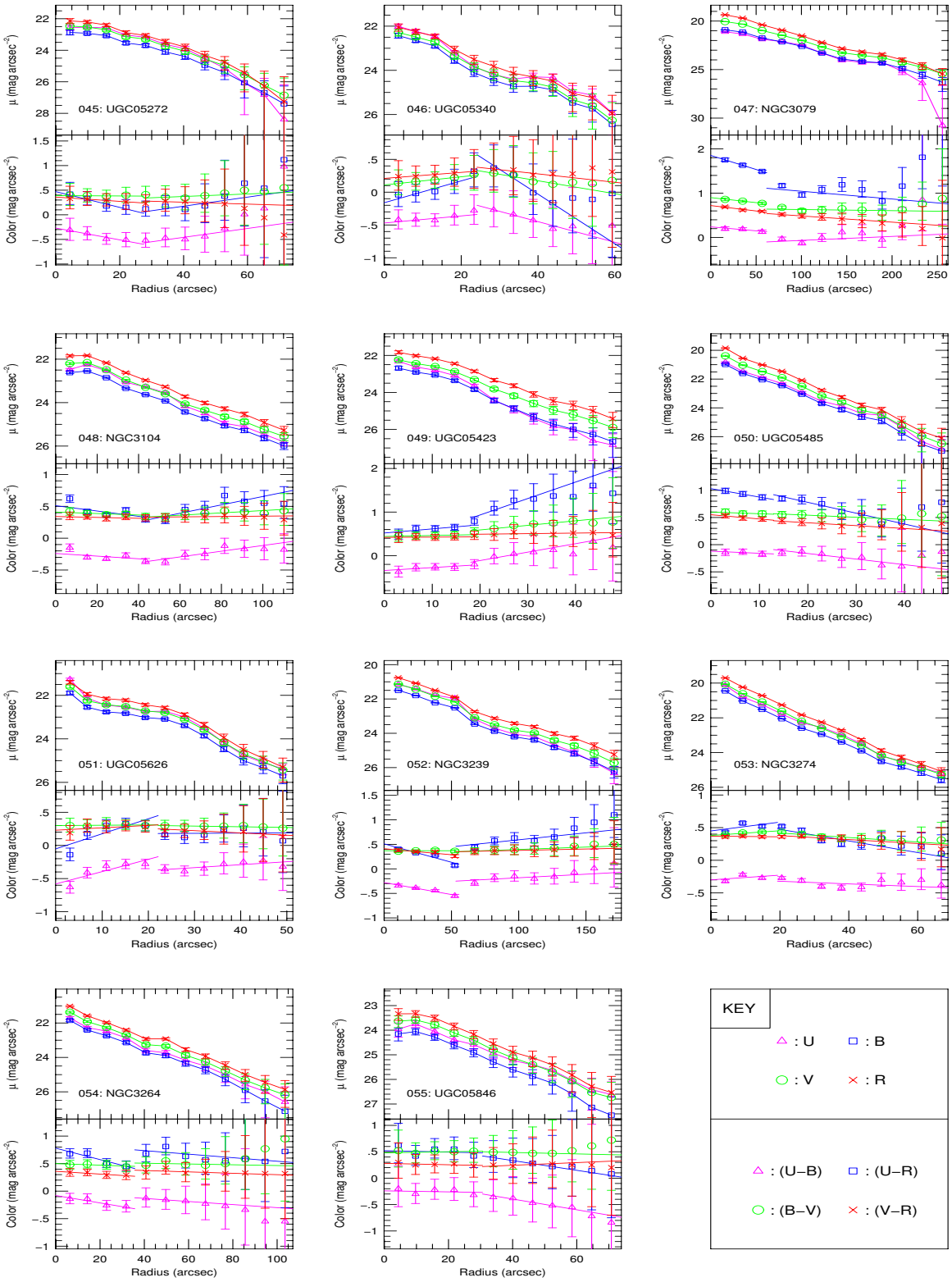
045: UGC05272
046: UGC05340
047: NGC3079
048: NGC3104
049: UGC05423
050: UGC05485
051: UGC05626
052: NGC3239
053: NGC3274
054: NGC3264
055: UGC05846
μ (mag arcsec⁻²)
Color (mag arcsec⁻²)
Radius (arcsec)
KEY
△ : U
□ : B
○ : V
× : R
△ : (U–B)
□ : (U–R)
○ : (B–V)
× : (V–R)

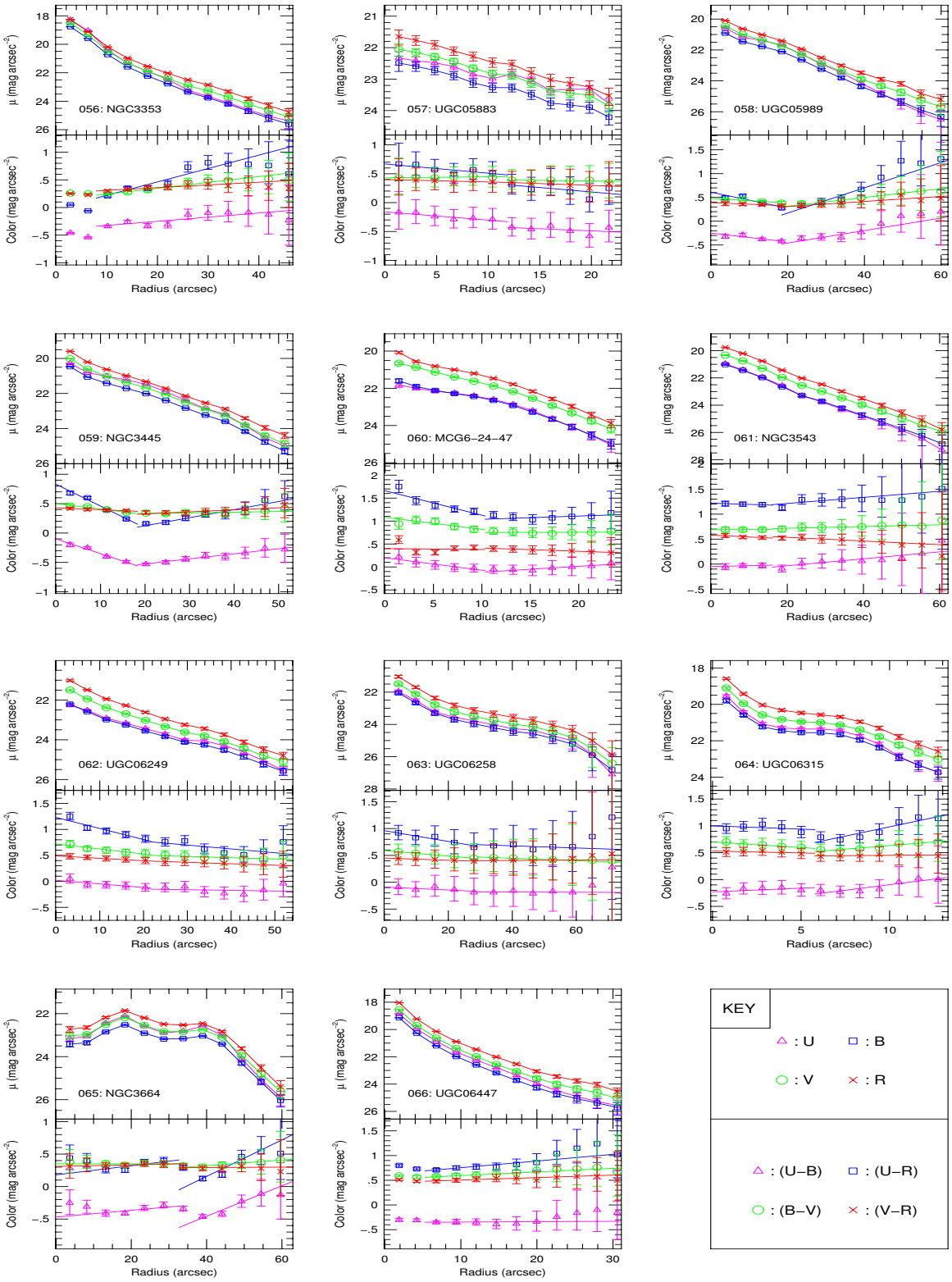
056: NGC3353
057: UGC05883
058: UGC05989
059: NGC3445
060: MCG6−24−47
061: NGC3543
062: UGC06249
063: UGC06258
064: UGC06315
065: NGC3664
066: UGC06447
μ (mag arcsec⁻²)
Color (mag arcsec⁻²)
Radius (arcsec)
KEY
△ : U
□ : B
○ : V
× : R
△ : (U−B)
□ : (U−R)
○ : (B−V)
× : (V−R)

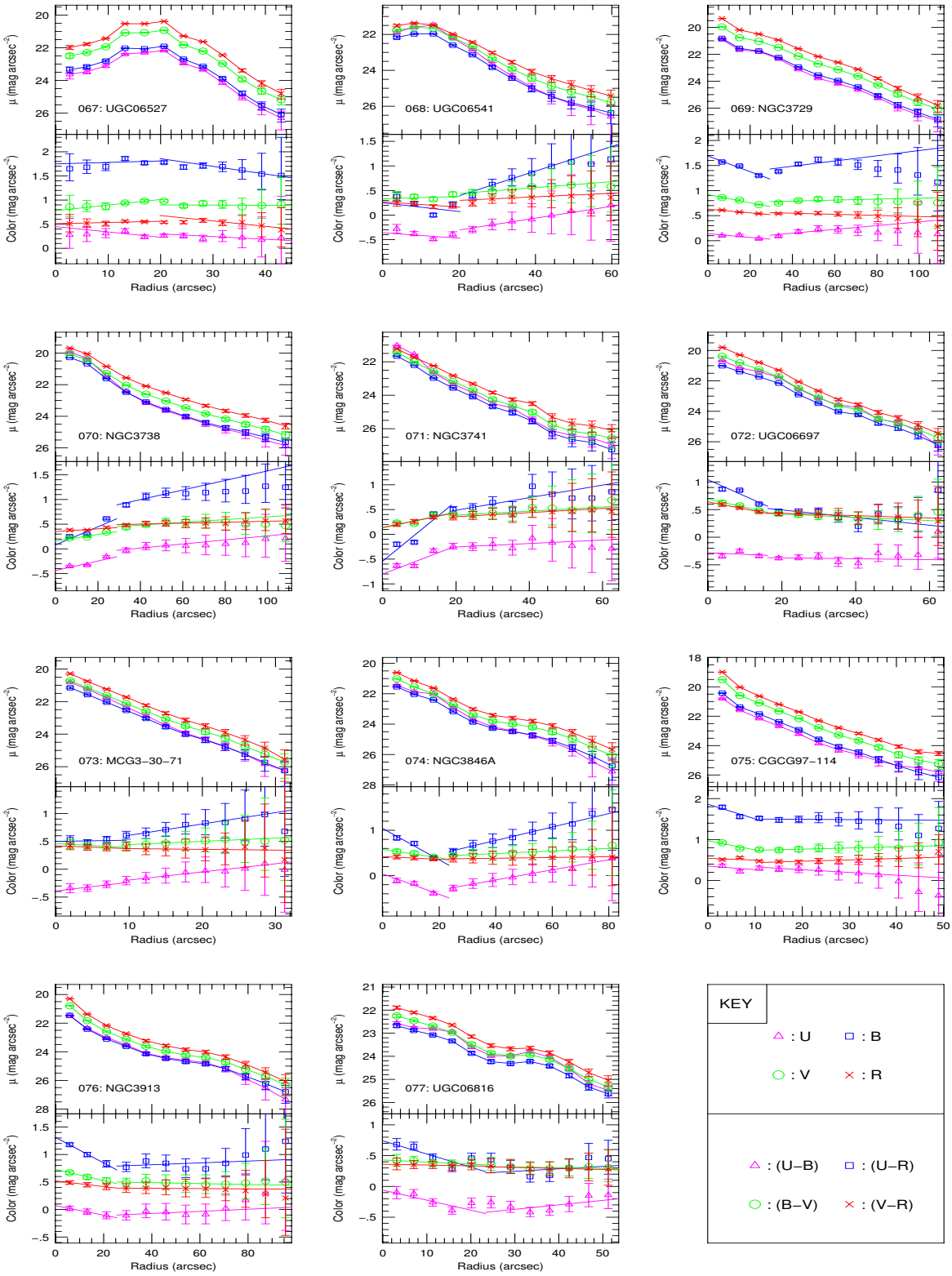
067: UGC06527
068: UGC06541
069: NGC3729
070: NGC3738
071: NGC3741
072: UGC06697
073: MCG3−30−71
074: NGC3846A
075: CGCG97−114
076: NGC3913
077: UGC06816
μ (mag arcsec⁻²)
Color (mag arcsec⁻²)
Radius (arcsec)
KEY
△ : U
□ : B
○ : V
× : R
△ : (U−B)
□ : (U−R)
○ : (B−V)
× : (V−R)

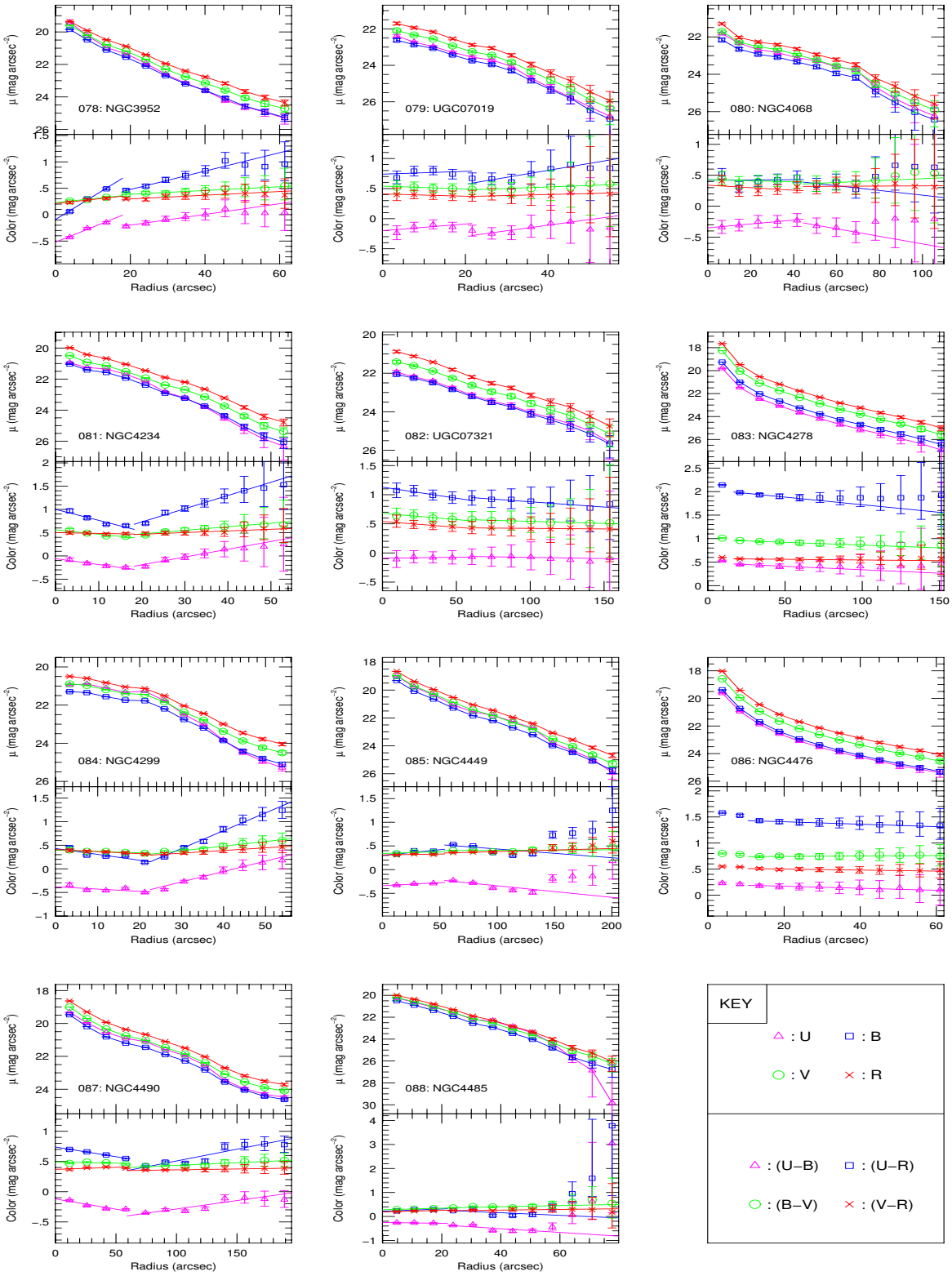
078: NGC3952
079: UGC07019
080: NGC4068
081: NGC4234
082: UGC07321
083: NGC4278
084: NGC4299
085: NGC4449
086: NGC4476
087: NGC4490
088: NGC4485
μ (mag arcsec^{-2})
Color (mag arcsec^{-2})
Radius (arcsec)
KEY
△ : U
□ : B
○ : V
× : R
△ : (U–B)
□ : (U–R)
○ : (B–V)
× : (V–R)

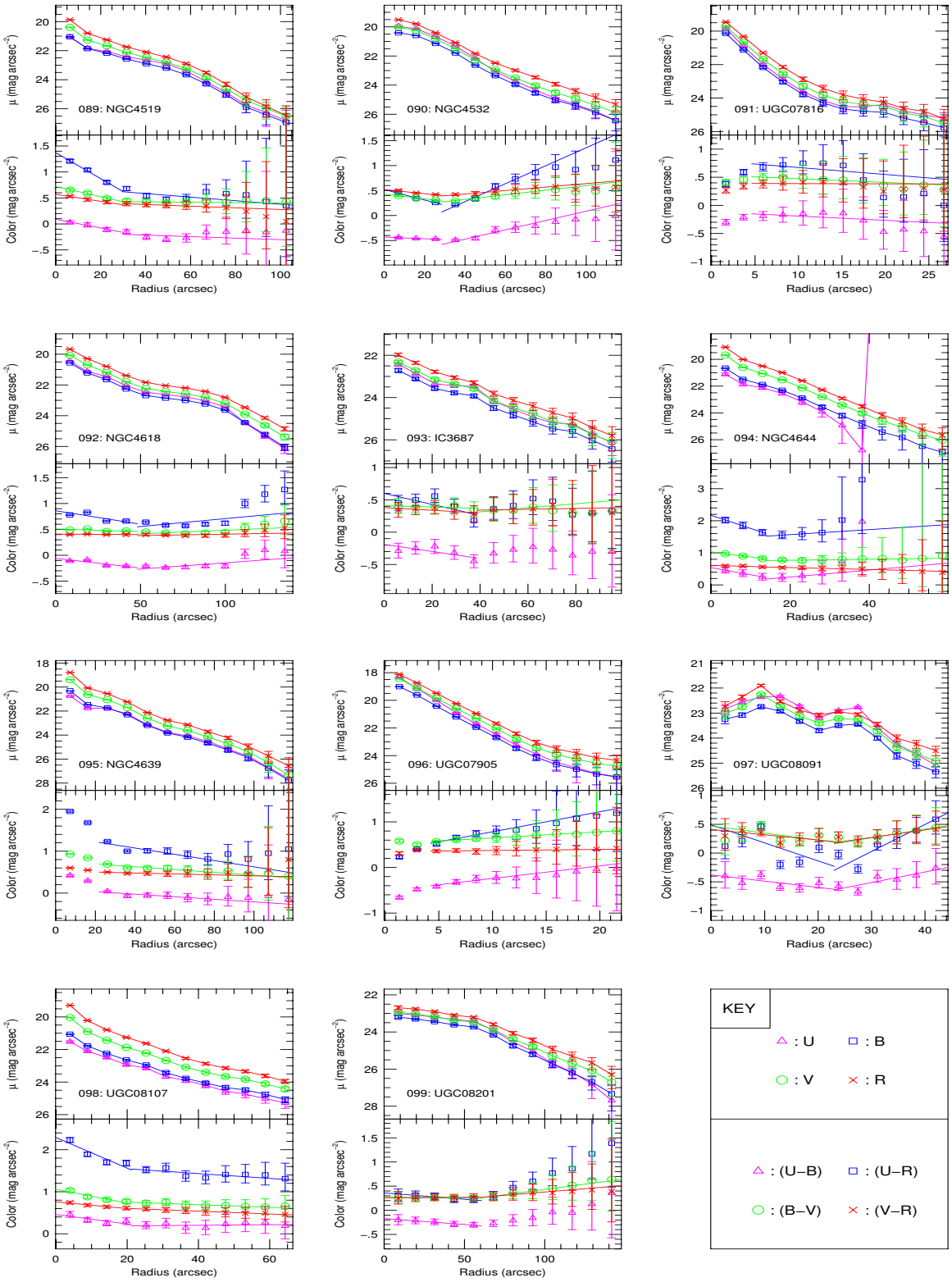
089: NGC4519
090: NGC4532
091: UGC07816
092: NGC4618
093: IC3687
094: NGC4644
095: NGC4639
096: UGC07905
097: UGC08091
098: UGC08107
099: UGC08201
μ (mag arcsec^{-2})
Color (mag arcsec^{-2})
Radius (arcsec)
KEY
△ : U
□ : B
○ : V
× : R
△ : (U–B)
□ : (U–R)
○ : (B–V)
× : (V–R)

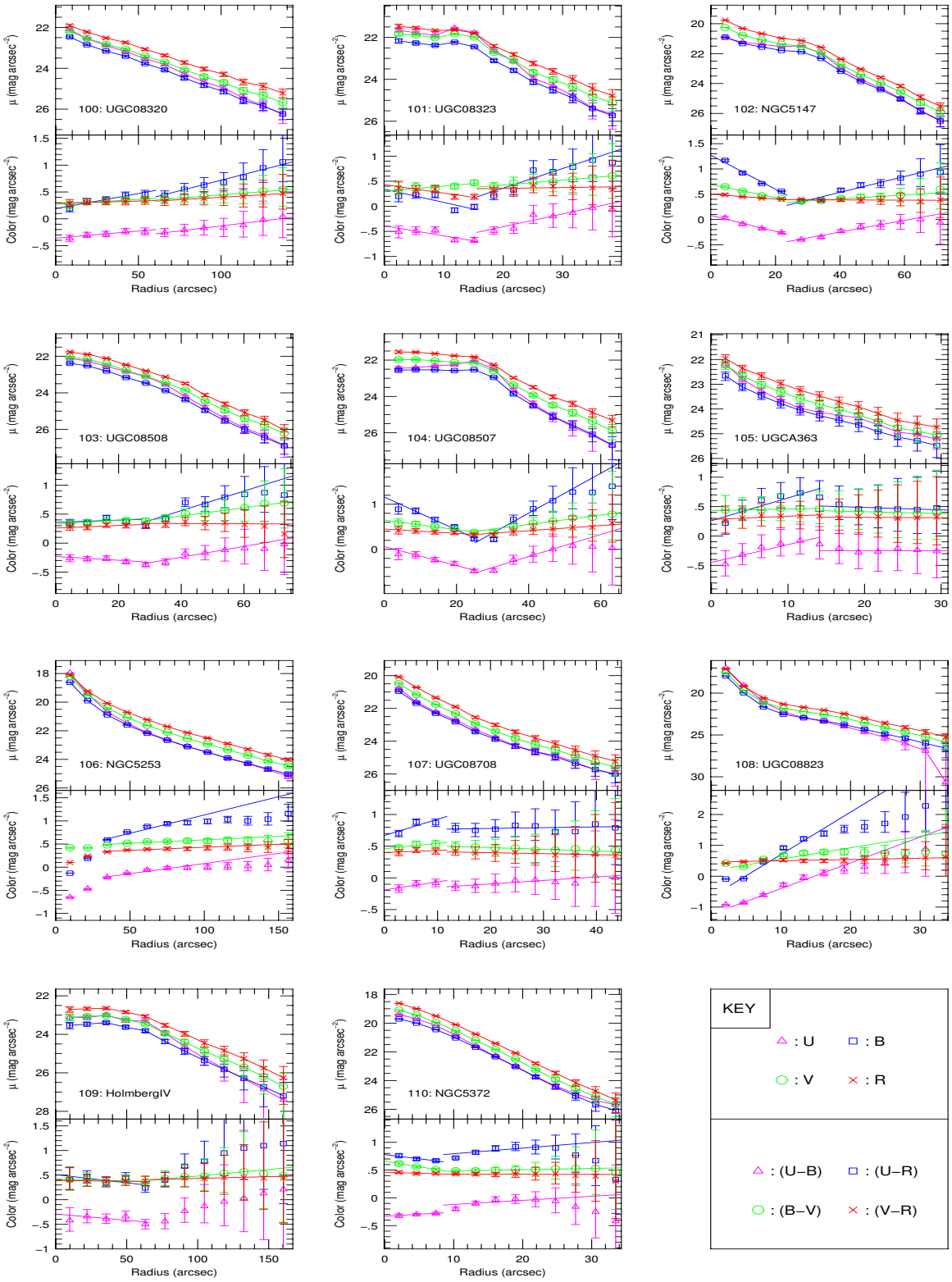
100: UGC08320
101: UGC08323
102: NGC5147
103: UGC08508
104: UGC08507
105: UGCA363
106: NGC5253
107: UGC08708
108: UGC08823
109: HolmbergIV
110: NGC5372
μ (mag arcsec⁻²)
Color (mag arcsec⁻²)
Radius (arcsec)
KEY
△ : U
□ : B
○ : V
× : R
△ : (U−B)
□ : (U−R)
○ : (B−V)
× : (V−R)

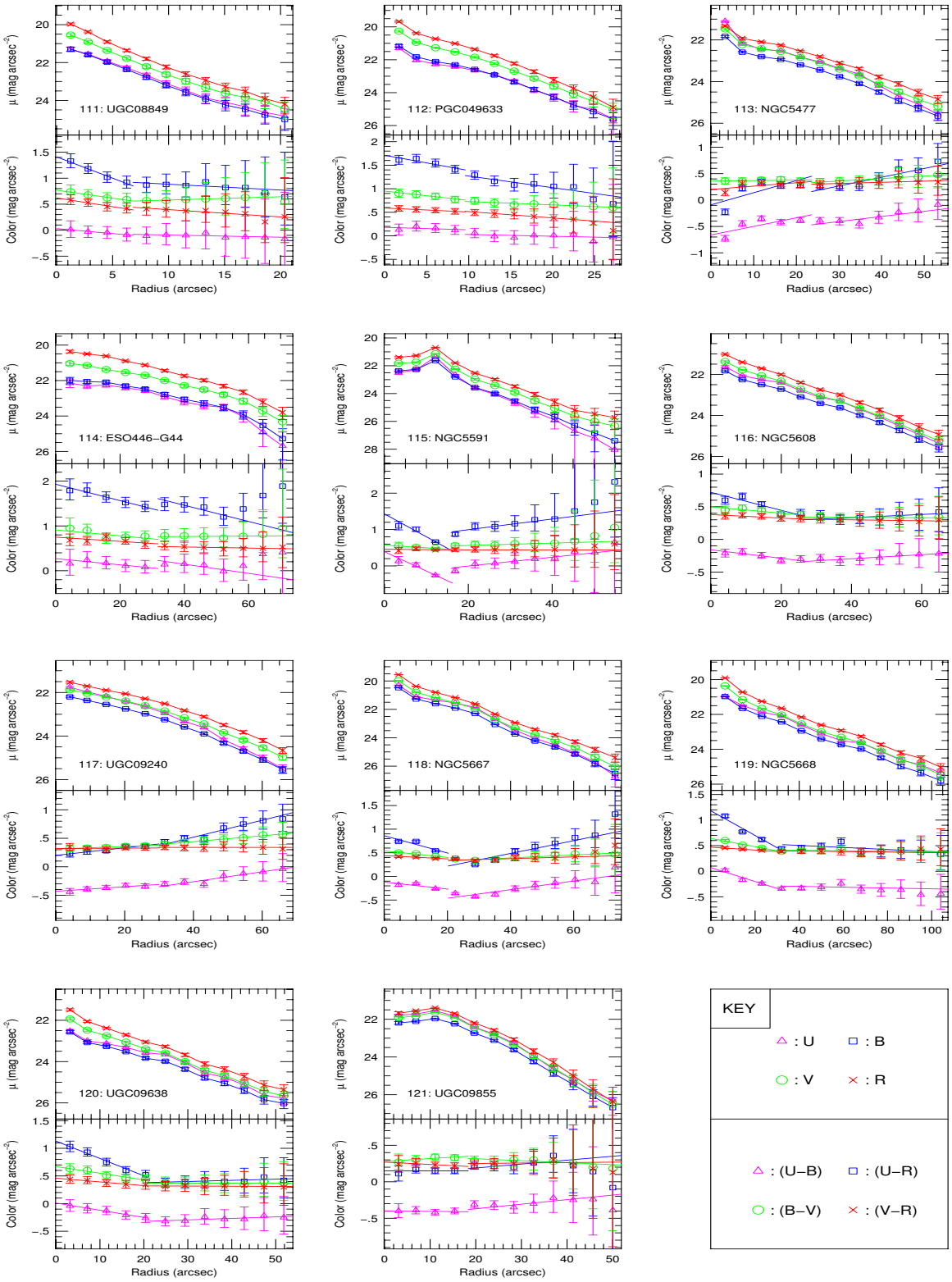
111: UGC08849
112: PGC049633
113: NGC5477
114: ESO446–G44
115: NGC5591
116: NGC5608
117: UGC09240
118: NGC5667
119: NGC5668
120: UGC09638
121: UGC09855
μ (mag arcsec^{-2})
Color (mag arcsec^{-2})
Radius (arcsec)
KEY
△ : U
□ : B
○ : V
× : R
△ : (U–B)
□ : (U–R)
○ : (B–V)
× : (V–R)

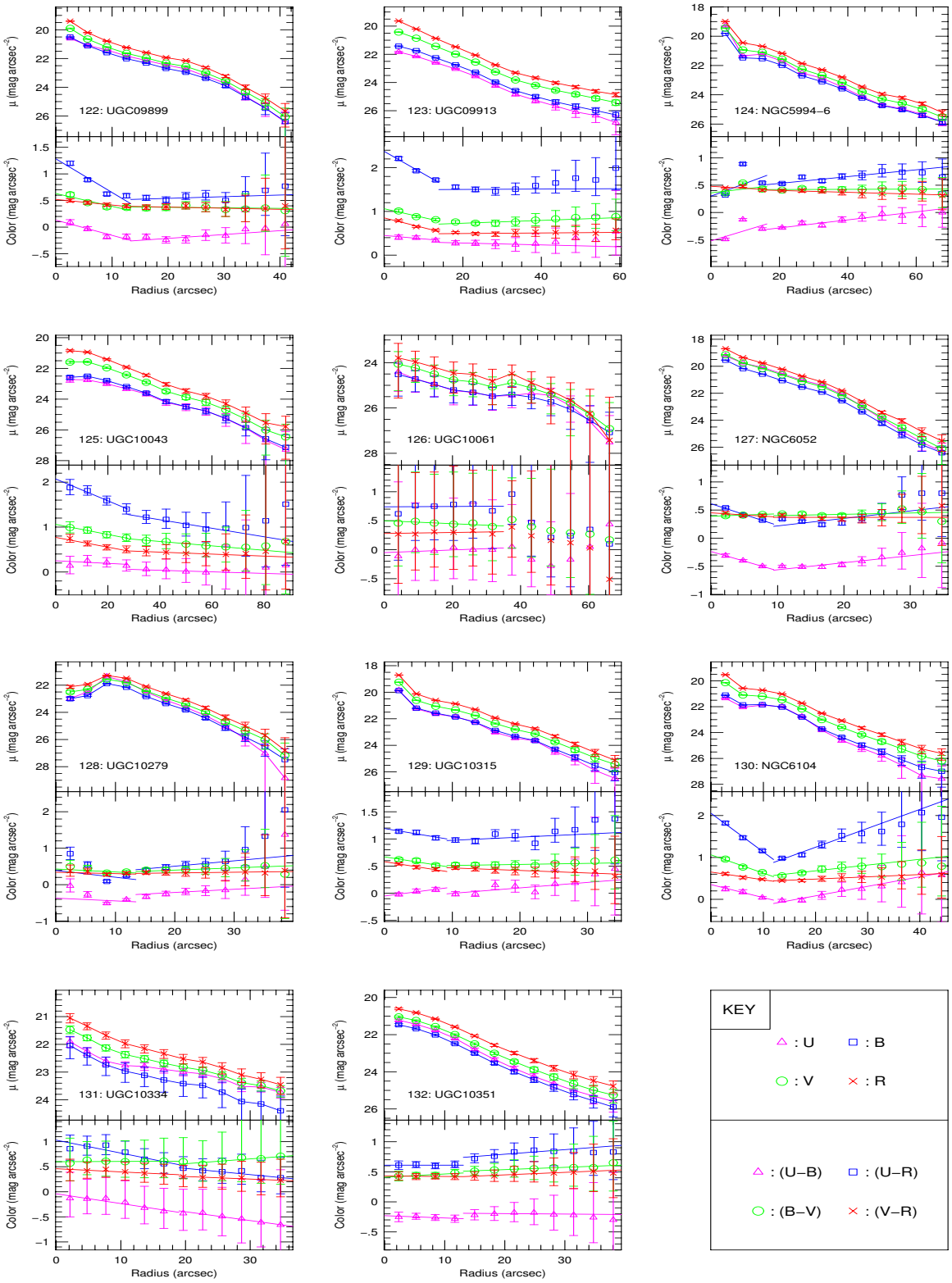
122: UGC09899
123: UGC09913
124: NGC5994–6
125: UGC10043
126: UGC10061
127: NGC6052
128: UGC10279
129: UGC10315
130: NGC6104
131: UGC10334
132: UGC10351
μ (mag arcsec⁻²)
Color (mag arcsec⁻²)
Radius (arcsec)
KEY
△ : U
□ : B
○ : V
× : R
△ : (U–B)
□ : (U–R)
○ : (B–V)
× : (V–R)

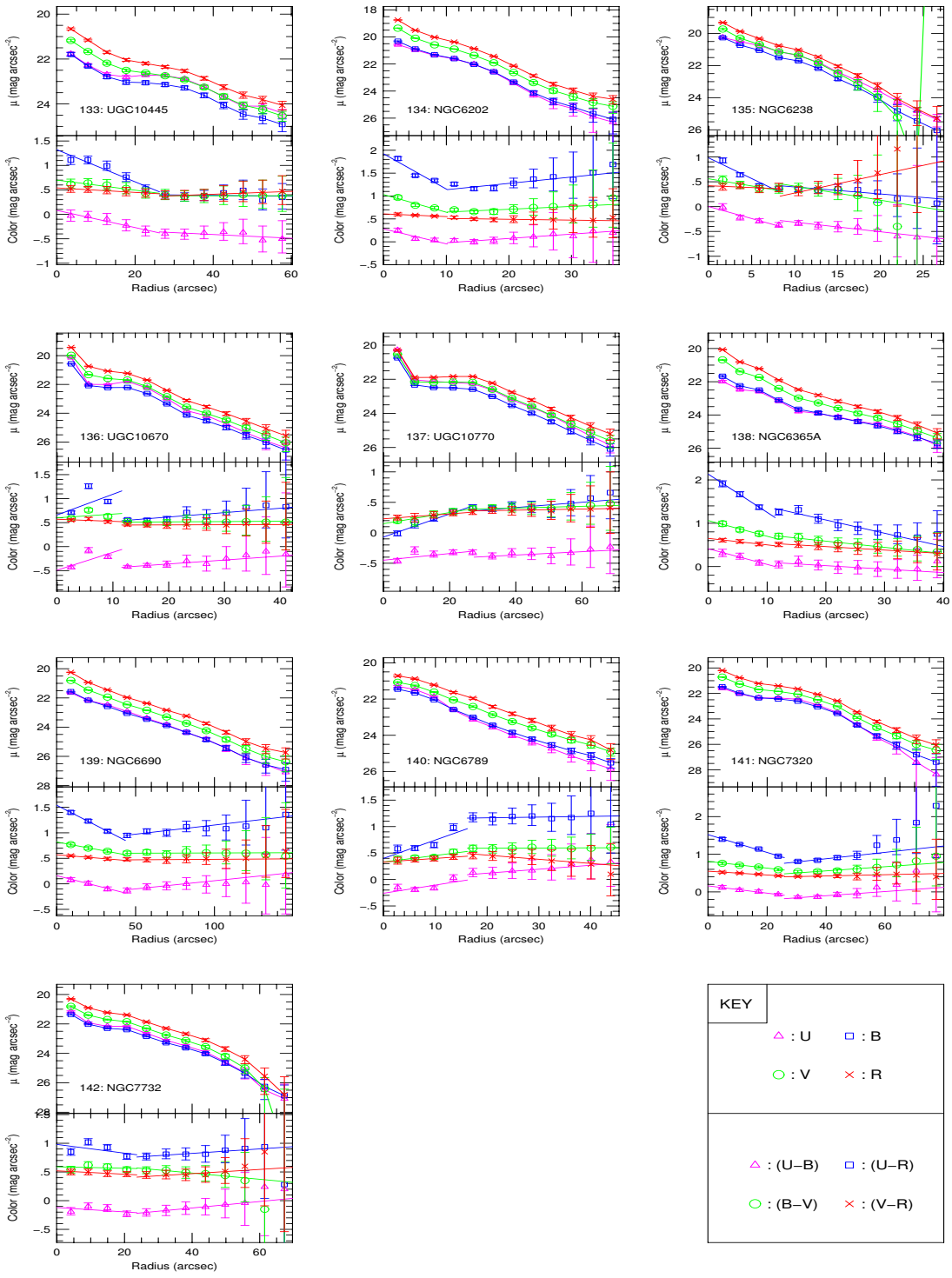

Figure 5 For this and previous 12 pages of figures: **(Top panels:)** Surface Brightness (μ) profiles and **(Bottom panels:)** color profiles for each of the 142 galaxies imaged at the VATT. The lines in the color profile plots are the error-weighted linear-least-squares fit to the data points inside r_e and outside r_e. No fit was made if there would be fewer than three good (signal-to-noise ratio above sky > 0.5) points in the fit.

2.4. Results

2.4.1. *VATT (U − R) Radial Color Gradients*

Figure 6 shows examples of the surface brightness and color profiles for a few VATT galaxies with notable radial color gradient trends, along with images of the galaxies in U and R with ellipses marking the outer annulus used to calculate the final point in the surface brightness profiles. NGC4476 is an early-type galaxy (T = −1.0) with no significant radial color gradient, although it does become slightly bluer with radius. UGC04095 is a mid-type spiral (T = 6.0) which becomes similarly slightly bluer with increasing radius. UGC01104 and UGC00156 are late-type galaxies (T = 10.0 and 9.3, respectively) that become redder with increasing radius. UGC01104 and UGC00156 differ in that UGC01104 gets redder with increasing radius throughout (in the inner parts ($r < r_e$), and the outer parts ($r > r_e$)), while UGC00156 gets bluer with radius in the inner parts ($r < r_e$) and redder in the outer parts ($r > r_e$). This flip in color slope sign is common, occurring in about half of our galaxies.

The slopes of the outer "disk" ($r > r_e$) ($U - R$) color profile fits measured in our VATT images are plotted vs. Hubble type, total absolute B magnitude, r_e in kpc (for H_o = 71 km s^{-1} Mpc^{-1}), and axis ratio (b/a) in Figure 7. The ($U - R$) color is shown because it provides the largest wavelength baseline, but the same trends are seen in all other possible $UBVR$ color combinations. The color slope is zero if there is no change in color with radius, positive if the galaxy becomes redder at larger radii, and negative if the galaxy becomes bluer at larger radii. An error bar in the upper left panel shows the representative median uncertainty on the ($U - R$) color gradient slopes, as derived from the linear-least-squares fit. Median color slopes for several type bins are plotted as open triangles on top of the individual data points in the Hubble type plot. Boxes surrounding each median value enclose the type bin and the color slope 25% and 75% quartile ranges. Vertical error bars on these points indicate the error on the median (T50), which is calculated from the 25% (T25) and 75% (T75) quartile values with:

$$\sigma_{T50} = \frac{1.483(T75 - T25)}{2\sqrt{N-1}} \tag{2.3}$$

The median color slope becomes larger (redder with increasing radius), and the overall scatter, or range of possible color slopes, increases with later Hubble types, less luminous total magnitudes, smaller effective radii, and, to a lesser extent, rounder axis ratios. This similarity in trends is not surprising, since all of these parameters are not entirely independent, with later Hubble type galaxies tending to be fainter, smaller, and sometimes rounder than earlier type galaxies, with disks that are less rotationally supported.

The median color gradients in the plot of slope vs. Hubble type (Figure 7) show that galaxies with types E through S0 have no significant radial color slope within the 1-σ error on the median (-0.02 ± 0.03 mag arcsec^{-2} per r_e), or at most a very slight negative slope that would indicate a weak trend of bluer colors with increasing radius. Although this is determined from small number statistics (four galaxies), it is consistent with the findings

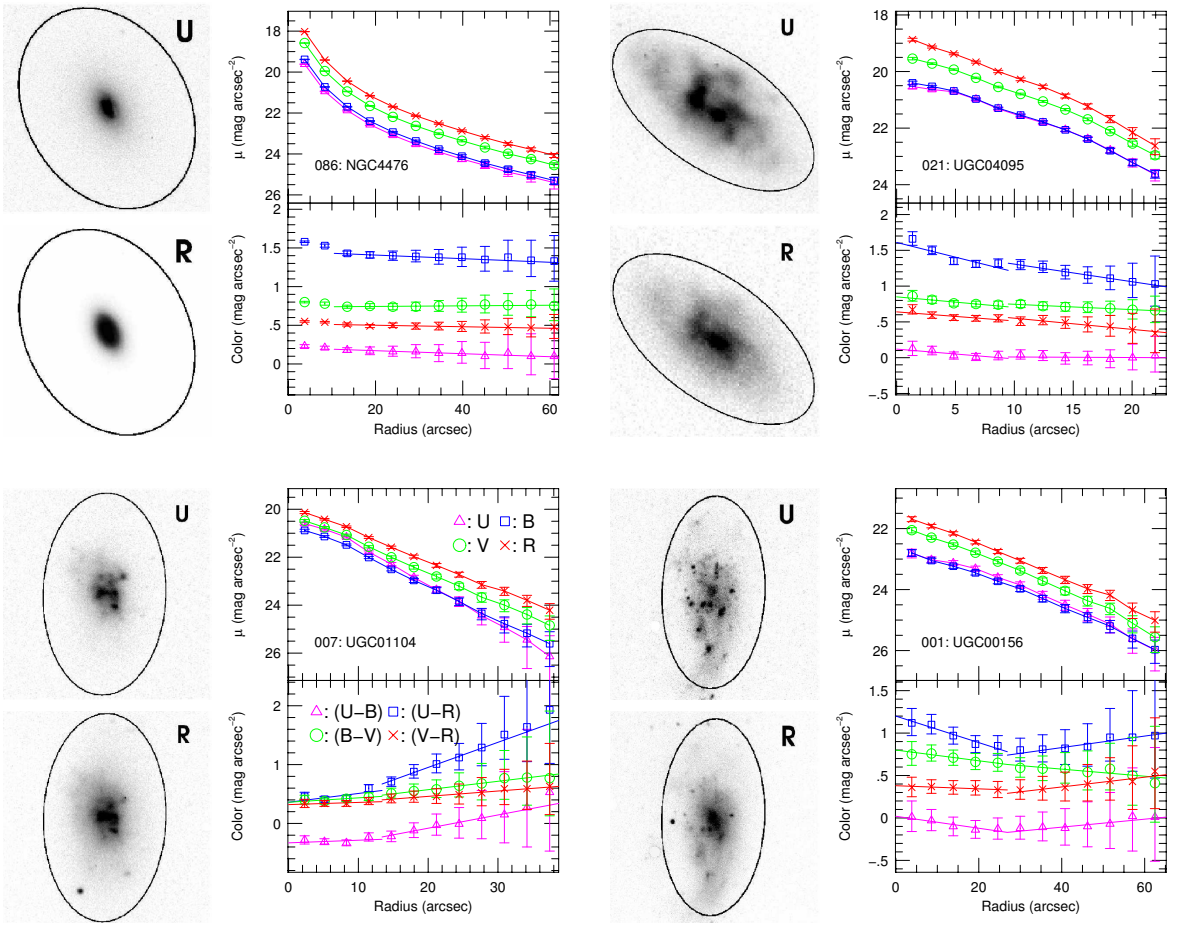

Figure 6 Examples of surface brightness (μ) and color profiles for some notable galaxies. The ellipses in the images mark the last annulus used in the profile calculation. Note that the images were scaled to highlight interesting galaxy structure, such that not all low-surface brightness structure may be visible in these images. The upper right panel for each galaxy is the surface brightness profile, and the lower right panel is the color profile, with the same color legend as in Figure 5. The key printed in the UGC01104 plot applies to all of the plots. NGC4476 is an early-type (T = −1.0) galaxy with constant to slightly bluer colors with increasing radius, which is typical of early-type galaxies. UGC04095 is a mid-type (T = 6.0) spiral that also gets slightly bluer with radius, which is typical of mid-type galaxies. UGC01104 is an irregular galaxy (T = 10.0) that gets redder with radius, which is more typical of late-type galaxies. UGC00156 is a late-type spiral galaxy (T = 9.3) which actually gets bluer in the inner regions with radius, but redder in the outer regions. This change in color gradient sign is common, occurring in about half of the galaxies in our sample.

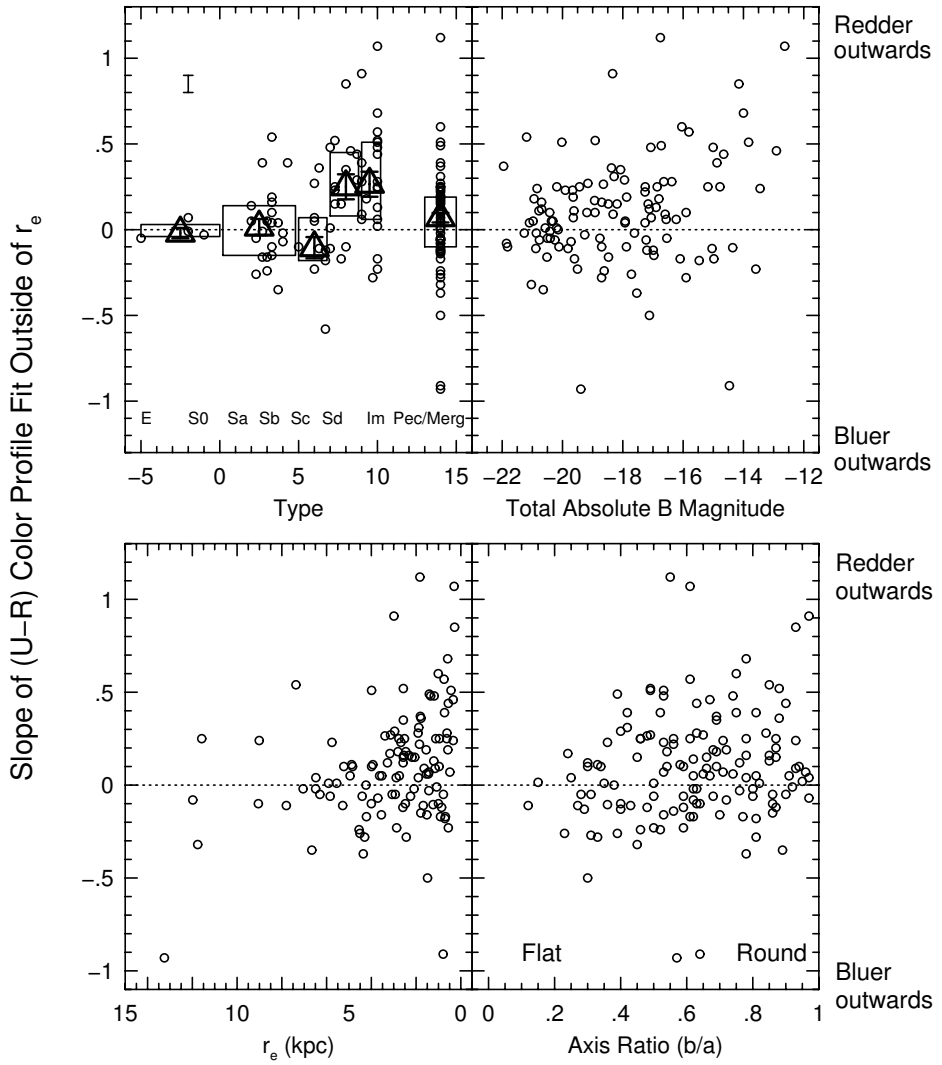

Figure 7 The $(U-R)$ color gradient slope outside r_e (i.e. in the outer "disk") plotted against several galaxy parameters. The error bar in the upper left corner of the type panel (upper left) shows the representative median error of the $(U-R)$ color gradient slope. The triangles in this panel represent the median color slope for several type bins. Boxes surrounding each median value enclose the type bin and the color slope 25% and 75% quartile ranges. Vertical error bars mark the errors on the medians. There is no significant median color slope within the errors for early-type (E-S0) galaxies, or for early-type (Sa-Sb) spirals. Mid-type (Sc) spiral galaxies get slightly bluer with increasing radius, and late-type (Sd-Im) galaxies get significantly redder with increasing radius. Mergers/peculiars get on average slightly redder with increasing radius, although they have a large range in color slopes. The scatter in this panel increases with increasing Hubble type, such that there is a wider range of possible color slopes with increasing type. The other panels show an average trend of fainter, smaller, and rounder galaxies (which tend to have later Hubble types) becoming increasingly redder with radius, with an increasingly larger range of possible slope values (larger scatter).

from other studies of elliptical galaxy color gradients (Vader et al. 1988; Franx et al. 1989; Peletier et al. 1990). There is also no significant color gradient for early-type spirals (Sa-Sb), which at most get slightly redder with increasing radius (0.02 ± 0.05 mag arcsec^{-2} per r_e). Mid-type spirals (Sc) tend to get bluer with increasing radius by 1.8-σ (-0.11 ± 0.06 mag arcsec^{-2} per r_e). This is also consistent with the findings in previous studies (de Jong 1996; Tully et al. 1996; Jansen et al. 2000; Bell & de Jong 2000; MacArthur et al. 2004). We see a significant (~ 3.6-σ) trend of redder colors with increasing radius for most of the late-type spirals and irregulars, with a median color gradient of 0.25 ± 0.07 mag arcsec^{-2} per r_e for late-type spirals and a gradient of 0.27 ± 0.07 mag arcsec^{-2} per r_e for irregular galaxies. This suggests a distinction between the radial color gradient properties of elliptical and early to mid-type spiral galaxies (typically zero color gradients to a slightly bluer color with increasing radius, with some scatter between individual galaxies) vs. those of late-type spiral and irregular galaxies (typically redder color with increasing radius, with large scatter between individual galaxies). The peculiar and merger group (T = 14) becomes on average slightly redder with increasing radius (0.07 ± 0.03 mag arcsec^{-2} per r_e), although it has a large scatter in measured color gradients. This large scatter may be due to the particular physics of each galaxy interaction, since wide-spread massive star formation can be triggered anywhere in such galaxies and result in either positive or negative color gradients. Dust may also play a role in reddening the inner parts of these galaxies, which would further decrease the color gradient. These two factors are particularly pronounced in currently merging galaxies, and therefore may account for the more modest median color gradient we find for the interacting/merging group compared to the irregular galaxy group.

Figure 8 contains plots of the $(U - R)$ outer color slope vs. several other galaxy quantities derived from the RC3. Galaxies that did not have the relevant parameters listed in the RC3 were left out of the plot. The Hubble types from the RC3 show a similar trend with radial color gradient as our visual classifications (Figure 7), with on average more galaxies becoming increasingly redder with increasing radius, and a larger gradient scatter with increasing Hubble type. This same trend is seen with increasing major axis diameter (which was converted to kpc using $H_0 = 71$ km s^{-1} Mpc^{-1}), and with increasing radial velocity with respect to the Galactic standard of rest, V_{GSR}. The former is not surprising, since later-type galaxies tend to be intrinsically smaller than earlier-type galaxies. The trend with radial velocity is likely due to Malmquist Bias: since late-type galaxies tend to have a lower surface brightness than earlier-types, they will be preferentially selected at nearer distances when using surface brightness limited samples.

There is a weaker trend of increasingly redder outer regions with fainter B_T^0 (the absolute extinction corrected total B-band magnitude), M_{21} (the absolute H I 21 cm emission line magnitude), and, to a lesser extent, M_{FIR} (the absolute far infrared magnitude). This trend is also seen with mean B-band surface brightness, μ_B, within r_e, although the low number statistics in this plot are due to the absence of effective radii (r_e) information for many galaxies in the RC3. The H I index ((M_{21}–B_T^0) color) does not display a strong trend with color gradient, even though it is apparent in B_T^0 and M_{21}. This suggests that

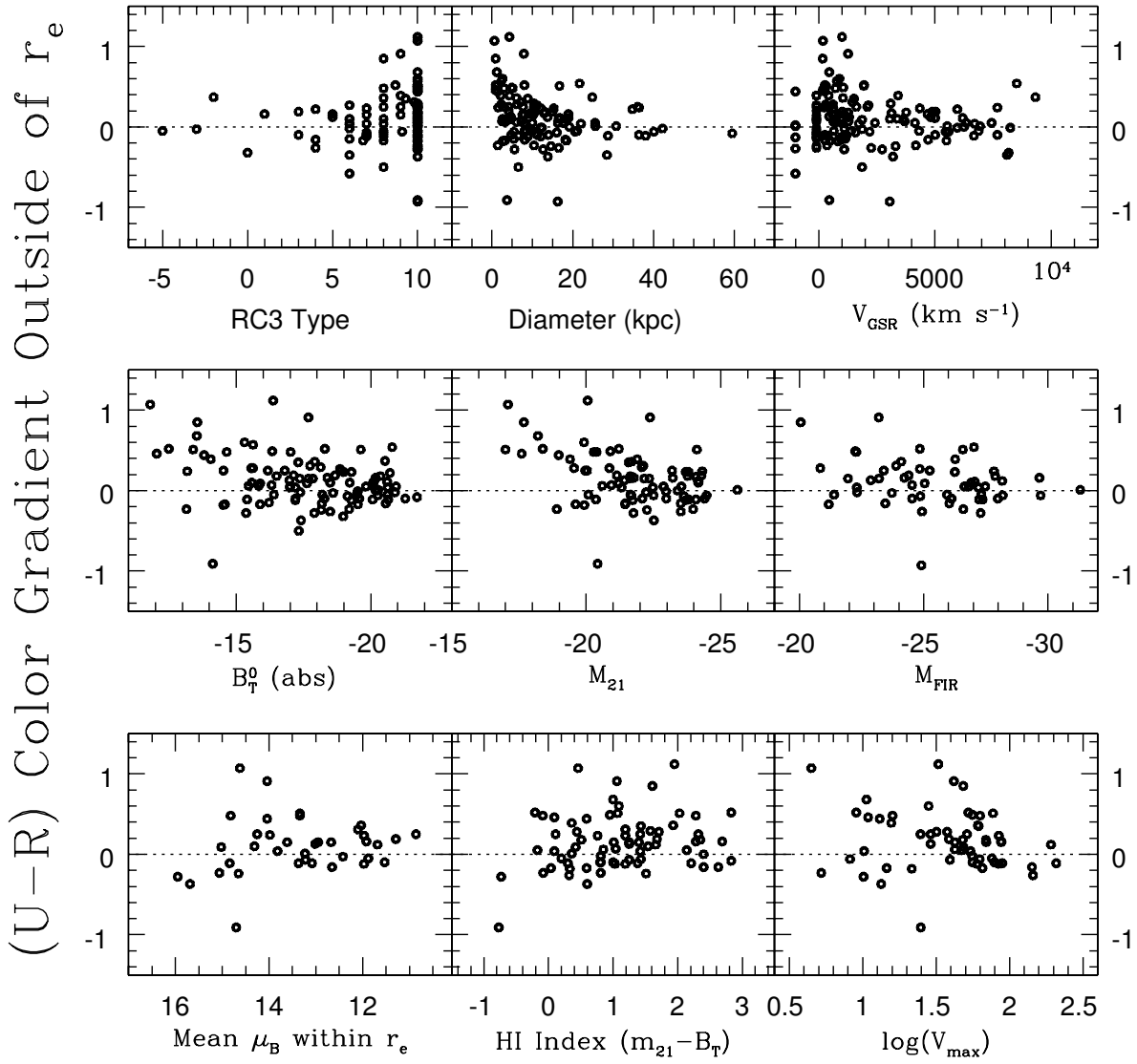

Figure 8 Radial $(U-R)$ color gradient slope vs. (left to right, top to bottom): RC3 Hubble type, major axis diameter in kpc ($H_0 = 71$ km s^{-1} Mpc^{-1} for all calculations), radial velocity with respect to the Galactic standard of rest, extinction corrected total absolute B-magnitude, 21 cm emission line absolute magnitude, far infrared $(60-100\mu$m) absolute magnitude, mean B surface brightness within r_e, HI index = $(M_{21}$–$B_T^0)$, and the log of the maximum rotational velocity in km s^{-1}.

galaxies that are overall intrinsically faint in all bands, which tends to be the case for late-type galaxies, have on average stronger gradients of redder colors with increasing radius, but that these are not necessarily caused by an excess of H I. This coupled with the very weak trend seen in M_{FIR}, suggests that the increasingly redder outer regions of late-type galaxies may not be due to excess dust, but perhaps to other factors such as stellar population gradients. This is in agreement with the conclusions of other authors, who find that the observed color gradients for mid- to late-type galaxies are most likely due to stellar population effects (Vader et al. 1988; de Jong 1996; Jansen et al. 2000; Bell & de Jong 2000; MacArthur et al. 2004). It would be interesting to verify this with a thorough study of the spatial stellar population and dust content of late-type galaxies. There is no strong trend seen with $log(V_{max})$, which is the log of the maximum rotational velocity in km s^{-1} of the galaxy, although this is based on low number statistics due to the absence of this information for most of the galaxies in the RC3. The four galaxies with the largest V_{max}, however, have small color gradient slopes, which is consistent with the most massive galaxies being earlier type galaxies, which have been shown in multiple studies to have small color gradients with bluer regions typically at larger radii (Vader et al. 1988; Franx et al. 1989; Peletier et al. 1990).

These results raise the question of whether the late-type galaxies that get redder with increasing radius actually have redder colors in their outskirts than other galaxies (perhaps due to a particularly old stellar population in the outer disk, or a radially increasing dust content), or whether they simply have uncommonly blue inner regions (perhaps due to younger or more metal poor stars in the inner parts of the galaxy). Figure 9 addresses this with a plot of the $(U-R)$ color profile slope vs. the total integrated $(U-R)$ color inside r_e ("bulge" color), and vs. extrapolated $(U-R)$ color at 2 r_e (outer "disk" color). Different symbols represent different Hubble type bins. The early-type ($T < 3$), mid-type ($3 \leqq T < 7$), and merger/interacting ($T = 14$) galaxies do not show any significant trend in inner or outer color with color slope. Thus, the non-zero color gradients are not simply a mathematical artifact of these galaxies having an overall blue or red color, but are a meaningful measure of a radial gradient in other physical properties of these galaxies. Late Hubble type ($7 \leqq T \leqq 10$) galaxies also show little trend in general, although as these galaxies get redder with increasing radius, they tend to be bluer in their inner regions, *as well as* redder in their outer regions than other galaxies. *This suggests that, for late-type galaxies, most of the galaxies that get redder with radius are actually bluer in their inner regions* and *redder in their outskirts than late-type galaxies that get bluer with radius.* If this is due to stellar population differences (which is the favored explanation of previous studies for color gradients), and not dust or other possible factors, this could be an indicator that late-type galaxies that get redder with increasing radius form from the outside-in, with a relatively high amount of recent star formation in the inner regions (compared to other galaxies), and a relatively low amount of recent star formation in the outer regions.

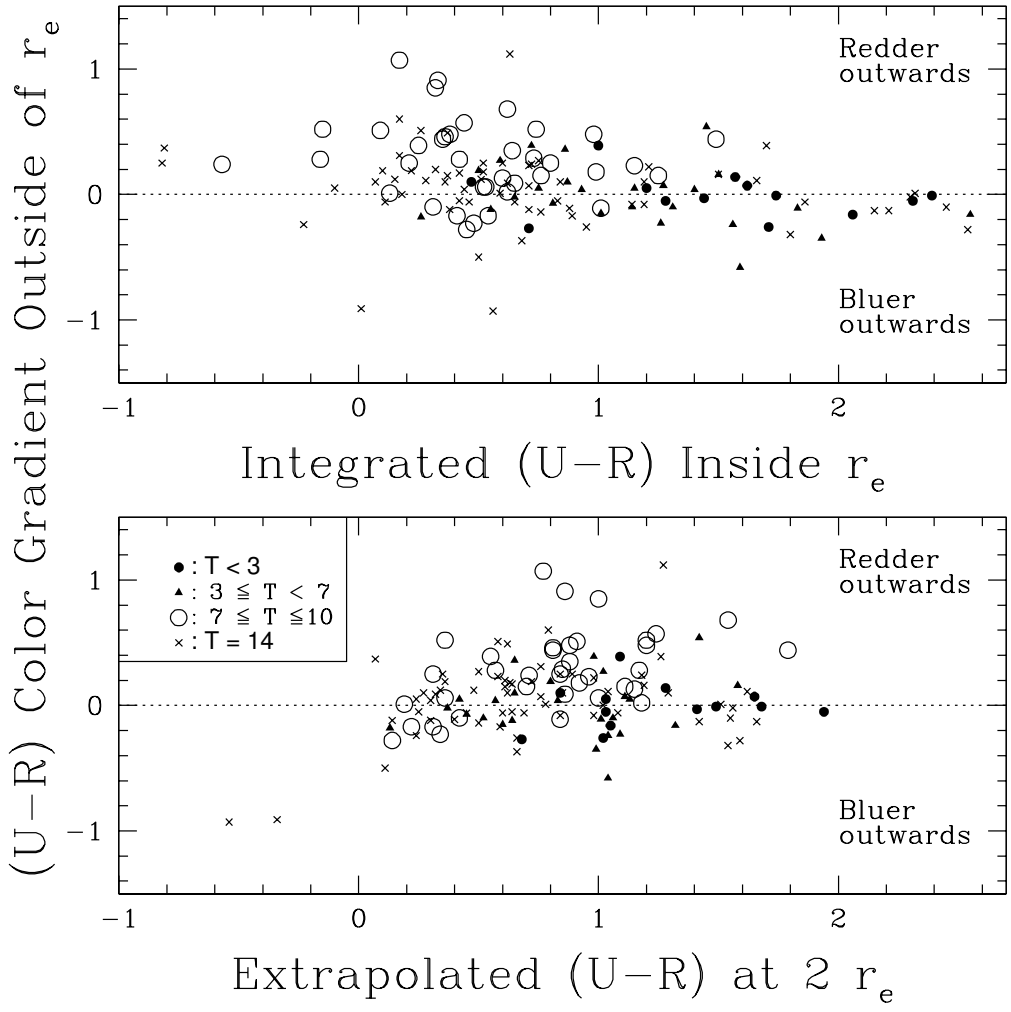

Figure 9 Radial $(U-R)$ outer color gradient slope vs. total inner $(U-R)$ color within r_e (top), and vs. outer disk color at $2r_e$ (bottom). Different type bins are indicated with different symbols. The early-type (T $<$ 3), mid-type (3 $\leqq$ T $<$ 7), and merger/interacting (T = 14) galaxies do not show any significant trend in inner or outer color with color slope. Late Hubble type (7 $\leqq$ T $\leqq$ 10) galaxies also show little trend in general, although as the galaxies get redder with increasing radius, they tend to be somewhat bluer in their inner regions, *and* redder in their outer regions than other galaxies.

2.4.2. HST *Radial Color Gradients*

Figure 10 shows all six *HST* surface brightness and color profiles with images of each galaxy in all three pass-bands. The ellipse on each image marks the outer annulus used for the last point in the profiles. NGC3516 is an early-type galaxy ($T_{RC3}=-2.0$) that becomes slightly bluer with radius in each of the colors (*F300W–F814W*), (*F300W–F160W*), and (*F814W–F160W*). NGC2551, which is also an early-type galaxy ($T_{RC3}= 0.2$), gets significantly bluer with increasing radius in (*F300W–F814W*) and (*F300W–F160W*), but is fairly constant in color with radius in (*F814W–F160W*) (or, at most, gets slightly bluer with radius). NGC1679 ($T_{RC3}= 9.5$) and ESO418-G008 ($T_{RC3}= 8.0$) are late-type galaxies that get slightly bluer with increasing radius in all colors, which is true for half of the late-type galaxies. Of the other two late-type galaxies, NGC6789 is an irregular galaxy ($T_{RC3}= 10$) that gets significantly redder with increasing radius in (*F300W–F814W*) and (*F300W–F160W*), but gets slightly bluer with increasing radius in (*F814W–F160W*). NGC1311 is a late-type magellanic spiral (Sm) galaxy ($T_{RC3}= 9$) that gets redder with increasing radius in (*F300W–F814W*) and (*F300W–F160W*). It is the only one of these six galaxies that gets redder with increasing radius in (*F814W–F160W*).

We plot the color slopes for the six *HST* galaxies vs. RC3 Hubble type in Figure 11. Due to small-number statistics, broad conclusions cannot be confidently drawn from these results, but it is encouraging to note that the (*F300W–F814W*) and (*F300W–F160W*) color gradients show similar trends as those of $(U-R)$ in the VATT data, with earlier galaxy types getting bluer with increasing radius, and later galaxy types becoming either bluer or redder with increasing radius. Five out of the six galaxies get slightly bluer with increasing radius in (*F814W–F160W*). The magnitude of the (*F814W–F160W*) color gradient does not depend on Hubble type, at least for these five galaxies. This may not be a surprising result since the F814W (8002 Å) and F160W (15,500 Å) filters don't sample significantly different portions of galaxy spectra. The only outlier is NGC1311, which becomes significantly redder with increasing radius in (*F814W–F160W*). Comparison of the NGC1311 images to the others reveal no inconsistencies in image quality that might cause this difference.

The F300W filter samples mid-UV light shortward of the atmospheric cut-off and the Balmer break, which contributes to color gradients that are sensitive to the presence of recent star formation. This may indicate that the redder outer parts of later Hubble type galaxies in (*F300W–F814W*) may be primarily due to recent star formation concentrated near the center of these particular galaxy types. This young stellar population may exist amongst an underlying redder, older, population that becomes more dominant toward the center of the galaxy, as evidenced by the bluer (*F814W–F160W*) color with increasing radius for most of the galaxies. The degenerate possibilities of increasing metallicity or dust toward the center of the galaxy may also explain the (*F814W–F160W*) gradients.

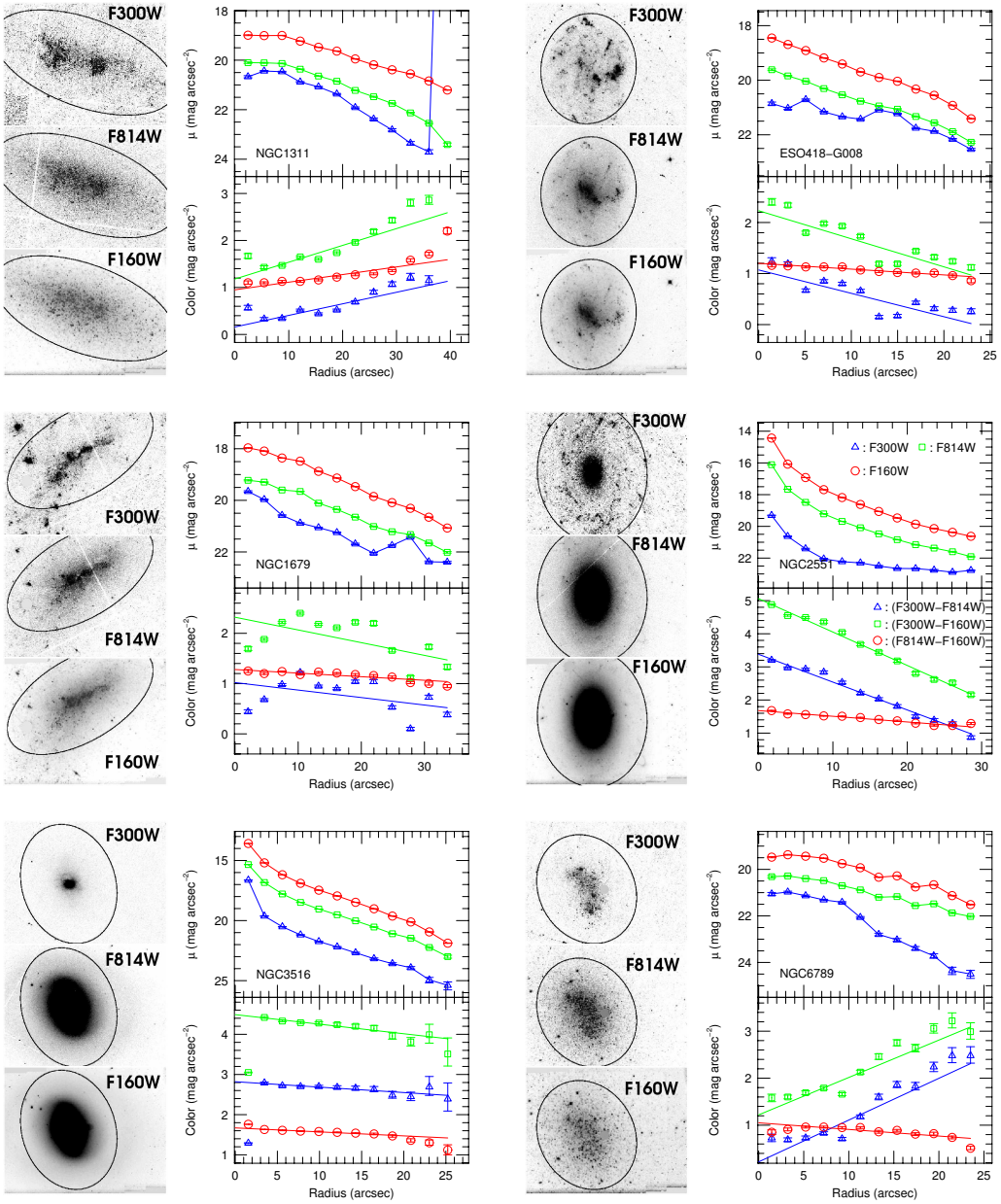

Figure 10 All six *HST* surface brightness (μ) and color profiles with images of each galaxy in all three pass-bands. The ellipse on each image marks the last annulus used in the profile calculation. Note that the images were scaled to highlight interesting galactic structure, such that existing low-surface brightness material may not be visible in these images. The upper right panel for each galaxy is the surface brightness profile, and the lower right panel is the color profile. The key printed in the NGC2551 plots apply to all of the plots. The lines in the color profile plots are the error-weighted linear-least-squares fits to all of the data points.

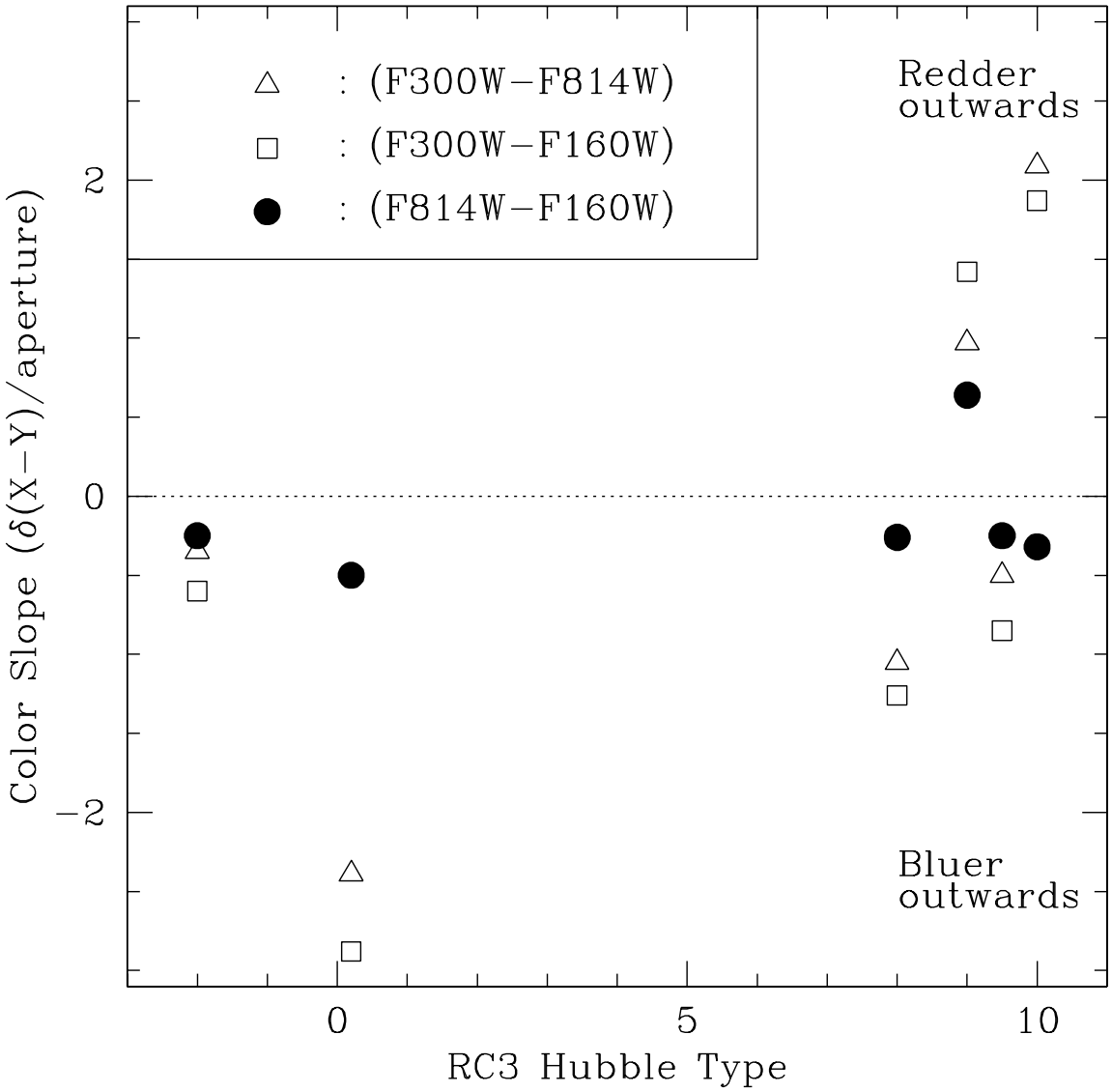

Figure 11 Color gradient vs. RC3 Hubble type for each of our *HST* galaxies. (F300W–F814W) and (F300W–F160W) gradients show a similar trend as the $(U - R)$ gradients in the VATT data, with earlier galaxy types getting bluer with increasing radius and later galaxy types either getting bluer or redder with increasing radius. The (F814W–F160W) colors get slightly bluer with increasing radius for all but one galaxy (NGC1311). For those galaxies that get bluer with radius in (F814W–F160W), the (F814W–F160W) gradients are roughly constant with Hubble type. Errors from the linear-least squares fit on the color slopes are comparable to the size of the symbols in this plot.

2.5. Discussion

The bottom-up hierarchical structure formation model suggests that galaxies as they exist today were formed by the initial collapse of small mass fluctuations in the early Universe, and the subsequent merging of these small systems into larger ones (e.g., White 1979; White & Frenk 1991; Cole et al. 1994; Kauffmann et al. 1997; Roukema et al. 1997; Baugh et al. 1998). In this formation model, galaxy mergers and interactions would be common factors in galaxy evolution. Mergers and interactions have been shown to trigger starbursts (e.g., Mihos & Hernquist 1994, 1996; Hernquist & Mihos 1995; Barnes & Hernquist 1996; Somerville et al. 2001), which affect the radial color gradients of the galaxies. Starbursts can also be caused by bar instabilities (e.g., Noguchi 1988; Shlosman et al. 1989, 1990; Mihos & Hernquist 1994; Friedli & Benz 1993, 1995) or triggered by superwind shocks created by a combination of supernovae and winds from massive stars (e.g., De Young 1978; Dekel & Silk 1986; Mathews 1989; Heckman et al. 1990), but at high redshift, galaxy mergers and interactions should be the most common cause. In this case, mergers and interactions would funnel gas to the central regions of the galaxy and trigger nuclear starbursts. In the simplest picture, this would result in galaxies that recently underwent a merger or strong interaction becoming redder outward (Moth & Elston 2002). Many gas-rich interacting galaxies, however, show significant star formation in their outer parts, where tidal disturbances can trigger star formation. Dust in the interiors of these galaxies may also redden their colors. Thus, given the complexities of galaxy interactions and the large range in properties of the galaxies involved in such interactions, some galaxies that recently underwent an interaction will become redder while others will become bluer with increasing radius — consistent with our results.

If this overall picture of galaxy assembly is correct, then galaxies that more recently underwent a hierarchical merger or accretion event would be *more likely* to become redder than to become bluer with increasing radius than galaxies that have remained unperturbed and are substantially more relaxed today. Because the merger rate at high redshift is higher, higher redshift galaxies would on average be redder with increasing radius than lower redshift galaxies, and nearby low-mass, low-luminosity, late-type and interacting galaxies would on average be redder with increasing radius than their high-mass, high-luminosity, early-type counterparts that formed predominantly at higher redshift. This scenario can therefore be tested by examining how color gradients depend on galaxy type, luminosity, and redshift.

The process of galaxy formation may be more complicated, depending in part on the galaxy's type, luminosity, and mass, and on its surrounding environment, as discussed by Tamura & Ohta (2003), who determined that elliptical galaxies in rich galaxy clusters get bluer with increasing radius, and that larger and more luminous galaxies have steeper color gradients. These trends are consistent with models for formation through monolithic collapse (Eggen et al. 1962; Larson 1974; Carlberg 1984). In field E/SO galaxies, there is no such strong trend of color gradient with galaxy luminosity and size, which suggests that early-type galaxies in less-dense environments may form instead through hierarchical

merging. Balcells & Peletier (1994) discuss the implications of early-type spiral galaxy bulge luminosity on the galaxy's formation process. They find that bright bulges show a steeper color gradient with increasing bulge luminosity, while faint bulges become significantly bluer outward, and show no such color gradient relation with luminosity. This suggests that the brighter, more massive bulges in early-type spiral galaxies may have formed through dissipative collapse, with the presence of the disk having little effect on the the bulge's formation. Fainter, less massive bulges, however, would have a different formation mechanism due to interactions with the disk (e.g. Kannappan et al. 2004).

Although the formation and evolution of specific galaxies may depend on various factors, our general results are consistent with the predictions of bottom-up hierarchical galaxy formation, where our more relaxed high-mass, high-luminosity, early- to mid-type galaxies become either bluer with increasing radius or have no color gradient, and our low-mass, low-luminosity late-type galaxies tend to be redder on average with increasing radius. This is in agreement with trends seen in the high redshift Universe in the Hubble Deep Field North by Moth & Elston (2002), who found that galaxies at intermediate redshifts (z = 0.5–1.2) tend to on average get bluer with increasing radius, while high redshift galaxies (z = 2–3.5), which are expected to be experiencing more interactions and mergers, get on average redder with increasing radius. Moth et al. (2002) determined that dust is unable to account for the strongly bluer central regions at high redshifts, and that it must therefore be due to more centrally concentrated star formation. They argue that this can be explained by hierarchical galaxy formation models, which predict that mergers and interactions are important in galaxy evolution, and more important at higher redshift. The resemblance of the color gradient trends in high redshift galaxies to those of our late-type galaxies would be consistent with the apparent similarity in morphology between high redshift galaxies and nearby irregular and peculiar galaxies. Therefore, the galaxies that most recently underwent mergers at both high and low redshift are the most likely ones to have color gradients that get significantly redder outwards, reflecting this merger.

CHAPTER 3

DEPENDENCE OF ASYMMETRY, CONCENTRATION, AND CLUMPINESS INDICES ON REST-FRAME WAVELENGTH AND GALAXY TYPE

3.1. Overview of Chapter 3

In this chapter we investigate the dependence of galaxy structure on galaxy type and color through measurements of the asymmetry, concentration, and clumpiness indices of all 199 galaxies that we observed at the VATT and with HST and GALEX in various combinations of filters from the far-UV through the near-IR. We confirm the results of previous studies on normal galaxies, and add our results for the peculiar and merger galaxies in our sample. We break the peculiar/merging galaxies into sub-classes that we use to investigate how the CAS parameters change as a merger progresses from the pre-merger through the merger remnant stages.

With this dataset, we also investigate how these structural parameters vary with rest-frame wavelength, which gives a measure of the morphological k-correction. The morphological k-correction can be used to better interpret the galaxy structure seen at high redshift in the rest-frame UV. We find almost no morphological k-correction for early-type (E–S0) galaxies at wavelengths longward of the Balmer break. We do, however, find a significant morphological k-correction for later-type galaxies, which we quantify with a difference in the CAS parameters as a function of rest-frame wavelength between the UV and the red.

We describe the observations in Section 2 and the data reduction in Section 3. In Section 4 we present the data analysis, explaining our galaxy classification system and how the CAS parameters were measured. We also investigate how resolution affects these parameters and make the appropriate corrections to the data. In Section 5 we present our results, including an analysis of the dependence of the CAS parameters on galaxy color and type, the distribution of galaxies within the CAS parameter space, and the rest-frame wavelength dependence of the CAS parameters.

3.2. Observations

As described in detail in Chapter 2.2.1, we selected a sample of 199 nearby galaxies that consists mostly of late-type spiral, irregular, and peculiar/merging galaxies. These late-types are among the galaxies at z $\sim$ 0 that most resemble the majority of high redshift galaxies, and are less studied and less well-understood than nearby earlier-type galaxies. Also, Jansen (2000) found that most of the wavelength dependence of the asymmetry is due to galaxies of type Sbc and later (T $\gtrsim$ 4). Thus, most of the difference in asymmetries between the U and R-band occurs for later morphological Hubble types. As such, late-type galaxies are more suited for this analysis than early-type galaxies.

Of the 199 galaxies in our sample, 143 (including CGCG97-114, which was not included in the analysis in Chapter 2) were observed with the Vatican Advanced Technology Telescope (VATT) in $UBVR$ (λ_c = 3597, 4359, 5395, and 6338$\AA$, respectively). A total of 90 galaxies were observed with HST WFPC2 in the UV (F300W, λ_c = 2930Å), 34 of which also have VATT data. Of these 90 galaxies observed with HST, 37 were observed in our Cycle 9 GO program #8645 (Windhorst et al. 2002), and 53 were observed in our Cycle 10 SNAPshot program #9124 (P.I.: R. Windhorst; Jansen et al. 2006, in preparation). During these programs, a subset of 11 galaxies were also imaged with a shorter wavelength UV filter (F255W, λ_c = 2550Å), and 60 were observed in the red (F814W, λ_c = 8230Å). These observations are explained in greater detail in Chapter 2.2.2. At the time the present analysis was completed, 13 of the galaxies in our sample had deep ($t_{exp} \gtrsim$ 670 s) GALEX mid-UV (NUV, λ_c = 2275Å) and far-UV (FUV, λ_c = 1550Å) imaging available; a 14th galaxy, NGC0569, was observed only in the NUV filter. Of these, 4 were observed with our GALEX Cycle 1 SNAP program #036, and 10 were obtained from the archived Nearby Galaxies Survey (NGS), Medium Imaging Survey (MIS), and Deep Imaging Survey (DIS). Seven of the 14 galaxies observed with GALEX also have VATT data, and 10 also have HST data. Three of these galaxies have data from all of these telescopes (VATT, HST, and GALEX).

In Table 5 we identify the galaxies in this extended sample, and list their relevant global properties. Column (1) lists the galaxy identification numbers as used throughout this chapter, while column (2) gives the common catalog names, and columns (3) and (4) contain the equatorial coordinates (J2000.0). Column (6) lists the total $(B-V)$ color as measured for the galaxies for which we have B and V images, or from the RC3 (de Vaucouleurs et al. 1991) otherwise. All recessional velocities with respect to the Galactic Standard of Rest (V_{GSR}; column 7) are from the RC3. In column (8), we identified the edge-on spiral galaxies in our sample. The numeric types adopted throughout the present chapter are listed in column (5), and were assigned as described in Section 3.1. Figure 12 shows the distribution of morphological types within our sample. Note the deliberate emphasis on late-type galaxies for the purposes of high redshift comparison.

Table 5. Observed Galaxy List.

ID#	Galaxy	RA	DEC	Type	B-V	V_{GSR}	comment
001	UGC00006	00:03:09.46	+21:57:37.6	15.0	0.370	6763	···
002	NGC0014	00:08:46.32	+15:48:56.4	10.0	0.580	1012	···
003	UGC00156	00:16:46.30	+12:21:13.1	9.3	0.576	1267	···
004	NGC0178	00:39:08.25	-14:10:20.7	9.5	0.470	1496	···
005	UGC00404	00:39:19.17	+13:06:40.3	13.0	0.362	10742	···
006	Mrk960	00:48:35.44	-12:42:59.9	8.0	···	6447	···
007	UGC00512	00:50:02.59	+07:54:55.3	15.0	-0.004	5496	···
008	UGC00644	01:03:16.65	+14:02:01.6	13.0	0.662	···	···
009	UGC00685	01:07:22.29	+16:41:04.1	10.0	···	271	···
010	UGC00749	01:11:30.28	+01:19:10.9	14.5	0.653	6882	···
011	NGC0428	01:12:55.62	+00:58:52.2	9.0	0.440	1231	···
012	UGC00849	01:19:23.03	+12:26:57.4	14.5	0.572	14410	···
013	NGC0569	01:29:07.16	+11:07:53.3	13.0	···	5862	···
014	UGC01104	01:32:43.47	+18:19:01.4	10.0	0.533	775	···
015	UGC01133	01:35:00.85	+04:23:11.8	15.0	0.077	2031	···
016	NGC0625	01:35:05.12	-41:26:08.9	10.0	0.560	312	···
017	UGC01219	01:44:20.13	+17:28:42.9	3.0	0.709	4708	···
018	UGC01240	01:46:19.56	+04:15:52.5	15.0	0.401	1862	···
019	UGC01449	01:58:04.15	+03:05:57.2	14.0	0.487	5590	···
020	UGC01753	02:16:34.98	+28:12:16.1	8.7	0.559	3098	···
021	NGC0959	02:32:23.45	+35:29:20.1	7.0	0.588	715	···
022	NGC1140	02:54:33.43	-10:01:42.4	15.0	0.350	1479	···
023	NGC1156	02:59:41.41	+25:13:37.5	10.0	0.618	452	···
024	NGC1311	03:20:06.66	-52:11:12.5	10.0	0.460	331	···
025	ESO418-G008	03:31:30.58	-30:12:46.6	8.0	0.410	1146	···
026	ESO418-G009	03:31:55.88	-31:20:21.0	10.0	···	862	···
027	NGC1396	03:38:06.63	-35:26:24.5	-3.0	···	771	···
028	NGC1510	04:03:32.55	-43:24:03.0	10.0	0.450	838	···
029	NGC1602	04:27:54.42	-55:03:24.5	13.0	0.350	1402	···
030	NGC1614	04:33:59.20	-08:35:56.3	14.5	0.637	4681	···
031	NGC1679	04:49:55.31	-31:58:05.5	9.5	···	904	···
032	NGC1741	05:01:37.59	-04:15:40.2	14.0	···	3956	···

Table 5—Continued

ID#	Galaxy	RA	DEC	Type	B-V	V_{GSR}	comment
033	NGC1800	05:06:26.07	-31:57:14.0	10.0	0.540	637	···
034	ESO033-G022	05:31:41.58	-73:45:04.2	7.0	···	4376	edge-on
035	IC2129-30	05:31:50.32	-23:08:47.6	8.0	···	1671	···
036	UGC03426	06:15:36.33	+71:02:13.8	-2.0	1.060	4124	···
037	UGC03690	07:09:10.37	+53:24:59.8	10.0	0.547	3200	···
038	UGC03748	07:15:26.12	+65:26:18.7	15.0	0.524	···	···
039	UGC03860	07:28:19.58	+40:46:22.6	10.0	0.458	356	···
040	Mrk8	07:29:25.31	+72:07:39.8	14.0	···	3712	···
041	NGC2415	07:36:45.09	+35:14:38.7	13.0	0.413	3764	···
042	UGC04079	07:55:07.13	+55:42:31.6	13.5	0.535	6195	···
043	UGC04095	07:56:50.08	+66:36:24.5	6.0	0.714	4178	···
044	UGC04098	07:57:18.19	+66:26:09.2	3.3	0.580	5010	···
045	UGC04182	08:03:47.95	+61:20:11.5	15.0	0.482	···	···
046	UGC04261	08:11:01.71	+36:50:42.2	14.5	0.407	6347	···
047	NGC2551	08:24:50.16	+73:24:43.0	1.0	0.990	2384	···
048	UGC04434	08:28:54.30	+34:39:04.9	14.5	0.530	6256	···
049	UGC04438	08:29:58.87	+52:41:51.3	2.3	0.582	4322	···
050	UGC04459	08:34:07.45	+66:10:16.7	10.0	0.329	114	···
051	UGC04483	08:37:09.12	+69:47:29.9	10.0	0.199	···	···
052	NGC2623	08:38:26.40	+25:44:24.0	14.5	0.750	5464	···
053	UGC04564	08:45:20.48	+55:06:35.3	13.5	0.844	···	···
054	UGC04671	08:56:41.58	+52:06:11.8	3.0	0.573	4138	···
055	UGC04687	08:58:50.83	+66:27:33.9	-2.0	0.865	3694	···
056	NGC2719	09:00:19.51	+35:43:59.5	13.0	0.414	3135	···
057	UGC04722	09:00:21.87	+25:37:32.1	14.5	0.340	1728	···
058	UGC04739	09:03:47.80	+69:29:08.1	6.0	0.573	···	···
059	NGC2742A	09:09:56.11	+62:14:18.7	3.5	0.751	7682	···
060	NGC2785	09:15:14.37	+40:54:50.4	15.0	0.969	2732	···
061	UGC04879	09:16:00.23	+52:50:28.6	10.0	0.583	643	···
062	UGC04998	09:25:07.47	+68:23:05.8	8.7	0.623	···	···
063	UGC05028	09:27:56.94	+68:24:56.9	9.0	···	3801	···
064	UGC05101	09:35:55.74	+61:21:24.8	14.5	0.795	12022	···

Table 5—Continued

ID#	Galaxy	RA	DEC	Type	B-V	V_{GSR}	comment
065	NGC2922	09:36:50.75	+37:41:33.5	7.3	0.514	4350	···
066	UGC05119	09:37:14.23	+38:05:26.9	-2.0	0.911	5968	···
067	UGC05189	09:42:56.73	+09:28:26.3	14.5	0.385	3058	···
068	NGC2909	09:44:06.19	+65:58:27.5	4.3	0.503	···	···
069	UGC05272	09:50:20.20	+31:29:29.5	10.0	0.404	480	···
070	UGC05288	09:51:16.87	+07:49:41.5	9.0	···	429	···
071	UGC05340	09:56:47.11	+28:49:19.4	15.0	0.192	454	···
072	NGC3079	10:01:58.00	+55:39:26.1	6.3	0.712	1182	···
073	NGC3104	10:03:56.94	+40:44:58.3	9.0	0.383	612	···
074	UGC05423	10:05:35.79	+70:21:20.1	10.0	0.613	454	···
075	UGC05485	10:11:20.65	+65:16:48.5	15.0	0.548	···	···
076	UGC05626	10:24:24.19	+57:22:59.1	7.0	0.296	···	···
077	NGC3239	10:25:04.76	+17:08:58.3	14.5	0.393	666	···
078	NGC3256	10:27:51.24	-43:54:14.8	14.5	0.640	2558	···
079	NGC3274	10:32:17.03	+27:39:58.0	7.7	0.384	491	···
080	NGC3264	10:32:23.77	+56:04:43.3	6.7	0.516	1005	···
081	NGC3310	10:38:45.99	+53:30:10.1	4.0	0.350	1043	···
082	UGC05846	10:44:26.24	+60:22:06.3	9.7	0.529	1100	···
083	NGC3353	10:45:22.53	+55:57:32.9	14.5	0.319	1009	···
084	UGC05883	10:47:15.41	+54:02:11.1	6.7	0.354	825	···
085	UGC05989	10:52:30.00	+19:48:00.1	15.0	0.438	1056	···
086	NGC3432	10:52:31.11	+36:37:09.5	9.0	0.420	609	···
087	NGC3445	10:54:41.17	+56:59:33.2	13.5	0.371	2092	···
088	MCG6-24-47	11:05:09.97	+38:03:57.0	6.0	0.793	···	···
089	NGC3516	11:06:47.48	+72:34:06.7	-2.0	0.810	2749	···
090	NGC3543	11:10:58.26	+61:21:21.3	9.0	0.718	···	···
091	UGC06249	11:13:18.57	+59:55:02.0	3.3	0.492	1142	···
092	UGC06258	11:13:47.03	+21:31:31.4	15.0	0.461	1398	···
093	UGC06315	11:18:15.59	+53:45:37.2	2.7	0.618	···	···
094	NGC3664	11:24:23.90	+03:18:49.5	9.0	0.346	1267	···
095	UGC06447	11:26:42.47	+59:09:26.3	15.0	0.611	1284	···
096	UGC06471-2	11:28:31.49	+58:33:45.9	14.0	···	3215	···

Table 5—Continued

ID#	Galaxy	RA	DEC	Type	B-V	V_{GSR}	comment
097	UGC06527	11:32:37.59	+52:56:53.4	14.0	0.935	8180	···
098	ESO503-G022	11:33:29.58	-26:56:50.7	10.0	···	1726	···
099	UGC06541	11:33:37.56	+49:14:33.2	10.0	0.449	302	···
100	NGC3729	11:33:48.69	+53:07:12.9	3.3	0.791	1089	···
101	NGC3738	11:35:50.46	+54:30:53.9	10.0	0.424	299	···
102	NGC3741	11:36:06.39	+45:16:59.5	10.0	0.379	249	···
103	UGC06697	11:43:46.78	+19:58:20.9	15.0	0.454	6678	edge-on
104	MCG3-30-71	11:44:03.76	+19:47:06.0	3.3	0.457	4886	···
105	NGC3846A	11:44:21.21	+55:02:40.7	8.0	0.499	1518	···
106	CGCG97-114	11:44:47.51	+19:46:42.3	9.0	0.520	8470	···
107	NGC3860	11:44:49.20	+19:47:42.0	2.7	0.800	5540	···
108	ESO504-G017	11:48:46.36	-27:22:47.5	8.0	···	1886	···
109	NGC3913	11:50:38.96	+55:20:47.0	3.3	0.505	1032	···
110	UGC06816	11:50:46.86	+56:27:59.3	8.0	0.319	970	···
111	NGC3921	11:51:06.78	+55:04:44.4	15.0	0.680	5930	···
112	NGC3952	11:53:39.20	-04:00:40.6	15.0	0.374	1453	···
113	UGC07019	12:02:31.22	+62:25:04.0	7.3	0.514	1616	···
114	NGC4068	12:04:02.40	+52:34:55.2	10.0	0.418	283	···
115	NGC4234	12:17:07.78	+03:40:35.6	7.3	0.514	1946	···
116	UGC07321	12:17:34.80	+22:32:51.2	7.0	0.560	384	edge-on
117	NGC4278	12:20:06.85	+29:16:18.6	-5.0	0.949	647	···
118	NGC4299	12:21:41.87	+11:29:29.7	8.0	0.412	171	···
119	UGC07577	12:27:40.11	+43:29:55.6	10.0	0.500	246	···
120	NGC4449	12:28:15.67	+44:06:15.5	8.0	0.383	255	···
121	NGC4476	12:29:59.71	+12:20:48.3	-1.0	0.765	1873	···
122	NGC4478	12:30:17.33	+12:19:41.7	-5.0	0.910	1329	···
123	NGC4490	12:30:31.71	+41:38:26.4	15.0	0.459	625	···
124	NGC4485	12:30:35.45	+41:39:56.4	13.0	0.369	542	···
125	NGC4519	12:33:30.36	+08:39:26.4	5.0	0.481	1157	···
126	NGC4532	12:34:19.39	+06:28:39.7	10.0	0.364	1938	···
127	UGC07816	12:38:55.49	+38:05:53.4	14.5	0.421	···	···
128	NGC4618	12:41:32.00	+41:08:59.1	7.7	0.475	592	···

Table 5—Continued

ID#	Galaxy	RA	DEC	Type	B-V	V_{GSR}	comment
129	IC3687	12:42:14.62	+38:29:57.5	8.3	0.355	399	···
130	NGC4644	12:42:50.43	+55:08:34.7	13.0	0.837	4856	···
131	NGC4639	12:42:53.15	+13:15:17.7	2.7	0.713	963	···
132	UGC07905	12:43:51.12	+54:54:13.6	13.0	0.588	5026	···
133	UGC08091	12:58:41.78	+14:12:58.6	10.0	0.327	183	···
134	UGC08096	12:58:52.29	+27:49:21.6	3.0	0.840	7460	edge-on
135	UGC08107	12:59:39.06	+53:20:27.3	15.0	0.681	···	···
136	UGC08201	13:06:27.32	+67:42:45.6	10.0	0.357	169	···
137	UGC08320	13:14:27.47	+45:55:36.3	10.0	0.415	272	···
138	UGC08323	13:14:49.73	+34:52:52.6	15.0	0.463	893	···
139	UGC08335	13:15:32.91	+62:07:36.6	14.0	···	9364	···
140	Mrk66	13:25:53.68	+57:15:16.4	10.0	0.020	6638	···
141	NGC5147	13:26:18.62	+02:05:09.5	6.3	0.450	1044	···
142	UGC08508	13:30:42.31	+54:55:03.7	8.3	0.455	171	···
143	UGC08507	13:31:00.05	+19:27:30.4	10.0	0.501	1004	···
144	UGCA363	13:33:37.21	+60:23:40.8	15.0	-0.178	2190	···
145	NGC5257	13:39:52.30	+00:50:22.0	13.0	0.490	6758	···
146	NGC5253	13:39:54.84	-31:38:34.7	10.0	0.497	271	···
147	NGC5258	13:39:57.70	+00:49:51.0	13.0	0.600	6719	···
148	NGC5278-9	13:41:39.96	+55:40:12.4	13.5	···	7656	···
149	UGC08696	13:44:42.29	+55:53:11.1	14.5	···	11390	···
150	UGC08708	13:46:51.33	+07:24:05.4	14.5	0.480	6946	···
151	UGC08823	13:53:11.38	+69:18:11.9	13.0	0.491	9323	···
152	HolmbergIV	13:54:44.34	+53:53:55.3	10.0	0.446	259	···
153	NGC5372	13:54:45.08	+58:39:11.0	9.0	0.525	1863	···
154	UGC08837	13:54:45.89	+53:54:16.9	9.5	0.430	259	···
155	UGC08849	13:56:01.41	+17:30:22.1	14.5	0.613	···	···
156	PGC049633	13:57:09.86	+34:31:44.9	3.0	0.736	···	···
157	NGC5477	14:05:33.27	+54:28:00.0	9.0	0.393	425	···
158	ESO446-G044	14:17:49.66	-31:21:04.8	6.7	0.785	···	edge-on
159	NGC5591	14:22:33.53	+13:43:22.1	14.0	0.569	7688	···
160	NGC5608	14:23:18.73	+41:47:00.3	9.0	0.360	762	···

Table 5—Continued

ID#	Galaxy	RA	DEC	Type	B-V	V_{GSR}	comment
161	UGC09240	14:24:49.88	+44:32:08.8	10.0	0.457	259	···
162	NGC5667	14:30:18.74	+59:29:09.4	5.0	0.416	2141	···
163	NGC5668	14:33:26.64	+04:26:23.0	4.0	0.436	1581	···
164	Arp261	14:49:30.58	-10:10:23.9	14.0	0.550	1846	···
165	UGC09638	14:58:03.21	+58:52:51.5	6.0	0.415	2419	···
166	UGC09855	15:25:00.32	+66:14:21.3	15.0	0.300	3644	···
167	UGC09899	15:31:56.35	+68:14:24.1	3.7	0.404	6709	···
168	UGC09913	15:34:56.32	+23:29:33.8	14.5	0.824	5531	···
169	NGC5994-6	15:46:58.09	+17:54:42.2	15.0	0.419	3375	···
170	UGC10043	15:48:41.79	+21:51:31.9	2.3	0.734	2254	edge-on
171	UGC10061	15:51:15.74	+16:21:16.9	10.0	0.303	2171	···
172	NGC6052	16:05:11.54	+20:32:05.9	14.5	0.417	4820	···
173	UGC10279	16:11:51.93	+60:34:40.2	14.0	0.388	···	···
174	UGC10315	16:15:42.63	+68:22:56.2	2.0	0.553	7435	···
175	NGC6104	16:16:29.13	+35:42:51.9	3.3	0.711	8526	···
176	UGC10334	16:17:13.68	+63:51:09.6	15.0	1.325	3307	···
177	UGC10351	16:21:28.16	+28:38:17.5	8.0	0.509	1025	···
178	UGC10445	16:33:48.35	+28:58:52.1	4.0	0.396	1102	···
179	NGC6202	16:43:22.31	+61:58:15.2	2.0	0.755	···	···
180	NGC6238	16:47:12.46	+62:08:41.4	15.0	0.317	···	···
181	UGC10670	17:01:26.92	+63:42:14.7	3.3	0.560	···	···
182	UGC10770	17:13:08.44	+59:20:19.9	14.5	0.367	1301	···
183	NGC6365A	17:22:45.63	+62:09:23.4	3.7	0.619	8100	···
184	IC4662	17:47:08.79	-64:38:30.9	10.0	0.410	198	···
185	NGC6690	18:34:45.88	+70:31:06.9	7.3	0.637	693	···
186	NGC6753	19:11:23.75	-57:02:57.7	3.0	0.830	3073	···
187	NGC6789	19:16:40.89	+63:58:05.6	10.0	0.543	···	···
188	NGC6782	19:23:57.96	-59:55:21.6	1.0	0.920	3815	···
189	NGC7252	22:20:44.66	-24:40:39.2	15.0	0.660	4820	···
190	NGC7320	22:36:01.57	+33:57:32.8	13.0	0.622	990	···
191	NGC7465	23:02:00.90	+15:57:53.6	15.0	0.750	2135	···
192	NGC7468	23:02:59.20	+16:36:19.0	10.0	0.460	2271	···

Table 5—Continued

ID#	Galaxy	RA	DEC	Type	B-V	V_{GSR}	comment
193	UGC12638	23:30:33.40	+03:54:04.0	5.0	0.660	5775	···
194	NGC7714	23:36:13.99	+02:09:19.9	13.0	0.520	2925	···
195	NGC7713	23:36:15.45	-37:56:14.0	7.0	0.320	677	···
196	NGC7732	23:41:33.03	+03:43:26.7	13.0	0.479	3059	···
197	Arp295A	23:41:47.29	-03:40:02.0	5.0	0.930	6954	edge-on
198	ESO471-G006	23:43:45.82	-31:57:31.3	8.0	0.450	275	edge-on
199	UGC12808	23:51:03.90	+20:09:01.0	3.0	···	4380	···

Note. — **Columns:** (1) ID number assigned to this galaxy, (2) galaxy name, (3) Right Ascension (J2000), (4) Declination (J2000), (5) classification (de Vaucouleurs numerical types were used for normal galaxies, with the following types assigned to peculiar/merging galaxies: 13.0=pre-merger, 13.5=minor merger,14.0=major merger,14.5=merger remnant, 15.0=peculiar), (6) total $(B-V)$ color (mag), (7) Galactic standard of rest velocity (km s^{-1}, and (8) special comment for this galaxy. "Edge-on" galaxies appear to be edge-on spiral galaxies.

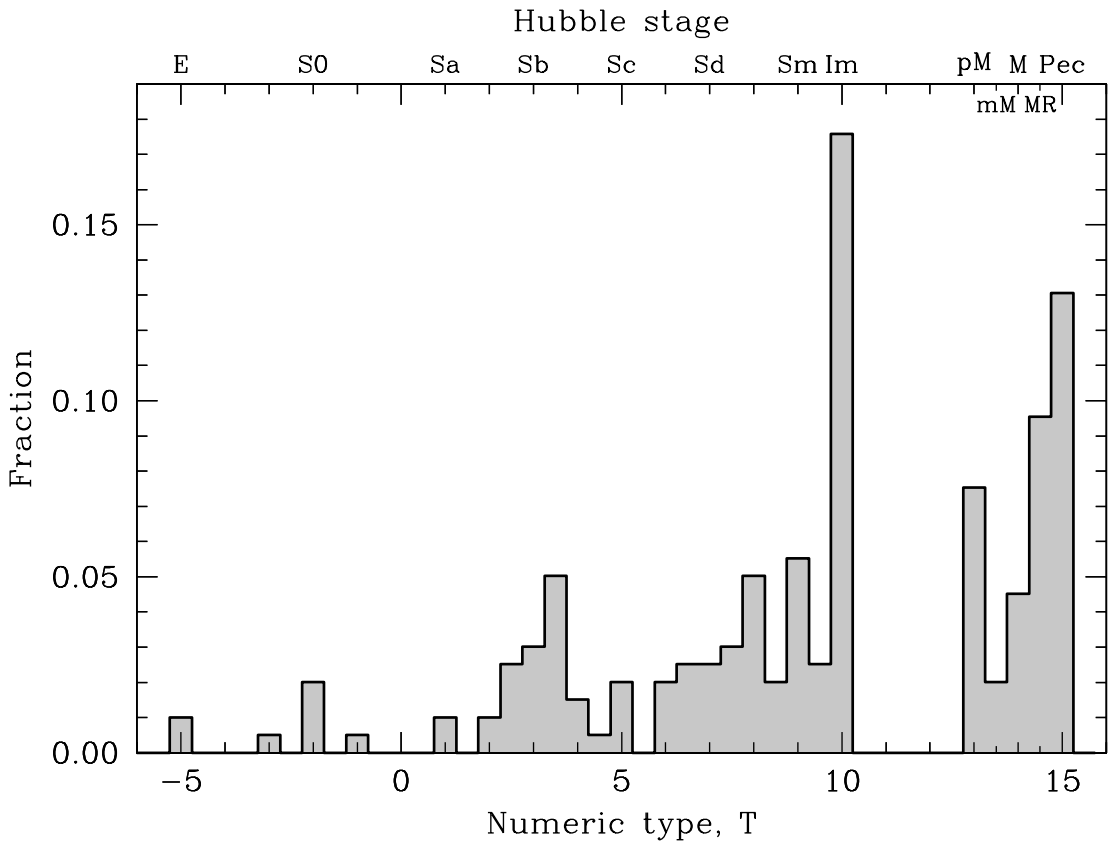

Figure 12 Distribution of types within the present sample of nearby galaxies. Since the vast majority of galaxies observed at high redshift display morphologies resembling those of nearby late-type spiral, irregular, and peculiar/merging galaxies, our sample is heavily weighted toward such galaxy types. The subdivision of types later than 11 is discussed in the text.

3.3. Data Reduction

The $UBVR$ CCD images obtained at the VATT were reduced and calibrated as described in Chapter 2.2.3. For the data analysis in Chapter 2, all of the non-target objects in the images were replaced with a constant local sky-level. This was suitable for computing radial profiles of surface brightness and color, which are not sensitive to structure on small scales within a galaxy. However, the deviations from the true underlying galaxy light distribution at the locations of non-target objects, as replaced with the local sky-level, are larger than is acceptable for CAS measurements, which are particularly sensitive to high frequency structure within the galaxy. Therefore, in these cases we applied a more sophisticated means of removing the non-target objects, interpolating from adjacent pixels with valid data over these masked pixels along both vertical and horizontal directions (implemented by R. Jansen as task `IMCLEAN` within IRAF[1]). This routine preserves the surrounding sky properties as much as possible inside the interpolated region.

We obtained stacked images for most of our HST Cycle 9 galaxies as type B associations from the Space Telescope Science Institute (STSCI) data archive.[2] Seven of the Cycle 9 images do not have associations available for at least one of the filters. These individual images were thus combined and cosmic-ray rejected using an IDL routine developed by Cohen et al. (2003). The HST Cycle 10 images were combined using an IRAF task developed by R. Jansen that rejects bad pixels based on the noise characteristics of the images (Jansen et al. 2006, in preparation). For each galaxy, the stacked images for the individual WFPC2 CCD's were then mosaiced using `WMOSAIC` within the `STSDAS` package in IRAF. Non-target objects were interpolated-over with `IMCLEAN`.

We retrieved pipe-line processed images of each of the sample galaxies observed by GALEX through the STSCI data archive. Since GALEX has a field-of-view of 1.2°, and most of our galaxies are only around $1'$ in size, we cut 512×512 pixel stamps centered on our target galaxy for use in the data analysis. This corresponds to an image size of about $12'$, which is sufficient for viewing the entire galaxy and measuring the sky from surrounding regions that are far enough away from the galaxy that they are uncontaminated by its light. Non-target objects were interpolated-over with `IMCLEAN`, as before.

3.4. Data Analysis

3.4.1. *Visual Classifications*

We assigned visual types to these galaxies using the average of three experienced classifiers to classify the galaxies observed with the VATT (as described in Chapter 2.2.1, only with peculiar/merging galaxies split up into separate sub-classes), and the average of two experienced classifiers (V. Taylor, and C. Conselice) for the galaxies observed with

[1]IRAF is distributed by the National Optical Astronomy Observatories, which are operated by the Association of Universities for Research in Astronomy, Inc., under cooperative agreement with the National Science Foundation.

[2]http://archive.stsci.edu/hst/wfpc2/index.html

HST. For each of the normal galaxies in our sample, we assigned morphological types on the numeric 16-step de Vaucouleurs system, which ranges from T= −5 (Elliptical) through T= 10 (irregular). For merging and peculiar galaxies, we used the following typing scheme, which was partially adapted from Hibbard et al. (2001). Pre-mergers (pM, T= 13.0) are galaxies that are tidally interacting with another nearby galaxy, but they are at a large enough distance from each-another that the individual galaxies can be easily distinguished and treated separately. Minor mergers (mM, T= 13.5) are two or more galaxies showing signs of merging, in which one of the galaxies is much larger or brighter than the others (at least about 4 times larger or brighter). Major mergers (M, T= 14.0) are galaxies of apparently similar mass or luminosity that are interacting or merging. Major merger remnants (MR, T= 14.5) are objects in the later stages of merging, such that it is difficult to say exactly what has merged, or how. Peculiar galaxies (P, T= 15.0) are abnormal or unclassifiable galaxies which do not fit on the normal Hubble sequence, but were not obviously involved in a merger. A subset of these may, however, be late-stage merger remnants. Figure 13 shows an example of each of the four major types of merging galaxies.

3.4.2. *CAS Parameter Measurements*

We adopt the definitions of the CAS parameters of Conselice et al. (2000) and Conselice (2003b), as described below, and measured CAS parameters for our galaxy sample using the IRAF task `CAS`, developed by C. Conselice (Conselice, et al. 2000; Conselice 2003b).

The concentration index, C, is computed by determining the total light contained within 1.5× the Petrosian radius (r_{pet}), and finding the logarithmic ratio of the radius within which 80% of this light is contained (r_{80}) to the radius within which 20% of this light is contained (r_{20}) (Conselice, et al. 2000). The concentration index is given by the formula:

$$C = 5 \times log(r_{80}/r_{20}) \tag{3.1}$$

Therefore, galaxies that are highly concentrated in their centers (e.g., ellipticals) will have high values of C, and galaxies that have less-centrally concentrated light distributions (e.g., disk galaxies or low surface brightness galaxies) will have lower values of C.

The asymmetry index, A, is computed by rotating the galaxy by 180° from its center and subtracting the light within 1.5× r_{pet} in the rotated image (I_{180}) from that in the original image (I_o). The ratio of the residual subtracted flux to the original galaxy flux yields A:

$$A = min(\frac{\Sigma\ |I_o - I_{180}|}{\Sigma\ |I_o|}) - min(\frac{\Sigma\ |B_o - B_{180}|}{\Sigma\ |I_o|}) \tag{3.2}$$

Noise corrections were applied by subtracting the asymmetry of an empty background region (B), and iterative centering corrections were applied to minimize A. Asymmetries range from 0 to 2, with A = 0 corresponding to a truly symmetric galaxy (e.g., some ellipticals; see Jansen(2000) for an example of a highly symmetric spiral galaxy), and A = 2 corresponding to a completely asymmetric galaxy.

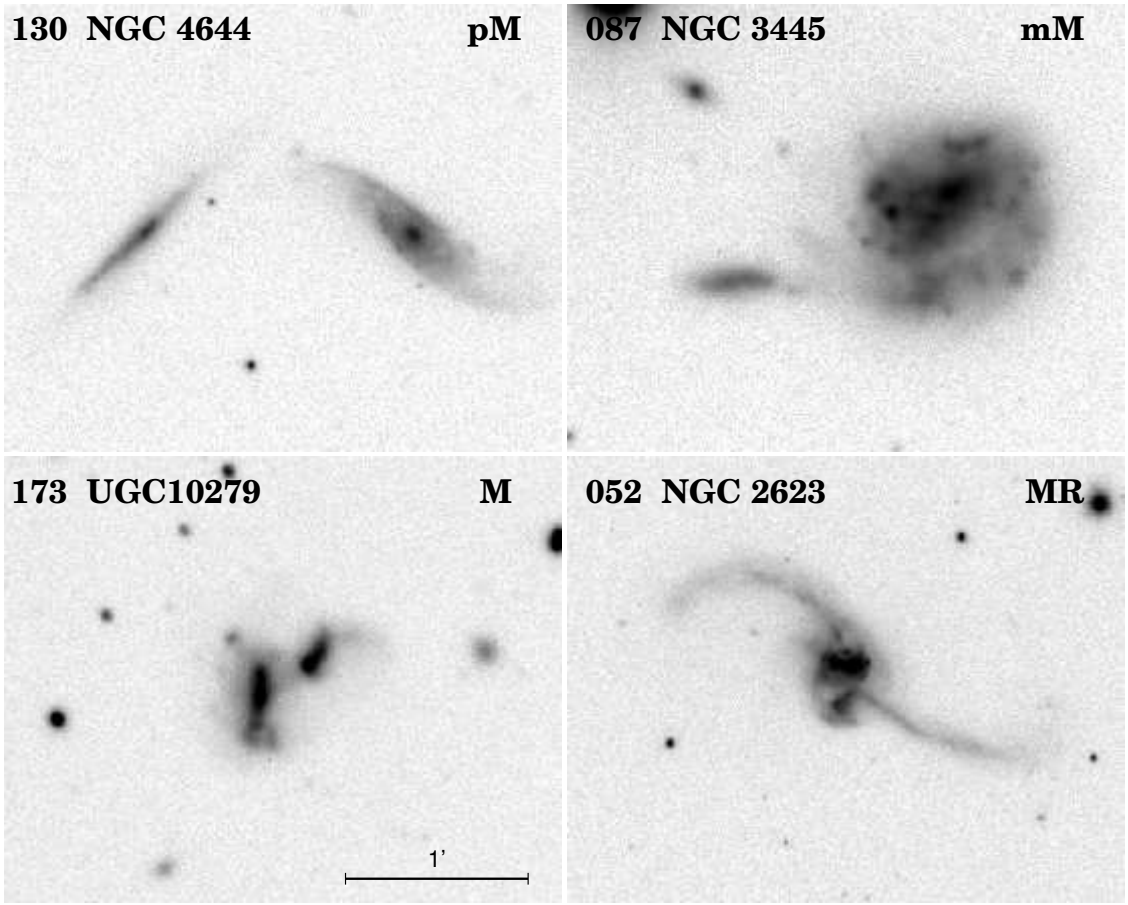

Figure 13 Examples of the sub-classifications assigned to the merging galaxies in our sample. Each of the the B-filter VATT images measures $3.0' \times 2.4'$. **Top left:** NGC4644 (the galaxy on the right) is in strong interaction with its neighbor NGC4644B (PGC42725), and is classified as a pre-merger (pM). **Top right:** NGC3445 appears to be accreting a smaller companion, PGC32784, and is classified as a minor merger (mM). **Bottom left:** UGC10279 represents a major merger event (M) between two galaxies of similar mass, Holmberg 734A and B. **Bottom right:** in NGC2623 the properties of the galaxies that merged are no longer exactly discernible, so it is classified as a merger remnant (MR, early stage).

The clumpiness index, S, is defined as the ratio of the amount of light in high-frequency structures within 1.5× r_{pet}, to the total amount of light in the galaxy within that radius (Conselice 2003b). This was done by subtracting a smoothed image from the original image to produce an image that contains only the high-frequency structure. S is given by the following equation, where $I_{x,y}$ is the intensity of light in a given pixel, $I^s_{x,y}$ is the intensity of that pixel in the smoothed image, and $B^s_{x,y}$ is an intensity value of a pixel from a smoothed background region:

$$S = 10 \times \left(\frac{\Sigma^{N,N}_{x,y=1,1}\ (I_{x,y} - I^s_{x,y})}{\Sigma^{N,N}_{x,y=1,1}\ I_{x,y}} - \frac{\Sigma^{N,N}_{x,y=1,1}\ B^s_{x,y}}{\Sigma^{N,N}_{x,y=1,1}\ I_{x,y}}\right) \tag{3.3}$$

A clumpiness of S = 0 corresponds to a galaxy that has no high frequency structure, and is therefore completely smooth (e.g., some ellipticals). Galaxies with more high-frequency structure are more patchy in appearance, and will have a higher value of S.

3.4.3. *Resolution Effects*

Conselice (2003b) found that the asymmetry index does not depend strongly on the resolution or seeing of the image, with 70% of the value of A attributable to overall global distortions in the galaxy, and 30% due to localized high-frequency structures, such as star-forming regions. Our sample, however, contains data from a variety of telescopes with vast differences in resolution, which may have a measurable effect on our comparison of the CAS parameters as a function of wavelength. For the $UBVR$ images observed at the VATT, each galaxy's images were convolved to the worst seeing for that galaxy (typically in the U-band), using a Gaussian of the appropriate width within the task `GAUSS` in IRAF. The seeing of each image was determined by finding the average FWHM (full width at half max) of all stars detected with SExtractor (Bertin & Arnouts 1996), as described in Chapter 4. For a small number of galaxies that had significant differences in data quality between filters, convolving the images to the worst seeing had a measurable effect on the CAS measurements. There was no significant impact on the CAS measurements, however, for the majority of the galaxies.

The issue of resolution is more pronounced, however, when, comparing images of a galaxy with ground-based seeing to those from HST WFPC2 (PSF FWHM $\sim 0.04''$ in F300W and $0.09''$ in F814W). To test the difference in CAS parameter measurements at these resolutions, we convolved the HST images to the $1.75''$ average seeing at the VATT, using the same method as for the VATT images. We subsequently measured the CAS parameters in both the original and convolved images. The left three panels in Figure 14 show the difference between the CAS measurements from the convolved and unconvolved HST images in each filter vs. the measurements in the unconvolved images. The right-most panels show the median of these differences for each filter. Horizontal dotted lines indicate where the value of the CAS parameter did not change between the convolved and unconvolved images.

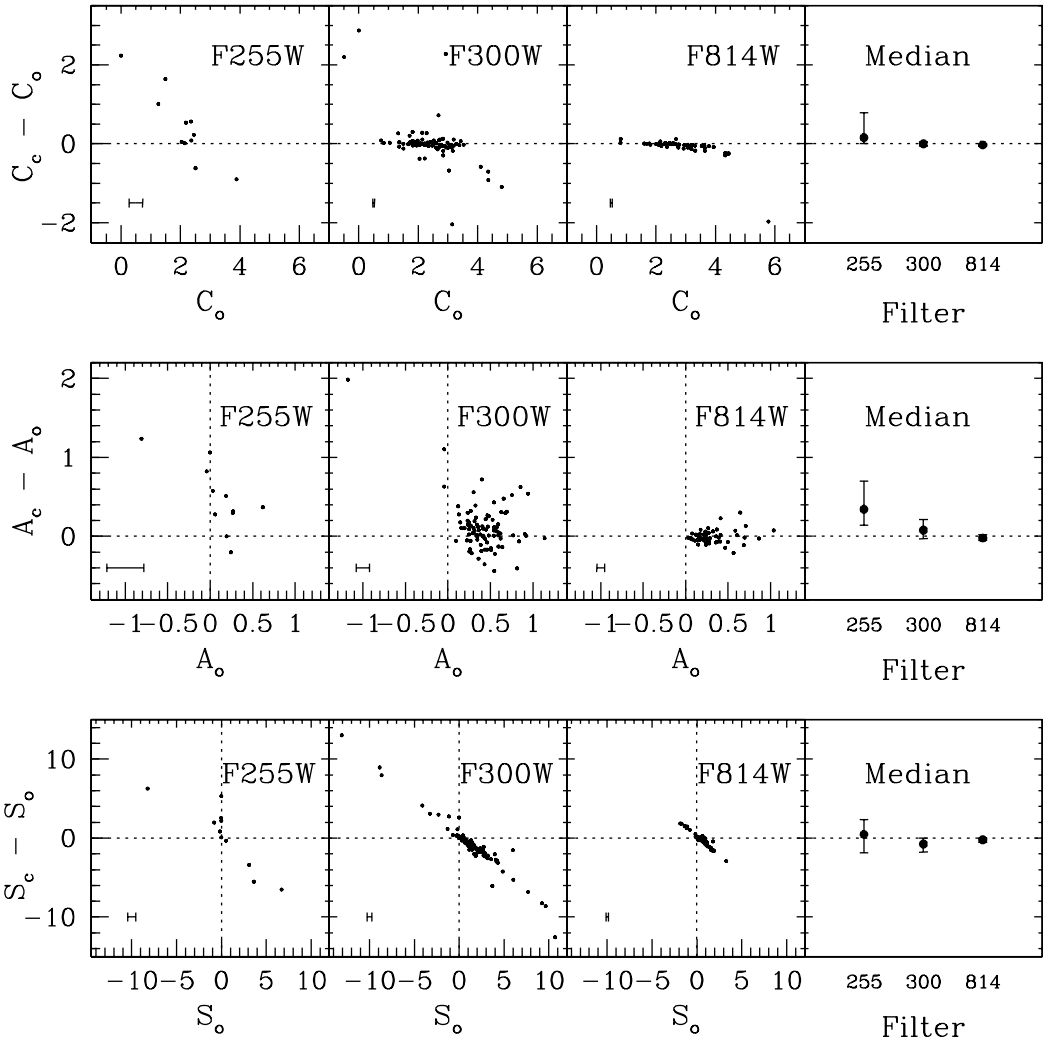

Figure 14 The difference between CAS parameters measured from HST images convolved to the average ground-based seeing of 1.75″ (C_c, and those measured from the original high resolution (0.04″–0.09″ stellar FWHM) images (C_o), plotted versus the measurements in the original images. **Left 3 panels:** *TOP:* Change in concentration index, $C_c - C_o$, versus C_o. *MIDDLE:* Change in asymmetry index, $A_c - A_o$, versus A_o. *BOTTOM:* Change in clumpiness index, $S_c - S_o$, versus S_o. Each panel shows data from a different pass-band, as labeled in the panels. The horizontal error bar in the lower left corner of each panel represents the median uncertainties for each parameter in the original images. **Right-most panels:** Median difference in each filter between C_c and C_o (top), A_c and A_o (middle), and S_c and S_o (bottom). Error bars represent the 25% – 75% quartile range. Horizontal dotted lines indicate where the value of the CAS parameter did not change between the convolved and unconvolved images. Vertical dotted lines in the A and S panels represent the cutoff for meaningful values. Data-points to the left of these lines were unreliable, and physically meaningless in the original images due to WFPC2 CTE effects and large noise spikes that resulted in an over-subtraction of the background. Most of these outlying values were, however, increased to meaningful values after convolving the images.

The differences between CAS parameters at the two different resolutions are most pronounced in the F255W images, which had the lowest signal-to-noise ratio, and thus the highest uncertainties in these parameters. Due to the low signal in these images, the greatest effect of convolving them was smoothing over high-frequency structure in the noisy background, which is strongly affected by the charge transfer effect (CTE) in the old WFPC2 chip. This results in more reliable CAS values that are not as severely affected by spikes in the sky background, as can be seen by considering the A and S panels in Figure 14. Vertical dotted lines in these panels represent the cut-off for meaningful values ($A < 0$, $S < 0$), with data appearing to the left of this line being unreliable and physically meaningless. Convolving the images increased most of these values into the positive regime, where they are physically meaningful. CTE noise effects are also present in data for the other WFPC2 filters, although it is not as strong of a factor in the longer wavelength pass-bands due to the higher signal-to-noise ratio of the galaxies and the more significant zodiacal sky filling in the CTE traps. A combination of smoothing over the noise and the high-frequency structure of the galaxy itself has an effect on the CAS parameters in all filters, to varying extents.

Overall, the concentration index does not change significantly with resolution, especially at longer wavelengths. The median values of the change in C after convolving the images are 0.156, –0.002, and –0.028 in F255W, F300W, and F814W, respectively (these values will be given in this filter order for the rest of this paragraph). This is well within the median uncertainties on individual values of C in the unconvolved images, which are 0.227, 0.030, and 0.030, respectively. The asymmetry index is more affected by resolution, although there is no trend in this effect with increasing A. Convolving the images changed A by a median value of 0.343, 0.079, and –0.021, respectively. Except for the noisy F255W images, this is roughly within the median uncertainties of 0.217, 0.078, and 0.046, respectively. The clumpiness index, however, was more strongly affected by the resolution change, with a strong correlation of more clumpy galaxies at high-resolution becoming less clumpy at low-resolution in all filters. This is to be expected, as S is highly dependent on high-frequency structure, and star clusters and associations may be resolved in the unconvolved HST images. Convolving the images changed the median S by 0.470, –0.750, and –0.210, respectively. These are relatively significant differences, and are larger than the median uncertainties on S of 0.437, 0.263, and 0.135, illustrating that real structure being smoothed over lowers the measured S values.

Throughout the remainder of this chapter we use the CAS values measured in HST images convolved to match the resolution of our ground-based VATT images to reduce the effects of background noise and to offer a more systematic comparison. The GALEX images have a stellar FWHM of about $5''$, and are used as is. Comparisons of the GALEX NUV and FUV CAS values may therefore be affected by these high resolution effects, and should be treated with caution.

3.5. Results

3.5.1. *Relating CAS Parameters to Galaxy Color and Type*

Tables 6, 7, and 8 list our C, A, and S measurements and errors, respectively, for each galaxy in each pass-band. Ellipsis indicate that there are no images available for that galaxy in that particular pass-band. Figures 15, 16, and 17 show the C, A, and S parameters, respectively, versus the total $(B-V)$ color of each galaxy. Values for each pass-band are shown in separate panels within each figure, with different colored symbols used to designate early-type (E–S0), mid-type (Sa-Sc), late-type (Sd–Im), and peculiar/merging galaxies, as indicated by the legend in each figure. Representative error bars are shown in each panel with the median uncertainty in the CAS parameters of the individual data points, and the average $(B-V)$ uncertainty of 0.04 mag. These figures show a general trend of galaxies becoming generally more concentrated, less asymmetric, and less clumpy with redder $B-V$ color. There is a large spread and overlap in galaxy type, such that galaxy classification can be only loosely determined from these plots. Early-type galaxies are most clearly separated from the later galaxy types, since they are the reddest, the most concentrated, the least asymmetric, and the least clumpy. Later galaxy types are increasingly bluer, less concentrated, more asymmetric, and more clumpy than earlier galaxy types. This result is in agreement with previous authors (e.g. Takamiya 1999; Bershady et al. 2000; Conselice et al. 2000, 2003a; Conselice 2003b). The correlation of bluer galaxies being more clumpy becomes tighter at longer wavelengths, such that there is a much higher spread in S at shorter wavelengths. This trend also changes slope with filter, such that blue galaxies tend to be more clumpy at shorter wavelengths than they are at longer wavelengths. This logically results from bluer late-type galaxies containing more recent star formation, and therefore having more blue knots from recently formed star clusters and associations that will increase the clumpiness in the bluer filters. The CAS values of peculiar/merging galaxies vary considerably, but their median values are slightly offset from the locus of normal galaxies, with peculiar/merging galaxies being generally bluer, more asymmetric, and and more clumpy than normal galaxies.

Table 6. Concentration Index (C)

ID#	FUV	σ_{FUV}	MUV	σ_{MUV}	F255W	σ_{F255W}	F300W	σ_{F300W}	U	σ_U	B	σ_B	V	σ_V	R	σ_R	F814W	σ_{F814W}
001	2.617	0.756	2.950	0.728	...	...	3.722	0.102	...	...	...	...	...	...	...	...	...	...
002	...	...	...	...	...	...	2.254	0.023	...	...	...	...	...	...	...	...	2.346	0.022
003	...	...	...	...	...	...	...	...	2.507	0.044	2.720	0.039	2.404	0.051	2.866	0.039	...	...
004	...	...	...	...	...	...	2.247	0.025	...	...	...	...	...	...	...	...	2.211	0.024
005	...	...	...	...	...	...	...	...	2.488	0.126	2.669	0.115	2.581	0.122	2.343	0.154	...	...
006	2.487	0.487	2.784	0.489	...	...	2.704	0.043	...	...	...	...	...	...	...	...	3.164	0.049
007	...	...	...	...	...	...	...	...	2.632	0.113	2.652	0.107	2.770	0.110	2.767	0.125	...	...
008	...	...	...	...	...	...	...	...	2.125	0.116	2.275	0.116	2.512	0.127	2.851	0.122	...	...
009	...	...	...	...	...	...	1.801	0.018	...	...	...	...	...	...	...	...	...	...
010	...	...	...	...	...	...	...	...	4.426	0.165	4.242	0.143	4.088	0.147	4.195	0.140	...	...
011	...	...	...	...	...	...	1.407	0.015	...	...	...	...	...	...	...	...	...	...
012	...	...	...	...	...	...	...	...	2.848	0.115	2.860	0.106	2.924	0.109	2.937	0.113	...	...
013	...	...	3.150	0.378	...	...	2.852	0.062	...	...	...	...	...	...	...	...	3.060	0.064
014	2.489	0.485	2.622	0.448	...	...	2.510	0.032	2.490	0.112	2.682	0.105	2.785	0.096	3.341	0.072	2.571	0.026
015	...	...	...	...	...	...	...	...	2.373	0.062	2.442	0.064	2.537	0.080	2.528	0.114	...	...
016	...	...	...	...	...	...	2.958	0.031	...	...	...	...	...	...	...	...	...	...
017	...	...	...	...	...	...	...	...	3.022	0.096	3.399	0.113	3.816	0.135	3.997	0.147	...	...
018	...	...	...	...	...	...	...	...	3.101	0.127	3.041	0.127	2.941	0.133	2.603	0.168	...	...
019	...	...	...	...	...	...	...	...	1.602	0.058	1.665	0.057	1.629	0.057	1.548	0.057	...	...
020	...	...	...	...	...	...	...	...	2.526	0.106	2.458	0.106	2.595	0.100	2.546	0.101	...	...
021	...	...	...	...	...	...	...	...	2.133	0.044	2.250	0.042	2.363	0.042	2.420	0.043	...	...
022	...	...	...	...	...	...	3.654	0.095	...	...	...	...	...	...	...	...	3.488	0.051
023	...	...	...	...	...	...	1.905	0.018	2.760	0.034	2.745	0.032	2.718	0.031	2.681	0.030	1.790	0.017
024	...	...	...	...	...	...	1.970	0.021	...	...	...	...	...	...	...	...	2.046	0.020
025	...	...	...	...	...	...	1.974	0.020	...	...	...	...	...	...	...	...	2.271	0.023
026	...	...	...	...	...	...	1.813	0.018	...	...	...	...	...	...	...	...	...	...
027	3.479	0.328	1.727	0.016	...	...	2.841	0.028	...	...	...	...	...	...	...	...	3.021	0.034
028	...	...	...	...	...	...	2.896	0.077	...	...	...	...	...	...	...	...	3.584	0.045
029	...	...	...	...	...	...	2.088	0.019	...	...	...	...	...	...	...	...	...	...
030	...	...	...	...	...	...	...	...	2.902	0.145	2.948	0.121	3.319	0.133	4.038	0.188	...	...
031	...	...	...	...	...	...	2.288	0.020	...	...	...	...	...	...	...	...	2.130	0.020
032	...	...	...	...	...	...	0.838	0.014	...	...	...	...	...	...	...	...	...	...

Table 6—Continued

ID#	FUV	σ_{FUV}	MUV	σ_{MUV}	F255W	σ_{F255W}	F300W	σ_{F300W}	U	σ_U	B	σ_B	V	σ_V	R	σ_R	F814W	σ_{F814W}
033	···	···	···	···	···	···	3.082	0.029	···	···	···	···	···	···	···	···	2.566	0.026
034	···	···	···	···	···	···	2.663	0.068	···	···	···	···	···	···	···	···	2.929	0.030
035	···	···	···	···	···	···	1.888	0.019	···	···	···	···	···	···	···	···	2.323	0.022
036	···	···	···	···	2.989	0.025	3.445	0.134	···	···	···	···	···	···	···	···	4.203	0.059
037	···	···	···	···	···	···	···	···	2.202	0.064	2.332	0.054	2.400	0.052	2.343	0.057	···	···
038	···	···	···	···	···	···	···	···	2.548	0.098	2.700	0.094	2.754	0.097	2.926	0.091	···	···
039	···	···	···	···	···	···	1.663	0.017	2.232	0.052	2.325	0.050	2.389	0.048	2.371	0.050	···	···
040	···	···	···	···	2.160	0.022	1.780	0.025	···	···	···	···	···	···	···	···	2.000	0.024
041	···	···	···	···	···	···	2.348	0.034	2.370	0.134	2.457	0.129	2.512	0.127	2.528	0.128	···	···
042	···	···	···	···	···	···	3.519	0.101	4.243	0.219	4.388	0.204	4.286	0.181	4.235	0.177	4.102	0.063
043	···	···	···	···	···	···	···	···	2.595	0.119	2.659	0.123	2.717	0.127	2.732	0.132	···	···
044	···	···	···	···	···	···	···	···	2.022	0.085	2.205	0.089	2.368	0.094	2.443	0.098	···	···
045	···	···	···	···	···	···	···	···	3.104	0.120	3.009	0.125	2.936	0.124	2.967	0.122	···	···
046	···	···	···	···	···	···	···	···	3.153	0.235	3.303	0.208	3.215	0.191	3.122	0.191	···	···
047	2.427	0.139	1.786	0.151	···	···	3.342	0.030	···	···	···	···	···	···	···	···	4.195	0.060
048	···	···	···	···	···	···	5.208	0.073	4.356	0.270	3.942	0.202	3.744	0.173	3.644	0.165	3.725	0.048
049	2.453	0.291	2.112	0.300	···	···	···	···	2.254	0.088	2.468	0.093	2.679	0.102	2.785	0.108	···	···
050	···	···	···	···	···	···	3.402	0.037	1.557	0.030	2.111	0.026	2.133	0.025	1.346	0.036	···	···
051	···	···	···	···	···	···	···	···	2.092	0.061	3.540	0.038	3.463	0.034	3.381	0.032	···	···
052	···	···	···	···	···	···	1.911	0.032	3.024	0.122	3.026	0.126	3.087	0.134	3.181	0.145	···	···
053	···	···	···	···	···	···	···	···	3.032	0.149	3.029	0.154	3.082	0.165	3.166	0.179	···	···
054	3.227	0.291	3.343	0.329	···	···	···	···	3.615	0.104	3.792	0.100	3.923	0.107	4.118	0.105	···	···
055	···	···	···	···	···	···	···	···	3.520	0.189	3.472	0.179	3.408	0.173	3.575	0.181	···	···
056	···	···	···	···	···	···	···	···	3.495	0.134	3.442	0.124	3.444	0.121	3.356	0.125	···	···
057	···	···	···	···	···	···	···	···	3.041	0.063	3.214	0.064	3.276	0.067	3.315	0.064	···	···
058	···	···	···	···	···	···	···	···	3.071	0.253	3.145	0.234	3.351	0.213	3.433	0.204	···	···
059	···	···	···	···	···	···	···	···	2.899	0.069	3.036	0.069	3.213	0.074	3.340	0.082	···	···
060	···	···	···	···	···	···	···	···	2.543	0.052	2.752	0.054	2.970	0.063	3.173	0.073	···	···
061	···	···	···	···	···	···	···	···	3.023	0.039	2.933	0.037	2.805	0.036	2.730	0.033	···	···
062	···	···	···	···	···	···	···	···	2.601	0.047	2.672	0.045	2.645	0.046	2.483	0.051	···	···
063	···	···	···	···	···	···	1.880	0.029	···	···	···	···	···	···	···	···	2.083	0.033
064	···	···	···	···	2.676	0.050	2.870	0.048	2.927	0.147	3.190	0.136	3.297	0.153	3.422	0.174	3.465	0.064

Table 6—Continued

ID#	FUV	σ_{FUV}	MUV	σ_{MUV}	F255W	σ_{F255W}	F300W	σ_{F300W}	U	σ_U	B	σ_B	V	σ_V	R	σ_R	F814W	σ_{F814W}
065	···	···	···	···	···	···	···	···	2.778	0.074	2.849	0.077	2.993	0.079	3.013	0.089	···	···
066	···	···	···	···	···	···	···	···	3.764	0.332	3.826	0.362	3.854	0.366	3.871	0.369	···	···
067	···	···	···	···	···	···	2.473	0.032	1.399	0.016	1.461	0.016	1.525	0.017	1.538	0.017	2.651	0.029
068	···	···	···	···	···	···	···	···	2.600	0.227	2.718	0.212	2.756	0.204	2.788	0.207	···	···
069	···	···	···	···	···	···	···	···	2.438	0.038	2.632	0.038	2.777	0.034	2.761	0.035	···	···
070	···	···	···	···	···	···	3.282	0.032	···	···	···	···	···	···	···	···	···	···
071	···	···	···	···	···	···	···	···	3.135	0.055	3.079	0.051	3.128	0.046	3.133	0.044	···	···
072	···	···	···	···	···	···	1.777	0.017	2.775	0.026	2.850	0.029	2.973	0.032	3.051	0.035	···	···
073	···	···	···	···	···	···	···	···	2.597	0.028	2.618	0.028	2.636	0.028	2.611	0.027	···	···
074	···	···	···	···	···	···	···	···	2.468	0.068	2.910	0.054	3.101	0.047	2.910	0.047	···	···
075	···	···	···	···	···	···	···	···	2.876	0.116	2.887	0.117	2.928	0.119	2.929	0.127	···	···
076	···	···	···	···	2.719	0.028	2.607	0.027	2.424	0.073	2.698	0.079	2.704	0.081	2.695	0.083	2.474	0.024
077	···	···	···	···	···	···	···	···	1.826	0.023	2.030	0.023	2.030	0.022	2.062	0.022	···	···
078	···	···	···	···	···	···	3.147	0.042	···	···	···	···	···	···	···	···	···	···
079	···	···	···	···	···	···	···	···	3.129	0.060	3.094	0.062	3.026	0.063	3.026	0.063	···	···
080	···	···	···	···	···	···	···	···	2.948	0.034	2.987	0.033	2.911	0.038	2.955	0.038	···	···
081	···	···	···	···	···	···	1.863	0.024	···	···	···	···	···	···	···	···	2.567	0.030
082	···	···	···	···	···	···	···	···	2.472	0.037	2.473	0.036	2.571	0.033	2.582	0.033	···	···
083	···	···	···	···	···	···	···	···	3.320	0.178	3.240	0.154	3.393	0.151	3.471	0.132	···	···
084	···	···	···	···	···	···	···	···	2.278	0.061	2.561	0.059	3.582	0.042	3.625	0.038	···	···
085	···	···	···	···	···	···	···	···	2.673	0.093	2.763	0.090	2.843	0.089	2.909	0.088	···	···
086	···	···	···	···	···	···	1.906	0.018	···	···	···	···	···	···	···	···	···	···
087	···	···	···	···	···	···	1.932	0.018	2.360	0.055	2.572	0.057	2.671	0.059	2.721	0.059	2.563	0.024
088	···	···	···	···	···	···	2.058	0.027	2.136	0.112	2.302	0.113	2.383	0.118	2.438	0.122	2.508	0.035
089	···	···	···	···	2.266	0.263	2.596	0.212	···	···	···	···	···	···	···	···	4.162	0.063
090	···	···	···	···	···	···	···	···	2.951	0.105	3.221	0.099	3.261	0.099	3.280	0.102	···	···
091	···	···	···	···	···	···	···	···	2.529	0.044	2.716	0.042	2.862	0.045	2.924	0.047	···	···
092	···	···	···	···	···	···	···	···	2.436	0.058	2.720	0.054	2.631	0.057	2.648	0.057	···	···
093	···	···	···	···	···	···	···	···	2.483	0.248	2.588	0.225	2.822	0.211	2.775	0.232	···	···
094	···	···	···	···	···	···	···	···	1.896	0.031	1.611	0.029	1.720	0.029	1.680	0.028	···	···
095	···	···	···	···	···	···	···	···	3.531	0.232	3.579	0.238	3.552	0.235	3.616	0.232	···	···
096	···	···	···	···	2.450	0.024	2.616	0.027	···	···	···	···	···	···	···	···	2.918	0.027

Table 6—Continued

ID#	FUV	σ_{FUV}	MUV	σ_{MUV}	F255W	σ_{F255W}	F300W	σ_{F300W}	U	σ_U	B	σ_B	V	σ_V	R	σ_R	F814W	σ_{F814W}
097	···	···	···	···	···	···	1.107	0.014	1.436	0.045	1.419	0.044	1.375	0.044	1.395	0.043	0.831	0.014
098	···	···	···	···	···	···	2.315	0.023	···	···	···	···	···	···	···	···	2.317	0.024
099	···	···	···	···	···	···	···	···	2.651	0.087	2.620	0.074	2.716	0.070	2.588	0.067	···	···
100	···	···	···	···	···	···	···	···	2.568	0.035	2.584	0.035	2.685	0.035	2.728	0.037	···	···
101	···	···	···	···	···	···	1.757	0.019	2.518	0.050	3.012	0.042	3.031	0.039	3.013	0.037	···	···
102	···	···	···	···	···	···	2.039	0.027	3.150	0.086	3.037	0.070	2.866	0.065	2.774	0.063	···	···
103	···	···	···	···	···	···	2.229	0.021	2.651	0.057	2.877	0.061	2.955	0.066	2.996	0.070	2.744	0.027
104	···	···	···	···	···	···	2.852	0.053	2.896	0.163	3.063	0.141	3.261	0.129	3.294	0.132	3.269	0.038
105	···	···	···	···	···	···	···	···	2.776	0.047	3.049	0.046	3.148	0.047	3.189	0.047	···	···
106	···	···	···	···	···	···	3.298	0.055	3.033	0.222	3.013	0.198	2.991	0.206	2.955	0.202	2.807	0.065
107	···	···	···	···	···	···	···	···	3.378	0.089	3.321	0.090	3.345	0.101	3.372	0.109	···	···
108	···	···	···	···	···	···	1.875	0.037	···	···	···	···	···	···	···	···	2.458	0.036
109	···	···	···	···	···	···	···	···	3.263	0.038	3.402	0.038	3.577	0.043	3.636	0.049	···	···
110	···	···	···	···	···	···	···	···	2.501	0.042	2.658	0.040	2.710	0.042	2.708	0.043	···	···
111	···	···	···	···	···	···	3.494	0.046	···	···	···	···	···	···	···	···	4.034	0.056
112	···	···	···	···	···	···	···	···	3.124	0.109	3.119	0.094	3.118	0.085	3.276	0.076	···	···
113	···	···	···	···	···	···	···	···	2.570	0.057	2.733	0.054	2.824	0.053	3.557	0.041	···	···
114	···	···	···	···	···	···	···	···	2.392	0.027	2.384	0.026	2.385	0.027	2.391	0.027	···	···
115	···	···	···	···	···	···	···	···	2.223	0.056	2.374	0.054	2.499	0.053	2.546	0.053	···	···
116	···	···	···	···	···	···	···	···	3.100	0.033	3.133	0.034	3.179	0.034	3.223	0.034	···	···
117	···	···	···	···	···	···	···	···	4.217	0.063	4.321	0.068	4.338	0.073	4.344	0.076	···	···
118	···	···	···	···	···	···	···	···	2.072	0.047	2.134	0.044	2.183	0.042	2.234	0.042	···	···
119	···	···	···	···	···	···	1.380	0.014	···	···	···	···	···	···	···	···	···	···
120	···	···	···	···	···	···	···	···	2.691	0.028	2.687	0.028	2.670	0.028	2.662	0.028	···	···
121	···	···	···	···	···	···	···	···	4.044	0.106	4.082	0.111	4.110	0.115	4.033	0.123	···	···
122	···	···	···	···	···	···	3.020	0.035	···	···	···	···	···	···	···	···	3.134	0.036
123	···	···	···	···	···	···	2.085	0.020	2.643	0.027	2.696	0.027	2.688	0.028	2.668	0.027	···	···
124	···	···	···	···	···	···	···	···	2.513	0.046	2.523	0.049	2.483	0.048	2.463	0.047	···	···
125	···	···	···	···	···	···	···	···	2.366	0.030	2.578	0.033	2.757	0.035	2.873	0.038	···	···
126	···	···	···	···	···	···	···	···	2.403	0.046	2.454	0.046	2.571	0.046	2.649	0.046	···	···
127	···	···	···	···	···	···	···	···	3.158	0.323	3.178	0.304	3.114	0.294	3.137	0.278	···	···
128	···	···	···	···	···	···	···	···	1.960	0.021	2.234	0.022	2.172	0.022	2.233	0.022	···	···

Table 6—Continued

ID#	FUV	σ_{FUV}	MUV	σ_{MUV}	F255W	σ_{F255W}	F300W	σ_{F300W}	U	σ_U	B	σ_B	V	σ_V	R	σ_R	F814W	σ_{F814W}
129	···	···	···	···	···	···	2.113	0.019	2.527	0.026	2.605	0.027	2.630	0.028	2.654	0.026	···	···
130	···	···	···	···	···	···	···	···	2.745	0.116	3.168	0.117	3.287	0.128	3.294	0.132	···	···
131	···	···	···	···	···	···	···	···	2.609	0.035	2.867	0.048	3.134	0.059	3.260	0.062	···	···
132	···	···	···	···	···	···	···	···	3.099	0.339	3.180	0.304	3.050	0.285	2.993	0.277	···	···
133	···	···	···	···	···	···	···	···	2.134	0.051	2.234	0.050	2.410	0.051	2.460	0.050	···	···
134	···	···	···	···	···	···	2.787	0.040	···	···	···	···	···	···	···	···	3.541	0.045
135	···	···	···	···	···	···	···	···	3.423	0.054	3.558	0.057	3.775	0.063	3.865	0.069	···	···
136	···	···	···	···	···	···	1.652	0.016	2.098	0.022	2.137	0.022	2.136	0.022	2.124	0.021	···	···
137	···	···	···	···	···	···	···	···	2.468	0.026	2.470	0.025	2.383	0.024	2.356	0.024	···	···
138	···	···	···	···	···	···	···	···	2.132	0.066	2.316	0.064	2.258	0.060	2.414	0.060	···	···
139	···	···	···	···	···	···	0.867	0.013	···	···	···	···	···	···	···	···	0.935	0.014
140	···	···	···	···	···	···	2.980	0.070	···	···	···	···	···	···	···	···	3.149	0.074
141	···	···	···	···	···	···	···	···	1.864	0.039	2.127	0.041	2.314	0.044	2.372	0.046	···	···
142	···	···	···	···	···	···	···	···	2.307	0.046	2.497	0.043	2.461	0.042	2.400	0.043	···	···
143	···	···	···	···	···	···	···	···	1.701	0.046	1.963	0.047	2.123	0.046	2.219	0.045	···	···
144	···	···	···	···	···	···	···	···	2.886	0.072	2.969	0.058	3.073	0.054	3.050	0.055	···	···
145	···	···	···	···	···	···	1.072	0.021	···	···	···	···	···	···	···	···	2.096	0.027
146	···	···	···	···	···	···	2.503	0.029	3.308	0.088	3.880	0.058	3.919	0.057	3.650	0.049	2.293	0.022
147	···	···	···	···	···	···	1.985	0.020	···	···	···	···	···	···	···	···	2.655	0.075
148	···	···	···	···	1.886	0.018	1.940	0.018	···	···	···	···	···	···	···	···	1.606	0.016
149	···	···	···	···	2.924	0.027	3.014	0.057	···	···	···	···	···	···	···	···	2.983	0.070
150	···	···	···	···	···	···	···	···	3.224	0.124	3.527	0.108	3.569	0.106	3.555	0.105	···	···
151	···	···	···	···	···	···	2.352	0.231	2.613	0.516	2.780	0.485	2.986	0.473	3.113	0.449	3.813	0.127
152	···	···	···	···	···	···	···	···	2.344	0.024	2.390	0.025	2.315	0.024	2.299	0.024	···	···
153	···	···	···	···	···	···	···	···	2.446	0.147	2.497	0.138	2.589	0.138	2.603	0.140	···	···
154	···	···	···	···	···	···	1.703	0.023	···	···	···	···	···	···	···	···	1.785	0.017
155	···	···	···	···	···	···	···	···	2.816	0.144	3.148	0.134	3.370	0.129	3.310	0.145	···	···
156	···	···	···	···	···	···	···	···	2.504	0.117	2.660	0.123	2.706	0.136	2.702	0.147	···	···
157	2.447	0.195	2.425	0.193	···	···	···	···	2.551	0.050	2.598	0.045	2.743	0.042	2.592	0.044	···	···
158	···	···	···	···	···	···	2.452	0.023	3.117	0.038	3.215	0.045	3.327	0.050	3.299	0.049	2.683	0.027
159	···	···	···	···	···	···	···	···	2.612	0.070	2.544	0.064	2.367	0.063	2.363	0.059	···	···
160	···	···	···	···	···	···	···	···	2.567	0.041	2.689	0.041	2.676	0.045	2.696	0.046	···	···

Table 6—Continued

ID#	FUV	σ_{FUV}	MUV	σ_{MUV}	F255W	σ_{F255W}	F300W	σ_{F300W}	U	σ_U	B	σ_B	V	σ_V	R	σ_R	F814W	σ_{F814W}
161	···	···	···	···	···	···	···	···	2.257	0.037	2.369	0.034	2.357	0.032	2.347	0.032	···	···
162	···	···	···	···	···	···	···	···	2.512	0.058	2.709	0.062	2.808	0.065	2.869	0.068	···	···
163	···	···	···	···	···	···	···	···	2.596	0.027	2.776	0.029	2.918	0.032	2.974	0.032	···	···
164	···	···	···	···	···	···	3.498	0.032	···	···	···	···	···	···	···	···	···	···
165	···	···	···	···	···	···	···	···	2.642	0.040	2.688	0.045	2.859	0.047	3.019	0.046	···	···
166	···	···	···	···	2.088	0.019	2.766	0.028	2.923	0.074	2.879	0.075	2.898	0.079	2.902	0.080	2.763	0.028
167	···	···	···	···	···	···	···	···	2.533	0.076	2.763	0.080	2.922	0.085	3.003	0.089	···	···
168	···	···	···	···	···	···	···	···	2.941	0.051	2.779	0.060	2.880	0.067	2.987	0.075	···	···
169	···	···	···	···	···	···	···	···	4.142	0.111	3.525	0.080	3.424	0.081	3.496	0.090	···	···
170	···	···	···	···	···	···	1.848	0.038	3.722	0.054	3.832	0.062	3.624	0.076	3.447	0.086	2.491	0.033
171	···	···	···	···	···	···	···	···	1.908	0.023	2.025	0.024	2.032	0.025	1.966	0.027	···	···
172	···	···	···	···	···	···	2.692	0.033	2.560	0.112	2.714	0.118	2.653	0.118	2.677	0.119	···	···
173	···	···	···	···	···	···	···	···	2.858	0.097	2.838	0.091	2.841	0.089	2.830	0.089	···	···
174	···	···	···	···	···	···	···	···	3.071	0.125	3.068	0.117	3.215	0.127	3.384	0.138	···	···
175	···	···	···	···	···	···	···	···	1.800	0.076	2.028	0.079	2.345	0.084	2.499	0.089	···	···
176	···	···	···	···	···	···	···	···	2.456	0.062	2.545	0.069	2.704	0.064	2.756	0.073	···	···
177	···	···	···	···	···	···	2.538	0.028	2.558	0.108	2.752	0.100	2.685	0.099	2.697	0.097	2.611	0.028
178	1.872	0.099	1.973	0.101	···	···	1.973	0.017	2.213	0.028	2.463	0.031	2.694	0.035	2.836	0.035	2.587	0.023
179	···	···	···	···	···	···	···	···	2.438	0.109	2.579	0.113	2.722	0.122	2.796	0.127	···	···
180	···	···	···	···	···	···	···	···	2.481	0.131	2.557	0.136	2.688	0.135	2.695	0.147	···	···
181	···	···	···	···	···	···	···	···	2.481	0.073	2.568	0.079	2.713	0.085	2.868	0.088	···	···
182	3.286	0.403	3.645	0.333	···	···	···	···	3.102	0.076	2.970	0.066	2.767	0.060	2.676	0.058	···	···
183	···	···	···	···	···	···	···	···	2.806	0.050	3.062	0.053	2.958	0.068	2.995	0.072	···	···
184	···	···	···	···	···	···	1.285	0.015	···	···	···	···	···	···	···	···	1.681	0.017
185	···	···	···	···	···	···	2.185	0.020	2.752	0.029	2.891	0.031	2.990	0.033	3.033	0.034	···	···
186	···	···	···	···	···	···	1.928	0.019	···	···	···	···	···	···	···	···	3.140	0.031
187	···	···	···	···	2.233	0.025	2.058	0.028	2.878	0.075	2.943	0.062	2.619	0.065	2.346	0.075	2.132	0.021
188	···	···	···	···	3.136	0.033	1.589	0.054	···	···	···	···	···	···	···	···	3.859	0.044
189	···	···	···	···	···	···	2.554	0.098	···	···	···	···	···	···	···	···	···	···
190	2.121	0.122	2.051	0.123	···	···	1.503	0.016	2.219	0.043	2.384	0.045	2.554	0.047	2.628	0.048	···	···
191	···	···	···	···	···	···	3.027	0.075	···	···	···	···	···	···	···	···	···	···
192	···	···	···	···	···	···	2.428	0.060	···	···	···	···	···	···	···	···	2.792	0.049

Table 6—Continued

ID#	FUV	σ_{FUV}	MUV	σ_{MUV}	F255W	σ_{F255W}	F300W	σ_{F300W}	U	σ_U	B	σ_B	V	σ_V	R	σ_R	F814W	σ_{F814W}
193	...	...	...	...	...	...	2.147	0.018	...	...	...	...	...	...	...	...	2.540	0.022
194	...	...	...	...	...	...	2.518	0.191	...	...	...	...	...	...	...	...	...	...
195	...	...	...	...	...	...	1.724	0.017	...	...	...	...	...	...	...	...	...	...
196	...	...	...	...	...	...	...	...	2.599	0.063	2.767	0.062	2.578	0.076	2.517	0.083	...	...
197	1.735	0.623	1.792	0.055	...	...	2.411	0.037	...	...	...	...	...	...	...	...	3.535	0.040
198	...	...	...	...	...	...	2.320	0.020	...	...	...	...	...	...	...	...	...	...
199	2.461	0.292	2.867	0.328	...	...	2.552	0.221	...	...	...	...	...	...	...	...	3.216	0.032

Note. — **Columns:** Concentration indices in each filter and their uncertainties (σ_{filter}). The ID# is the identification number assigned to each galaxy in Table 1.

Table 7. Asymmetry Index (A)

ID#	FUV	σ_{FUV}	MUV	σ_{MUV}	F255W	σ_{F255W}	F300W	σ_{F300W}	U	σ_U	B	σ_B	V	σ_V	R	σ_R	F814W	σ_{F814W}
001	0.354	0.022	0.208	0.006	···	···	0.292	0.010	···	···	···	···	···	···	···	···	···	···
002	···	···	···	···	···	···	0.383	0.013	···	···	···	···	···	···	···	···	0.180	0.005
003	···	···	···	···	···	···	···	···	0.373	0.049	0.368	0.025	0.391	0.018	0.226	0.092	···	···
004	···	···	···	···	···	···	0.745	0.005	···	···	···	···	···	···	···	···	0.359	0.003
005	···	···	···	···	···	···	···	···	0.309	0.069	0.479	0.019	0.371	0.017	0.245	0.043	···	···
006	0.635	0.001	0.534	0.001	···	···	0.668	0.005	···	···	···	···	···	···	···	···	0.293	0.006
007	···	···	···	···	···	···	···	···	0.504	0.035	0.541	0.016	0.539	0.011	0.460	0.030	···	···
008	···	···	···	···	···	···	···	···	0.329	0.034	0.273	0.026	0.271	0.008	0.248	0.006	···	···
009	···	···	···	···	···	···	0.264	0.038	···	···	···	···	···	···	···	···	···	···
010	···	···	···	···	···	···	···	···	0.424	0.021	0.416	0.016	0.379	0.009	0.407	0.006	···	···
011	···	···	···	···	···	···	0.306	0.013	···	···	···	···	···	···	···	···	···	···
012	···	···	···	···	···	···	···	···	0.448	0.028	0.524	0.004	0.461	0.004	0.444	0.007	···	···
013	···	···	0.348	0.064	···	···	1.480	0.027	···	···	···	···	···	···	···	···	0.620	0.004
014	0.380	0.009	0.287	0.005	···	···	0.323	0.041	0.235	0.024	0.150	0.036	0.157	0.021	0.171	0.022	0.132	0.018
015	···	···	···	···	···	···	···	···	0.211	0.176	0.235	0.118	0.350	0.074	0.073	0.129	···	···
016	···	···	···	···	···	···	0.593	0.004	···	···	···	···	···	···	···	···	···	···
017	···	···	···	···	···	···	···	···	0.250	0.008	0.162	0.011	0.132	0.006	0.119	0.004	···	···
018	···	···	···	···	···	···	···	···	0.287	0.040	0.277	0.014	0.209	0.035	0.158	0.025	···	···
019	···	···	···	···	···	···	···	···	0.837	0.023	0.956	0.004	0.991	0.003	1.034	0.004	···	···
020	···	···	···	···	···	···	···	···	0.231	0.095	0.292	0.030	0.266	0.022	0.211	0.041	···	···
021	···	···	···	···	···	···	···	···	0.268	0.025	0.188	0.021	0.166	0.012	0.156	0.010	···	···
022	···	···	···	···	···	···	0.330	0.000	···	···	···	···	···	···	···	···	0.132	0.001
023	···	···	···	···	···	···	0.385	0.007	0.402	0.035	0.409	0.008	0.392	0.007	0.373	0.005	0.219	0.003
024	···	···	···	···	···	···	0.341	0.022	···	···	···	···	···	···	···	···	0.206	0.008
025	···	···	···	···	···	···	0.605	0.008	···	···	···	···	···	···	···	···	0.198	0.002
026	···	···	···	···	···	···	0.301	0.034	···	···	···	···	···	···	···	···	···	···
027	0.249	0.287	0.187	0.261	···	···	0.175	0.075	···	···	···	···	···	···	···	···	0.055	0.004
028	···	···	···	···	···	···	0.269	0.001	···	···	···	···	···	···	···	···	0.167	0.000
029	···	···	···	···	···	···	0.407	0.009	···	···	···	···	···	···	···	···	···	···
030	···	···	···	···	···	···	···	···	0.645	0.012	0.661	0.007	0.573	0.006	0.475	0.002	···	···
031	···	···	···	···	···	···	0.594	0.010	···	···	···	···	···	···	···	···	0.284	0.003
032	···	···	···	···	···	···	1.487	0.006	···	···	···	···	···	···	···	···	···	···

Table 7—Continued

ID#	FUV	σ_{FUV}	MUV	σ_{MUV}	F255W	σ_{F255W}	F300W	σ_{F300W}	U	σ_U	B	σ_B	V	σ_V	R	σ_R	F814W	σ_{F814W}
033	···	···	···	···	···	···	0.534	0.011	···	···	···	···	···	···	···	···	0.164	0.003
034	···	···	···	···	···	···	0.502	0.070	···	···	···	···	···	···	···	···	0.372	0.004
035	···	···	···	···	···	···	0.272	0.032	···	···	···	···	···	···	···	···	0.231	0.004
036	···	···	···	···	0.192	0.064	0.095	0.001	···	···	···	···	···	···	···	···	0.040	0.000
037	···	···	···	···	···	···	···	···	0.203	0.174	0.238	0.131	0.408	0.060	0.487	0.056	···	···
038	···	···	···	···	···	···	···	···	0.162	0.034	0.078	0.063	0.146	0.020	0.189	0.018	···	···
039	···	···	···	···	···	···	0.587	0.093	0.174	0.148	0.156	0.102	0.169	0.056	0.122	0.097	···	···
040	···	···	···	···	0.608	0.062	1.134	0.005	···	···	···	···	···	···	···	···	0.837	0.001
041	···	···	···	···	···	···	0.653	0.003	0.357	0.004	0.337	0.000	0.331	0.000	0.309	0.000	···	···
042	···	···	···	···	···	···	0.209	0.006	0.298	0.012	0.293	0.005	0.270	0.005	0.270	0.004	0.253	0.006
043	···	···	···	···	···	···	···	···	0.197	0.019	0.160	0.011	0.135	0.011	0.093	0.030	···	···
044	···	···	···	···	···	···	···	···	0.206	0.046	0.255	0.007	0.211	0.007	0.204	0.010	···	···
045	···	···	···	···	···	···	···	···	0.329	0.019	0.192	0.022	0.245	0.003	0.229	0.005	···	···
046	···	···	···	···	···	···	···	···	0.518	0.012	0.580	0.002	0.510	0.003	0.462	0.002	···	···
047	0.919	0.040	0.298	0.021	···	···	0.209	0.008	···	···	···	···	···	···	···	···	0.034	0.000
048	···	···	···	···	···	···	0.425	0.014	0.394	0.016	0.457	0.007	0.425	0.006	0.420	0.006	0.370	0.013
049	0.511	0.034	0.228	0.012	···	···	···	···	0.141	0.038	0.164	0.005	0.143	0.003	0.060	0.031	···	···
050	···	···	···	···	···	···	1.008	0.029	0.559	0.100	0.689	0.028	0.680	0.021	0.714	0.063	···	···
051	···	···	···	···	···	···	···	···	0.579	0.036	0.468	0.022	0.423	0.016	0.373	0.026	···	···
052	···	···	···	···	···	···	0.860	0.044	0.434	0.027	0.430	0.010	0.347	0.006	0.294	0.007	···	···
053	···	···	···	···	···	···	···	···	0.103	0.059	0.123	0.016	0.123	0.004	0.101	0.006	···	···
054	0.515	0.022	0.420	0.009	···	···	···	···	0.176	0.034	0.174	0.016	0.169	0.008	0.139	0.011	···	···
055	···	···	···	···	···	···	···	···	0.081	0.013	0.098	0.007	0.091	0.001	0.091	0.002	···	···
056	···	···	···	···	···	···	···	···	0.370	0.020	0.414	0.007	0.420	0.006	0.415	0.005	···	···
057	···	···	···	···	···	···	···	···	0.255	0.092	0.396	0.021	0.383	0.022	0.296	0.033	···	···
058	···	···	···	···	···	···	···	···	0.117	0.010	0.124	0.007	0.144	0.004	0.149	0.004	···	···
059	···	···	···	···	···	···	···	···	0.126	0.074	0.224	0.006	0.241	0.003	0.271	0.006	···	···
060	···	···	···	···	···	···	···	···	0.102	0.108	0.303	0.035	0.293	0.006	0.254	0.002	···	···
061	···	···	···	···	···	···	···	···	0.323	0.040	0.246	0.043	0.369	0.013	0.359	0.015	···	···
062	···	···	···	···	···	···	···	···	0.016	0.192	0.067	0.083	0.045	0.041	0.101	0.027	···	···
063	···	···	···	···	···	···	0.780	0.006	···	···	···	···	···	···	···	···	0.427	0.001
064	···	···	···	···	0.699	0.281	0.412	0.104	0.189	0.050	0.237	0.022	0.159	0.025	0.129	0.021	0.120	0.015

Table 7—Continued

ID#	FUV	σ_{FUV}	MUV	σ_{MUV}	F255W	σ_{F255W}	F300W	σ_{F300W}	U	σ_U	B	σ_B	V	σ_V	R	σ_R	F814W	σ_{F814W}
065	···	···	···	···	···	···	···	···	0.591	0.022	0.561	0.009	0.524	0.010	0.452	0.022	···	···
066	···	···	···	···	···	···	···	···	0.063	0.008	0.054	0.001	0.087	0.000	0.052	0.000	···	···
067	···	···	···	···	···	···	0.637	0.008	1.128	0.045	1.433	0.014	1.405	0.013	1.378	0.017	0.455	0.005
068	···	···	···	···	···	···	···	···	0.211	0.007	0.183	0.004	0.178	0.002	0.206	0.000	···	···
069	···	···	···	···	···	···	···	···	0.379	0.072	0.391	0.017	0.325	0.026	0.345	0.015	···	···
070	···	···	···	···	···	···	0.590	0.020	···	···	···	···	···	···	···	···	···	···
071	···	···	···	···	···	···	···	···	0.509	0.039	0.357	0.059	0.433	0.035	0.402	0.050	···	···
072	···	···	···	···	···	···	0.334	0.031	0.365	0.028	0.438	0.003	0.508	0.003	0.464	0.003	···	···
073	···	···	···	···	···	···	···	···	0.486	0.049	0.392	0.033	0.337	0.028	0.337	0.019	···	···
074	···	···	···	···	···	···	···	···	0.223	0.113	0.199	0.094	0.313	0.043	0.303	0.057	···	···
075	···	···	···	···	···	···	···	···	0.345	0.029	0.356	0.009	0.315	0.013	0.332	0.004	···	···
076	···	···	···	···	1.060	0.163	0.716	0.027	0.534	0.039	0.403	0.013	0.378	0.013	0.313	0.016	0.292	0.005
077	···	···	···	···	···	···	···	···	1.074	0.009	0.899	0.012	0.973	0.005	0.937	0.006	···	···
078	···	···	···	···	···	···	0.937	0.003	···	···	···	···	···	···	···	···	···	···
079	···	···	···	···	···	···	···	···	0.334	0.027	0.245	0.014	0.237	0.006	0.218	0.005	···	···
080	···	···	···	···	···	···	···	···	0.475	0.052	0.334	0.064	0.462	0.026	0.406	0.025	···	···
081	···	···	···	···	···	···	0.466	0.000	···	···	···	···	···	···	···	···	0.298	0.000
082	···	···	···	···	···	···	···	···	0.159	0.203	0.115	0.190	0.176	0.117	0.218	0.131	···	···
083	···	···	···	···	···	···	···	···	0.437	0.006	0.352	0.004	0.385	0.002	0.348	0.004	···	···
084	···	···	···	···	···	···	···	···	0.342	0.098	0.137	0.108	0.223	0.056	0.143	0.141	···	···
085	···	···	···	···	···	···	···	···	0.507	0.010	0.353	0.016	0.316	0.014	0.253	0.024	···	···
086	···	···	···	···	···	···	0.491	0.007	···	···	···	···	···	···	···	···	···	···
087	···	···	···	···	···	···	0.738	0.006	0.490	0.022	0.483	0.003	0.444	0.004	0.403	0.006	0.259	0.005
088	···	···	···	···	···	···	0.441	0.019	0.158	0.017	0.128	0.020	0.177	0.006	0.169	0.007	0.196	0.004
089	···	···	···	···	0.041	0.000	0.065	0.000	···	···	···	···	···	···	···	···	0.030	0.000
090	···	···	···	···	···	···	···	···	0.271	0.029	0.249	0.025	0.246	0.010	0.219	0.007	···	···
091	···	···	···	···	···	···	···	···	0.170	0.141	0.221	0.033	0.208	0.020	0.194	0.024	···	···
092	···	···	···	···	···	···	···	···	0.360	0.107	0.476	0.045	0.508	0.027	0.521	0.028	···	···
093	···	···	···	···	···	···	···	···	0.321	0.032	0.263	0.021	0.226	0.015	0.177	0.029	···	···
094	···	···	···	···	···	···	···	···	0.919	0.017	0.687	0.033	0.758	0.011	0.726	0.015	···	···
095	···	···	···	···	···	···	···	···	0.203	0.009	0.143	0.004	0.121	0.002	0.130	0.001	···	···
096	···	···	···	···	0.989	0.009	1.115	0.001	···	···	···	···	···	···	···	···	0.836	0.000

Table 7—Continued

ID#	FUV	σ_{FUV}	MUV	σ_{MUV}	F255W	σ_{F255W}	F300W	σ_{F300W}	U	σ_U	B	σ_B	V	σ_V	R	σ_R	F814W	σ_{F814W}
097	···	···	···	···	···	···	1.060	0.019	0.879	0.013	0.997	0.009	1.036	0.003	0.981	0.008	0.679	0.001
098	···	···	···	···	···	···	0.404	0.030	···	···	···	···	···	···	···	···	0.147	0.016
099	···	···	···	···	···	···	···	···	0.644	0.035	0.550	0.026	0.578	0.023	0.546	0.024	···	···
100	···	···	···	···	···	···	···	···	0.228	0.027	0.217	0.007	0.205	0.002	0.158	0.009	···	···
101	···	···	···	···	···	···	0.646	0.003	0.385	0.015	0.262	0.003	0.221	0.003	0.233	0.003	···	···
102	···	···	···	···	···	···	0.732	0.008	0.555	0.015	0.538	0.023	0.638	0.015	0.587	0.013	···	···
103	···	···	···	···	···	···	0.692	0.006	0.583	0.019	0.491	0.019	0.497	0.008	0.425	0.022	0.657	0.002
104	···	···	···	···	···	···	0.514	0.017	0.187	0.028	0.179	0.018	0.156	0.019	0.182	0.014	0.261	0.018
105	···	···	···	···	···	···	···	···	0.518	0.024	0.431	0.026	0.475	0.013	0.457	0.014	···	···
106	···	···	···	···	···	···	0.549	0.010	0.426	0.007	0.380	0.006	0.346	0.005	0.258	0.016	0.386	0.005
107	···	···	···	···	···	···	···	···	0.072	0.021	0.113	0.007	0.119	0.003	0.069	0.011	···	···
108	···	···	···	···	···	···	0.403	0.010	···	···	···	···	···	···	···	···	0.141	0.006
109	···	···	···	···	···	···	···	···	0.174	0.096	0.135	0.041	0.117	0.026	0.113	0.032	···	···
110	···	···	···	···	···	···	···	···	0.646	0.031	0.398	0.055	0.346	0.052	0.323	0.075	···	···
111	···	···	···	···	···	···	0.653	0.009	···	···	···	···	···	···	···	···	0.574	0.000
112	···	···	···	···	···	···	···	···	0.392	0.009	0.291	0.009	0.291	0.004	0.258	0.006	···	···
113	···	···	···	···	···	···	···	···	0.237	0.093	0.279	0.039	0.258	0.025	0.159	0.044	···	···
114	···	···	···	···	···	···	···	···	0.358	0.047	0.231	0.067	0.297	0.018	0.267	0.042	···	···
115	···	···	···	···	···	···	···	···	0.374	0.033	0.370	0.006	0.321	0.004	0.300	0.007	···	···
116	···	···	···	···	···	···	···	···	0.113	0.118	0.111	0.057	0.113	0.021	0.105	0.028	···	···
117	···	···	···	···	···	···	···	···	0.040	0.018	0.038	0.006	0.035	0.003	0.029	0.002	···	···
118	···	···	···	···	···	···	···	···	0.494	0.020	0.381	0.014	0.345	0.012	0.324	0.015	···	···
119	···	···	···	···	···	···	0.531	0.064	···	···	···	···	···	···	···	···	···	···
120	···	···	···	···	···	···	···	···	0.486	0.000	0.344	0.000	0.297	0.000	0.255	0.004	···	···
121	···	···	···	···	···	···	···	···	0.071	0.028	0.070	0.011	0.057	0.005	0.051	0.003	···	···
122	···	···	···	···	···	···	0.039	0.005	···	···	···	···	···	···	···	···	0.011	0.000
123	···	···	···	···	···	···	0.410	0.005	0.442	0.006	0.488	0.001	0.481	0.000	0.454	0.001	···	···
124	···	···	···	···	···	···	···	···	0.539	0.012	0.450	0.001	0.427	0.002	0.409	0.003	···	···
125	···	···	···	···	···	···	···	···	0.430	0.039	0.336	0.023	0.299	0.010	0.274	0.009	···	···
126	···	···	···	···	···	···	···	···	0.543	0.010	0.377	0.007	0.299	0.009	0.283	0.007	···	···
127	···	···	···	···	···	···	···	···	0.116	0.004	0.101	0.002	0.111	0.002	0.083	0.010	···	···
128	···	···	···	···	···	···	···	···	0.651	0.019	0.734	0.005	0.670	0.004	0.667	0.004	···	···

Table 7—Continued

ID#	FUV	σ_{FUV}	MUV	σ_{MUV}	F255W	σ_{F255W}	F300W	σ_{F300W}	U	σ_U	B	σ_B	V	σ_V	R	σ_R	F814W	σ_{F814W}
129	···	···	···	···	···	···	1.120	0.044	0.239	0.137	0.367	0.041	0.341	0.049	0.299	0.054	···	···
130	···	···	···	···	···	···	···	···	0.078	0.136	0.125	0.030	0.140	0.007	0.131	0.006	···	···
131	···	···	···	···	···	···	···	···	0.234	0.011	0.131	0.009	0.111	0.002	0.095	0.003	···	···
132	···	···	···	···	···	···	···	···	0.299	0.008	0.325	0.003	0.297	0.002	0.272	0.002	···	···
133	···	···	···	···	···	···	···	···	0.671	0.059	0.613	0.040	0.594	0.032	0.547	0.042	···	···
134	···	···	···	···	···	···	0.420	0.027	···	···	···	···	···	···	···	···	0.156	0.004
135	···	···	···	···	···	···	···	···	0.265	0.110	0.294	0.070	0.374	0.018	0.259	0.024	···	···
136	···	···	···	···	···	···	0.383	0.074	0.246	0.090	0.264	0.045	0.286	0.021	0.246	0.044	···	···
137	···	···	···	···	···	···	···	···	0.297	0.037	0.212	0.038	0.217	0.034	0.228	0.023	···	···
138	···	···	···	···	···	···	···	···	0.618	0.039	0.546	0.032	0.380	0.025	0.432	0.039	···	···
139	···	···	···	···	···	···	0.934	0.010	···	···	···	···	···	···	···	···	0.945	0.001
140	···	···	···	···	···	···	0.407	0.003	···	···	···	···	···	···	···	···	0.194	0.001
141	···	···	···	···	···	···	···	···	0.338	0.027	0.287	0.004	0.245	0.003	0.247	0.003	···	···
142	···	···	···	···	···	···	···	···	0.384	0.026	0.272	0.033	0.253	0.017	0.244	0.025	···	···
143	···	···	···	···	···	···	···	···	0.441	0.020	0.329	0.012	0.274	0.013	0.213	0.035	···	···
144	···	···	···	···	···	···	···	···	0.452	0.065	0.181	0.138	0.401	0.034	0.301	0.062	···	···
145	···	···	···	···	···	···	0.664	0.008	···	···	···	···	···	···	···	···	0.317	0.003
146	···	···	···	···	···	···	0.504	0.000	0.209	0.004	0.222	0.001	0.260	0.001	0.225	0.001	0.337	0.000
147	···	···	···	···	···	···	0.775	0.017	···	···	···	···	···	···	···	···	0.353	0.002
148	···	···	···	···	0.782	0.139	1.277	0.011	···	···	···	···	···	···	···	···	1.113	0.000
149	···	···	···	···	0.336	0.161	0.489	0.016	···	···	···	···	···	···	···	···	0.278	0.000
150	···	···	···	···	···	···	···	···	0.350	0.040	0.370	0.026	0.391	0.015	0.314	0.021	···	···
151	···	···	···	···	···	···	0.061	0.000	0.098	0.000	0.069	0.000	0.121	0.000	0.105	0.000	0.042	0.000
152	···	···	···	···	···	···	···	···	0.366	0.085	0.368	0.052	0.402	0.029	0.358	0.038	···	···
153	···	···	···	···	···	···	···	···	0.171	0.008	0.180	0.005	0.197	0.000	0.167	0.001	···	···
154	···	···	···	···	···	···	0.805	0.046	···	···	···	···	···	···	···	···	0.150	0.036
155	···	···	···	···	···	···	···	···	0.651	0.015	0.381	0.062	0.570	0.018	0.577	0.011	···	···
156	···	···	···	···	···	···	···	···	0.168	0.058	0.163	0.024	0.143	0.017	0.116	0.023	···	···
157	0.744	0.017	0.626	0.014	···	···	···	···	0.350	0.074	0.315	0.026	0.263	0.032	0.266	0.026	···	···
158	···	···	···	···	···	···	0.503	0.028	0.052	0.211	0.118	0.069	0.193	0.035	0.169	0.023	0.220	0.001
159	···	···	···	···	···	···	···	···	0.857	0.045	0.958	0.025	0.998	0.007	1.095	0.011	···	···
160	···	···	···	···	···	···	···	···	0.374	0.066	0.353	0.033	0.357	0.013	0.345	0.013	···	···

Table 7—Continued

ID#	FUV	σ_{FUV}	MUV	σ_{MUV}	F255W	σ_{F255W}	F300W	σ_{F300W}	U	σ_U	B	σ_B	V	σ_V	R	σ_R	F814W	σ_{F814W}
161	···	···	···	···	···	···	···	···	0.349	0.007	0.204	0.036	0.254	0.010	0.283	0.011	···	···
162	···	···	···	···	···	···	···	···	0.385	0.014	0.287	0.011	0.246	0.011	0.201	0.015	···	···
163	···	···	···	···	···	···	···	···	0.333	0.037	0.298	0.004	0.248	0.006	0.217	0.007	···	···
164	···	···	···	···	···	···	0.738	0.007	···	···	···	···	···	···	···	···	···	···
165	···	···	···	···	···	···	···	···	0.237	0.108	0.243	0.047	0.262	0.032	0.220	0.047	···	···
166	···	···	···	···	0.590	0.089	0.973	0.015	0.715	0.020	0.556	0.034	0.695	0.009	0.609	0.017	0.640	0.004
167	···	···	···	···	···	···	···	···	0.337	0.042	0.300	0.025	0.327	0.009	0.316	0.010	···	···
168	···	···	···	···	···	···	···	···	0.267	0.106	0.476	0.019	0.425	0.009	0.396	0.005	···	···
169	···	···	···	···	···	···	···	···	0.586	0.011	0.575	0.007	0.575	0.005	0.563	0.004	···	···
170	···	···	···	···	···	···	0.970	0.019	0.240	0.125	0.538	0.020	0.512	0.010	0.359	0.012	0.429	0.003
171	···	···	···	···	···	···	···	···	0.181	0.218	0.409	0.094	0.425	0.080	0.359	0.107	···	···
172	···	···	···	···	···	···	0.660	0.009	0.412	0.008	0.403	0.001	0.395	0.003	0.412	0.001	···	···
173	···	···	···	···	···	···	···	···	0.782	0.028	0.752	0.014	0.736	0.012	0.636	0.027	···	···
174	···	···	···	···	···	···	···	···	0.329	0.025	0.283	0.015	0.259	0.006	0.256	0.006	···	···
175	···	···	···	···	···	···	···	···	0.344	0.025	0.292	0.014	0.264	0.006	0.267	0.004	···	···
176	···	···	···	···	···	···	···	···	0.254	0.151	0.181	0.189	0.458	0.041	0.325	0.084	···	···
177	···	···	···	···	···	···	0.531	0.041	0.147	0.047	0.104	0.027	0.083	0.020	0.085	0.008	0.112	0.011
178	0.765	0.036	0.572	0.028	···	···	0.391	0.023	0.253	0.084	0.314	0.006	0.277	0.006	0.259	0.007	0.121	0.017
179	···	···	···	···	···	···	···	···	0.172	0.034	0.174	0.008	0.158	0.002	0.127	0.004	···	···
180	···	···	···	···	···	···	···	···	0.287	0.017	0.277	0.003	0.245	0.006	0.234	0.003	···	···
181	···	···	···	···	···	···	···	···	0.300	0.026	0.244	0.012	0.201	0.009	0.171	0.012	···	···
182	0.642	0.003	0.616	0.004	···	···	···	···	0.728	0.035	0.664	0.025	0.631	0.019	0.598	0.025	···	···
183	···	···	···	···	···	···	···	···	0.229	0.088	0.220	0.049	0.277	0.011	0.227	0.012	···	···
184	···	···	···	···	···	···	0.927	0.002	···	···	···	···	···	···	···	···	0.319	0.002
185	···	···	···	···	···	···	0.338	0.021	0.158	0.070	0.214	0.014	0.210	0.008	0.195	0.009	···	···
186	···	···	···	···	···	···	0.335	0.004	···	···	···	···	···	···	···	···	0.089	0.000
187	···	···	···	···	0.427	0.129	0.566	0.017	0.121	0.068	0.151	0.019	0.240	0.013	0.263	0.018	0.186	0.004
188	···	···	···	···	0.560	0.101	0.357	0.009	···	···	···	···	···	···	···	···	0.043	0.000
189	···	···	···	···	···	···	0.107	0.002	···	···	···	···	···	···	···	···	···	···
190	0.943	0.041	0.992	0.023	···	···	0.618	0.010	0.135	0.074	0.197	0.023	0.207	0.012	0.147	0.028	···	···
191	···	···	···	···	···	···	0.278	0.005	···	···	···	···	···	···	···	···	···	···
192	···	···	···	···	···	···	0.355	0.006	···	···	···	···	···	···	···	···	0.238	0.004

Table 7—Continued

ID#	FUV	σ_{FUV}	MUV	σ_{MUV}	F255W	σ_{F255W}	F300W	σ_{F300W}	U	σ_U	B	σ_B	V	σ_V	R	σ_R	F814W	σ_{F814W}
193	···	···	···	···	···	···	0.475	0.017	···	···	···	···	···	···	···	···	0.175	0.004
194	···	···	···	···	···	···	0.077	0.000	···	···	···	···	···	···	···	···	···	···
195	···	···	···	···	···	···	0.407	0.009	···	···	···	···	···	···	···	···	···	···
196	···	···	···	···	···	···	···	···	0.456	0.024	0.352	0.033	0.346	0.014	0.360	0.006	···	···
197	0.205	0.269	0.135	0.268	···	···	0.407	0.113	···	···	···	···	···	···	···	···	0.152	0.003
198	···	···	···	···	···	···	0.431	0.022	···	···	···	···	···	···	···	···	···	···
199	0.455	0.007	0.323	0.005	···	···	0.076	0.000	···	···	···	···	···	···	···	···	0.121	0.000

Note. — **Columns:** Asymmetry indices in each filter and their uncertainties (σ_{filter}). The ID# is the identification number assigned to each galaxy in Table 1.

Table 8. Clumpiness Index (S)

ID#	FUV	σ_{FUV}	MUV	σ_{MUV}	F255W	σ_{F255W}	F300W	σ_{F300W}	U	σ_U	B	σ_B	V	σ_V	R	σ_R	F814W	σ_{F814W}
001	0.00	0.000	0.00	0.000	···	···	-0.01	0.038	···	···	···	···	···	···	···	···	···	···
002	···	···	···	···	···	···	0.16	0.194	···	···	···	···	···	···	···	···	0.25	0.187
003	···	···	···	···	···	···	···	···	0.75	0.092	0.44	0.078	0.53	0.057	0.25	0.036	···	···
004	···	···	···	···	···	···	0.57	0.256	···	···	···	···	···	···	···	···	0.27	0.154
005	···	···	···	···	···	···	···	···	0.30	0.041	0.52	0.062	0.51	0.051	0.22	0.026	···	···
006	0.53	0.883	0.32	0.380	···	···	0.63	0.225	···	···	···	···	···	···	···	···	0.37	0.162
007	···	···	···	···	···	···	···	···	0.42	0.034	0.43	0.035	0.42	0.032	0.18	0.015	···	···
008	···	···	···	···	···	···	···	···	0.50	0.037	0.32	0.030	0.32	0.021	0.34	0.017	···	···
009	···	···	···	···	···	···	-0.40	0.468	···	···	···	···	···	···	···	···	···	···
010	···	···	···	···	···	···	···	···	0.67	0.019	0.61	0.028	0.53	0.019	0.64	0.018	···	···
011	···	···	···	···	···	···	0.50	0.332	···	···	···	···	···	···	···	···	···	···
012	···	···	···	···	···	···	···	···	0.27	0.023	0.40	0.031	0.35	0.022	0.38	0.017	···	···
013	···	···	0.57	2.095	···	···	1.01	0.628	···	···	···	···	···	···	···	···	0.32	0.156
014	0.81	1.873	0.28	0.619	···	···	0.61	0.448	0.20	0.017	0.15	0.018	0.17	0.016	0.11	0.013	-0.10	0.144
015	···	···	···	···	···	···	···	···	0.18	0.048	0.38	0.090	0.44	0.082	-0.84	0.094	···	···
016	···	···	···	···	···	···	0.71	0.188	···	···	···	···	···	···	···	···	···	···
017	···	···	···	···	···	···	···	···	0.69	0.030	0.42	0.019	0.32	0.010	0.31	0.007	···	···
018	···	···	···	···	···	···	···	···	0.58	0.038	0.38	0.034	0.31	0.025	0.08	0.010	···	···
019	···	···	···	···	···	···	···	···	0.81	0.024	0.99	0.030	0.97	0.023	0.93	0.018	···	···
020	···	···	···	···	···	···	···	···	0.36	0.037	0.40	0.045	0.38	0.036	0.31	0.027	···	···
021	···	···	···	···	···	···	···	···	0.68	0.039	0.40	0.034	0.33	0.024	0.31	0.019	···	···
022	···	···	···	···	···	···	0.30	0.035	···	···	···	···	···	···	···	···	0.35	0.056
023	···	···	···	···	···	···	0.04	0.076	0.75	0.035	0.65	0.038	0.59	0.028	0.56	0.023	0.16	0.132
024	···	···	···	···	···	···	0.51	0.353	···	···	···	···	···	···	···	···	0.15	0.162
025	···	···	···	···	···	···	0.77	0.265	···	···	···	···	···	···	···	···	0.20	0.104
026	···	···	···	···	···	···	0.61	0.586	···	···	···	···	···	···	···	···	···	···
027	-0.68	12.120	2.12	12.560	···	···	-2.36	1.301	···	···	···	···	···	···	···	···	0.03	0.042
028	···	···	···	···	···	···	0.22	0.050	···	···	···	···	···	···	···	···	0.13	0.039
029	···	···	···	···	···	···	0.58	0.280	···	···	···	···	···	···	···	···	···	···
030	···	···	···	···	···	···	···	···	0.52	0.013	0.60	0.016	0.42	0.010	0.38	0.005	···	···
031	···	···	···	···	···	···	0.52	0.223	···	···	···	···	···	···	···	···	0.17	0.122
032	···	···	···	···	···	···	1.36	0.239	···	···	···	···	···	···	···	···	···	···

Table 8—Continued

ID#	FUV	σ_{FUV}	MUV	σ_{MUV}	F255W	σ_{F255W}	F300W	σ_{F300W}	U	σ_U	B	σ_B	V	σ_V	R	σ_R	F814W	σ_{F814W}
033	···	···	···	···	···	···	0.65	0.247	···	···	···	···	···	···	···	···	0.20	0.116
034	···	···	···	···	···	···	-1.84	1.008	···	···	···	···	···	···	···	···	0.12	0.110
035	···	···	···	···	···	···	0.50	0.456	···	···	···	···	···	···	···	···	0.13	0.149
036	···	···	···	···	-1.91	1.571	0.18	0.076	···	···	···	···	···	···	···	···	0.07	0.016
037	···	···	···	···	···	···	···	···	0.37	0.073	0.25	0.074	0.53	0.087	0.67	0.078	···	···
038	···	···	···	···	···	···	···	···	0.18	0.044	0.15	0.042	0.22	0.037	0.35	0.038	···	···
039	···	···	···	···	···	···	0.08	0.333	0.26	0.051	0.22	0.056	0.37	0.059	0.11	0.028	···	···
040	···	···	···	···	1.18	1.019	1.08	0.318	···	···	···	···	···	···	···	···	0.57	0.136
041	···	···	···	···	···	···	0.79	0.191	0.36	0.007	0.45	0.010	0.41	0.008	0.39	0.007	···	···
042	···	···	···	···	···	···	0.12	0.086	0.29	0.011	0.19	0.010	0.22	0.009	0.18	0.007	0.25	0.105
043	···	···	···	···	···	···	···	···	0.33	0.021	0.29	0.020	0.18	0.011	0.06	0.004	···	···
044	···	···	···	···	···	···	···	···	0.17	0.021	0.30	0.026	0.20	0.015	0.19	0.011	···	···
045	···	···	···	···	···	···	···	···	0.27	0.021	0.18	0.019	0.28	0.019	0.27	0.016	···	···
046	···	···	···	···	···	···	···	···	0.28	0.009	0.27	0.014	0.32	0.013	0.38	0.012	···	···
047	1.18	6.197	0.45	1.766	···	···	0.37	0.185	···	···	···	···	···	···	···	···	0.07	0.015
048	···	···	···	···	···	···	0.22	0.160	0.32	0.013	0.48	0.020	0.41	0.016	0.50	0.015	0.58	0.226
049	1.89	5.406	0.37	1.095	···	···	···	···	0.17	0.018	0.28	0.023	0.20	0.013	-0.01	0.003	···	···
050	···	···	···	···	···	···	-0.30	0.313	0.61	0.064	0.57	0.100	0.85	0.111	1.56	0.124	···	···
051	···	···	···	···	···	···	···	···	0.49	0.036	0.57	0.078	0.62	0.079	0.35	0.054	···	···
052	···	···	···	···	···	···	0.91	0.502	0.45	0.026	0.46	0.025	0.43	0.017	0.35	0.011	···	···
053	···	···	···	···	···	···	···	···	0.07	0.014	0.15	0.017	0.21	0.012	0.14	0.007	···	···
054	1.38	4.293	0.61	1.081	···	···	···	···	0.16	0.014	0.15	0.014	0.10	0.008	0.01	0.002	···	···
055	···	···	···	···	···	···	···	···	0.10	0.009	0.10	0.008	0.12	0.006	0.09	0.004	···	···
056	···	···	···	···	···	···	···	···	0.50	0.021	0.72	0.029	0.74	0.025	0.62	0.019	···	···
057	···	···	···	···	···	···	···	···	0.53	0.046	0.87	0.067	0.68	0.050	0.46	0.039	···	···
058	···	···	···	···	···	···	···	···	0.19	0.011	0.12	0.011	0.18	0.011	0.12	0.008	···	···
059	···	···	···	···	···	···	···	···	0.15	0.024	0.38	0.033	0.38	0.021	0.36	0.014	···	···
060	···	···	···	···	···	···	···	···	0.16	0.035	0.25	0.036	0.41	0.026	0.56	0.019	···	···
061	···	···	···	···	···	···	···	···	0.71	0.062	0.44	0.058	0.62	0.056	0.70	0.050	···	···
062	···	···	···	···	···	···	···	···	0.00	0.001	0.17	0.051	0.11	0.028	0.21	0.030	···	···
063	···	···	···	···	···	···	1.08	0.245	···	···	···	···	···	···	···	···	0.57	0.099
064	···	···	···	···	0.18	0.799	0.00	0.068	0.02	0.011	0.19	0.024	0.09	0.010	0.09	0.007	0.16	0.053

Table 8—Continued

ID#	FUV	σ_{FUV}	MUV	σ_{MUV}	F255W	σ_{F255W}	F300W	σ_{F300W}	U	σ_U	B	σ_B	V	σ_V	R	σ_R	F814W	σ_{F814W}
065	···	···	···	···	···	···	···	···	0.62	0.037	0.51	0.034	0.40	0.023	0.18	0.012	···	···
066	···	···	···	···	···	···	···	···	0.28	0.010	0.15	0.006	0.15	0.003	0.16	0.003	···	···
067	···	···	···	···	···	···	0.81	0.217	1.92	0.061	1.62	0.077	1.50	0.065	1.44	0.060	0.32	0.168
068	···	···	···	···	···	···	···	···	0.19	0.007	0.14	0.007	0.13	0.006	0.17	0.005	···	···
069	···	···	···	···	···	···	···	···	0.78	0.063	0.85	0.088	0.61	0.065	0.78	0.065	···	···
070	···	···	···	···	···	···	-0.01	0.047	···	···	···	···	···	···	···	···	···	···
071	···	···	···	···	···	···	···	···	1.12	0.078	0.77	0.085	1.08	0.095	0.81	0.069	···	···
072	···	···	···	···	···	···	0.43	0.394	0.54	0.029	0.63	0.030	0.53	0.018	0.51	0.013	···	···
073	···	···	···	···	···	···	···	···	0.90	0.058	0.55	0.058	0.47	0.047	0.45	0.040	···	···
074	···	···	···	···	···	···	···	···	0.26	0.040	0.28	0.056	0.34	0.053	0.28	0.039	···	···
075	···	···	···	···	···	···	···	···	0.34	0.027	0.35	0.030	0.28	0.020	0.37	0.018	···	···
076	···	···	···	···	5.30	3.189	0.96	0.575	0.73	0.050	0.57	0.053	0.54	0.044	0.46	0.036	0.07	0.100
077	···	···	···	···	···	···	···	···	1.08	0.030	0.75	0.035	0.76	0.030	0.64	0.025	···	···
078	···	···	···	···	···	···	0.98	0.194	···	···	···	···	···	···	···	···	···	···
079	···	···	···	···	···	···	···	···	0.55	0.027	0.44	0.028	0.39	0.022	0.34	0.017	···	···
080	···	···	···	···	···	···	···	···	0.91	0.057	0.40	0.047	0.52	0.043	0.53	0.039	···	···
081	···	···	···	···	···	···	0.61	0.055	···	···	···	···	···	···	···	···	0.29	0.032
082	···	···	···	···	···	···	···	···	0.18	0.059	0.52	0.123	0.72	0.118	0.53	0.087	···	···
083	···	···	···	···	···	···	···	···	0.47	0.008	0.43	0.011	0.53	0.011	0.47	0.010	···	···
084	···	···	···	···	···	···	···	···	0.71	0.059	0.22	0.046	0.49	0.069	0.49	0.059	···	···
085	···	···	···	···	···	···	···	···	0.62	0.029	0.43	0.030	0.36	0.023	0.31	0.018	···	···
086	···	···	···	···	···	···	0.60	0.258	···	···	···	···	···	···	···	···	···	···
087	···	···	···	···	···	···	-0.13	0.142	0.54	0.024	0.46	0.027	0.37	0.021	0.26	0.014	0.23	0.158
088	···	···	···	···	···	···	0.46	0.376	0.15	0.023	0.08	0.017	0.13	0.014	0.13	0.011	0.12	0.077
089	···	···	···	···	0.10	0.035	0.12	0.021	···	···	···	···	···	···	···	···	0.11	0.015
090	···	···	···	···	···	···	···	···	0.42	0.032	0.53	0.039	0.50	0.028	0.47	0.021	···	···
091	···	···	···	···	···	···	···	···	0.09	0.028	0.38	0.062	0.29	0.041	0.26	0.031	···	···
092	···	···	···	···	···	···	···	···	0.44	0.054	0.67	0.079	0.72	0.063	0.88	0.058	···	···
093	···	···	···	···	···	···	···	···	0.20	0.013	0.33	0.020	0.21	0.013	0.11	0.007	···	···
094	···	···	···	···	···	···	···	···	1.21	0.053	0.76	0.056	0.83	0.050	0.81	0.043	···	···
095	···	···	···	···	···	···	···	···	0.13	0.007	0.10	0.006	0.06	0.004	0.07	0.003	···	···
096	···	···	···	···	0.69	0.342	1.07	0.138	···	···	···	···	···	···	···	···	0.57	0.058

Table 8—Continued

ID#	FUV	σ_{FUV}	MUV	σ_{MUV}	F255W	σ_{F255W}	F300W	σ_{F300W}	U	σ_U	B	σ_B	V	σ_V	R	σ_R	F814W	σ_{F814W}
097	···	···	···	···	···	···	1.60	0.395	1.55	0.049	1.58	0.043	1.75	0.028	1.72	0.021	1.39	0.095
098	···	···	···	···	···	···	0.97	0.759	···	···	···	···	···	···	···	···	0.27	0.293
099	···	···	···	···	···	···	···	···	0.62	0.029	0.51	0.038	0.32	0.027	0.32	0.025	···	···
100	···	···	···	···	···	···	···	···	0.47	0.032	0.39	0.029	0.32	0.018	0.23	0.011	···	···
101	···	···	···	···	···	···	0.47	0.169	0.40	0.016	0.43	0.023	0.40	0.020	0.34	0.015	···	···
102	···	···	···	···	···	···	0.81	0.372	0.77	0.040	0.74	0.058	0.80	0.053	0.81	0.045	···	···
103	···	···	···	···	···	···	0.91	0.248	1.54	0.045	1.44	0.052	1.51	0.042	1.12	0.029	0.75	0.150
104	···	···	···	···	···	···	-0.37	0.228	0.14	0.017	0.09	0.018	0.05	0.011	0.09	0.012	0.19	0.152
105	···	···	···	···	···	···	···	···	0.95	0.053	0.59	0.052	0.48	0.039	0.37	0.028	···	···
106	···	···	···	···	···	···	0.21	0.159	0.28	0.130	0.11	0.098	0.14	0.086	0.05	0.047	0.18	0.100
107	···	···	···	···	···	···	···	···	0.04	0.012	0.10	0.015	0.08	0.008	0.03	0.003	···	···
108	···	···	···	···	···	···	-0.32	0.217	···	···	···	···	···	···	···	···	0.24	0.155
109	···	···	···	···	···	···	···	···	0.51	0.049	0.26	0.036	0.07	0.014	0.13	0.015	···	···
110	···	···	···	···	···	···	···	···	1.10	0.085	0.63	0.084	0.53	0.066	0.46	0.051	···	···
111	···	···	···	···	···	···	0.54	0.192	···	···	···	···	···	···	···	···	0.20	0.030
112	···	···	···	···	···	···	···	···	0.39	0.015	0.36	0.018	0.40	0.017	0.42	0.017	···	···
113	···	···	···	···	···	···	···	···	0.42	0.058	0.39	0.065	0.38	0.052	0.20	0.035	···	···
114	···	···	···	···	···	···	···	···	0.65	0.051	0.51	0.055	0.34	0.037	0.29	0.027	···	···
115	···	···	···	···	···	···	···	···	0.56	0.030	0.49	0.033	0.39	0.024	0.34	0.018	···	···
116	···	···	···	···	···	···	···	···	1.28	0.084	0.91	0.075	1.04	0.061	0.93	0.047	···	···
117	···	···	···	···	···	···	···	···	-0.07	0.006	0.00	0.001	0.02	0.001	0.02	0.001	···	···
118	···	···	···	···	···	···	···	···	0.99	0.030	0.69	0.036	0.61	0.029	0.55	0.024	···	···
119	···	···	···	···	···	···	0.99	0.794	···	···	···	···	···	···	···	···	···	···
120	···	···	···	···	···	···	···	···	0.61	0.012	0.45	0.013	0.37	0.010	0.25	0.007	···	···
121	···	···	···	···	···	···	···	···	0.16	0.012	0.08	0.007	0.08	0.005	0.11	0.004	···	···
122	···	···	···	···	···	···	0.01	0.033	···	···	···	···	···	···	···	···	0.03	0.011
123	···	···	···	···	···	···	0.40	0.158	0.79	0.018	0.65	0.018	0.56	0.014	0.50	0.011	···	···
124	···	···	···	···	···	···	···	···	0.64	0.021	0.53	0.025	0.47	0.020	0.37	0.016	···	···
125	···	···	···	···	···	···	···	···	0.78	0.042	0.53	0.038	0.48	0.028	0.44	0.021	···	···
126	···	···	···	···	···	···	···	···	0.79	0.020	0.69	0.025	0.61	0.021	0.61	0.017	···	···
127	···	···	···	···	···	···	···	···	0.13	0.010	0.09	0.010	0.09	0.008	0.05	0.005	···	···
128	···	···	···	···	···	···	···	···	0.90	0.031	0.66	0.030	0.49	0.022	0.45	0.017	···	···

Table 8—Continued

ID#	FUV	σ_{FUV}	MUV	σ_{MUV}	F255W	σ_{F255W}	F300W	σ_{F300W}	U	σ_U	B	σ_B	V	σ_V	R	σ_R	F814W	σ_{F814W}
129	···	···	···	···	···	···	1.37	0.890	0.43	0.050	0.64	0.080	0.72	0.071	0.55	0.054	···	···
130	···	···	···	···	···	···	···	···	0.00	0.003	0.18	0.019	0.21	0.013	0.16	0.008	···	···
131	···	···	···	···	···	···	···	···	0.60	0.034	0.24	0.017	0.17	0.009	0.14	0.006	···	···
132	···	···	···	···	···	···	···	···	0.14	0.005	0.13	0.006	0.24	0.007	0.19	0.005	···	···
133	···	···	···	···	···	···	···	···	1.70	0.058	1.63	0.073	1.69	0.063	1.70	0.054	···	···
134	···	···	···	···	···	···	1.62	0.462	···	···	···	···	···	···	···	···	0.90	0.134
135	···	···	···	···	···	···	···	···	0.75	0.068	0.46	0.047	0.35	0.027	0.21	0.014	···	···
136	···	···	···	···	···	···	-0.69	0.844	0.25	0.042	0.33	0.055	0.40	0.054	0.37	0.046	···	···
137	···	···	···	···	···	···	···	···	0.59	0.056	0.45	0.058	0.35	0.044	0.46	0.044	···	···
138	···	···	···	···	···	···	···	···	1.20	0.033	0.74	0.042	0.81	0.033	0.52	0.030	···	···
139	···	···	···	···	···	···	1.92	0.302	···	···	···	···	···	···	···	···	0.93	0.120
140	···	···	···	···	···	···	0.55	0.120	···	···	···	···	···	···	···	···	0.31	0.079
141	···	···	···	···	···	···	···	···	0.70	0.030	0.51	0.030	0.41	0.021	0.38	0.017	···	···
142	···	···	···	···	···	···	···	···	0.78	0.059	0.49	0.059	0.65	0.057	0.65	0.050	···	···
143	···	···	···	···	···	···	···	···	0.71	0.035	0.55	0.045	0.49	0.037	0.39	0.029	···	···
144	···	···	···	···	···	···	···	···	0.21	0.054	0.15	0.056	0.45	0.081	0.12	0.035	···	···
145	···	···	···	···	···	···	0.77	0.307	···	···	···	···	···	···	···	···	0.38	0.149
146	···	···	···	···	···	···	0.55	0.054	0.35	0.006	0.34	0.010	0.37	0.008	0.32	0.008	0.27	0.042
147	···	···	···	···	···	···	1.19	0.579	···	···	···	···	···	···	···	···	0.37	0.126
148	···	···	···	···	-1.95	1.696	0.28	0.218	···	···	···	···	···	···	···	···	0.44	0.081
149	···	···	···	···	2.51	2.472	0.56	0.333	···	···	···	···	···	···	···	···	0.21	0.048
150	···	···	···	···	···	···	···	···	0.33	0.028	0.41	0.037	0.46	0.032	0.42	0.025	···	···
151	···	···	···	···	···	···	0.07	0.012	0.11	0.001	0.10	0.002	0.10	0.002	0.08	0.001	0.21	0.023
152	···	···	···	···	···	···	···	···	0.84	0.065	0.55	0.072	0.49	0.058	0.38	0.043	···	···
153	···	···	···	···	···	···	···	···	0.09	0.006	0.12	0.008	0.14	0.007	0.13	0.005	···	···
154	···	···	···	···	···	···	2.62	0.927	···	···	···	···	···	···	···	···	0.35	0.512
155	···	···	···	···	···	···	···	···	0.18	0.027	-0.06	0.016	0.05	0.011	0.16	0.015	···	···
156	···	···	···	···	···	···	···	···	0.23	0.031	0.17	0.025	0.14	0.015	0.08	0.009	···	···
157	1.32	3.058	1.01	1.514	···	···	···	···	0.57	0.045	0.53	0.060	0.41	0.047	0.44	0.042	···	···
158	···	···	···	···	···	···	0.75	0.500	-0.15	0.028	1.46	0.092	1.79	0.071	1.86	0.054	0.44	0.124
159	···	···	···	···	···	···	···	···	1.35	0.040	1.21	0.047	1.16	0.037	1.12	0.030	···	···
160	···	···	···	···	···	···	···	···	0.59	0.051	0.47	0.053	0.41	0.040	0.45	0.036	···	···

Table 8—Continued

ID#	FUV	σ_{FUV}	MUV	σ_{MUV}	F255W	σ_{F255W}	F300W	σ_{F300W}	U	σ_U	B	σ_B	V	σ_V	R	σ_R	F814W	σ_{F814W}
161	···	···	···	···	···	···	···	···	0.42	0.040	0.20	0.034	0.21	0.030	0.22	0.026	···	···
162	···	···	···	···	···	···	···	···	0.64	0.028	0.45	0.026	0.38	0.020	0.30	0.014	···	···
163	···	···	···	···	···	···	···	···	0.69	0.038	0.58	0.039	0.41	0.025	0.36	0.020	···	···
164	···	···	···	···	···	···	0.63	0.255	···	···	···	···	···	···	···	···	···	···
165	···	···	···	···	···	···	···	···	0.36	0.062	0.47	0.079	0.56	0.068	0.31	0.043	···	···
166	···	···	···	···	-0.31	0.623	0.73	0.371	0.48	0.033	0.27	0.030	0.50	0.035	0.40	0.028	0.22	0.136
167	···	···	···	···	···	···	···	···	0.74	0.036	0.57	0.033	0.58	0.026	0.57	0.020	···	···
168	···	···	···	···	···	···	···	···	0.29	0.040	0.45	0.039	0.37	0.023	0.35	0.016	···	···
169	···	···	···	···	···	···	···	···	0.62	0.013	0.58	0.019	0.55	0.016	0.51	0.013	···	···
170	···	···	···	···	···	···	4.48	0.552	0.68	0.082	1.26	0.101	0.98	0.053	0.73	0.033	0.38	0.137
171	···	···	···	···	···	···	···	···	0.22	0.064	0.50	0.120	0.61	0.094	0.60	0.067	···	···
172	···	···	···	···	···	···	0.92	0.295	0.37	0.012	0.38	0.015	0.34	0.012	0.35	0.010	···	···
173	···	···	···	···	···	···	···	···	0.88	0.032	0.69	0.038	0.63	0.032	0.48	0.025	···	···
174	···	···	···	···	···	···	···	···	0.54	0.024	0.41	0.022	0.35	0.015	0.32	0.011	···	···
175	···	···	···	···	···	···	···	···	0.45	0.032	0.31	0.026	0.26	0.017	0.25	0.013	···	···
176	···	···	···	···	···	···	···	···	0.28	0.038	-0.11	0.026	0.52	0.049	0.20	0.025	···	···
177	···	···	···	···	···	···	0.88	0.563	0.05	0.011	0.13	0.022	0.08	0.014	0.12	0.014	0.00	0.029
178	2.80	6.867	1.45	2.758	···	···	0.67	0.556	0.18	0.031	0.46	0.056	0.36	0.040	0.34	0.031	0.21	0.251
179	···	···	···	···	···	···	···	···	0.18	0.016	0.20	0.017	0.19	0.011	0.15	0.007	···	···
180	···	···	···	···	···	···	···	···	0.26	0.016	0.35	0.021	0.27	0.015	0.27	0.013	···	···
181	···	···	···	···	···	···	···	···	0.57	0.023	0.45	0.027	0.31	0.017	0.30	0.013	···	···
182	0.42	1.162	0.70	0.954	···	···	···	···	0.71	0.028	0.75	0.038	0.73	0.034	0.83	0.032	···	···
183	···	···	···	···	···	···	···	···	0.22	0.042	0.05	0.020	0.28	0.028	0.19	0.017	···	···
184	···	···	···	···	···	···	0.54	0.134	···	···	···	···	···	···	···	···	0.36	0.148
185	···	···	···	···	···	···	-0.17	0.266	0.34	0.037	0.42	0.042	0.42	0.030	0.39	0.023	···	···
186	···	···	···	···	···	···	0.69	0.202	···	···	···	···	···	···	···	···	0.13	0.019
187	···	···	···	···	2.18	2.034	0.03	0.098	0.17	0.022	0.35	0.037	0.38	0.030	0.46	0.026	0.20	0.124
188	···	···	···	···	0.17	0.414	0.30	0.127	···	···	···	···	···	···	···	···	0.09	0.019
189	···	···	···	···	···	···	0.13	0.056	···	···	···	···	···	···	···	···	···	···
190	0.74	3.996	0.39	1.448	···	···	1.20	0.345	-0.18	0.025	0.21	0.028	0.23	0.021	0.11	0.012	···	···
191	···	···	···	···	···	···	0.19	0.099	···	···	···	···	···	···	···	···	···	···
192	···	···	···	···	···	···	0.38	0.156	···	···	···	···	···	···	···	···	0.18	0.096

Table 8—Continued

ID#	FUV	σ_{FUV}	MUV	σ_{MUV}	F255W	σ_{F255W}	F300W	σ_{F300W}	U	σ_U	B	σ_B	V	σ_V	R	σ_R	F814W	σ_{F814W}
193	···	···	···	···	···	···	0.59	0.491	···	···	···	···	···	···	···	···	0.05	0.061
194	···	···	···	···	···	···	0.09	0.020	···	···	···	···	···	···	···	···	···	···
195	···	···	···	···	···	···	0.60	0.324	···	···	···	···	···	···	···	···	···	···
196	···	···	···	···	···	···	···	···	0.60	0.043	0.49	0.046	0.41	0.030	0.53	0.027	···	···
197	5.23	26.140	5.57	13.910	···	···	-0.07	0.387	···	···	···	···	···	···	···	···	0.38	0.150
198	···	···	···	···	···	···	0.48	0.405	···	···	···	···	···	···	···	···	···	···
199	0.83	1.892	0.60	0.790	···	···	0.07	0.020	···	···	···	···	···	···	···	···	0.12	0.033

Note. — **Columns:** Clumpiness indices in each filter and their uncertainties (σ_{filter}). The ID# is the identification number assigned to each galaxy in Table 1.

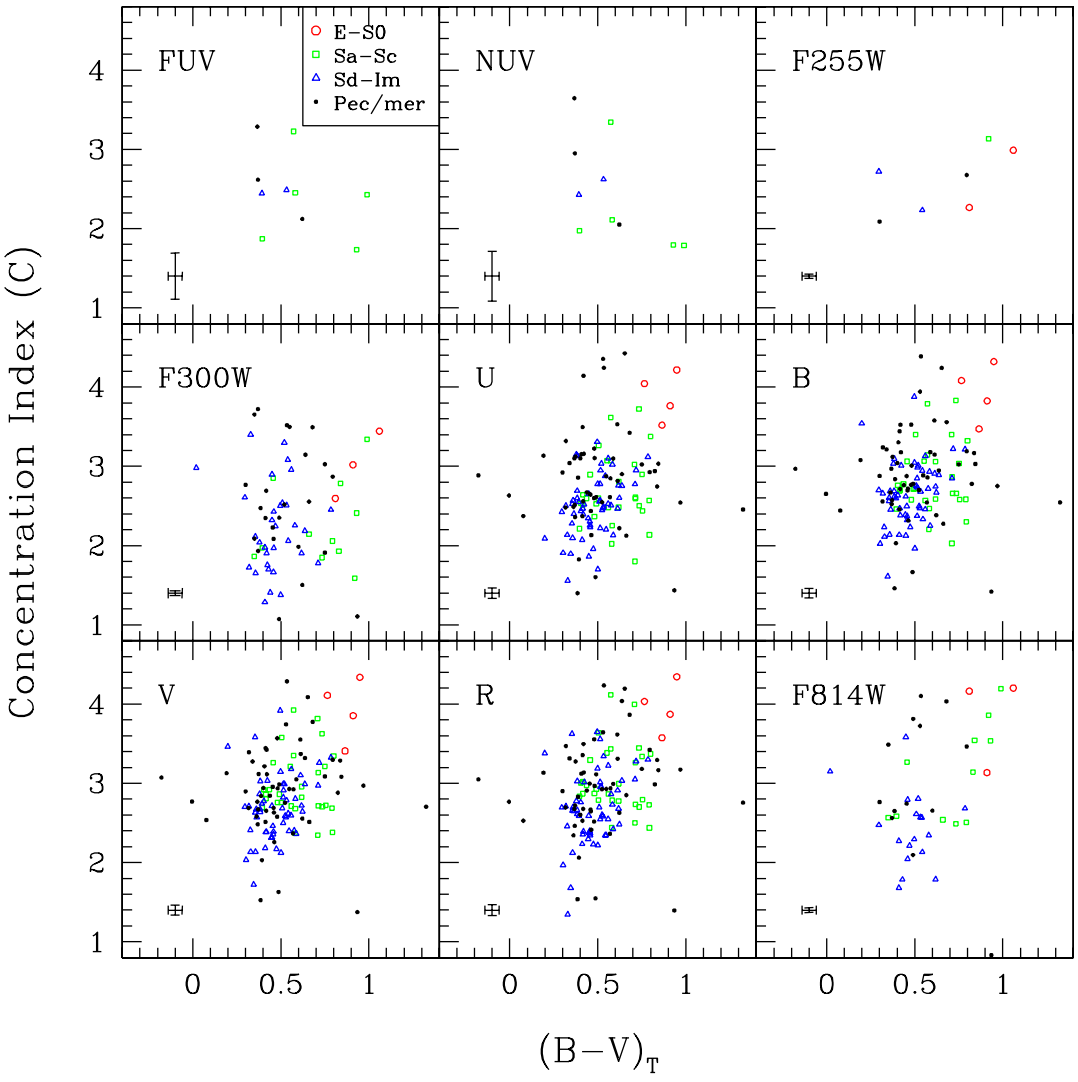

Figure 15 Concentration index as a function of total $(B-V)$ color. Each panel contains data from an individual filter, as labeled in the upper-left corner of the panel. The symbols are coded by galaxy type, as shown in the legend in the upper left (FUV) panel. Vertical error bars in the lower left corner of each panel represent the median error on the individual concentration index values. In general, galaxies tend to be more concentrated with redder color. Early-type (E-S0) galaxies are the reddest and most concentrated, with later galaxy types becoming increasingly bluer and less concentrated.

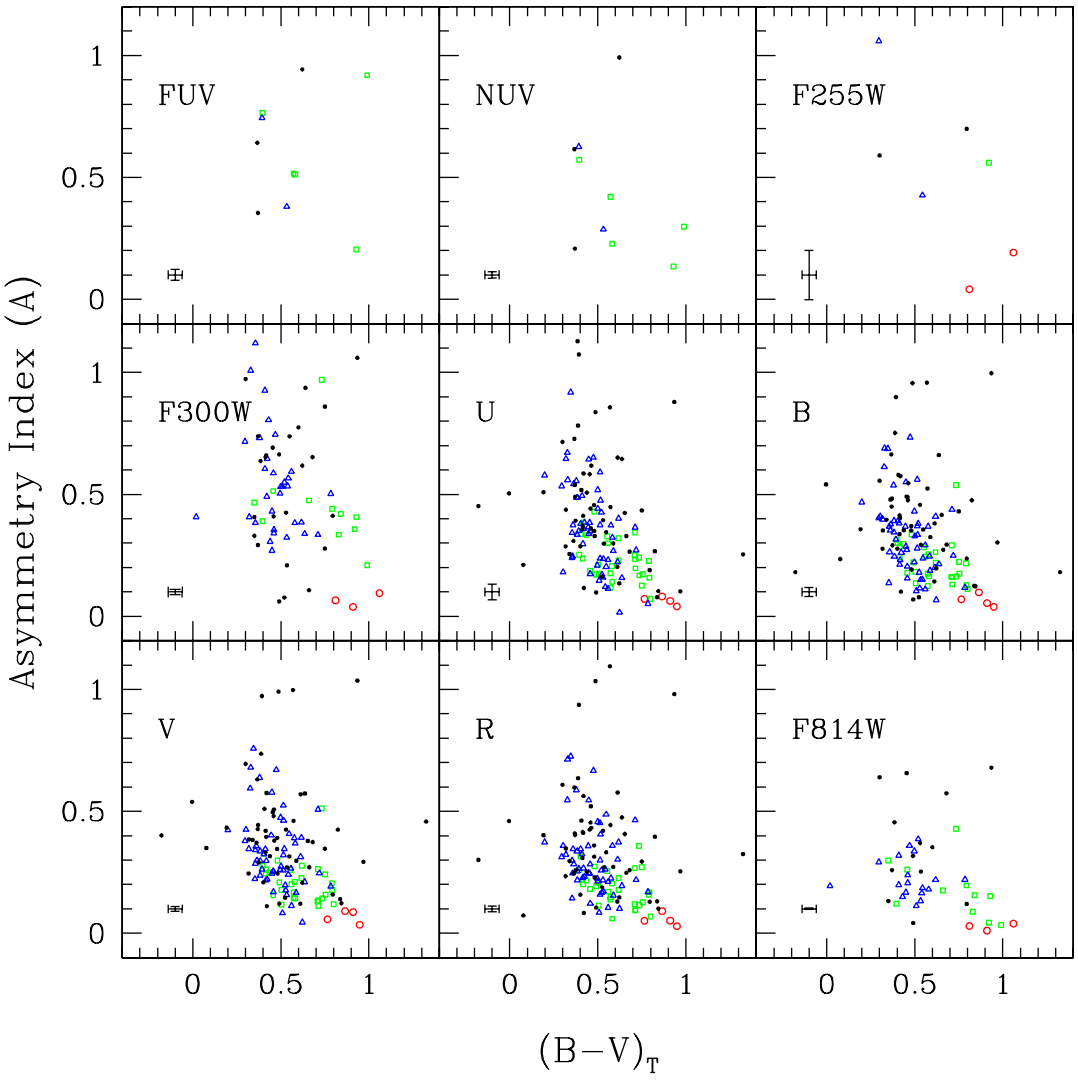

Figure 16 Asymmetry index as a function of total $(B-V)$ color. The symbols are coded by galaxy type, as in Figure 15. Error bars in the lower left corner of each panel represent the median error on the individual asymmetry values. In general, galaxies tend to be less asymmetric with redder color. Early-type (E-S0) galaxies are the reddest and most symmetric, with later galaxy types becoming increasingly bluer and more asymmetric. Peculiar/merging galaxies tend to in general be slightly bluer and more asymmetric than normal galaxies.

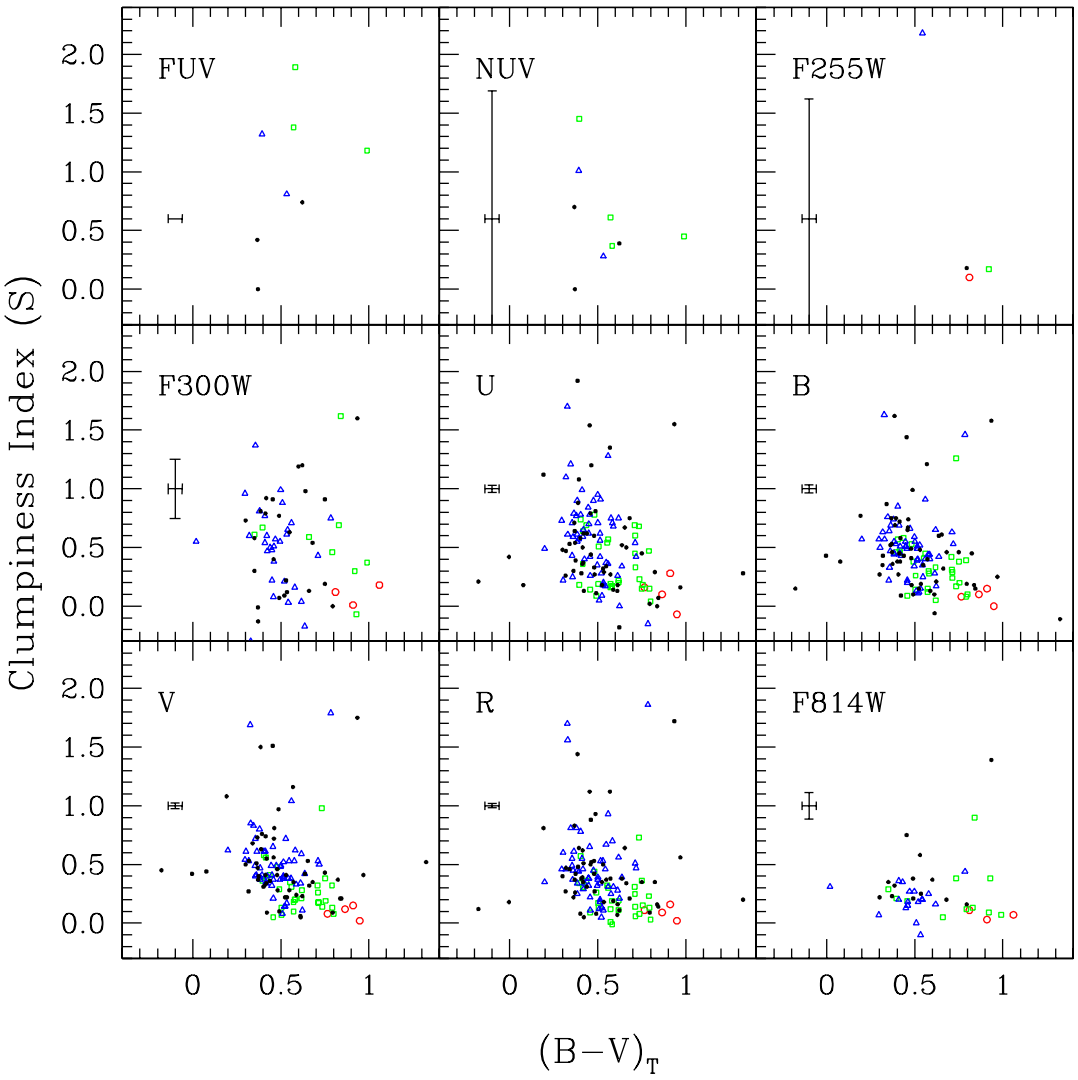

Figure 17 Clumpiness index as a function of total $(B-V)$ color. The symbols are coded by galaxy type, as in Figure 15. Error bars in the lower left corner of each panel represent the median error on the individual clumpiness values. No error bar is plotted in the upper left (FUV) panel because the error bar is larger than the panel itself. The large errors in S for FUV and NUV are due to the low resolution of the GALEX images (stellar FWHM $\gtrsim 5''$), while the large errors in F255W and F300W are likely due to the low signal-to-noise ratio of galaxies in these filters, and the significant CTE effects in WFPC2. In general, galaxies tend to be less clumpy with redder color. Early-type (E-S0) galaxies are the reddest and smoothest, with later galaxy types becoming increasingly bluer and more clumpy. This correlation is tighter at longer wavelengths, with a larger spread in S at shorter wavelengths. Blue galaxies are also more clumpy at shorter wavelengths than they are at longer wavelengths. Peculiar/merging galaxies tend to be in general slightly bluer and more clumpy than normal galaxies.

Figures 18, 19, and 20 show the C, A, and S parameters, respectively, of each galaxy as a function of galaxy type. As for Figures 15–17, separate panels show results from different filters. Median values of the CAS parameters in a particular filter within a particular type-bin are indicated with large symbols, and the spread of the data points is indicated by the 25–75% quartile range, represented by the vertical error bars. These median C, A, and S values are also listed in Tables 9, 10, and 11, respectively. Data from images where the galaxy was particularly faint were not included in the medians. In all three plots, the spread in the CAS parameters increases toward later galaxy type. There are few objects in the GALEX FUV and NUV filters, as well as the HST F255W filter, but the other filters show a trend of decreasing C, and increasing A and S toward later type for normal galaxies (E through Im). The slope of the dependence of A and S on type of normal galaxies decreases toward longer wavelengths, such that late-type galaxies are more asymmetric and clumpy at shorter wavelengths than at longer wavelengths, which is also seen in Figures 15–17. The peculiar/merging galaxies are plotted as their sub-types, as defined in Section 3.1, in Figures 18–20. Merging galaxies (solid triangles) tend to be in general much less concentrated and much more asymmetric and clumpy than any other galaxy type. Pre-merging galaxies (solid circles) have similar or slightly lower C and higher A and S values than normal mid- to late-type galaxies, because these galaxies are currently only slightly distorted by the tidal interactions with their neighbors. Minor mergers (solid squares) are slightly more concentrated and less asymmetric and clumpy than the pre-mergers, because the low mass of the smaller interacting galaxy has likely less of an effect on the brighter, larger galaxy's light distribution than a neighboring galaxy of similar size would have. Merger remnants (asterisks) are more concentrated, more asymmetric, and similar in clumpiness to pre-mergers and normal mid- to late-type galaxies. Peculiar galaxies (crosses) have similar CAS values as normal mid- to late-type galaxies, although they appear slightly more concentrated and more asymmetric in some filters.

Histograms of the distribution of the CAS parameters as separated by galaxy type are presented in Figure 21. These distributions demonstrate the amount of overlap in the CAS parameters between different galaxy type bins, and therefore are relevant to the reliability of using these parameters to classify galaxies. The left panels of this plot contain all data in filters with wavelengths shortward of the Balmer break ($\lambda_c < 400$ nm), and the right panels contain all data in filters with wavelengths longward of the Balmer break ($\lambda_c > 400$ nm). Measurements with excessively large uncertainties ($\sigma > 1.5$) in C, A, or S, were not included in this plot. There is a large amount of overlap between the concentration indices of all galaxy types, particularly at shorter wavelengths. Early galaxy types are better separated from other galaxy types by concentration at longer wavelengths, although there is still a significant amount of overlap for smaller values of C. Very few galaxies with types later than S0 have values of C $\gtrsim 4$. Therefore, there is a high probability that a galaxy

Table 9. Median C For Each Galaxy Type Bin

Type	FUV	NUV	F255W	F300W	*U*	*B*	*V*	*R*	F814W
E–S0	···	···	2.27	3.02	3.90	3.95	3.98	3.95	3.65
···	···	···	···	0.42	0.24	0.28	0.30	0.23	0.55
Sa–Sc	2.45	···	3.14	2.10	2.60	2.72	2.86	2.92	3.18
···	0.02	···	···	0.39	0.21	0.24	0.25	0.28	0.49
Sd–Im	2.49	···	···	2.25	2.50	2.63	2.67	2.65	2.40
···	0.02	···	···	0.34	0.26	0.27	0.29	0.32	0.28
pM	2.12	···	···	2.35	2.56	2.72	2.58	2.74	2.86
···	···	···	···	0.13	0.19	0.28	0.25	0.28	0.53
mM	···	···	···	1.94	3.03	3.03	3.08	3.17	2.56
···	···	···	···	0.79	0.94	0.91	0.81	0.76	1.25
M	···	···	2.30	1.44	2.11	2.10	2.00	1.96	1.47
···	···	···	0.15	0.67	0.61	0.57	0.55	0.56	0.79
MR	3.29	···	···	2.85	3.02	3.15	3.22	3.18	3.22
···	···	···	···	0.44	0.15	0.19	0.25	0.27	0.39
P	2.62	···	···	2.90	2.67	2.88	2.93	2.93	3.13
···	···	···	···	0.59	0.28	0.17	0.18	0.22	0.50

Note. — Median concentration indices in each type-bin and filter. Galaxies that were barely visible in the images of a particular filter were not included in the median. The second line for each type-bin lists half the range of the data within the 25 and 75% quartiles. When only one data point was available, the value listed is for that data point and the associated quartile range cannot be computed. The peculiar/merging galaxies are broken up into sub-types as follows: pre-merger (pM), minor merger (mM), merger (M), merger remnant (MR), and peculiar (P). In general, C increases with increasing rest-frame wavelength.

Table 10. Median A For Each Galaxy Type Bin

Type	FUV	NUV	F255W	F300W	*U*	*B*	*V*	*R*	F814W
E–S0	···	···	0.04	0.06	0.07	0.06	0.07	0.05	0.04
···	···	···	···	0.03	0.01	0.02	0.02	0.02	0.01
Sa–Sc	0.51	···	0.56	0.41	0.23	0.22	0.20	0.18	0.15
···	0.13	···	···	0.09	0.06	0.06	0.06	0.05	0.06
Sd–Im	0.63	···	···	0.52	0.36	0.31	0.30	0.27	0.22
···	0.18	···	···	0.12	0.13	0.09	0.08	0.07	0.07
pM	0.94	···	···	0.41	0.32	0.33	0.31	0.26	0.34
···	···	···	···	0.29	0.12	0.11	0.09	0.10	0. 15
mM	···	···	···	0.74	0.30	0.29	0.27	0.27	0.26
···	···	···	···	0.53	0.19	0.18	0.16	0.15	0.43
M	···	···	0.80	1.09	0.85	0.96	0.99	1.01	0.84
···	···	···	0.19	0.14	0.03	0.06	0.08	0.13	0.07
MR	0.64	···	···	0.65	0.43	0.43	0.43	0.41	0.32
···	···	···	···	0.15	0.15	0.10	0.09	0.08	0.11
P	0.35	···	···	0.37	0.36	0.30	0.37	0.30	0.61
···	···	···	···	0.19	0.12	0.13	0.10	0.10	0.15

Note. — Median Asymmetry indices in each type-bin and filter. Galaxies that were barely visible in the images of a particular filter were not included in the median. The second line for each type-bin lists half the range of the data within the 25 and 75% quartiles. Median values that were only calculated from one data point do not have an associated quartile range listed. The peculiar/merging galaxies are broken up into sub-types as follows: premerger (pM), minor merger (mM), merger (M), merger remnant (MR), and peculiar (P). In general, A decreases with increasing rest-frame wavelength.

Table 11. Median S For Each Galaxy Type Bin

Type	FUV	NUV	F255W	F300W	*U*	*B*	*V*	*R*	F814W
E–S0	···	···	0.10	0.12	0.13	0.09	0.10	0.10	0.05
···	···	···	···	0.09	0.10	0.04	0.04	0.04	0. 03
Sa–Sc	1.38	···	0.17	0.52	0.23	0.31	0.26	0.19	0.16
···	0.35	···	···	0.23	0.20	0.14	0.10	0.09	0.11
Sd–Im	0.81	···	···	0.55	0.59	0.50	0.48	0.44	0.20
···	0.39	···	···	0.14	0.21	0.10	0.12	0.12	0.07
pM	0.74	···	···	0.58	0.33	0.39	0.37	0.28	0.35
···	···	···	···	0.34	0.22	0.17	0.11	0.12	0.06
mM	···	···	···	0.12	0.29	0.19	0.22	0.18	0.25
···	···	···	···	0.20	0.24	0.16	0.08	0.06	0.11
M	···	···	0.94	1.22	1.12	1.10	1.06	1.02	0.75
···	···	···	0.25	0.31	0.30	0.28	0.33	0.36	0.29
MR	0.42	···	···	0.86	0.37	0.45	0.42	0.38	0.26
···	···	···	···	0.26	0.12	0.12	0.09	0.07	0.13
P	0.00	···	···	0.35	0.42	0.38	0.42	0.35	0.29
···	···	···	···	0.24	0.18	0.16	0.12	0.16	0.17

Note. — Median clumpiness indices in each type-bin and filter. Galaxies that were barely visible in the images of a particular filter were not included in the median. The second line for each type-bin lists half the range of the data within the 25 and 75% quartiles. Median values that were only calculated from one data point do not have an associated quartile range listed. The peculiar/merging galaxies are broken up into sub-types as follows: premerger (pM), minor merger (mM), merger (M), merger remnant (MR), and peculiar (P). In general, S decreases with increasing rest-frame wavelength.

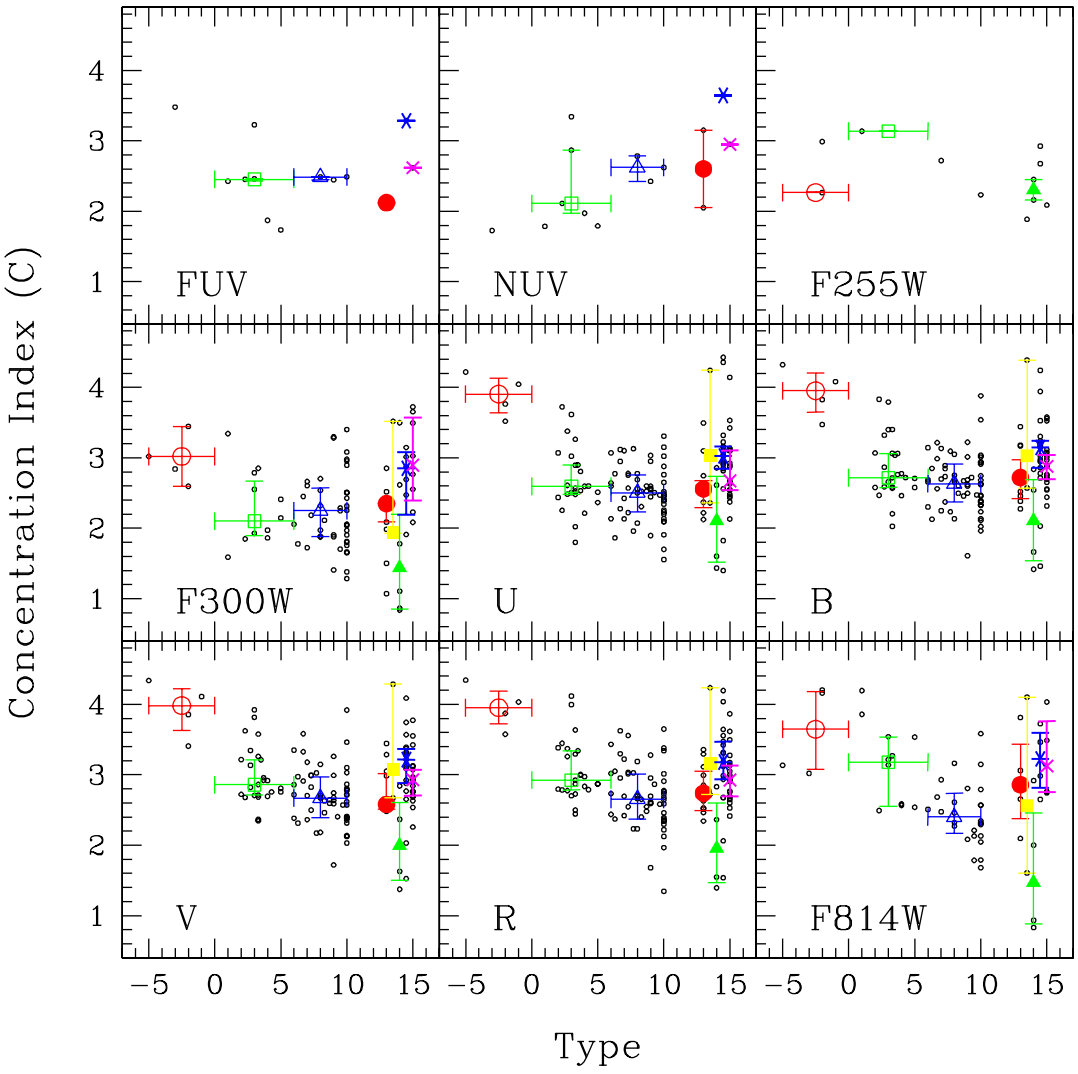

Figure 18 Concentration index as a function of galaxy type. Each panel contains data from a different filter, as labeled in the lower left corner of that panel. The large symbols are the median C values for a type-bin whose width is defined by the horizontal error bars. The vertical error bars show the 25–75% quartile ranges. These same symbols are used in subsequent figures to represent these galaxy types (as labeled in Figure 16). There is a larger spread in C for later galaxy types, with galaxies tending on average to be less concentrated with later normal galaxy type (E–Im). Merging galaxies are in general less concentrated than all other galaxy types.

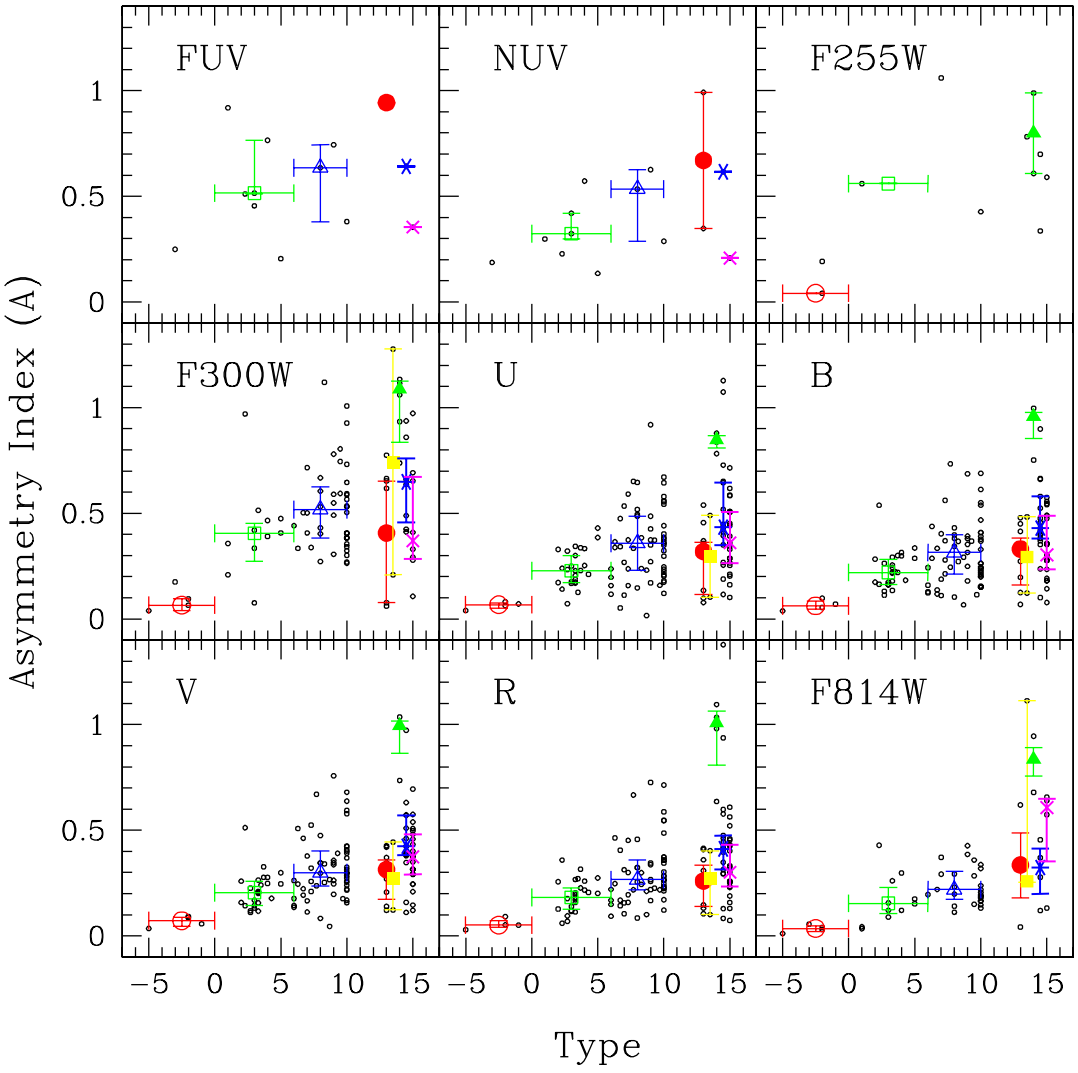

Figure 19 Asymmetry index as a function of galaxy type. The large symbols are the median A values for each type bin, with the error bars assigned as described in Figure 18. There is a larger spread in A for later galaxy types, with galaxies tending on average to be more asymmetric for later normal galaxy types (E–Im). Late-type galaxies are more asymmetric at shorter wavelengths than at longer wavelengths. Merging galaxies are in general more asymmetric than all other galaxy types.

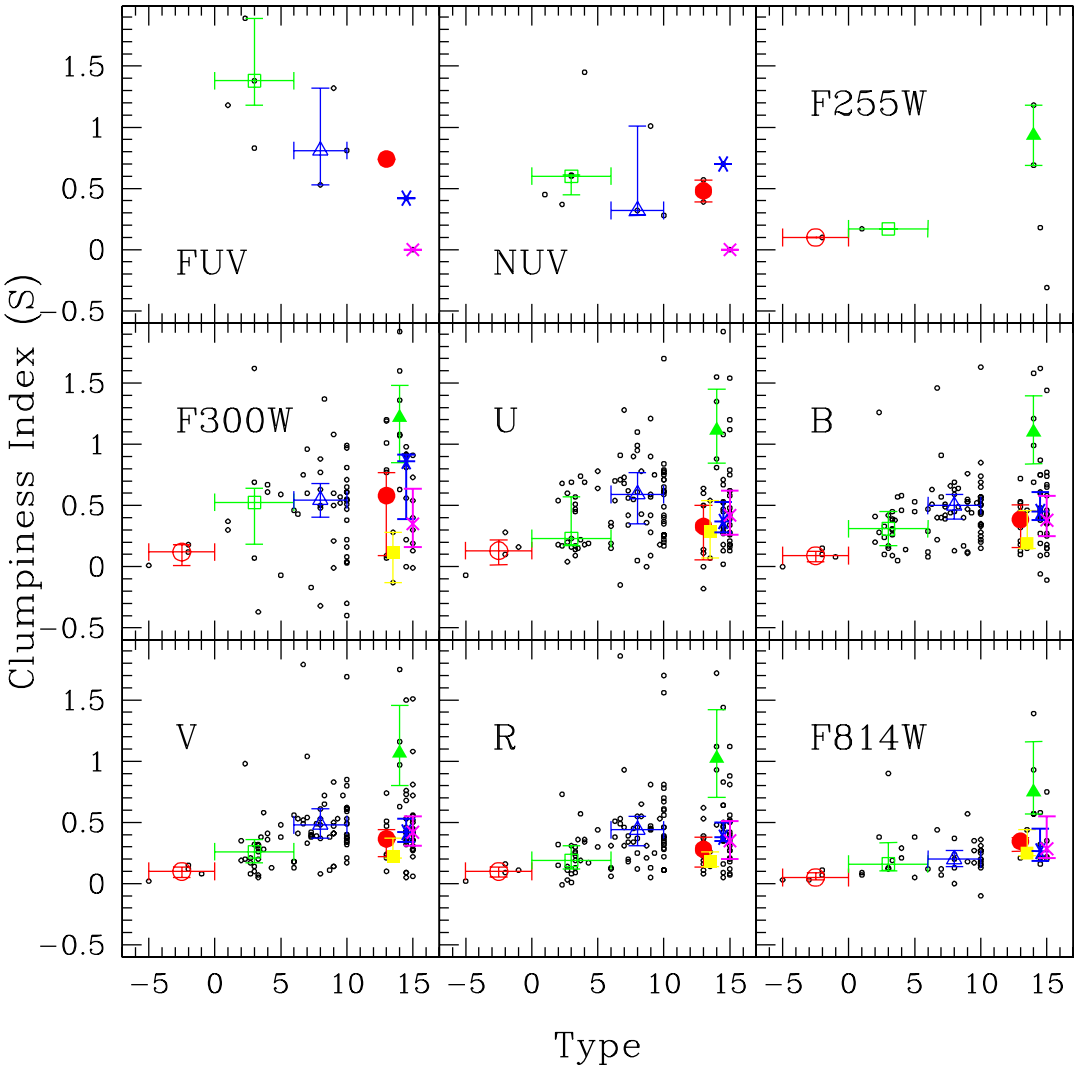

Figure 20 Clumpiness index as a function of galaxy type. The large symbols are the median S values for each type bin, with the error bars assigned as described in Figure 18. There is a larger spread in S for later galaxy types, with galaxies tending on average to be more clumpy for later normal galaxy types (E–Im). Late-type galaxies are more clumpy at shorter wavelengths than at longer wavelengths. Merging galaxies are in general more clumpy than any other galaxy type.

with high concentration index (C $\gtrsim$ 3.5) is an early type (E–S0) galaxy. Similarly, early type (E–S0) galaxies have very little overlap with later galaxy types in asymmetry index, particularly at longer wavelengths. Galaxies with A $\lesssim$ 0.1 are likely early types (E–S0), which is essentially true at all wavelengths. Although all early type (E–S0) galaxies have low clumpiness indices, there is a larger overlap with later-type galaxies for this index than for the concentration and asymmetry indices. In general, almost all early-type (E–S0) galaxies have S $\lesssim$ 0.2, but not all galaxies with S $\lesssim$ 0.2 are early-types. Although all of the later (Sa–Im, peculiar/merging) galaxy type distributions are offset slightly from one another in mean C, A, and S, there is a large overlap between their CAS parameter values. Therefore, the CAS parameters cannot be used independently to classify individual galaxies with types later than Sa, but they can be used to describe something about the overall distribution of types as a whole in a large sample. Nonetheless, it is note-worthy that a subset of the peculiar/merging galaxies, predominantly major mergers, display high asymmetry indices at longer wavelengths that are not seen for the other galaxy types. The next section discusses using a combination of the CAS parameters as a more reliable way of determining the morphological distributions within a galaxy sample.

3.5.2. *The Distribution of Galaxies in CAS Parameter Space*

The CAS parameters have been shown to correlate with one-another to form parameter spaces that can be used to classify galaxies, distinguish between interacting and merging galaxies, and determine the extent of recent star formation (Conselice 2003b). We examine the distribution of the galaxies within our sample in the CAS parameter space by plotting the three parameters against one-another in Figures 22–28.

Figure 22 shows the concentration index for each galaxy versus its asymmetry index, separated into different panels for each filter. Plot symbols are coded according to galaxy type as indicated in the legend. In this figure we do not separate the peculiar and merging galaxies into their sub-types. In order to examine the effects of linear resolution, dust, and signal-to-noise ratio, we also indicate whether galaxies are particularly nearby ($V_{GSR} < 200$ km sec^{-1}), appear to be edge-on spirals, or are barely visible in the images in a particular filter. In general, galaxies become less concentrated toward higher asymmetry, which agrees with the results of other studies (e.g., Conselice 2003b). Galaxy types overlap within this plot, but early-type galaxies (E–S0) are in general the most concentrated and the least asymmetric, while later galaxy types become in general less concentrated and more asymmetric. The merging/peculiar galaxy trend is offset from the normal galaxy trend, with merging/peculiar galaxies tending to be more asymmetric and more concentrated than other galaxy types. All of the extreme outliers from the general normal galaxy trend were determined to be particular faint, and have large associated measurement uncertainties. An edge-on orientation did not have a significant effect on the location of a galaxy within this parameter space. On average, the nearby galaxies tend to be slightly more asymmetric and less concentrated than their more distant counterparts, which results from their partial resolution into individual stars, as well as a possible selection bias favoring low luminosity

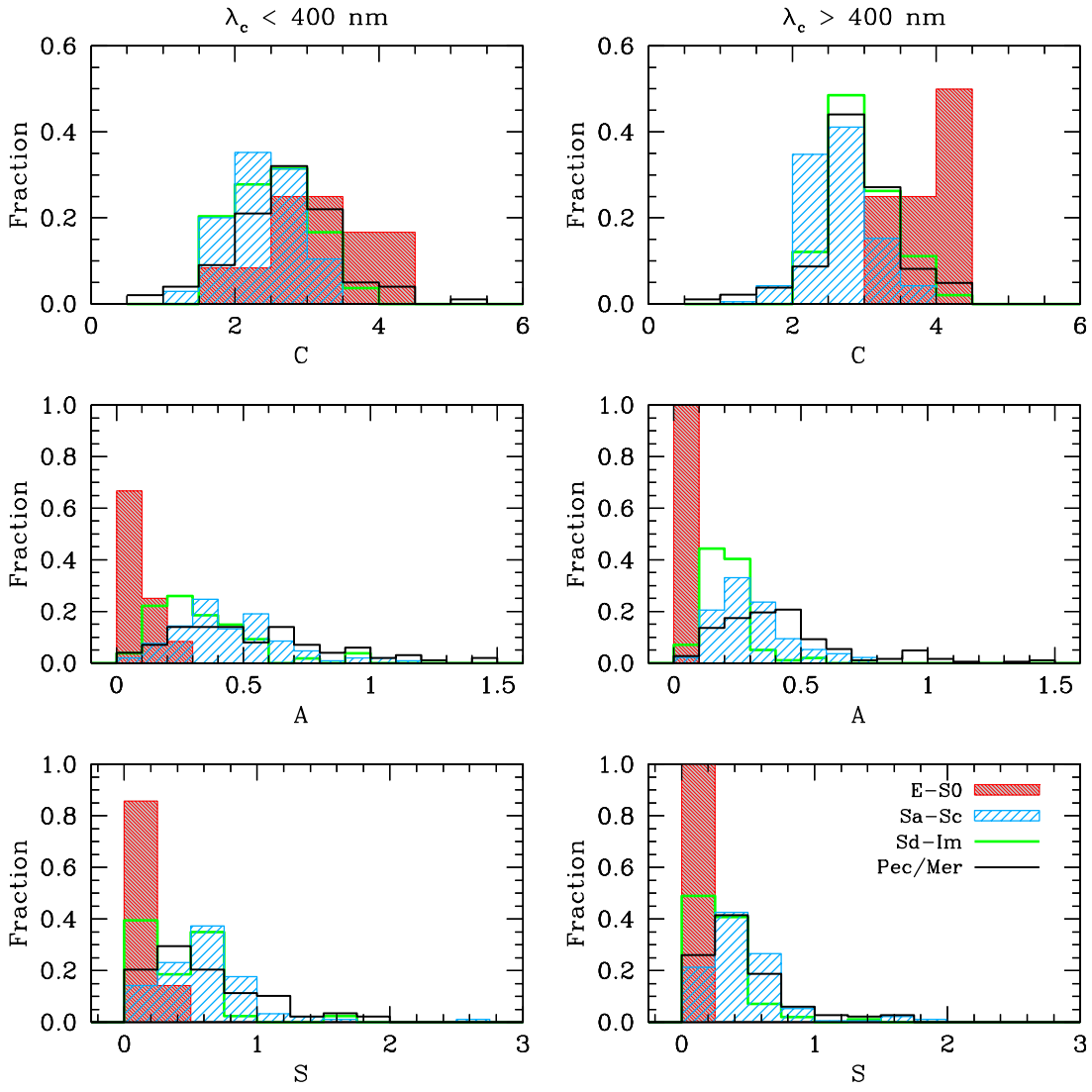

Figure 21 The distribution of C (upper panels), A (middle panels), and S (lower panels) for each galaxy type bin as denoted in the legend in the lower right panel. The left panels include all UV data from all filters shortward of the Balmer break ($\lambda_c < 400$ nm), and the right panels include all data from all filters longward of the Balmer break ($\lambda_c > 400$ nm). Data with errors larger than 1.5 in C, A, or S, were not included in this plot. Early-type galaxies (E–S0) have the least amount of overlap with other galaxy types, particularly in longer wavelengths, and particularly in A and S. Galaxies of type Sa and later, however, have considerable overlap in the CAS parameters, although their distributions are offset from one another. Asymmetry and clumpiness can therefore be used independently to classify individual early-type galaxies (E–S0) with some limited degree of certainty, but not individual later-type galaxies. The overall distribution of the CAS parameter in a large sample, however, can be used to describe the population distribution as a whole.

dwarf systems at that distance. No systematic trend was noticed in the CAS parameters for galaxies with $V_{GSR} > 200$ km sec^{-1}.

Figure 23 also shows C vs. A for each galaxy, as in Figure 22, but here the separate sub-classes of peculiar/merging galaxies are represented by different symbols instead of the different normal galaxy type-bins. Although there is some overlap, peculiar galaxies tend to be more asymmetric and more concentrated than normal galaxies. For some of these peculiar galaxies, their high concentration in the UV could be due to the presence of an AGN. The pre-mergers tend to be less asymmetric than the other types of mergers, and follow the general trend of normal galaxies except that they are on average slightly more asymmetric. This is to be expected, as the pre-mergers are normal galaxies that are only beginning to be tidally affected by their neighbors, and may show some enhanced star formation. There are very few minor mergers in our sample, with a large scatter in distribution on this plot, so any conclusions about that sub-class should be regarded with caution. Major mergers are clearly separated from the main trend, being much more asymmetric and less concentrated than any other galaxy type. Merger remnants, on the other hand, lie closer to the trend line for normal galaxies, although they are more asymmetric and more concentrated than both normal galaxies and pre-mergers.

Figure 24 shows the clumpiness index versus the asymmetry index for each galaxy, using the same normal galaxy type symbols as in Figure 22. Galaxies tend on average to be more clumpy with higher asymmetry, which agrees with the results of other studies (e.g., Conselice 2003b). This relation is fairly tight, especially at longer wavelengths, as S and A are not entirely independent from each other. Early-type galaxies (E–S0) are the least asymmetric and clumpy, with later galaxy types becoming progressively more asymmetric and more clumpy. All outliers from the general trend can be explained by one of the three special conditions marked on the plot: outliers in the shorter wavelengths had particularly low signal-to-noise in the images, while outliers in the longer wavelengths are either edge-on or very nearby. Due to the strong dust lanes visible in edge-on galaxies, they appear more clumpy than galaxies with lower inclinations, and lie well above the general S vs. A relation. On the whole, nearby galaxies tend to be only slightly more asymmetric and clumpy than their more distant counterparts.

Figure 25 also shows S vs. A for each galaxy, but with peculiar/merging sub-classes highlighted with different symbols, as in Figure 23. The pre-mergers are not clearly distinguished from normal galaxy types within the measurement uncertainties, but merging galaxies are much more asymmetric and show much more small scale structure (clumpiness) than any other galaxy type. Merger remnants tend to appear slightly smoother, but more asymmetric on average than the pre-merger and normal galaxies.

For completeness, we also show the third projection of the CAS parameter space in Figures 26 and 27. Figure 26 shows C vs. S for each galaxy, using the same normal galaxy type symbols as in Figure 22. Galaxies are on average much less concentrated for each modest increase in clumpiness index, which agrees with the results of previous studies (e.g., Conselice 2003b). Early galaxy types are more concentrated, with later galaxy types

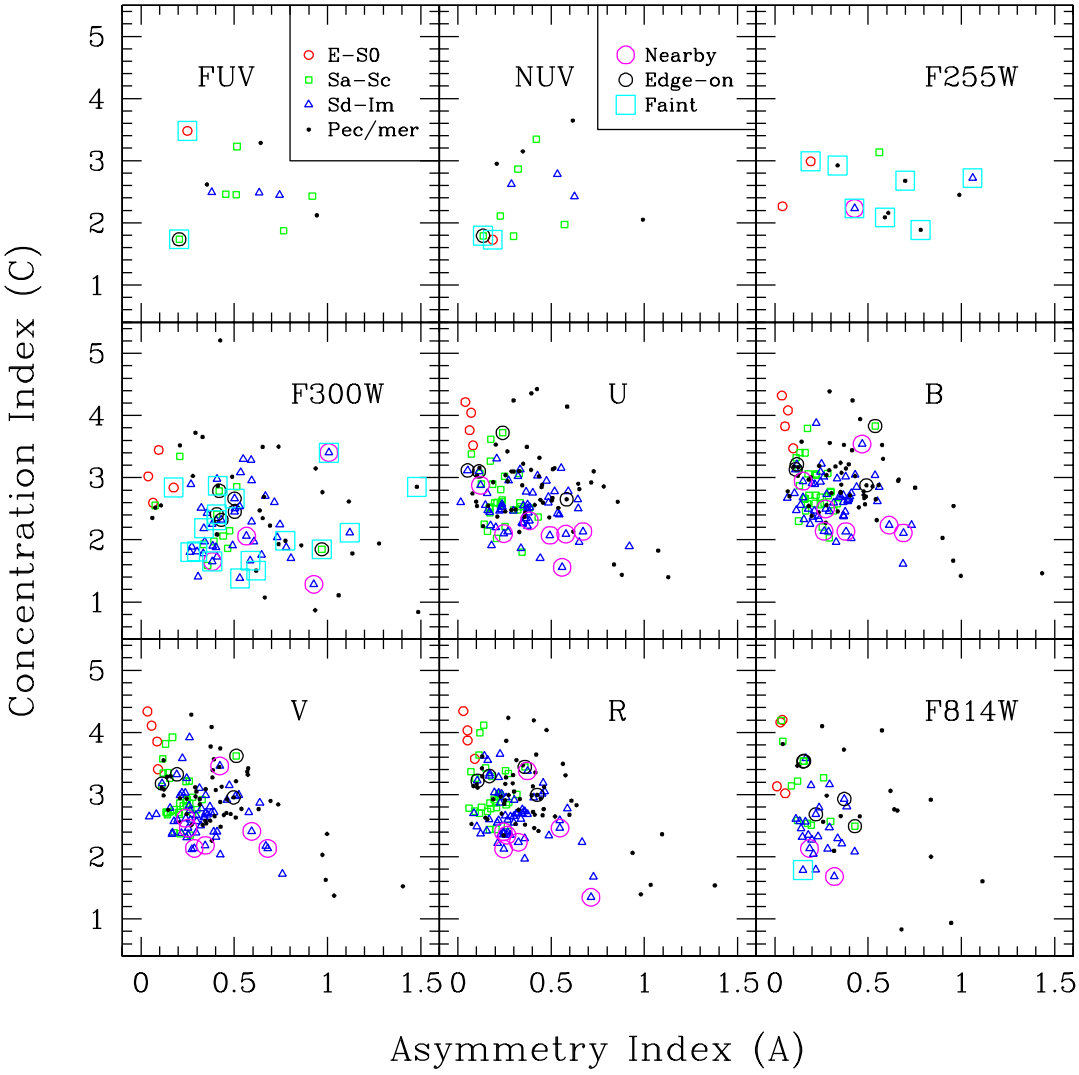

Figure 22 Concentration index vs. asymmetry index, separated into panels for each filter (as labeled). Plot symbols are coded according to galaxy type as indicated in the legend in the upper left (FUV) panel. Here, we do not separate the peculiar and merging galaxies into their sub-types. We furthermore highlight particularly nearby (V_{GSR} < 200 km sec^{-1}), highly inclined/edge-on and particularly low surface brightness/faint galaxies by over-plotting larger symbols coded according to the legend in the upper-middle (NUV) panel. In general, galaxies are less concentrated when they are more asymmetric. Increasingly later galaxy types become increasingly less concentrated and more asymmetric. The locus of merging/peculiar galaxies is offset from that of the normal galaxies toward higher asymmetries and concentrations. Extreme outliers from the general trend are usually very faint in that filter, and have large associated measurement uncertainties. Particularly nearby galaxies, which tend to be partially resolved into their individual stars, are on average slightly more asymmetric and less concentrated than more distant galaxies, due in part to physical resolution effects.

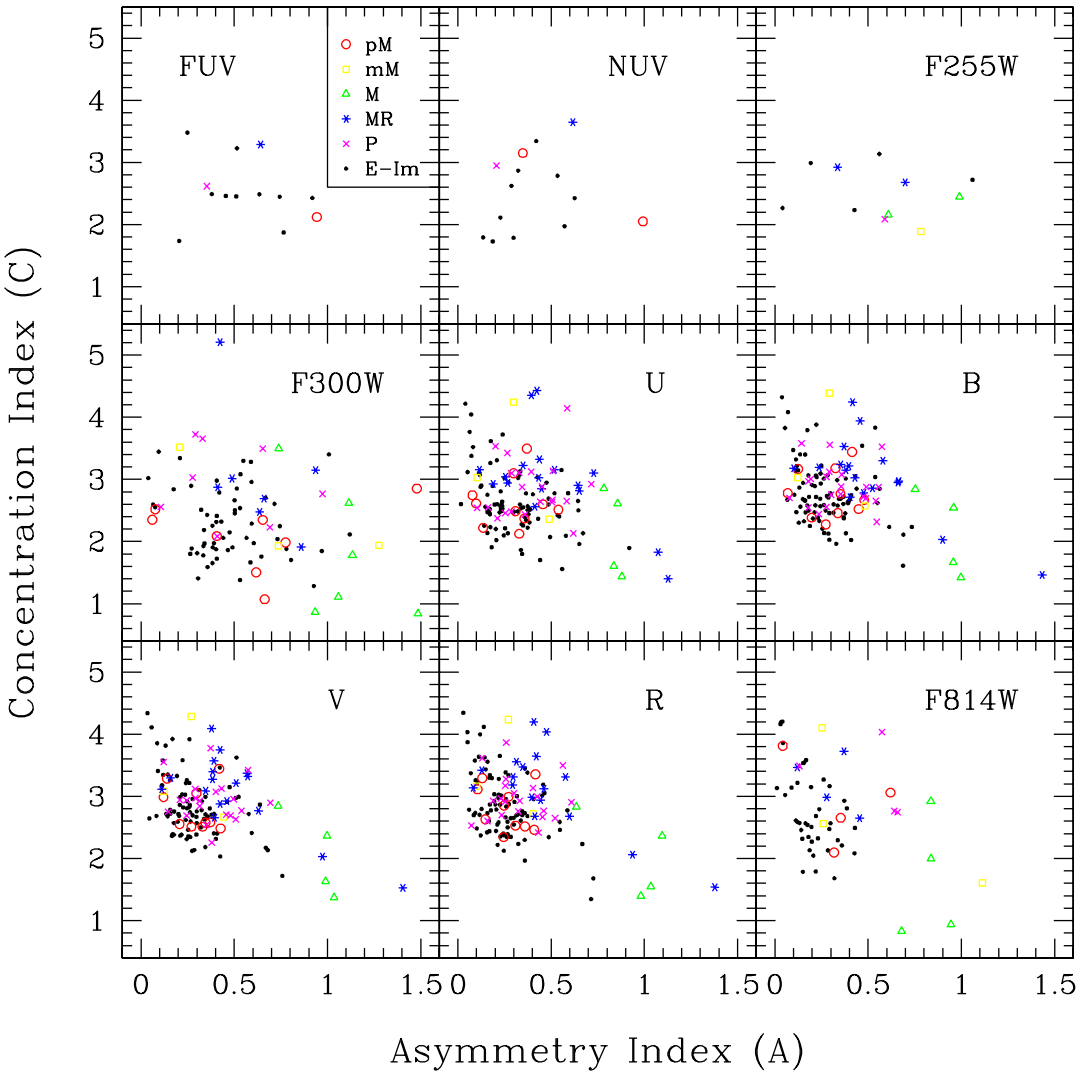

Figure 23 Concentration index vs. asymmetry index, as in Figure 22, but with plot symbols highlighting the individual sub-classes of merging and peculiar galaxies rather than normal morphological types. Peculiar galaxies (P) are on average more asymmetric and more concentrated than normal galaxies. For some of these peculiar galaxies, their high concentration in the UV could be due to the presence of an AGN. Pre-mergers (pM) tend to be slightly more asymmetric than normal galaxies. Major mergers (M) are much more asymmetric and less concentrated than any other galaxy type. Merger remnants (MR) are more asymmetric and more concentrated than both normal galaxies and pre-mergers.

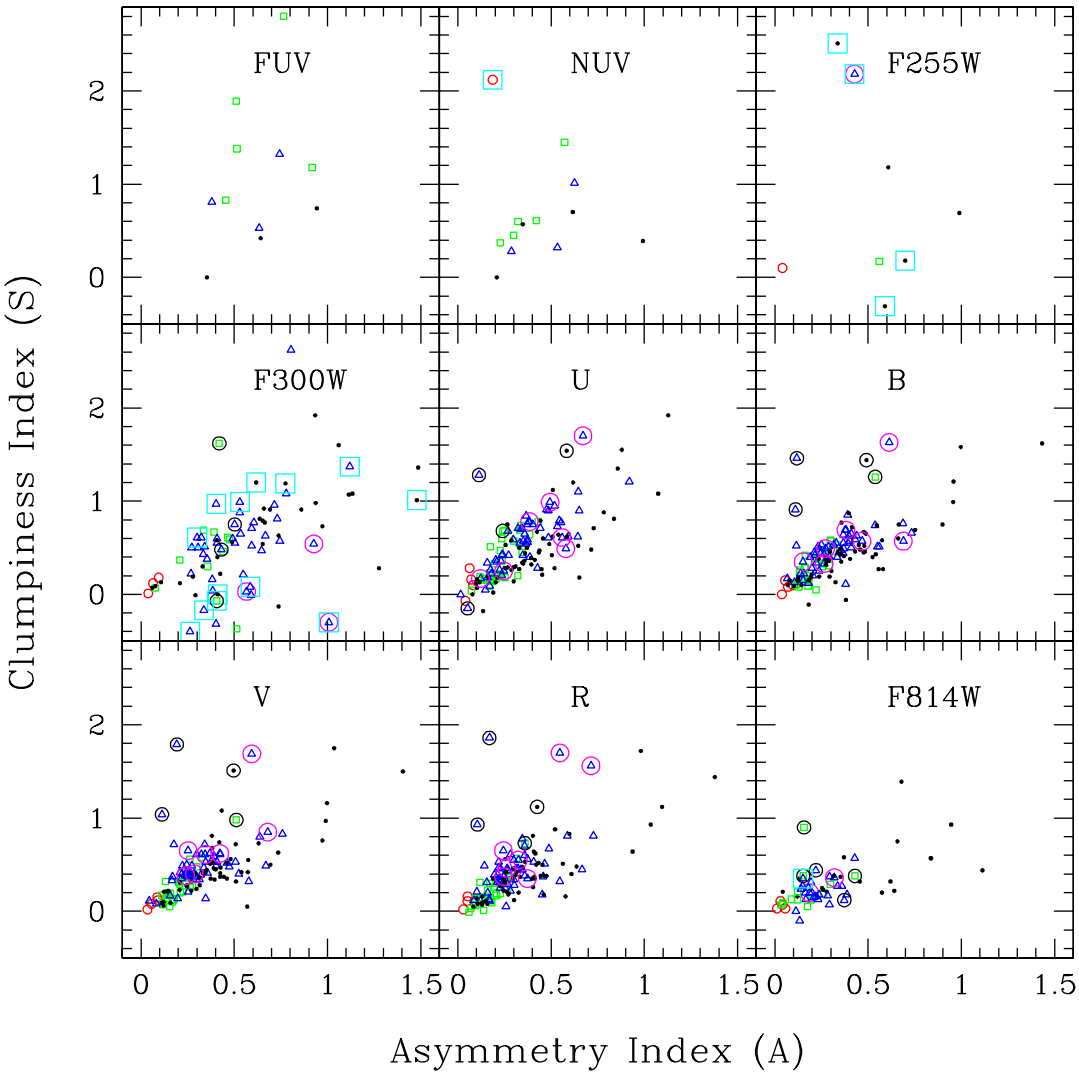

Figure 24 Clumpiness index vs. asymmetry index. Galaxy types and special conditions for each galaxy are coded by symbol as described in Figure 22. Galaxies are on average more clumpy when they are more asymmetric. Increasingly later galaxy types become progressively more asymmetric and more clumpy. Outliers in the shorter wavelengths have particularly low signal-to-noise ratio and large associated uncertainties. Edge-on spirals appear more clumpy than galaxies with lower inclinations, and are well separated from the general trend. Particularly nearby galaxies tend to be slightly more asymmetric and clumpy than more distant galaxies.

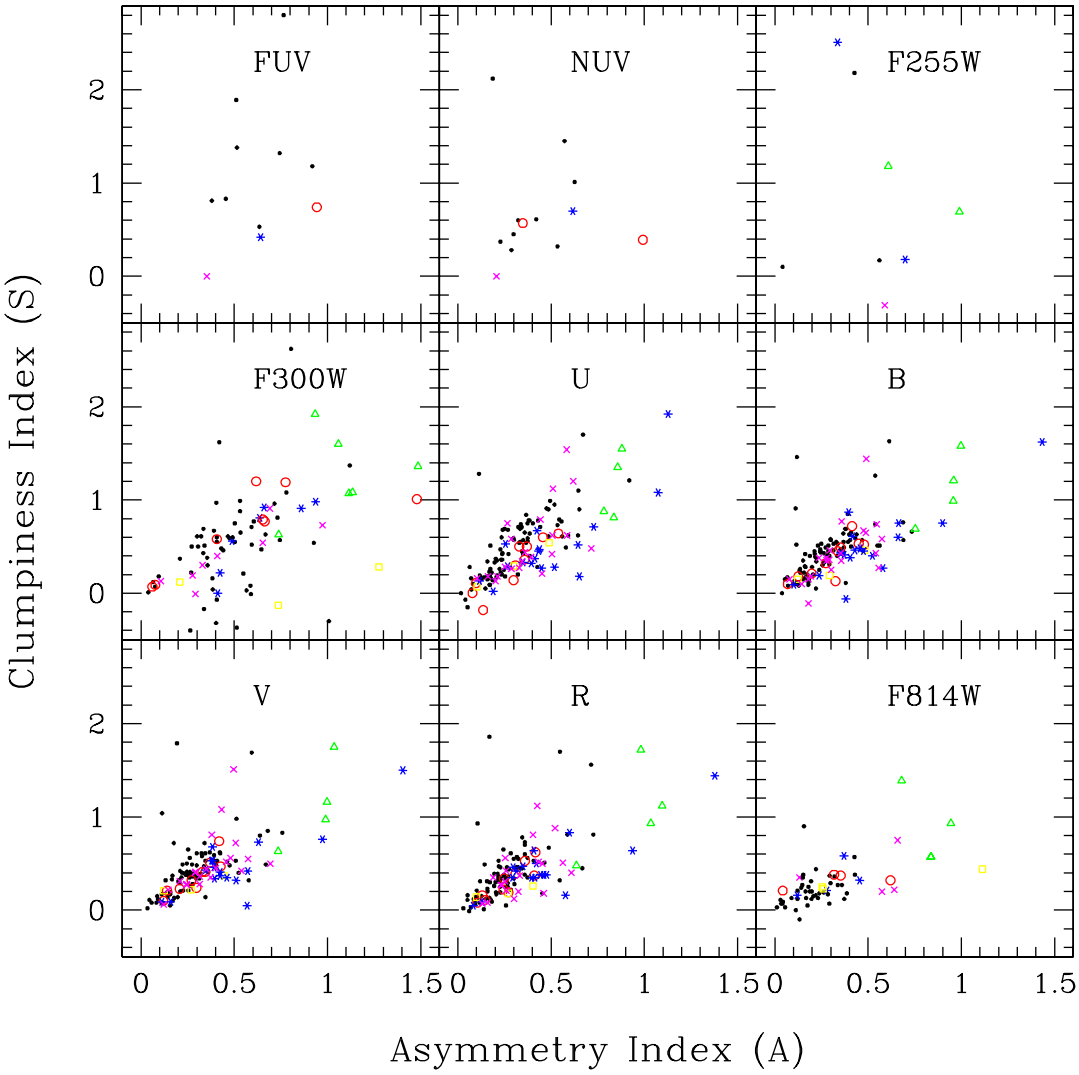

Figure 25 Clumpiness index vs. asymmetry index. Merging and peculiar vs. normal galaxy types are coded by symbol as described in Figure 23. Merging galaxies are much more asymmetric and clumpy than any other galaxy type. Merger remnants tend to be slightly less clumpy and more asymmetric than both pre-mergers and normal galaxies.

becoming less concentrated and slightly more clumpy. As in Figure 24, edge-on galaxies are separated from the main trend and are more clumpy than galaxies that are less inclined.

Figure 27 also shows C vs. S for each galaxy, but with peculiar/merging sub-classes highlighted with different symbols, as in Figure 23. Merging galaxies tend to be more clumpy and less concentrated than other galaxy types, and merger remnants are on average more concentrated than normal galaxies and pre-mergers.

In Figure 28, we examine the average trends in this CAS parameter space with a plot of the median values in each type-bin and filter of C and S as a function of A. The F255W filter is not included due to its small number statistics and low signal-to-noise ratio. The left panels contain the median values in all filters shortward of the Balmer break ($\lambda_c < 400$ nm). Therefore, there are multiple data points for each type-bin corresponding to the median values in each short wavelength filter (FUV, NUV, F300W, and U-band). The right panels contain the median values in all filters longward of the Balmer break ($\lambda_c > 400$ nm), such that individual data points for each type-bin correspond to each long wavelength filter (B, V, R, and F814W). There is a much larger scatter in the CAS parameters at shorter wavelengths, which may partially be due to larger measurement uncertainties for these filters and smaller number statistics. More, and higher quality data in the mid to far-UV is needed to further constrain these values. There is a clear trend among normal galaxies to show a progression from early to late-type galaxies (E to Im) of increasing asymmetry and clumpiness and decreasing concentration. The different peculiar/merging galaxy types are each located at different positions within this parameter space. There appears to be a general evolutionary trend from pre-mergers to mergers, and then to post-mergers, as shown by the dotted lines with arrows connecting the average of the median values for each type-bin. Mergers become significantly less concentrated, more asymmetric, and more clumpy than pre-mergers, then progress back toward the normal galaxy parameter space as they turn into merger remnants, which end up being significantly more concentrated than the pre-mergers, and slightly more asymmetric and less clumpy. From there, galaxies may take different paths on the CAS parameter space depending on whether they turn into elliptical or spiral galaxies, which depends on the details of the merger and of the individual galaxies taking part in that merger.

3.5.3. *The Rest-frame Wavelength Dependence of the CAS Parameters.*

Some of the galaxies in our sample appear different in the UV than they do in the optical, while some galaxies appear very similar. This was discussed qualitatively in detail in Windhorst et al. (2002). Figure 29 shows examples of each of these cases. The upper image for each galaxy was obtained with either the F814W near-IR filter, or the VATT R-band filter. The lower image for each galaxy was obtained with either the F300W UV filter, or the VATT U-band filter. UGC05189 is a merger remnant that has a large difference in asymmetries and clumpiness indices between the UV and the IR ($A_{F300W} - A_{F814W} =$ –0.768, and $S_{F300W} - S_{F814W} = 0.49$), mostly due to bright star-forming knots that are more apparent in the UV image. UGC06816 is a late-type barred spiral galaxy that has a

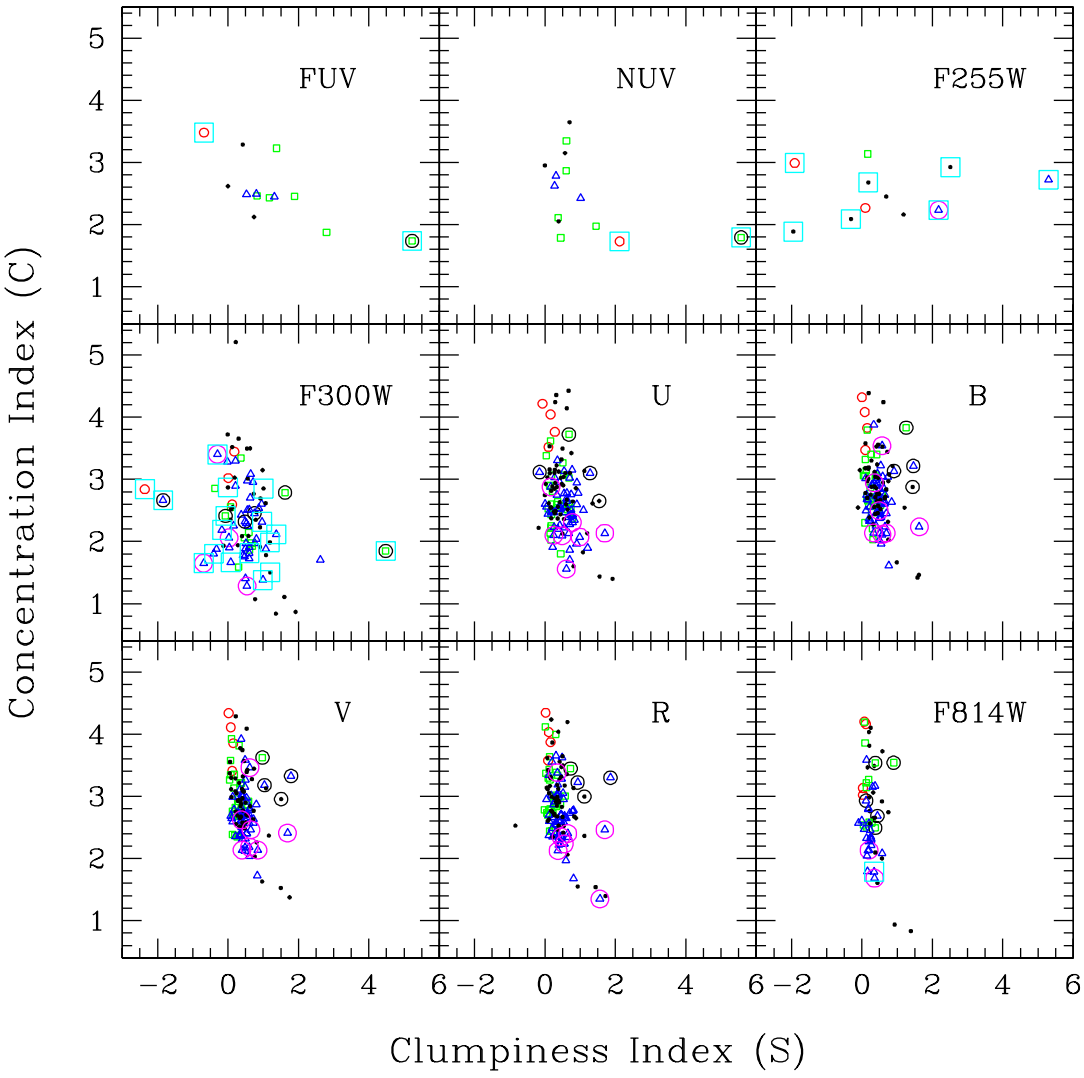

Figure 26 Concentration index vs. clumpiness index. Galaxy types and special conditions for each galaxy are coded by symbol as described in Figure 22. Galaxies are on average much less concentrated for every modest increase in clumpiness index. Increasingly later galaxy types are progressively less concentrated and slightly more clumpy. Edge-on galaxies are more clumpy than galaxies with lower inclination, and are well separated from the normal galaxy trend, likely due to more visible dust-lanes that increase the clumpiness index.

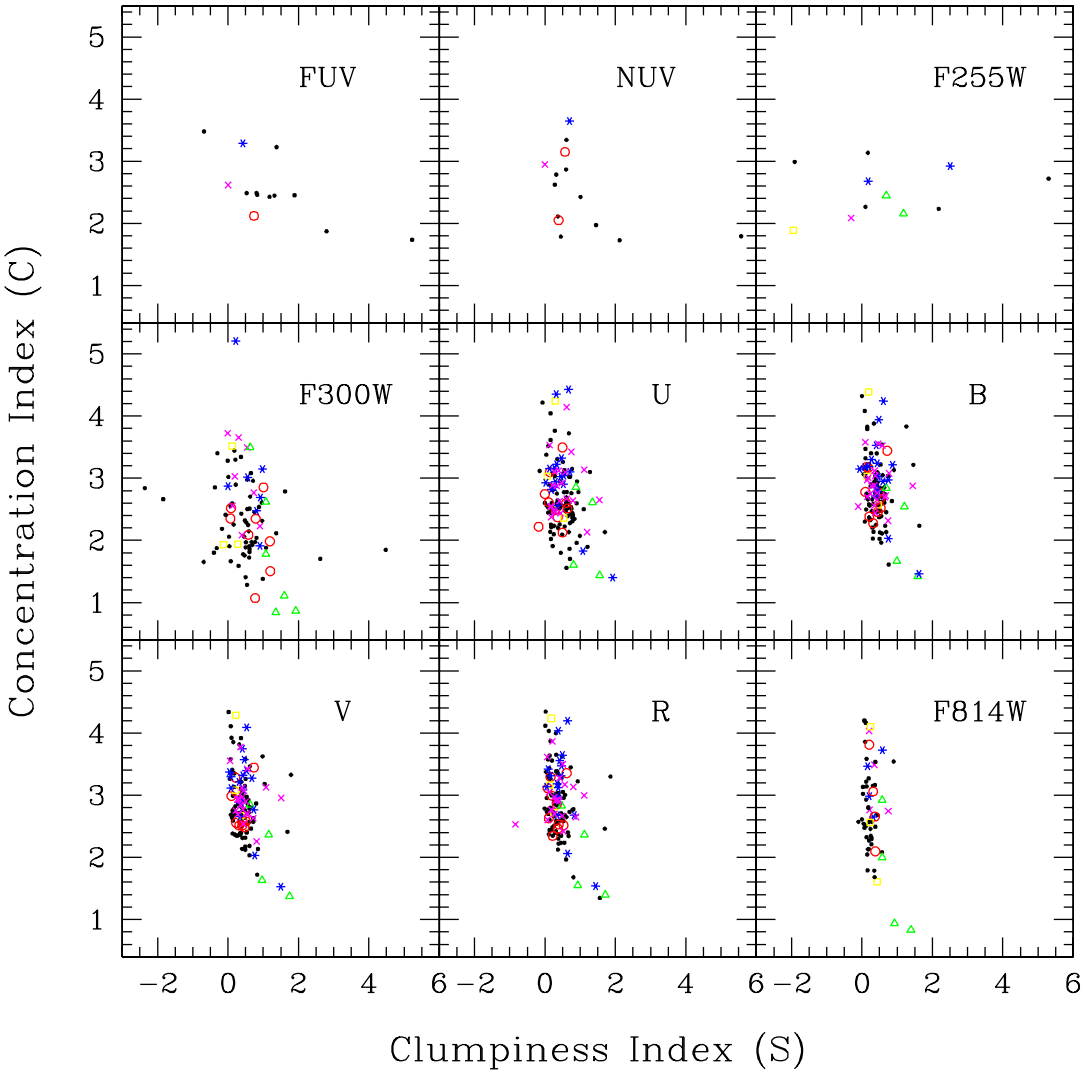

Figure 27 Concentration index vs. clumpiness index. Merging and peculiar vs. normal galaxy types are coded by symbol as described in Figure 23. Merging galaxies tend to be more clumpy and less concentrated than other galaxy types. Merger remnants tend to be more concentrated than both pre-mergers and normal galaxies.

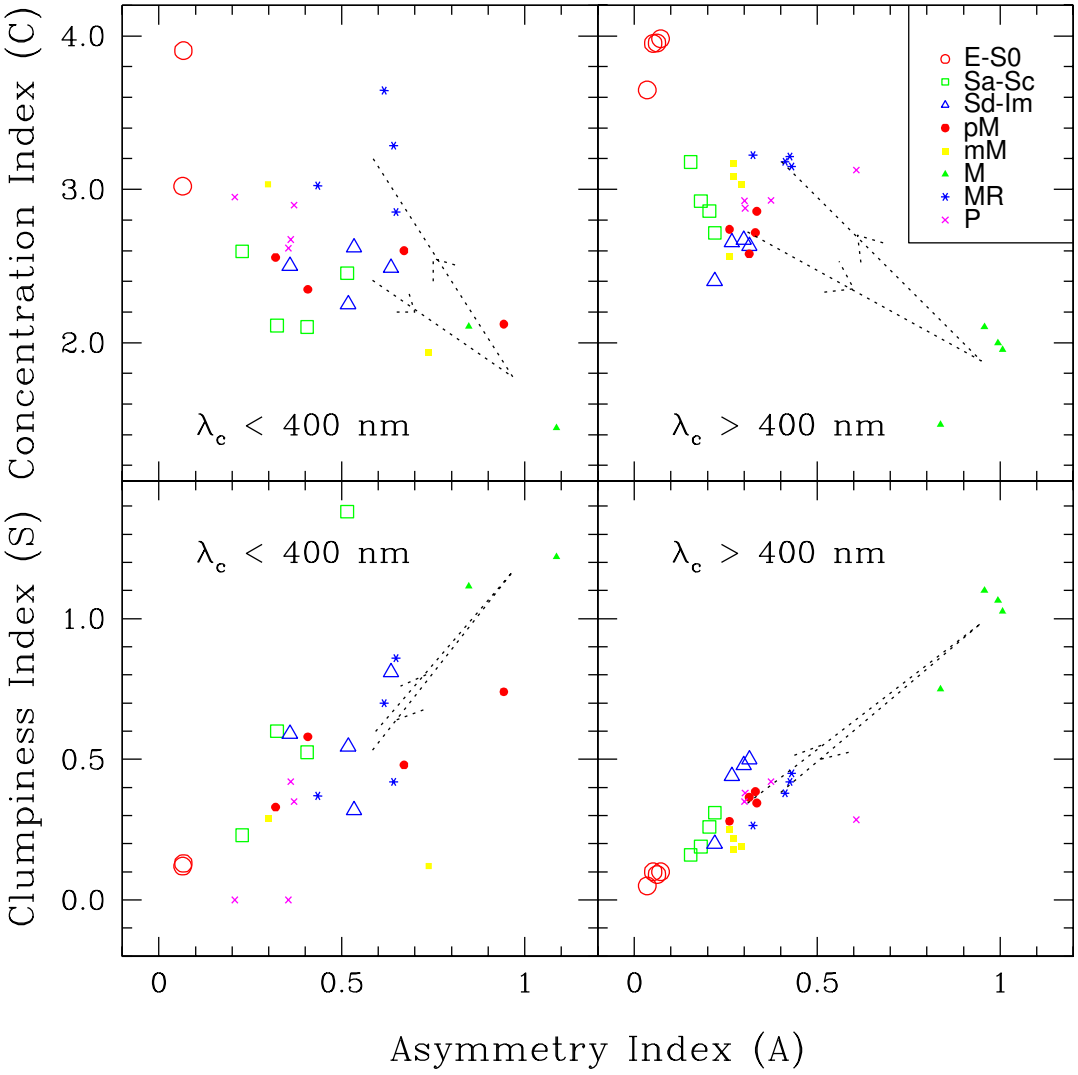

Figure 28 The median values of the concentration and clumpiness indices in each filter (excluding F255W) for each type bin vs. the median values of the asymmetry index in that filter and type-bin. Symbols are coded by type as described in the upper right panel. The left panels contain data for all filters short-ward of the Balmer break ($\lambda_c < 400$ nm), and the right panels contain data for all filters long-ward of the Balmer break ($\lambda_c > 400$ nm). There is a much larger scatter in the CAS parameters at shorter wavelengths, which may partially be due to lower galaxy number statistics and lower signal-to-noise ratio within the GALEX and HST UV images. Normal galaxies become more asymmetric and clumpy and less concentrated toward later Hubble type (E to Im). Dotted lines connect the average of the medians for pre-mergers to mergers, and then to post-mergers. This shows a progression through the CAS parameter space as the merging process progresses, with mergers becoming significantly less concentrated, more asymmetric, and more clumpy than pre-mergers, before returning as post-mergers near the locus of normal galaxies again. On average the merger remnants are significantly more concentrated than the pre-mergers, and slightly more asymmetric and less clumpy. This may define a duty cycle for the merging process.

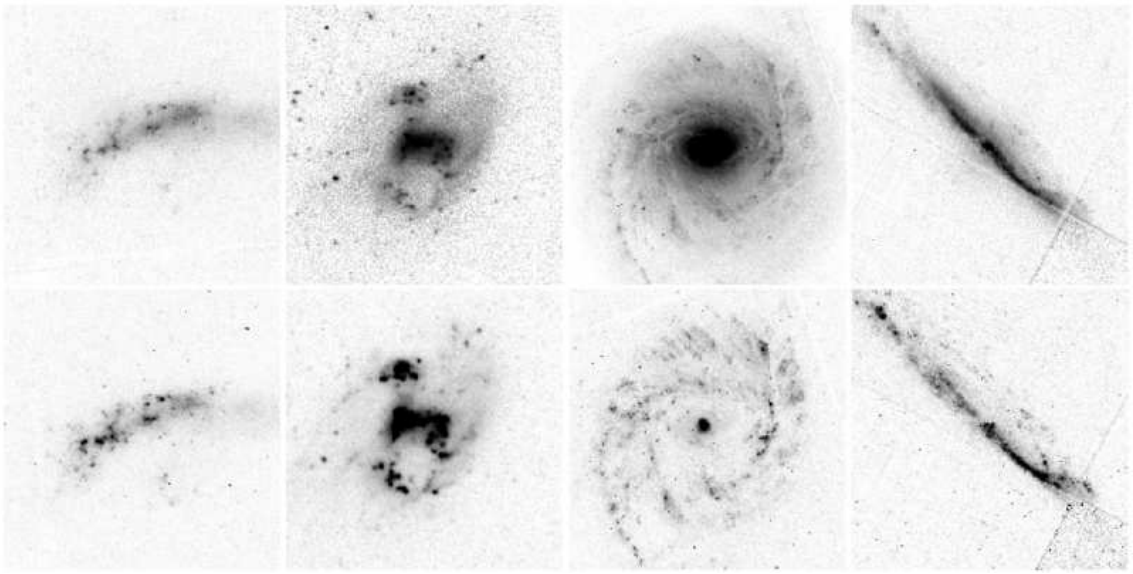

Figure 29 Examples of galaxies that have various differences in the CAS parameters as measured in the UV vs. the optical/near-IR. The upper panels are the red (R-band) or near-IR (F814W) images for each galaxy. The lower panels are the UV (U-band or F300W) images for these galaxies. From left to right: UGC05189 is a merger remnant with a large difference in A and S between the UV and the near-IR, but little difference in C. UGC06816 is a late-type spiral galaxy that also has a large difference in A and S between the near-UV and the red, but little difference in C. UGC12808 (NGC7769) is an early-type spiral galaxy that has little difference in A and S between the UV and the near-IR, but a large difference in C. UGC06697 is a peculiar galaxy that also has little difference in A and S between the UV and the near-IR, but a large difference in C.

large difference in A and S between the near-UV and the red ($A_U - A_R = 0.323$, and $S_U - S_R = 0.64$), which is also due to its UV-bright star-formating knots, particularly at the ends of its bar and at two sites of vigorous star formation along its poorly organized spiral pattern. Both of these galaxies have small differences in concentration index between these filters (–0.178 for UGC05189, and –0.207 for UGC06816). UGC12808 is an earlier-type spiral galaxy that has about the same asymmetry and clumpiness index in both pass-bands ($A_{F300W} - A_{F814W} = -0.045$, and $S_{F300W} - S_{F814W} = -0.05$). UGC06697 is a peculiar, highly inclined galaxy that also has about the same asymmetry and clumpiness index in both pass-bands ($A_{F300W} - A_{F814W} = 0.035$, and $S_{F300W} - S_{F814W} = 0.16$). Both of these galaxies, however, appear different in the UV than in the IR due to a large difference in concentration index between the filters (–0.664 for UGC12808 and –0.515 for UGC06697), which is largely due to the diminished appearance of their red bulges at shorter wavelengths.

Figure 30 shows the CAS parameters of each galaxy as a function of the central wavelength (λ_c) of each filter in nm. Different galaxy types are represented by different colored symbols. We find a large scatter, but there is a general trend discernible of increasing C and decreasing A and S toward longer wavelengths. This general trend is more evident in Figure 31, which shows the median values of the CAS parameters in each filter and galaxy type-bin. Error bars indicate the 25–75% quartile ranges. As in previous plots of the CAS

parameters, on average, the early-type, late-type, and merging/peculiar galaxy classes are clearly separated in C, A, and S, although there is considerable overlap among individual galaxies within each type class. The CAS values of early-type galaxies (E–S0) are relatively constant with increasing rest-frame wavelength longward of the Balmer break. Shortward of the Balmer break, the signal-to-noise of these red objects is very low, and therefore the CAS parameter measurement uncertainties are high. Due to this effect and due to the low number of early-type galaxies in our sample, we cannot yet draw definite conclusions about whether the CAS parameters of early-type galaxies would differ significantly at UV rest-frame wavelengths. Spiral, irregular, and peculiar/merging galaxies, however, all show a general trend of increasing C and decreasing S and A with increasing rest-frame wavelength. The concentrations measured in the HST/WFPC2 F814W images appear somewhat lower with respect to the general trend, which may be due to the fact that our WFPC2 images are more sensitive to point-sources than extended sources, so that outlying low surface brightness material may not have been detected in that particular filter.

Figure 32 also shows the CAS parameter dependence on wavelength, but presented in separate panels for each galaxy type bin. The median values are plotted over the individual data with different symbols. This separation in type makes the trends in each type bin more easily apparent. Linear-least-squares fits to the individual data points are shown as dashed lines. Data with errors in C, A, or S greater than 1.5 are not included in the fits. Linear fits are suitable for all but the wavelength dependence of the concentration index of early-type (E-S0) galaxies, which shows a more sharply decreasing concentration index at wavelengths shortward of the Balmer break. Therefore, we also include a 2nd order polynomial fit to the data in this panel, shown as a dotted line. This strong dependence of C shortward of the Balmer break is likely largely due to the very low signal-to-noise of these red galaxies in the UV images (see Windhorst et al. 2002 for the images). This 2nd order polynomial (–14.45 $\log(\lambda_c)^2$ + 78.83 $\log(\lambda_c)$ – 103.5) is a relatively good fit to the data, with 14% uncertainty on each of the coefficients (compared to a 39% error on the slope of the linear fit, and an error larger than the value of the y-intercept).

As determined from these fits, the early to mid-type spiral galaxies (Sa–Sc) show a significant increase in concentration index at longer rest-frame wavelengths, with a change in C of about 1.37 ± 0.32 per dex in λ_c. The late-type (Sd–Im) and peculiar/merging galaxies, however, have little to no trend with wavelength within the uncertainties (0.09 ± 0.24 and 0.39 ± 0.32 per dex in λ_c, respectively. There is, however, a significant decrease in asymmetry toward longer wavelengths for all galaxy types, with a larger difference seen for later galaxy types. The slopes of the fits for the asymmetry were -0.12 ± 0.02, -0.47 ± 0.08, -0.69 ± 0.12, and -0.39 ± 0.13 per dex in λ_c, for E–S0, Sa–Sc, Sd–Im, and peculiar/mergers, respectively. There is no significant change in clumpiness index with wavelength within the uncertainties for early-type (E–S0) and late-type galaxies (Sd–Im), but there is a small decrease in clumpiness at longer wavelengths for the early to mid-type spiral (-0.78 ± 0.15 per dex in λ_c) and peculiar/merging galaxies (-0.38 ± 0.14 per dex in λ_c).

Because the same galaxies were not observed at all wavelengths, it is more mean-

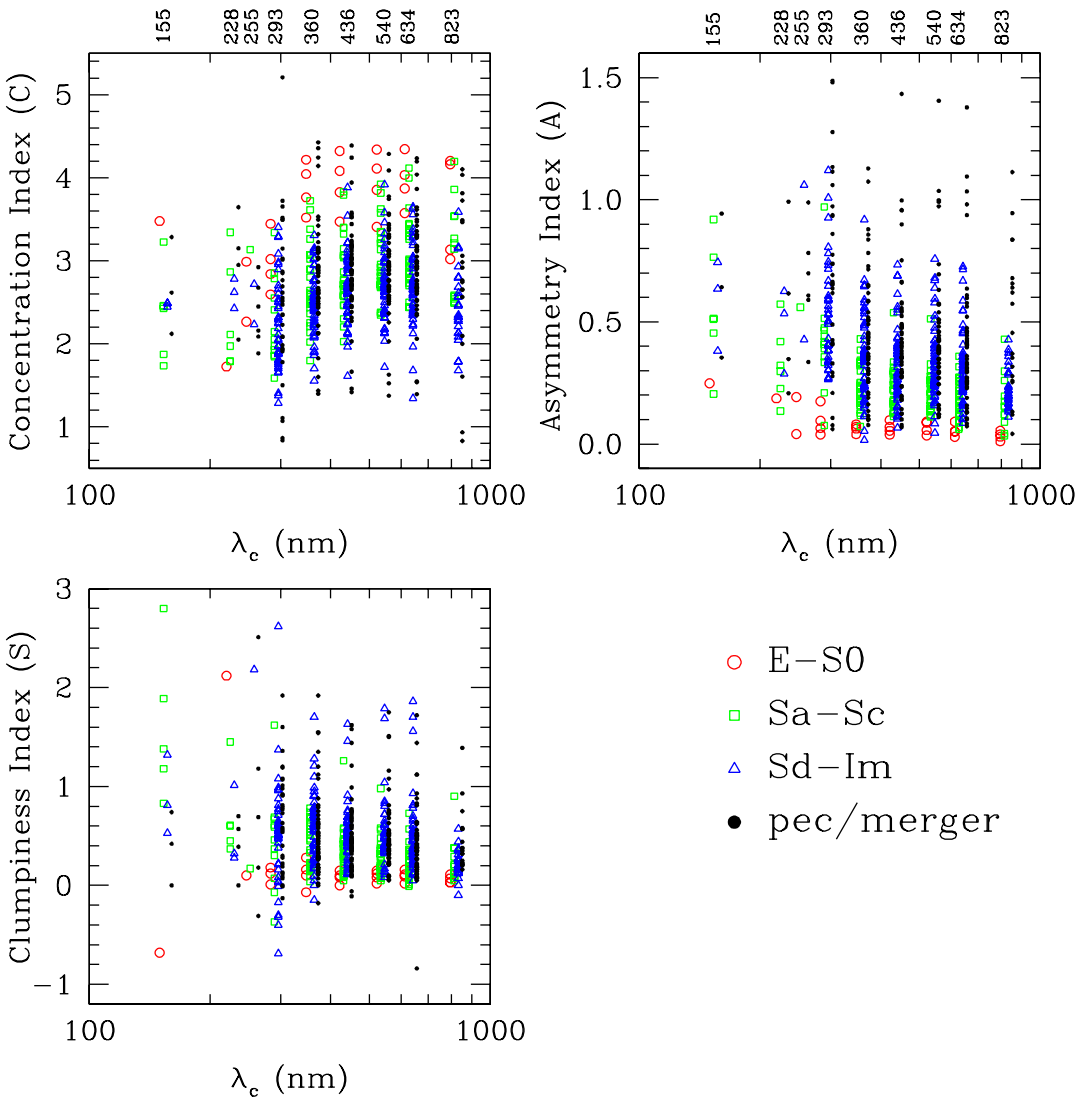

Figure 30 The CAS parameters as a function of the central wavelength in nm (λ_c) of each filter. Galaxy type is coded by symbol as shown in the lower right panel. Labels along the top axes of the top plots indicate λ_c for each filter in nm. Data from each type-bin are somewhat artificially offset in λ_c to reduce clutter. The scatter at any wavelength is large, but there is a general trend of increasing C and decreasing A and S toward longer wavelengths.

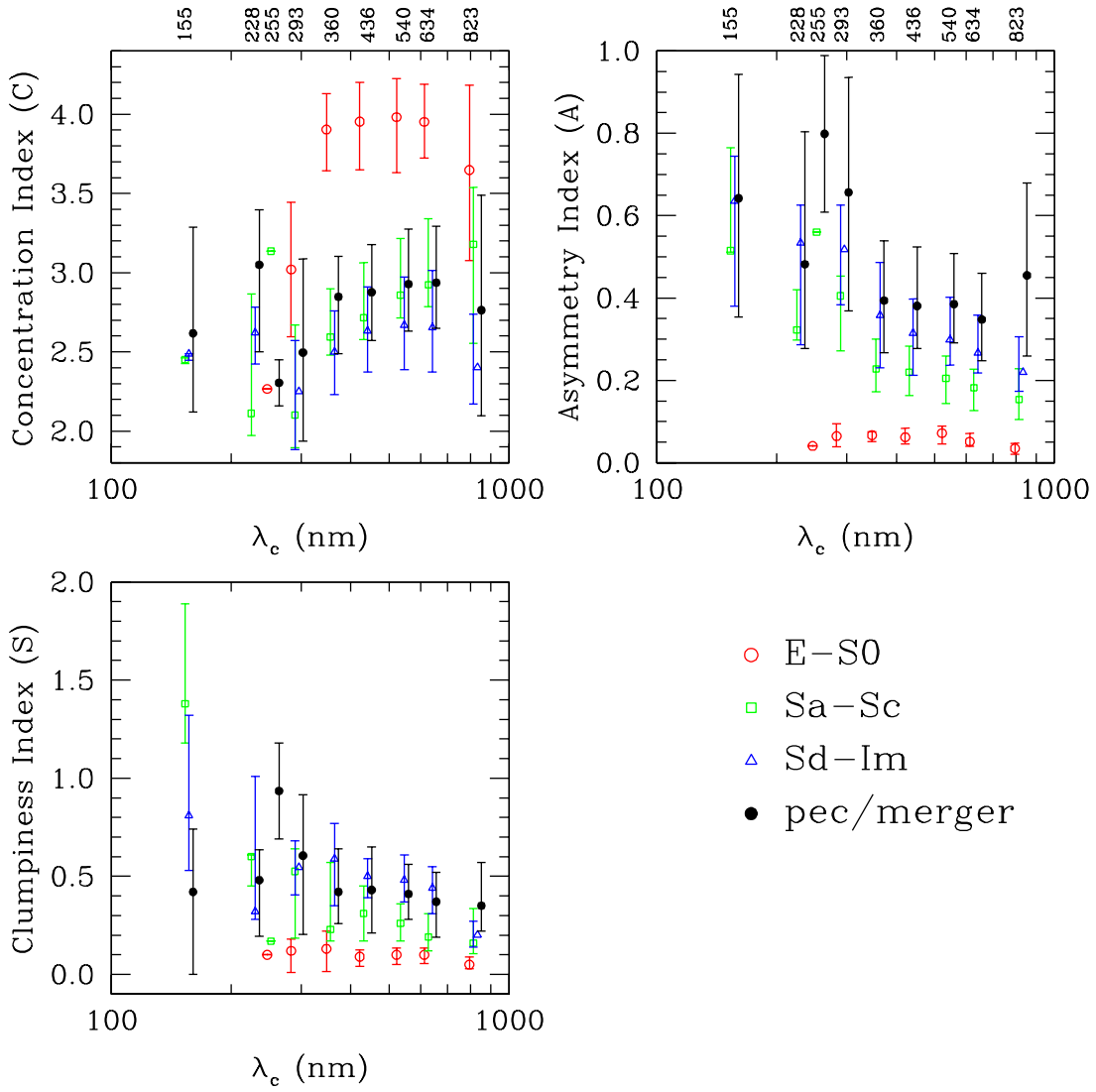

Figure 31 The median CAS parameters in each filter and type-bin as a function of the central wavelength in nm (λ_c) of each filter. Galaxy type is coded by symbol as shown in the lower right panel. Labels along the top axes of the top plots indicate λ_c for each filter in nm. Data from each type-bin are artificially offset in λ_c. Error bars show the 25–75% quartile range of the parameters for individual galaxies. Early-type galaxies (E–S0) are relatively constant in C, A, and S with increasing rest-frame wavelength longward of the Balmer break, but are unmeasurable shortward of the Balmer break due to the low signal-to-noise of these red galaxies in the UV images. All other galaxy types appear less concentrated, more asymmetric, and more clumpy at shorter wavelengths than at longer wavelengths.

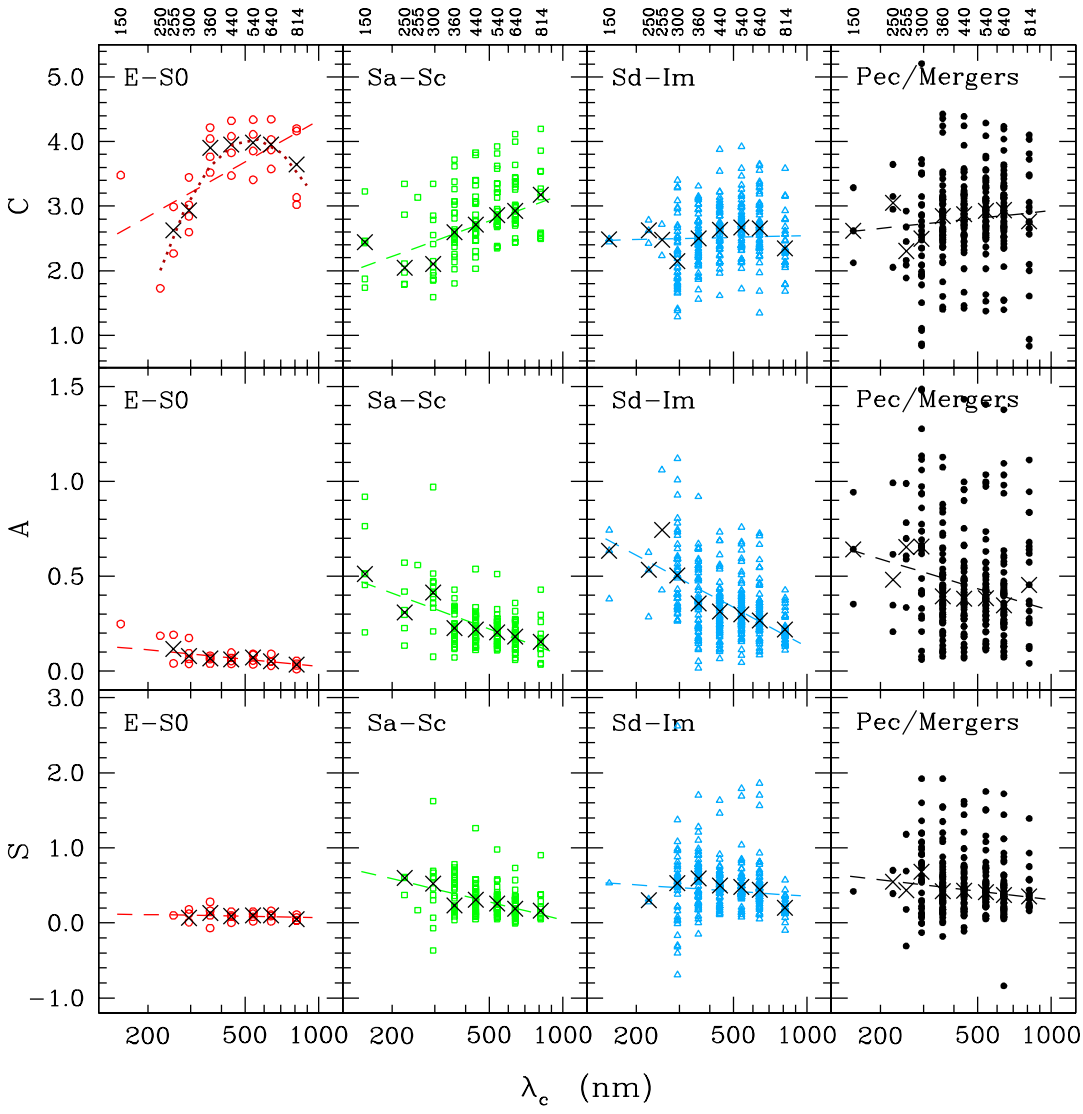

Figure 32 The CAS parameters as a function of the central wavelength in nm (λ_c) of each filter. The values for different type-bins are separated into different panels, from left to right. Crosses denote the median value of the C, A, or S parameters for each filter and type bin. Dashed lines are the linear-least-squares fit to the data. The dotted line in the upper left panel (C for galaxy types E–S0) is a 2nd order polynomial fit to the data. This may be the only panel where the trend is of higher order than linear. These fits show an increase in C, a decrease in A, and a slight decrease in S with increasing rest-frame wavelength.

ingful to determine the dependence of the CAS parameters on wavelength by examining the differences seen within individual galaxies, rather than fitting trends to the entire data set. Therefore, we also calculated the difference between the CAS parameters in long and short wavelength filters for each individual galaxy with type later than S0. We find median differences between the R- and U-band in the C, A, and S values of +0.24, –0.07, and –0.12, respectively, with a positive number indicating an increase in that index at longer wavelengths. We find median differences between FUV and U of +0.14, –0.24, and –0.54, for C, A, and S, respectively. This leads to a total median decrease in C from the red to the far-UV of 0.38, an increase in A of 0.31, and an increase in S of 0.66. The trends in the CAS parameters with type, however, are larger than the trends with wavelength. In conclusion, this quantitative discussion of the dependence of the CAS parameters on rest-frame wavelength and galaxy type serves as a zero-redshift benchmark for higher redshift galaxy classifications. The detailed application of our findings to classification of high redshift galaxy samples will be done in later works.

CHAPTER 4

ANALYSIS OF THE DATA QUALITY FROM THE VATT THROUGH MEASUREMENTS OF THE OBSERVING CONDITIONS AT MT. GRAHAM

4.1. Overview of Chapter 4

We present measurements of sky surface brightness and seeing on Mt. Graham obtained at the Vatican Advanced Technology Telescope (VATT) during 16 observing runs between April 1999 and December 2003. We show that the sky surface brightness is significantly darker during photometric conditions, and can be highly variable over the course of a single observing run as well as from one run to the next, regardless of photometricity. In our photometric observations we find an average low-airmass ($\sec z < 1.2$) sky surface brightness of 22.00, 22.53, 21.49, and 20.88 mag arcsec^{-2} in U, B, V, and R, respectively. The darkest run (02/00 in U and 02/01 in BVR) had an average sky surface brightness of 22.38, 22.86, 21.72, and 21.19 mag arcsec^{-2} in U, B, V, and R, respectively. With these results we show that under the best conditions, Mt. Graham can compete with the darkest sites in Hawaii and Chile, thanks in part to the strict dark-sky ordinances in place in Tucson and Safford. We expect the sky over Mt. Graham to be even darker than our 1999–2003 results during solar minimum (2006–2007).

We find a significant improvement of about $0.45''$ in our measured stellar FWHM after improvements to the telescope were made in Summer and Fall 2001. Stellar FWHM values are highly variable, with median R-band focus FWHM values in each observing run ranging from $0.97''$ to $2.15''$. Significantly sub-arcsecond seeing was occasionally achieved with values as low as $0.65''$ FWHM in R. There may possibly still be a significant telescope contribution to the seeing at the VATT, but nearby trees as high as the dome are currently the dominant factor.

4.2. Introduction to Chapter 4

Mount Graham International Observatory (MGIO) is located near Safford, Arizona at an altitude of 10,400 feet. It contains the Vatican Advanced Technology Telescope (VATT), the Heinrich Hertz Submillimeter Telescope, and the Large Binocular Telescope[1]

[1] http://medusa.as.arizona.edu/lbto/

(LBT; currently under construction with first light expected in late 2004). The observing conditions at the MGIO site are important limiting factors on the efficiency of observing faint objects, and are thus important to characterize with observations at the existing telescopes, as well as the LBT. Therefore, in this chapter we focus on two of the most important properties of an observing site: the sky surface brightness and the seeing over the course of four years.

Dark sites are in increasingly short supply due to metropolitan development, but reasonably dark sites do still exist. Other observers have studied sky surface brightness values at other observing sites, particularly in the context of determining the effects of nearby city lights. Massey and Foltz (2000) measured the sky brightness in various directions of the sky at Kitt Peak and Mt. Hopkins in 1988 and again in 1998 to determine the effects of increasing light pollution from the expansion of Tucson. They found that since 1988, the zenith BV sky brightness increased slightly by 0.1–0.2 mag arcsec^{-2} at Kitt Peak. At a larger zenith distance of 60°, however, there was a 0.35 mag arcsec^{-2} increase when pointing away from Tucson, and a 0.5 mag arcsec^{-2} increase when pointing toward Tucson. They mention that this increase in sky brightness would be worse if Tucson did not have good outdoor lighting ordinances, which also exist in Safford. Although Mt. Graham is near Safford, Safford is a much smaller city than Tucson and MGIO is located at a much higher elevation than Kitt Peak and Mt. Hopkins, with Tucson and Phoenix well below the horizon as viewed from the Mt. Graham summit. Hence, city lights should not have as large of an impact on the sky brightness at MGIO.

Other factors in addition to city lights impact the sky brightness, such as the presence of atmospheric dust, forest-fire smoke, cirrus, the solar cycle, airmass, galactic and ecliptic latitude of the observation, the phase and angular distance of the Moon from the observed object, and altitude and geomagnetic latitude of the observing site. Benn and Ellison (1998) measured the sky brightness at La Palma from 1987 to 1996, finding that the sky was 0.4 mag arcsec^{-2} brighter during solar maximum than solar minimum, and 0.25 mag arcsec^{-2} brighter at an airmass ($\sec z$) of 1.5 than an airmass of 1.0 (at the zenith). Krisciunas (1997) measured the sky brightness at Mauna Kea in Hawaii, and found that except for the solar cycle, the most important effect is random short term variations over tens of minutes, which makes sky brightness measurements highly variable and difficult to compare between sites. To quantify the quality of sky brightness at Mt. Graham, we present our sky surface brightness measurements from April 1999 to April 2002 at the VATT, compare our measurements to those known at Mt. Hopkins, Kitt Peak, Mauna Kea, La Palma, ESO, and Cerro Tololo, and discuss how the variability of sky brightness due to the factors listed above impact our conclusions. We also compare our measurements to a theoretical sky brightness for Mt. Graham (Garstang 1989) and investigate the effects of city lights and the variation of sky brightness with time of night.

The seeing of an astronomical site can be estimated by measuring the median full width at half max (FWHM) of stars in images taken at that site. We have done this for Mt. Graham by measuring the FWHM of stars in stacked galaxy images and in short focus

exposures taken at the VATT. This is only an estimate, because there are other factors in addition to atmospheric seeing that play a role in the stellar FWHM, such as telescope focus and telescope image quality due to mirror quality, telescope collimation, etc.. The FWHM results presented in this chapter are to be applied at face value to the VATT alone, and do not necessarily reflect on the Mt. Graham site or on the LBT site, since the VATT's specific location on the mountain-top makes it more susceptible to ground layer seeing, particularly in northeasterly winds.

4.3. Observations

We have obtained $UBVR$ surface photometry for 142 galaxies at the VATT, using the VATT 2k×2k Direct CCD Imager. Typical exposure times were 2×(600–1200)s in U, 2×(300–600)s in B, 2×(240–480)s in V, and 2×(180–360)s in R. The CCD gain is 1.9 electrons per ADU and the read-noise is 5.7 electrons. We binned the images 2×2, resulting in a pixel scale of 0.375 arcsec pixel^{-1}. Individual images were stacked with integer shifts, as the PSF is well sampled. Sky brightness values and FWHM values measured from stacked images are the signal-to-noise weighted average values from the individual images that make up the stack, which suffices to examine overall trends in the data. The details of our galaxy sample and galaxy surface photometry, and the methods we used for data reduction and calibration are presented Chapter 2.

Observations were spread over 9 runs between April 1999 and April 2002, for a total of 49 usable nights. Defining photometric nights as those with zeropoint magnitudes that vary no more than 3% throughout, 45% of the nights were photometric, 51% were mostly non-photometric (with parts of the night possibly photometric until clouds moved in), and 4% were lost entirely to telescope problems. During nights where clouds appeared toward the end of the night, we salvaged as much as possible of the first part of the night as photometric.

For comparison, additional focus exposure stellar FWHM values are presented for 8 VATT observing runs between November 2001 and December 2003, which were carried out independently by R.A. Jansen for other projects.

4.4. Trends in Sky Surface Brightness at the VATT

4.4.1. *Measurements of the Sky*

Sky values for each stacked galaxy image were calculated by finding the median of the median pixel value in each of 13 boxes, each 120 pixels wide, along the edges of the image. This was done to avoid including light from the galaxy, which was usually centered in the CCD. Taking the median values helps to reject stars and cosmic rays, which comprise a small percentage of the total number of pixels in the sky boxes. The average sky count-rates for all stacked galaxy images were 0.41 ± 0.01 ADU s^{-1} in U, 1.34 ± 0.11 ADU s^{-1} in B, 2.64 ± 0.10 ADU s^{-1} in V, and 4.26 ± 0.15 ADU s^{-1} in R. Sky surface brightness values were photometrically calibrated using Landolt standards (Landolt 1992). We defined

photometric nights as those with zeropoints that vary no more than 3% throughout the night, which defines the largest uncertainty in the calibrations.

4.4.2. *Sky Surface Brightness Results*

In Figure 33, the resulting $UBVR$ sky surface brightness values for each stacked galaxy image are plotted vs. the average airmass ($\sec z$) of the individual images that comprise each stack. Each observing run is broken up into a separate panel for comparison. Stacked images that are comprised solely of individual images taken during photometric conditions (change in magnitude zeropoint throughout the night $\lesssim$ 3%) are plotted as asterisks, while those comprised of images taken during non-photometric conditions are plotted as open circles. There is a clear, well defined difference in sky surface brightness between these two conditions: non-photometric nights have notably brighter skies, as expected due to the presence of cirrus. There is a trend of increasing sky surface brightness with increasing airmass, which is also to be expected, although there does not appear to be a single consistent slope to this trend throughout all observing runs, even for photometric runs. It is also apparent from the plots in Figure 33 that the sky surface brightness is highly variable as a function of time, both over the course of a single run and from one run to the next. Since the sky brightness is highly dependent on many factors, such as solar activity, atmospheric conditions, time since sunset, variable night sky-lines, and the location of the telescope pointing with respect to nearby city lights, the Moon, zodiacal light, and the Galaxy itself, this variability is not surprising.

The effect of the Moon on the sky surface brightness of a given galaxy field is a complicated function of the phase of the Moon, the airmass ($\sec z$) of both the Moon and the galaxy position, the angular distance between the Moon and the galaxy (θ_{Mg}), and the atmospheric extinction (Krisciunas & Schaefer 1991). We approximate the effect of Moon on our sky surface brightness (μ) results through a plot of the sky brightness of all stacked galaxy images vs. $\cos\theta_{Mg}$, which is shown in Figure 34. We use $\cos\theta_{Mg}$ because the effects from the Moon on the sky brightness of a target away from the Moon may behave as a spherical harmonic, so that some linear behavior in $\cos\theta_{Mg}$ may be expected. The secondary Moon effects due to airmass of the Moon and galaxy and atmospheric extinction are not separated out here, and are expected to be small compared to other large scale variations in the overall sky surface brightness, as discussed previously. The sky brightness values were normalized to the median sky brightness for the relevant observing run in order to remove large-scale seasonal effects. Four sub-panels show different Moon phases, ranging from a Moon illumination of 0% to 40%, which is the maximum illumination in our data. This plot shows that photometric nights (indicated by solid symbols) tend to have darker skies than non-photometric nights (open symbols), and show a smaller scatter in sky surface brightness from one image to the next. Both photometric and non-photometric exposures show no major trend with Moon angular distance within the scatter for Moon illumination $\leq$ 20%. There may be a slight anti-trend of increasing sky surface brightness at 180° from the Moon visible in the panel for Moon illumination $\leq$ 10%, which could be the result of

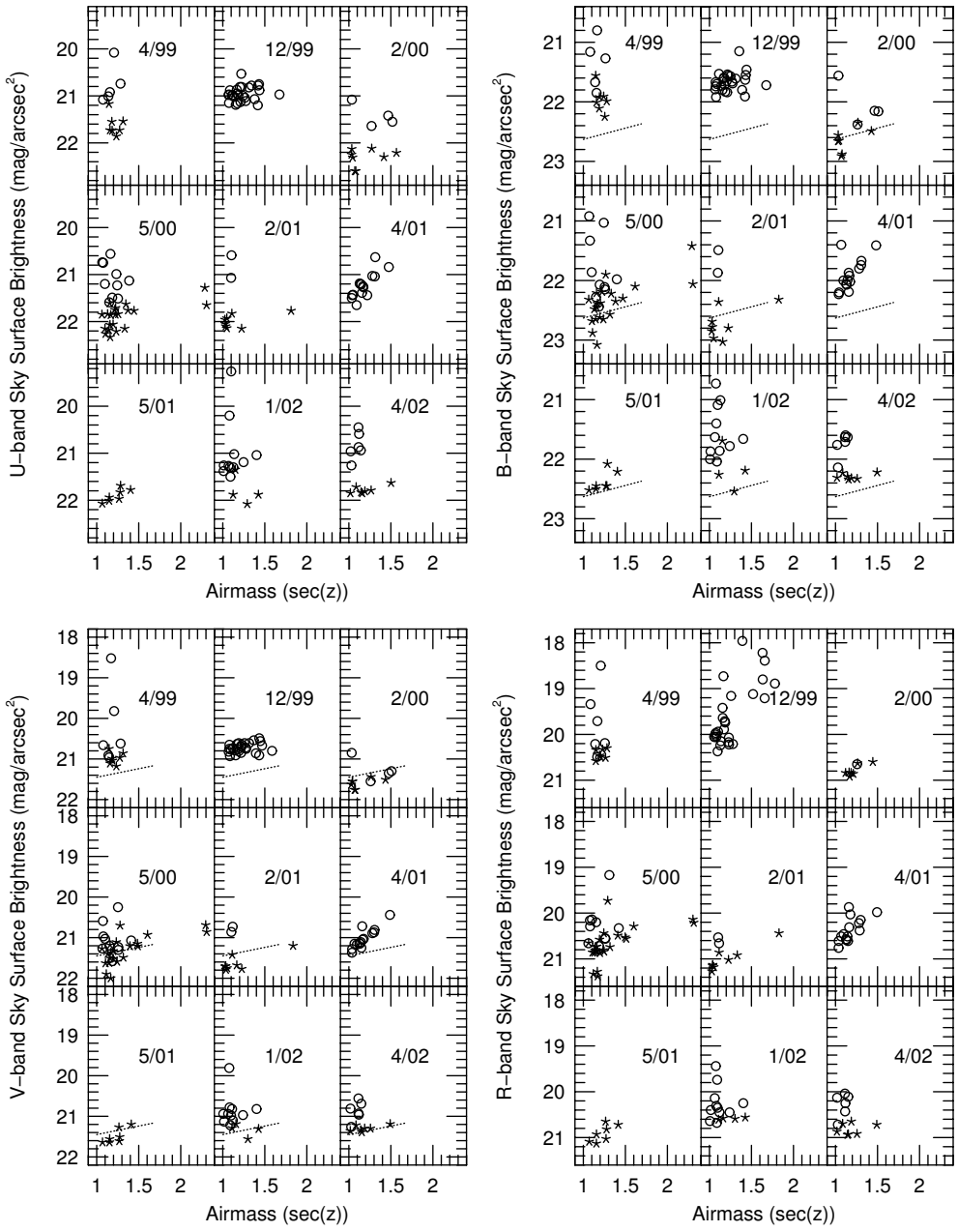

Figure 33 Sky surface brightness in stacked galaxy images taken at the VATT between April 1999 and April 2002 in U, B, V and R. Each of our observing runs is indicated in a separate sub-panel. Measurements obtained under non-photometric conditions are represented by open circles, while measurements from photometric nights (zeropoint variations $\lesssim 3\%$ throughout the night) are indicated by asterisks. Within a given run, the sky is brighter during non-photometric than photometric conditions. The sky surface brightness can be highly variable on monthly, nightly, and tens of minutes time scales. Dotted lines represent the average values at Mt. Hopkins/Kitt Peak (converted to broad-band from spectrophotometry) over four nights in 1998 and 1999 (Massey & Foltz 2000), just before solar maximum (2000–2001).

sun-light back-scattering off of the atmosphere. A stronger trend of increasing sky surface brightness with decreasing Moon angular distance is apparent when Moon illumination is $\geq 20\%$. We applied a linear least-squares fit of

$$\mu = m \cos\theta_{Mg} + b \tag{4.1}$$

to this trend for the mostly photometric data in the Moon illumination $\geq 30\%$ panel (eliminating points with airmass > 2), and determined slopes of 0.97 in U, 0.83 in B, 0.36 in V, and 0.29 in R. Thus, as expected, there is a stronger dependence on Moon angular distance for shorter wavelengths. There are only a small number ($\sim$5) of galaxy images that are affected by the Moon within the scatter of these plots, leading us to the conclusion that our median sky surface brightness values are largely unaffected by moonlight.

Solar maximum occurred around 2000–2001, in the middle of the time spanned by our observations, which could have raised the sky surface brightness by several tenths of a magnitude with respect to the sky surface brightness at solar minimum. For instance, Benn and Ellison (1998) saw an increase in sky brightness of 0.4 magnitudes in $UBVR$ from solar minimum to solar maximum at La Palma. We therefore expect the sky surface brightness to be fainter than these results by a similar amount during the upcoming solar minimum (2006–2007).

The dotted lines in Figure 33 (B and V panels) represent an estimate of the dependence of the sky surface brightness on airmass at Kitt Peak and Mt. Hopkins as measured by Massey and Foltz (2000) for comparison. Zenith values (airmass=1.00) were derived by taking the average of Massey and Foltz's measurements at both locations, which consisted of 1 exposure in each passband at Mt. Hopkins in Nov. 1998, and 4 exposures in each passband at Kitt Peak over three nights in Nov. 1999 (all of which were just before solar maximum, like our earlier runs. However, our later runs are closer to the solar maximum peak, and thus will be brighter). We calculated an average high airmass sky surface brightness by taking the average of 4 exposures in each passband at Mt. Hopkins at zenith distances of $34 - 53°$, and 6 exposures in each passband at Kitt Peak at zenith distances of $\sim 60°$. The dotted lines in Figure 33 connect these two points, assuming a linear dependence on airmass, which is roughly correct. One should be cautious when comparing sky brightness measurements for different sites, due to the strong variability over time visible in these figures, especially in a case like Mt. Hopkins/Kitt Peak, where we have no information on long-term variations. An additional source of uncertainty arises because Massey and Foltz (2000) derived their broadband sky brightness values from spectrophotometry, replacing the variable OI λ5577 line with an average value. Nonetheless, we can see that several VATT observing runs had sky surface brightness values that were significantly darker than the Mt. Hopkins/Kitt Peak numbers given by Massey and Foltz (2000), who point out that their numbers are comparable to Palomer Observatory in the early 1970's, which was considered a rather dark site at the time.

Figure 35 shows the median sky surface brightness at the VATT, per observing run, of all low airmass ($\sec z < 1.2$) stacked galaxy images taken during photometric conditions,

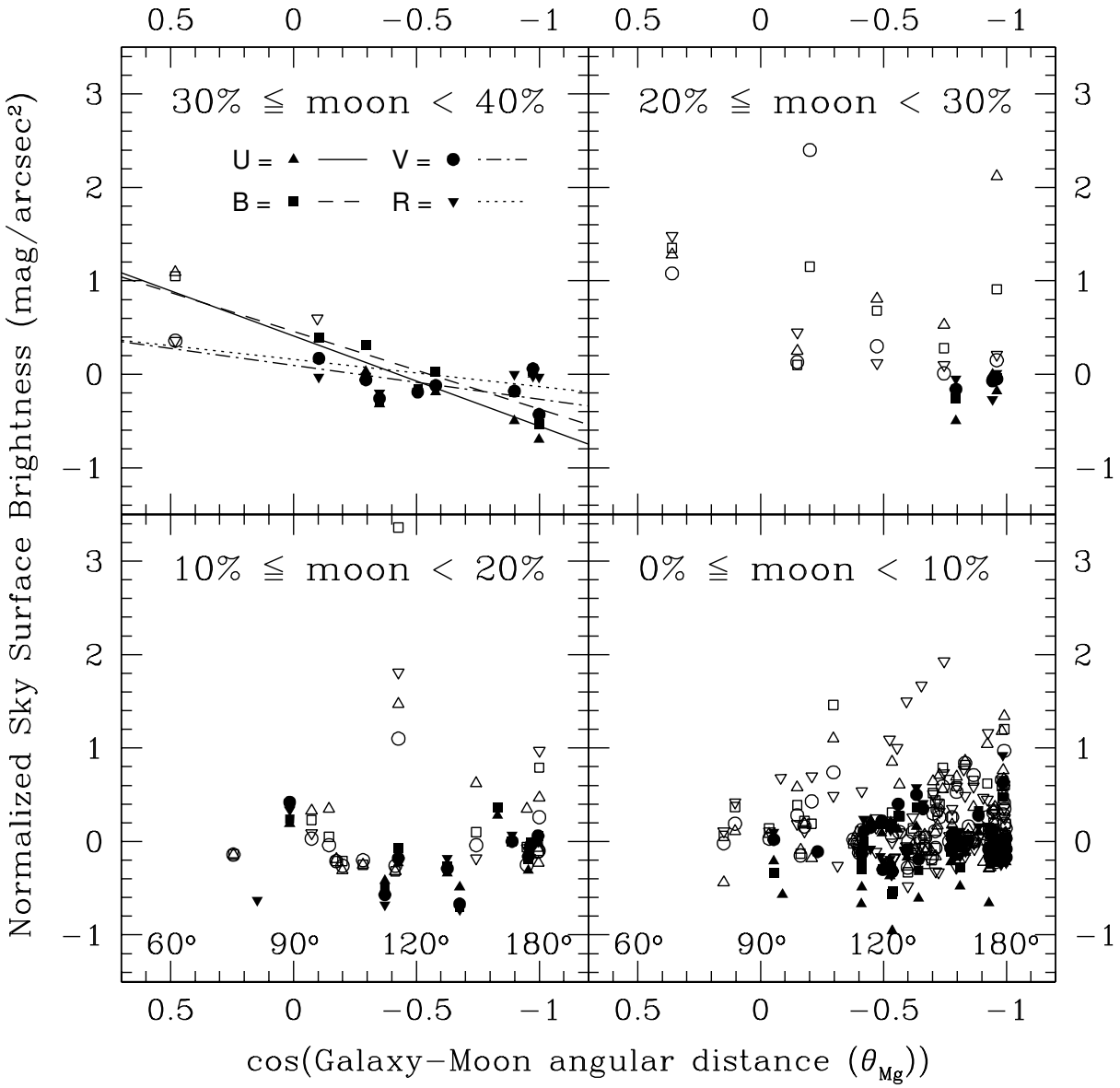

Figure 34 The dependence of the sky surface brightness, normalized to the median sky surface brightness for that observing run, on angular distance from the Moon for different Moon illuminations. Open symbols represent data that were taken during non-photometric nights, solid ones represent data taken during photometric nights. Points are coded according to filter of observation as indicated in the upper left panel. A clear dependence on angular distance to the Moon is only seen for illumination $\gtrsim 20\%$. Straight lines represent linear least-squares fits to the data in each passband for data with $\sec z < 2$. The dependence on Moon distance is stronger at shorter wavelengths. In general, our galaxy images were taken well away from the Moon and mostly during dark nights ($\lesssim 4$ days from New Moon), and thus the average sky surface brightness values presented in this chapter are not strongly affected by the Moon.

as a function of time. One obvious outlying sky brightness value was rejected in the 1/02 run in U and B, which was measured near morning twilight, and therefore contaminated our results. For comparison, we overlay the average values from Mt. Hopkins/Kitt Peak, (Massey & Foltz 2000), Cerro Tololo, (Walker 1987, and 1987–1988[2]), and La Palma, (Benn & Ellison 1998). Again, we caution against putting strong confidence in such comparisons for the reasons previously mentioned. On occasion the VATT was darker than Cerro Tololo, except in the V-band. The La Palma observations were taken from 1987 to 1996, and the values plotted in Figure 35 are the solar minimum values given by Benn and Ellison (1998) minus the quoted 0.4 magnitude difference between solar minimum and maximum, since our data was taken near solar maximum. For the most part, our values are consistently darker than La Palma's solar maximum skies, and similar to La Palma solar minimum skies (sometimes brighter, sometimes darker, although always brighter in the V-band). Figure 35 clearly shows a strong variability of several tenths of a magnitude in sky brightness from observing run to observing run, with a general brightening of the sky toward solar maximum (2000–2002). The anomalously bright point during solar minimum in 1999 may have been due to smoke from nearby forest fires.

In Table 12 we list our average photometric low airmass sky surface brightness values for the VATT, Mt. Graham, and for various other sites for comparison. We also give sky surface brightness values for our darkest and brightest runs. Excluding the Mauna Kea solar maximum values (Krisciunas 1997), which are significantly brighter than any of the measurements for the other sites, the darkest B-band sky surface brightness at sites other than Mt. Graham range from 22.6 to 22.84 mag arcsec^{-2}, compared to our average value of 22.53 mag arcsec^{-2}. Our darkest run was 22.86 mag arcsec^{-2}, which is marginally darker by 0.02 mag arcsec^{-2} than the darkest site (Mauna Kea at solar minimum). Since our observations were made near solar maximum, we can expect the Mt. Graham site to become darker still during periods of low solar activity in 2006–2007. Sites other than Mt. Graham had V-band sky brightness values that varied between 21.44 and 22.29 mag arcsec^{-2}, compared to the Mt. Graham average of 21.49 mag arcsec^{-2}. Our darkest run had a V-band sky surface brightness of 21.72 mag arcsec^{-2}, which is 0.28 mag arcsec^{-2} darker than the brightest site (Kitt Peak (Massey & Foltz 2000)) and 0.48 mag arcsec^{-2} brighter than the darkest site (CTIO during solar minimum (Phillips 1997[3])), although, again, our observations were at solar maximum. There are fewer published sky surface brightness values in U and R, but where we can make a comparison (La Palma (Benn & Ellison 1998), ESO (Patat 2003), and Cerro Tololo (Walker 1987)), our Mt. Graham averages are similar, and our darkest run was 0.08 mag arcsec^{-2} darker in U than ESO and 0.19 mag arcsec^{-2} darker in R than La Palma.

We can compare our measured sky brightness values to the Garstang (1989) predicted V- and B-band sky surface brightness values for Mt. Graham. Garstang calculated V-band sky brightness values for very clear air, during solar minimum, and using 1980 populations

[2]http://www.ctio.noao.edu/site/pachon_sky/
[3]http://www.ctio.noao.edu/site/pachon_sky/

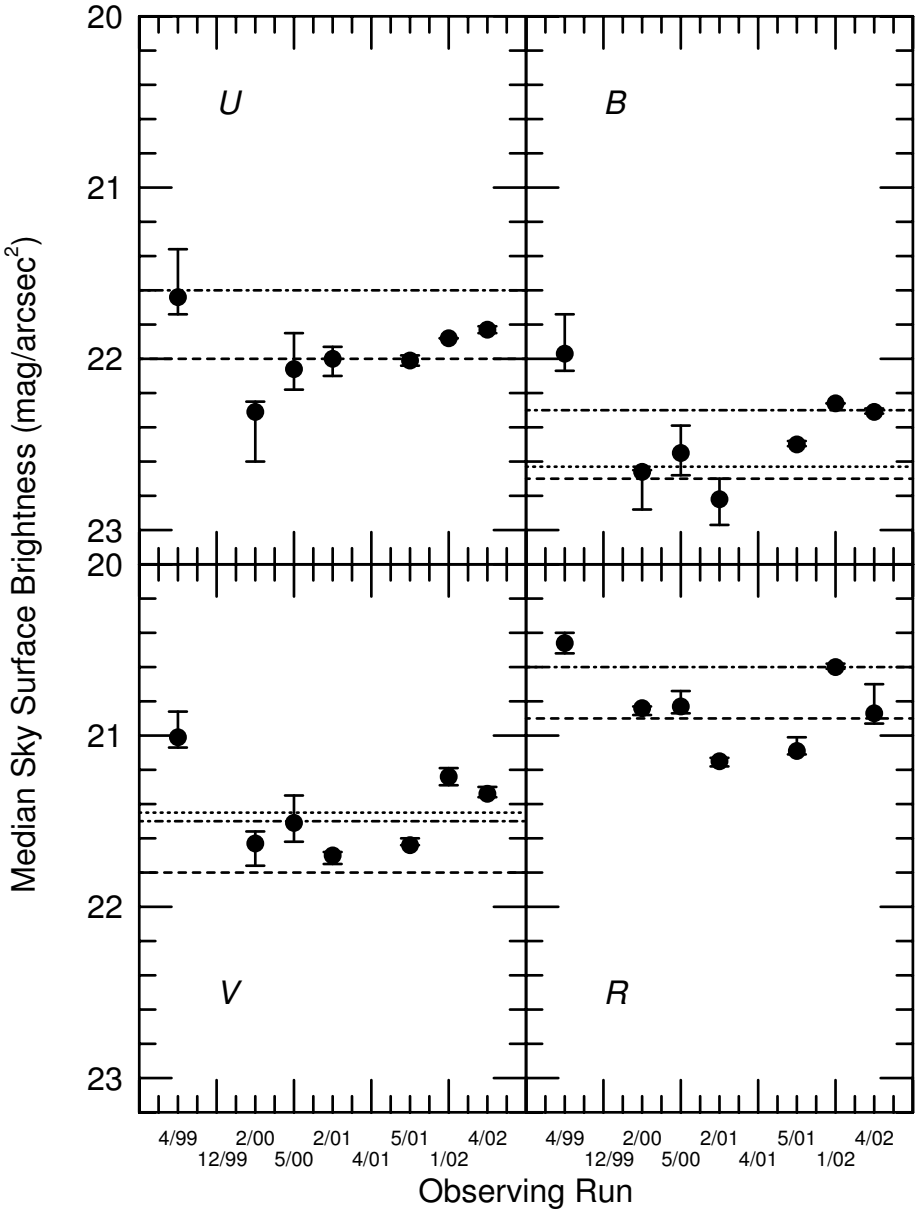

Figure 35 Median sky surface brightness of all photometric stacked galaxy images taken at the VATT with airmass ($\sec z$) < 1.2, rejecting no more than one obvious outlier per data point. Error bars represent the 25% – 75% quartile range. The horizontal lines represent the average sky surface brightness near zenith at Mt. Hopkins and Kitt Peak, Arizona (Massey & Foltz 2000; converted from spectrophotometry) [*dotted*], at Cerro Tololo, Chile (Walker 1987, and 1987–1988 results at *http* : *//www.ctio.noao.edu/site/pachon_sky/*) [*dashed*] and at La Palma, Canary Islands, Spain (Benn & Ellison 1998) [*dot-dashed*]. A comparison with other sites is given in Table 12.

Table 12. Average Photometric Sky Surface Brightness (μ) Near Zenith at Various Sites.

Site	Condition	Obs. Dates	μ_U	μ_B	μ_V	μ_R
Mt. Graham[1]	Darkest run	U: 02/00, BVR: 02/01	22.38	22.86	21.72	21.19
Mt. Graham[1]	All runs	04/99–04/02	22.00	22.53	21.49	20.88
Mt. Graham[1]	Brightest run	04/99	21.68	22.01	21.04	20.46
Mt. Hopkins[2]	···	11/98	···	22.63	21.46	···
Kitt Peak[2]	···	11/99	···	22.63	21.44	···
Mauna Kea[3]	Solar min.	96	···	22.84	21.91	···
Mauna Kea[3]	Solar max.	92	···	22.22	21.29	···
La Palma[4]	···	87-96	22.0	22.7	21.9	21.0
ESO/La Silla[5]	···	04/00–09/01	22.3	22.6	21.6	20.9
Cerro Tololo[6]	···	87–88	22.0	22.7	21.8	20.9
Cerro Tololo[7]	···	97	···	22.8	22.2	···

Note. — All sky surface brightness values have units of mag arcsec^{-2}.

[1]Mean error on mean Mt. Graham values $\lesssim 0.04$ mag arcsec^{-2}.

[2]Massey & Foltz 2000. Calculated from spectrophotometry.

[3]Krisciunas 1997.

[4]Benn & Ellison 1998. Solar min., high galactic and ecliptic latitude. Measured 0.4 mag arcsec^{-2} brighter at solar max.

[5]Patat 2003. Values corrected to zenith.

[6]Walker 1987, and 1987–1988 results at *http* : *//www.ctio.noao.edu/site/pachon_sky/*

[7]Phillips 1997 results at *http* : *//www.ctio.noao.edu/site/pachon_sky/*

for nearby towns and cities. This resulted in a predicted V-band sky brightness of 21.94 mag arcsec^{-2} for MGIO at the zenith, and 21.72 mag arcsec^{-2} at a zenith distance (z) of 45°. This agrees well with our darkest run which had an average V-band sky surface brightness of 21.72 ± 0.04 mag arcsec^{-2} for z $\lesssim$ 33.6°. Our measured value is slightly brighter than what would be expected from Garstang's predictions, but this can easily be explained by an increase in population since 1980 and the fact that our measurements were taken near solar maximum. Garstang also predicted B-band sky surface brightness values of 22.93 mag arcsec^{-2} at z=0° and 22.75 mag arcsec^{-2} at z=45°, which agrees well with our darkest run, with an average B-band sky surface brightness of 22.86 mag arcsec^{-2} for z $\lesssim$ 33.6°.

To determine how nearby city lights affect sky brightness, we plot sky surface brightness vs. the azimuth (az) of our observations in Figure 36. Data taken during nights where Moon illumination $\geq$ 20% were rejected from this plot. We normalized the sky brightness of each image to the median sky surface brightness for the sec $z \leq 1.3$ data in each observing run, and arbitrarily offset data-points taken during non-photometric conditions from those taken during photometric nights. Open circles (non-photometric) and solid circles (photometric) represent images taken at mid-zenith distances ($20° \leq z < 40°$), while asterisks (non-photometric) and triangles (photometric) represent images taken at high-zenith distances ($z \geq 40°$). Vertical dotted lines mark the general direction of three cities that may contribute to light-pollution at the Mt. Graham site.

Figure 36 shows that images observed toward the North during photometric conditions tend to have darker skies than all other directions. Darker northern skies are seen to a lesser extent with increasing wavelength (0.2, 0.1, 0.06, and 0.00 mag arcsec^{-2} darker than the median sky in U, B, V, and R, respectively), and not at all in the non-photometric data (due to the presence of cirrus). This implies that the effect may be due more to the large angular distance of these pointings from the zodiacal belt and Milky Way than to the absence of city lights in that direction. Phoenix and Tucson contribute somewhat to the sky brightness, with photometric skies between the two cities ($220° < az < 300°$) brighter than the median sky by 0.1 mag arcsec^{-2} in U, and 0.2 mag arcsec^{-2} in BVR. This brightening toward Tucson and Phoenix is strongest at high zenith distances ($z \geq 40°$) and during non-photometric conditions, which is consistent with the expected reflection of city lights off of clouds or cirrus. Safford has less of an effect on sky brightness, however, with no measurable brightening in that direction during photometric conditions. The only exception is in the R-band during non-photometric conditions, where the sky in that direction is 0.4 mag arcsec^{-2} brighter than the median. This might be at least in part due to sodium lamps from Safford, which emit at 5500–6500 Å, and are therefore most apparent in R ($\lambda_e \sim 6340$ Å). This is consistent with Massey & Foltz (2000), who estimated the contribution of such lamps in Tucson to be 0.17 mag arcsec^{-2} at the zenith of Kitt Peak and Mt. Hopkins, with a larger effect expected at higher zenith-distances and with the presence of clouds. Our brightest sky measurements toward Safford are outlying non-photometric, high-airmass data-points, and overall Safford contributes very little to the night sky brightness at the location of the VATT on Mt. Graham. Garstang (1989) predicted that the night sky would be brightest

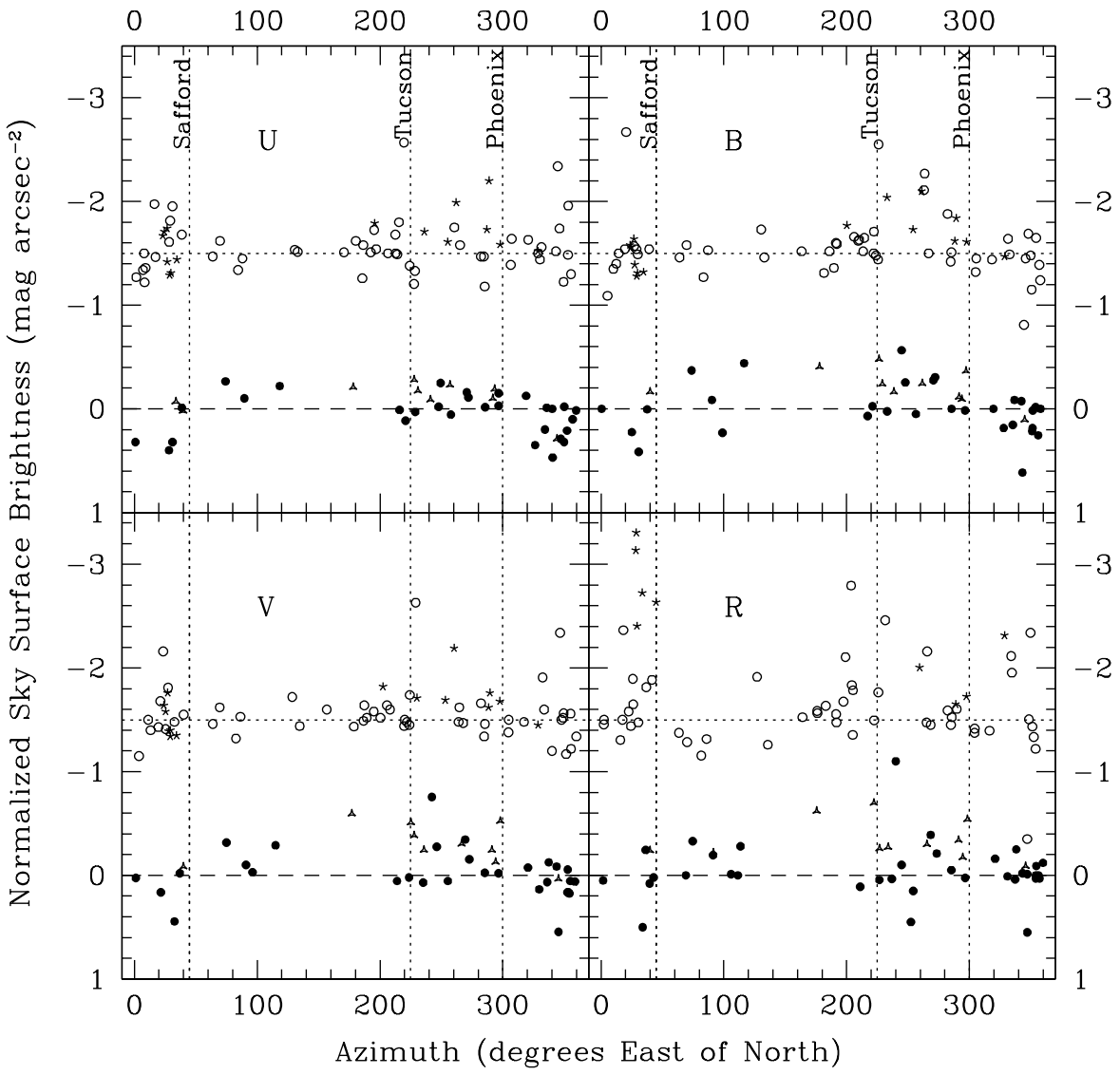

Figure 36 Sky brightness normalized to the median sky for the observing run, where $\sec z \leq 1.3$ and moon illumination $\leq 20°$. Non-photometric points (open circles for $20° \leq z < 40°$, and asterisks for $z \geq 40°$) are arbitrarily offset from photometric points (solid circles for $20° \leq z < 40°$, and triangles for $z \geq 40°$). The normalized median is marked with a dotted (non-photometric) or dashed (photometric) horizontal line. Vertical dotted lines mark the general direction of three cities that may affect the sky brightness.

toward Safford at a modest zenith distance of 45°, and considerably brighter toward Tucson than any other direction at the extreme zenith distance of 85°. However, Tucson affects our sky brightness measurements more than Safford in almost all cases. This is in part because the Safford lights are shielded by the mountain peak at the VATT's location, and in part because of the strict dark-sky ordinances in place in Safford, as well as faster growth in Tucson than Safford since Garstang's 1980 population calculations. Also, smog carried up from the Tucson valley to the nightly inversion layer likely reflects the city lights better than the clean air above Safford. Overall, city lights have little affect on the sky brightness at Mt. Graham, making it a prime dark-sky site.

Sky brightness can also vary with time of night, as addressed by Walker (1988). Walker found an exponential decrease in sky brightness at San Benito Mountain of 0.4 mag in B and V during the first half of the night. Since this decrease was observed near the zenith, and was independent of overall sky brightness, time of year, and the presence of fog, Walker concluded that it is more likely due to a natural phenomenon than a decrease in the contribution of city lights throughout the night. Walker mentions that this may be partially due to a decrease in the zodiacal light contribution throughout the night, but is likely mostly due to the recombination of ions that were excited during the day by solar EUV radiation.

We investigate this trend at Mt. Graham in Figure 37, which shows the dependence of sky surface brightness in $UBVR$ on fraction of the night, where the beginning and end of the night in each run is defined as the end and beginning of astronomical twilight for the mid-point of that run. We plot only data-points taken during moon illumination $\leq 20\%$ and at z $\leq 40°$. We normalized the sky brightness of each image to the median sky surface brightness for the $\sec z \leq 1.3$ data in each observing run, and arbitrarily offset data-points taken during non-photometric conditions from those taken during photometric nights by 1.5 mag. We approximate the nightly sky brightness trend with a linear least-squares fit that does not include measurements taken within 0.5 hours of twilight (solid lines). The UB photometric data show no significant trend with time of night. There is, however, a trend in photometric data in V and R (which is expected due to the nightly decrease in OI λ5577 and λ6300-34 emission line strengths), with a decrease in the first half of the night of 0.1 mag arcsec^{-2} in V and 0.2 mag arcsec^{-2} in R, followed by a slight increase in sky brightness toward the very end of the night. This is less than the 0.4 mag arcsec^{-2} decrease seen in B and V by Walker (1988), which may be due to the difference in elevation of Mt. Graham (10,400 feet) and San Benito Mountain (5248 feet). This highlights one of the advantages of Mt. Graham's high elevation, which contributes in many ways to making it a particularly dark site. Non-photometric data shows a stronger trend, with an overall decrease in sky brightness throughout the night of 0.2, 0.3, 0.3, and 0.4 mag arcsec^{-2} in U, B, V, and R, respectively. The reason for this decrease in sky brightness is uncertain at this time, but may be related to a general decrease of cloud-cover throughout the night, which we often recorded in the observing logs. Local humidity-driven weather induced by Mt. Graham itself may be responsible for this, especially in late spring–early fall, when the

humidity is higher.

4.5. Trends in Estimated Seeing, or Stellar FWHM at the VATT

4.5.1. *Measuring the Stellar FWHM*

The FWHM of stars measured with the VATT 2kCCD is affected by the telescope focus in addition to atmospheric effects. The actual focus value depends on several factors, such as optics, temperature, airmass, and filter. Since the VATT has a fast $\sim$ f/1 primary mirror, its focus is very sensitive to changes in temperature during the night. Once the telescope has reached equilibrium with the night air, the automated telescope software adjusts the focus to account for temperature and airmass changes. Particularly at the start of each night, however, it is necessary for the observer to frequently refocus the telescope as the temperature drops. Also, as the focus changes throughout the night the FWHM may deteriorate progressively over time, which raises the average stellar FWHM values with respect to the actual atmospheric seeing. Consistently rechecking the focus throughout the night can minimize this effect. Since these data were taken as part of a galaxy survey that focuses mainly on U-band galaxy surface photometry, we typically only focused in U. The change in focus between filters is small, since all of the filters are nearly par-focal, but focusing only in U may have resulted in a slightly larger average seeing value in B, V, and R than could have been obtained if the images had been focused in each filter separately. Therefore, we offer a cautionary note that the FWHM values in our galaxy images are likely larger than what we could achieve at the VATT if they each had been focused in their particular target filter, and if each galaxy image had been preceded by a focus check. Also, since the FWHM's from the galaxy images presented in this chapter were measured from stacked images, they will be marginally larger than if we measured them from the individual images. This is due to small errors in image alignment from the applied integer shifts.

We measured the stellar FWHM for all of our stacked galaxy images with the LMORPHO package (Odewahn, et al. 2002), which imports a list of all sources and their FWHM's produced with SExtractor (Bertin & Arnouts 1996). Stars are selected from the source list for each image by interactively defining limits on a plot of FWHM vs. magnitude, like the one shown in Figure 38. As can be seen on this plot, the FWHM of stars does not significantly depend on their brightness (except for bright saturated stars), while brighter galaxies tend to be larger in size, creating a quick way of identifying stars. This semi-automated method works well for most galaxy images, although problems may occur for fields that contain very few bright stars. In such cases, our seeing estimate may be too large, since the star selection may be contaminated by some faint extended objects.

To obtain more accurate measurements of the atmospheric seeing than can be measured with the galaxy images, we also measure the FWHM of the stars with the best focus in our focus exposures using `IMEXAM` within IRAF.[4] These focus exposures are single images

[4]IRAF is distributed by the National Optical Astronomy Observatories, which are operated by the As-

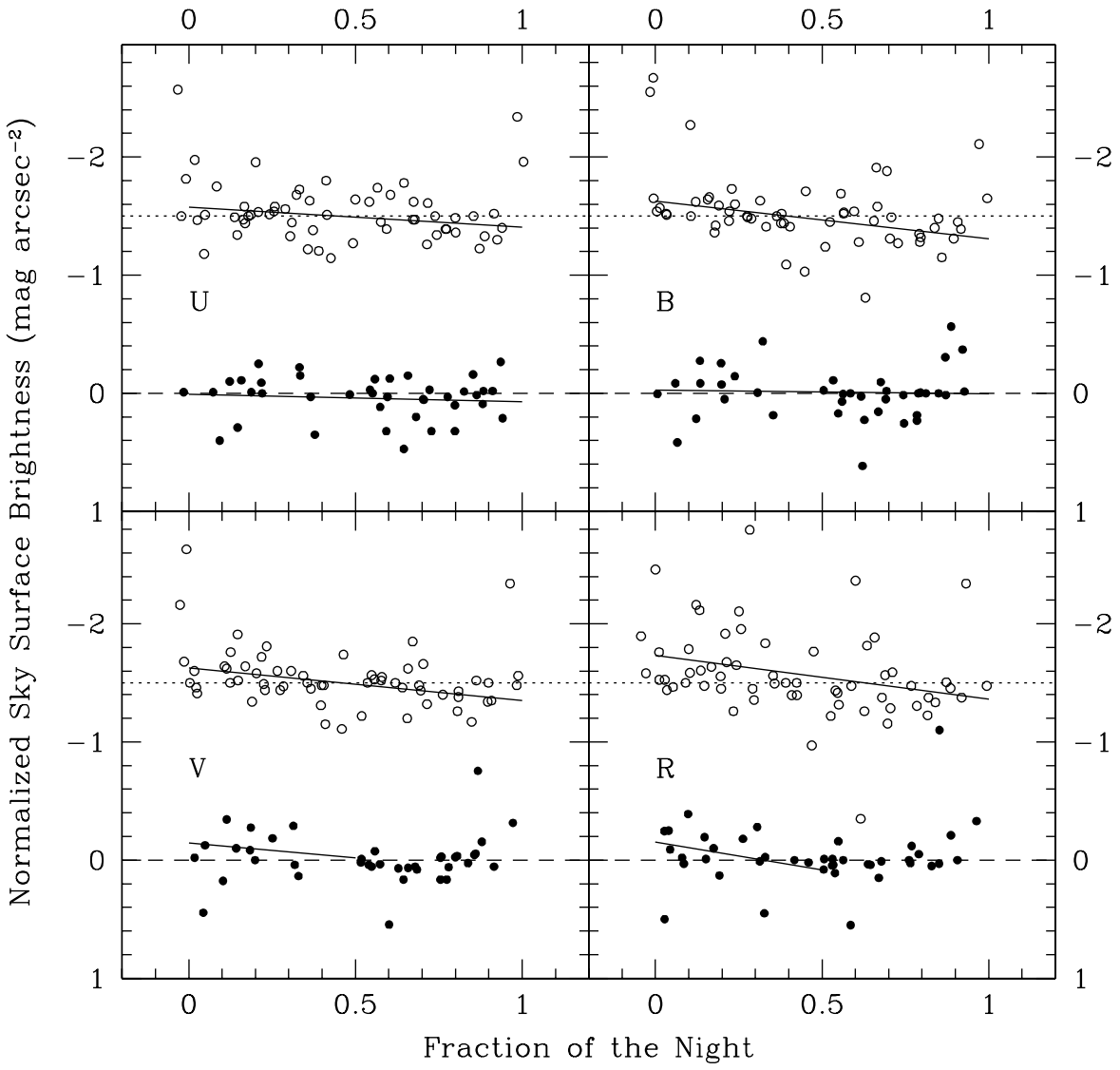

Figure 37 Sky brightness normalized to the median sky for the observing run, where sec $z \leq 1.3$ and moon illumination $\leq 20°$. Non-photometric points (open circles) are arbitrarily offset from photometric points (solid circles). The normalized median is marked with a dotted (non-photometric) or dashed (photometric) line. The beginning and end of the night is defined by the end and beginning of astronomical twilight for the mid-point of the observing run, such that dusk is at fraction=0, and dawn at fraction=1. Solid lines are the linear least-squares fit to the data, excluding measurements taken within 0.5 hours of twilight.

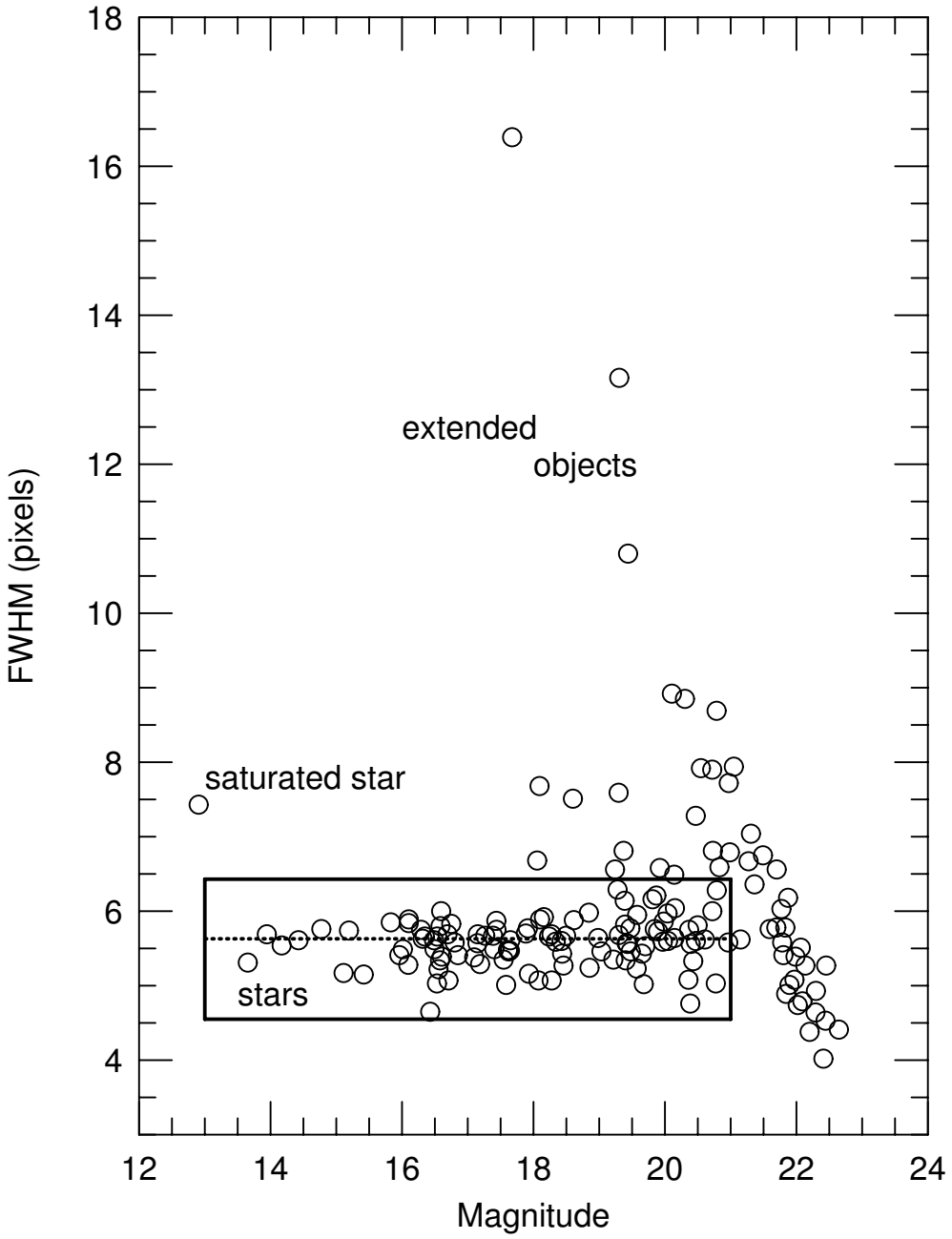

Figure 38 Object FWHM versus apparent magnitude in a single galaxy field. We use the fact that the FWHM of a star does not depend on its brightness to separate stars and extended objects, as labeled on the plot. For the purpose of our semi-automated seeing measurements, we excluded saturated stars and stars that are too faint to yield reliable measurements. The solid box encloses the objects that were used to compute the mean stellar FWHM for this field (*dotted horizontal line*).

in which 5-7 short exposures at different focus settings are recorded, where prior to each exposure the charge on the CCD is shifted by 50-100 pixels. Because these exposures are short, the stellar images are not affected by tracking and guiding errors or by telescope vibrations (as we will show below, this was particularly a problem in our earlier runs). Independent FWHM measurements by two of us (Taylor and Jansen) agree to within the measurement errors (typically $\sim$0.05–0.10$''$).

4.5.2. *Estimated Seeing Results*

Figure 39 shows the median FWHM of stars measured in our stacked galaxy images as a function of airmass in $UBVR$, and is split into separate panels for each observing run. There is a clear trend of increasing FWHM with airmass, which is to be expected from the theoretical relation[5] of

$$\mathrm{FWHM}(z) = \mathrm{FWHM}(0)\, sec(z)^{0.6} \tag{4.2}$$

but, like the sky surface brightness, this trend does not seem to have a particularly consistent slope from one run to the next (possibly because the automatic focus did not correct for airmass dependence accurately enough). Stacked images that are comprised solely of individual images taken during photometric conditions (variation in magnitude zeropoint throughout the night $\lesssim 3\%$) are plotted as asterisks, while those comprised of images taken during non-photometric conditions are plotted as open circles. This reveals that there does not seem to be a clear trend of seeing with photometricity. However, we note that in the two runs (April 1999 and May 2000) where there is a significant difference between the seeing in the photometric nights and in the non-photometric nights, the non-photometric nights had better seeing. The observation log sheets noted the presence of cirrus, which is often correlated with stable air and better seeing. Solid squares in this plot represent the FWHM of the stars with the best focus in the short focus exposures. These FWHM values tend to be smaller than or equal to the stellar FWHM measured in galaxy images taken immediately after the focus exposures, for the reasons mentioned in the previous section. As the telescope focus degrades with time between focus exposures, the stellar FWHM in the galaxy images will increase. Thus, the focus FWHM values are indeed a more accurate measurement of the atmospheric seeing.

Figure 40 shows the median low airmass ($\sec z < 1.2$) FWHM values for each run, with solid circles representing the stellar FWHM in the stacked galaxy images, and open circles representing the best focus FWHM in the focus exposures. In almost all cases, the median FWHM in the focus exposures is smaller than that in the galaxy images, as expected. Except for the February 2001 observing run, which had particularly good seeing, it is apparent that the average FWHM values and their uncertainties (which reflect the range of the data) are much larger for the runs before May 2001. This change in FWHM values corresponds to an engineering run at the telescope in Summer 2001, during which

sociation of Universities for Research in Astronomy, Inc., under cooperative agreement with the National Science Foundation.

[5] http://www.ing.iac.es/Astronomy/development/hap/dimm.html

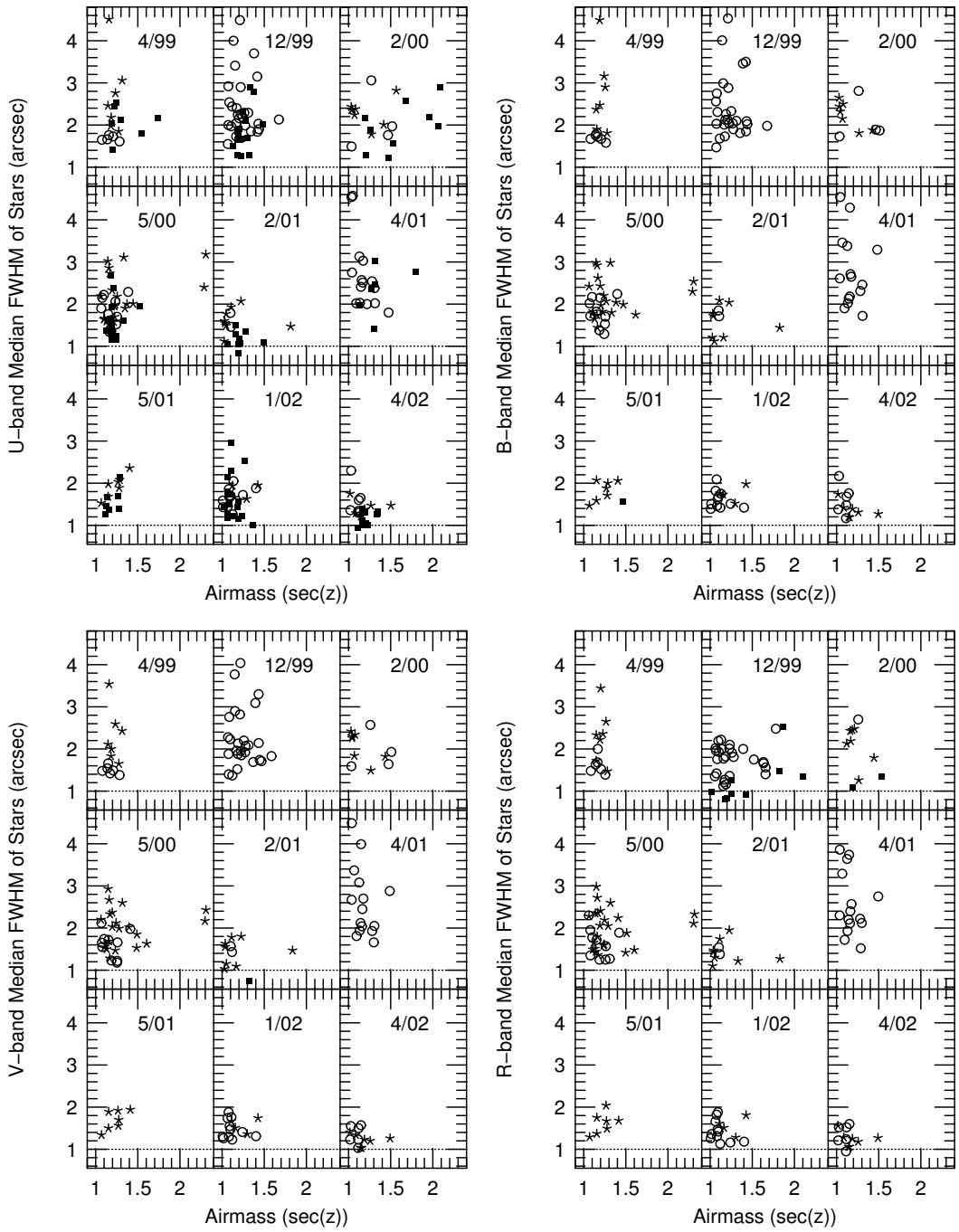

Figure 39 Median stellar FWHM in images taken at the VATT between April 1999 and April 2002 in U, B, V and R. Each of our observing runs is indicated in a separate sub-panel. Measurements obtained under non-photometric conditions are represented by open circles, while measurements from photometric nights (zeropoint variations $\lesssim 3\%$ throughout the night) are indicated by asterisks. The solid squares represent the stellar FWHM corresponding to the best focus setting as measured in short focus exposures. These tend to be smaller than or equal to the FWHM's measured in adjacent object exposures. We typically focused the telescope in U, since that is where most of our galaxy images would be taken.

Table 13. Median stellar FWHM measurements at the VATT.

type	date	U-band	B-band	V-band	R-band
Best median focus[1]	2/01 & 10/02	···	···	···	$0.97'' \pm 0.06''$
Worst median focus[1]	4/01	···	···	···	$2.15'' \pm 0.42''$
Best FWHM in single focus exposure[1]	2/01	···	···	···	$0.65''$
All galaxy images[2]	4/99–2/01	$2.01'' \pm 0.25''$	$2.01'' \pm 0.34''$	$1.86'' \pm 0.39''$	$1.81'' \pm 0.24''$
All galaxy images[3]	5/01–4/02	$1.57'' \pm 0.10''$	$1.56'' \pm 0.12''$	$1.41'' \pm 0.12''$	$1.36'' \pm 0.08''$
Best median in galaxy images[4]	4/02	$1.36'' \pm 0.03''$	$1.42'' \pm 0.06''$	$1.23'' \pm 0.04''$	$1.25'' \pm 0.05''$
Worst median in galaxy images[4]	4/01	$2.66'' \pm 0.12''$	$2.65'' \pm 0.22''$	$2.67'' \pm 0.26''$	$2.40'' \pm 0.11''$
Best FWHM in single galaxy image	UBV: 2/01, VR: 4/02	$1.12''$	$1.12''$	$1.03''$	$0.95''$

Note. — Stellar FWHM values measured in focus frames are closer to the true atmospheric seeing than stellar FWHM values measured in galaxy images, because focus exposures are short (a few seconds compared to a few minutes) and record the best telescope focus (which may have deteriorated in galaxy exposures). Focusing must be done frequently (at least once an hour, possibly more at the beginning of the night and less toward the end of the night) in order to obtain the best stellar FWHM values in deep object exposures. For our galaxy images we typically focused in U. Focusing in each filter separately would result in smaller stellar FWHM's in the other pass-bands.

[1]Exposures taken in filters other than R were reduced to R using the theoretical $\lambda^{-1/5}$ dependence and the observed contribution from the telescope added in quadrature. Median values are per observing run.

[2]Before telescope improvements in Summer and Fall 2001.

[3]After telescope improvements in Summer and Fall 2001.

[4]Median values are per observing run.

time a vibration in the secondary mirror mount that had contributed up to $0.4''$ to the FWHM was removed (M. Nelson, private communication). Adjustments were also made to the pointing map in Fall 2001. As Figure 40 shows, both of these improvements resulted in a significant reduction of the FWHM of the VATT PSF. Table 13 lists the average of the median stellar FWHM values in the galaxy images for all runs (ignoring the outlying April 2001 run) before and after the improvements. There was an overall improved seeing of about $0.45''$ in all filters, as well as a more stable focus, as can be seen in the decreased FWHM scatter between these two time periods in Figure 39, and the smaller uncertainties in Figure 40 and Table 13. After the improvements, we were able to obtain sub-arcsecond seeing in one of our combined images in R in April 2002 (see Figure 39), even though we focused in a different filter, and routinely measured sub-arcsecond seeing in the focus frames.

The stellar FWHM values from the galaxy images are useful in determining the average FWHM that one might realistically achieve in long (3–20 minute) object exposures at the VATT, with better results possible with more frequent focusing, and with refocusing done for each filter. However, the best FWHM values are obtained through the shorter (several second) focus exposures.

We can inter-compare the FWHM in focus exposures taken in different filters by determining the offset in the PSF between filters, which is a result of both the wavelength dependence of atmospheric seeing and the contribution of the telescope. Atmospheric see-

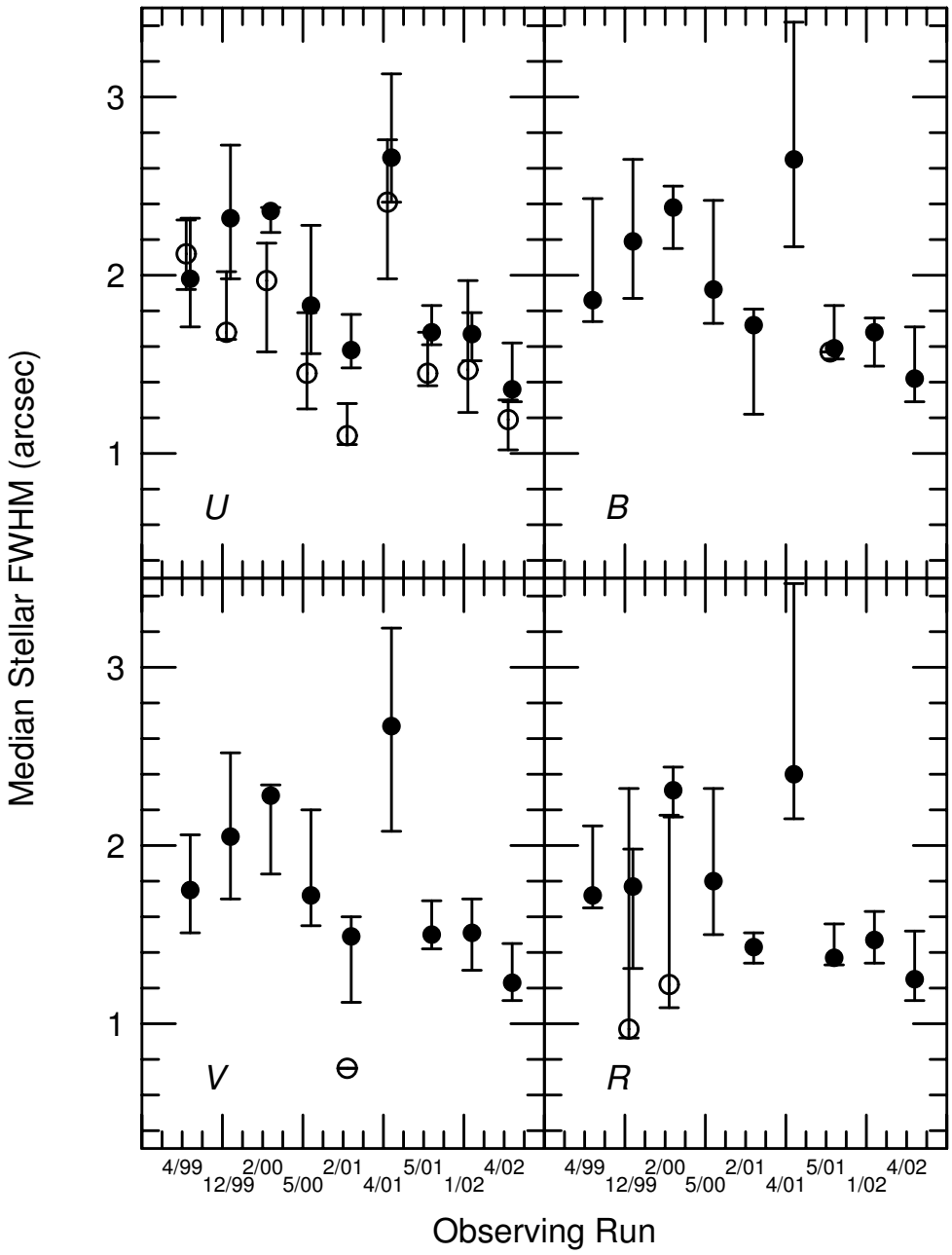

Figure 40 Historical trend in our FWHM measurements. **Solid circles:** Median stellar FWHM at low airmass ($\sec z < 1.2$) measured in our stacked galaxy images. **Open circles:** Median FWHM of the best focus setting measured in short focus exposures. Error bars represent the 25% – 75% quartile range for each run. Improvements to the telescope in Summer and Fall 2001 significantly reduced the stellar FWHM's measured during the later runs.

ing has been studied extensively in the past (e.g. Kolmogorov 1941, Tatarski 1961, and Fried 1965), and has been reviewed and summarized more recently by Coulman (1985) and Roddier (1981). The *Fried parameter*, r_0, is a measure of the average effective size at a given wavelength, λ, of the elements of air that are responsible for the angular deviations of light from a distant point source, which is the cause of atmospheric seeing. Where $r_0 \propto \lambda^{6/5}$, the FWHM measured in seeing estimates is related to r_0 by

$$\mathrm{FWHM} = 0.98\,\lambda\, r_0^{-1} \tag{4.3}$$

which results in a dependence of the FWHM on wavelength of $\lambda^{-1/5}$. To test this relation and find the FWHM contribution from the telescope, we plot the stellar FWHM of our images in each filter minus the stellar FWHM for that field in the R band (Figure 41). We only include galaxies where exposures in each filter were taken immediately after one another in order to limit the effects of airmass and large-scale seeing changes between exposures during the night. The outlying points were likely due to fields imaged during highly variable seeing conditions, or to fields where a focus exposure was taken in between observations. The solid curve in Figure 41 traces the theoretical $\lambda^{-1/5}$ FWHM dependence, while the crosses mark the median FWHM_λ – FWHM_R offset from the $\lambda^{-1/5}$ relation. The slight offset between the observational medians and the theoretical $\lambda^{-1/5}$ line gives the systematic contribution of the telescope to the wavelength dependence of the stellar FWHM. The scatter in this plot gives a measure of the random contribution of the atmosphere and telescope to the wavelength dependence, which can be due both to atmospheric variations and telescope vibrations (which is more important for the earlier runs, before the telescope improvements made in Summer and Fall 2001). These factors cannot be separated from one another in this plot, but we can put an upper limit on the random contribution from the telescope as the standard deviation in the points divided by $\sqrt{2}$ (since the errors in the target filter plus those in R combine in quadrature), which is $\simeq 0.1''$ in all filters.

In order to more carefully determine the telescope contribution to the wavelength dependence of the seeing, we plot the offsets between observation and the $\lambda^{-1/5}$ relation as a function of FWHM as measured in R in Figure 42. Points with offsets from theory greater than $0.3''$, which is significantly larger than the standard deviation of about $0.2''$, are rejected in order to exclude outliers caused by variable atmospheric seeing. Visual inspection of these plots reveal that the telescope's contribution to the wavelength dependence of stellar FWHM has no clear dependence on FWHM, which suggests a constant offset for all cases. The median FWHM_λ – FWHM_R offsets from theory found in this graph ($0.006''$ for $\lambda = U$, $0.055''$ for $\lambda = B$, and -0.050″ for $\lambda = V$) provide a measure of the telescope contribution to the FWHM wavelength dependence, which is small and well within the standard deviation of the observed FWHM's for all images. This telescope contribution, plus the atmospheric contribution given by the $\lambda^{-1/5}$ relation, have been applied to the FWHM in each filter to reduce it to the FWHM that would have been measured in an R-band exposure adjacent in time in Figure 43.

Figure 43 shows a plot of all focus FWHM values in our nine April 1999 – April 2002

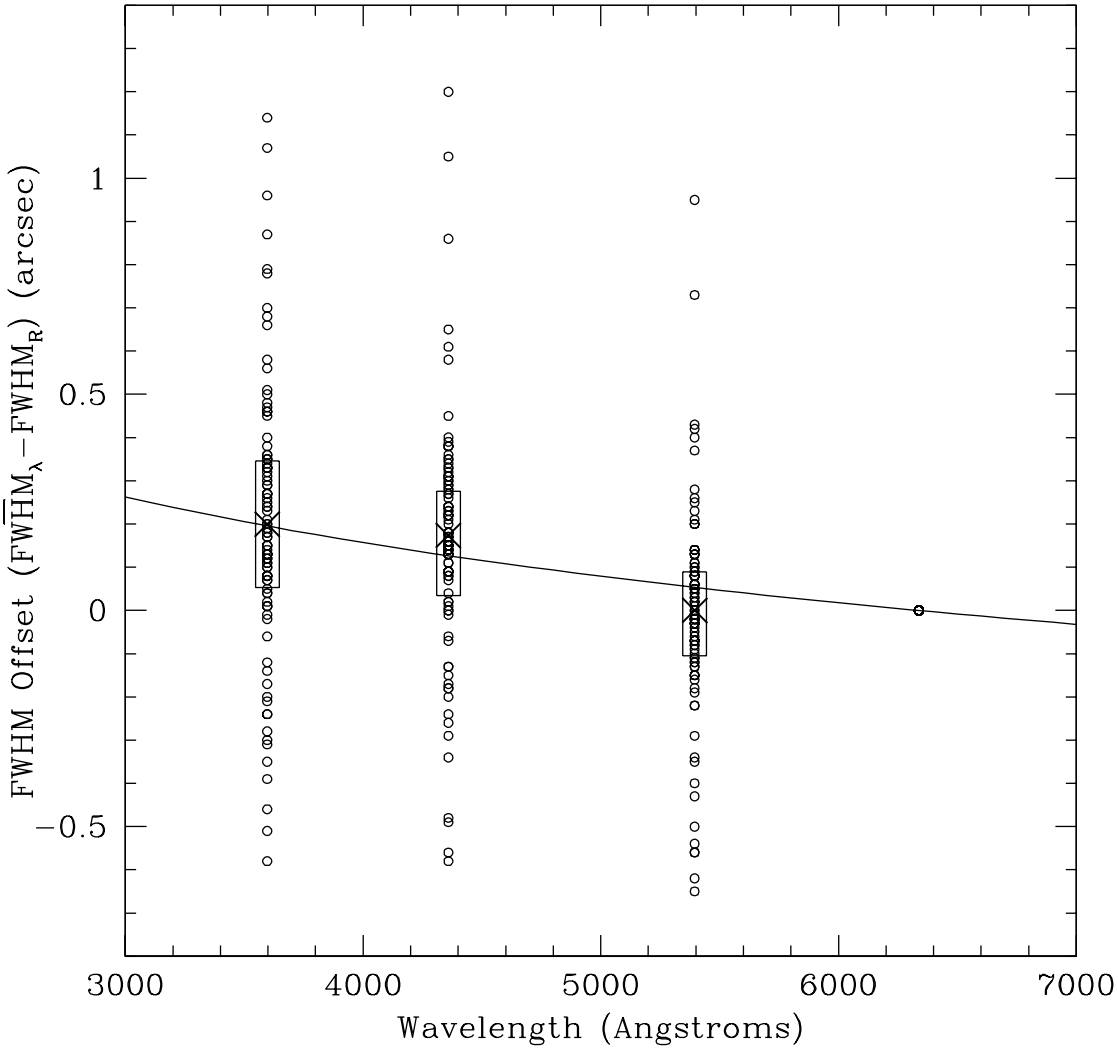

Figure 41 **Open circles:** stellar FWHM of each stacked galaxy image minus the stellar FWHM in the R-band image of that galaxy, producing a measure of the FWHM offset between filters at the VATT. Outliers are due to highly variable seeing conditions or cases where a focus exposure was taken in between observations for a single galaxy. Galaxies where observations in each filter were not carried out immediately after one another are not included on this plot. **Crosses:** the median FWHM_λ – FWHM_R offset from theory for each filter. The boxes surrounding the medians enclose the 25% – 75% quartile range. **Solid line:** The value offsets would have if the FWHM's followed the theoretical $\lambda^{-1/5}$ dependence, using the median FWHM_R value of $1.63''$. The divergence of theory from the median observed offsets are due to specific telescope properties at the VATT that cause a systematic contribution from the telescope to the wavelength dependence of the seeing. The scatter in this plot gives random offsets from theory which are partially due to atmospheric variations, and partly due to telescope vibrations (which is particularly important for the earlier runs). This vibrational component cannot be separated from the atmospheric effects, but it cannot be larger than the standard deviation of the points, which is $\simeq 0.2''$ in all filters.

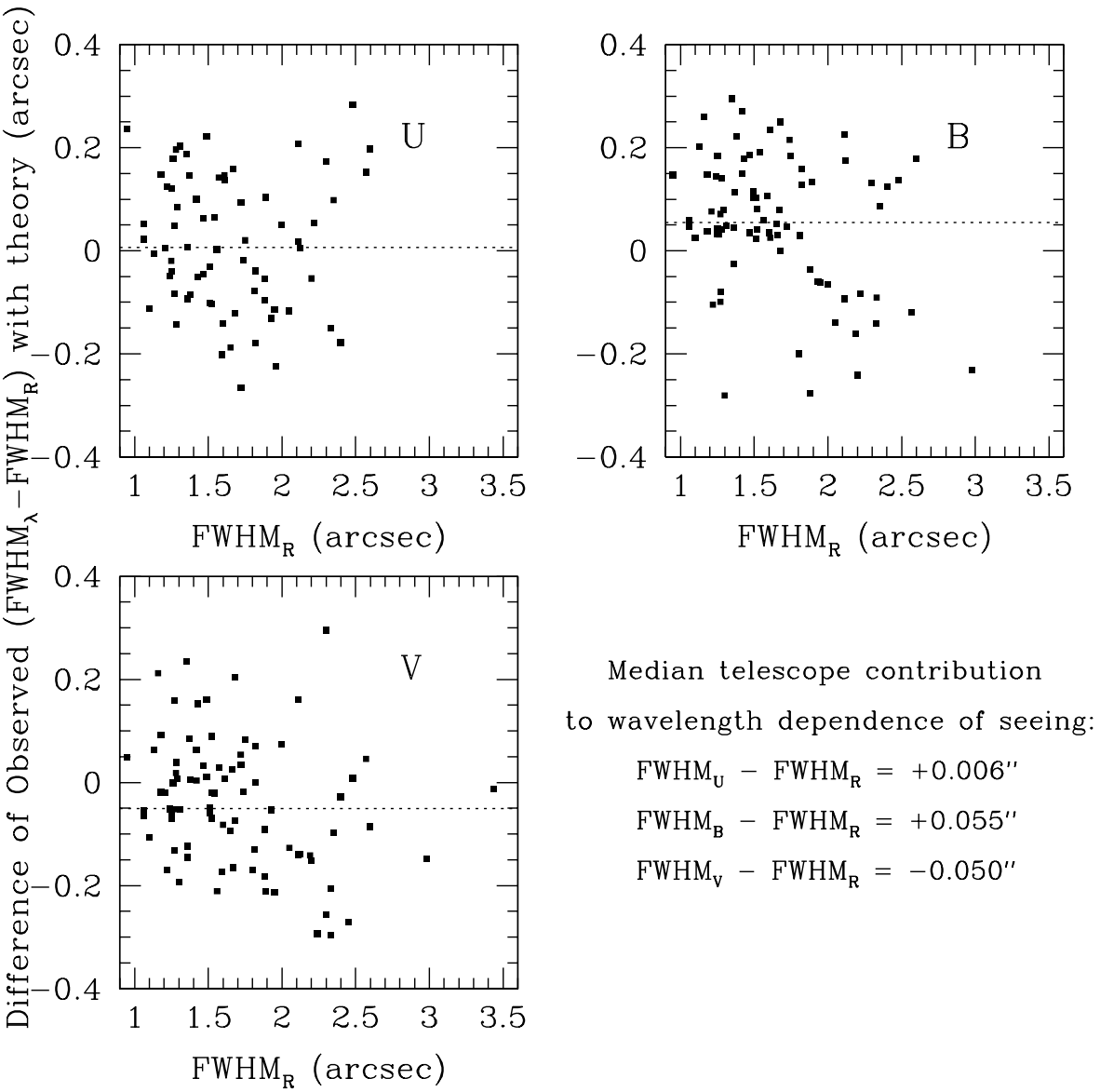

Figure 42 Comparison of the theoretical $\lambda^{-1/5}$ wavelength dependence of stellar FWHM to the observed wavelength dependence for each image, for the purpose of reducing FWHM values to the R-band in order to inter-compare focus exposures taken in different filters (as in Figure 43). We find the observed FWHM in each passband (UBV) minus the FWHM in the reference filter, R, and subtract this from the theoretical result, then plot this offset versus the observed FWHM in R. Galaxies where observations in each filter were not carried out immediately after one another are not included. Points with offsets from theory greater than $0.3''$ (which is outside the standard deviation of $0.2''$ for all of the points) were rejected to avoid outliers caused by variable atmospheric conditions. There is no strong dependence on FWHM$_R$ for this offset in any filter, and thus we apply a constant small telescope correction to all FWHM values in Figure 43 of the median (observation-theory) offset in UBV (listed in the figure and marked by dotted lines), plus the atmospheric contribution given by the $\lambda^{-1/5}$ relation.

observing runs, plus focus FWHM values for eight additional observing runs conducted by one of us (Jansen) for other projects spanning November 2001 – December 2003. All values have been reduced to the R-band using the $\lambda^{-1/5}$ theoretical relation, plus the observational telescope offsets from theory found in Figure 42. The nine April 1999 – April 2002 runs have values that are consistent with the eight November 2001 – December 2003 runs, even though each data set was observed and analyzed independently. The additional runs give us better statistics for more recent years, and thus verify that the observing runs before the telescope improvements (those to the left of the dotted line, which marks the end of the improvements in October 2001) have overall worse stellar FWHM values and larger scatter than those after the telescope improvements. The observing run with the worst individual FWHM measurements was noted to have strong winds from the northeast, which is well-known to cause bad atmospheric seeing conditions at the VATT. Under the best conditions, we were able to measure sub-arcsecond seeing for many of the focus exposures, especially after the telescope improvements in Summer and Fall 2001.

Table 13 summarizes the stellar FWHM's in the galaxy images and the focus exposures. Median stellar FWHM values range from $0.97''$ to $2.15''$ in R focus exposures, and $1.25''$ to $2.40''$ in R galaxy images. The best stellar FWHM measured was $0.65''$ in an R focus exposure, and $0.95''$ in an R galaxy image. This amounts to a linear increase in FWHM of $0.25''$ – $0.30''$ in long exposures, which is partially due to vibrations and variable atmospheric seeing, and partially due to the fact that galaxy images may not have been taken at the best telescope focus. Different values may be measured at other telescope sites on Mt. Graham, since there may be a significant telescope contribution to these values, and trees as high as the dome surrounding the VATT site negatively impact the seeing.

4.6. Conclusions for Chapter 4

Figures 33 and 35 and Table 12 suggest that Mt. Graham has a similar average sky brightness as other dark sites, and can occasionally have darker skies than some of the sites reviewed here. We have found that the sky brightness is highly variable with time, both throughout a single observing run and from one run to the next, which is consistent with other findings, as in Krisciunas (1997), who mentions that except for the solar cycle, the most important effect on sky brightness is random short term variations on timescales of tens of minutes. This makes it difficult to compare sky values from site to site. A more reliable way of comparison would be to amass a large collection of sky surface brightness data over years at each site in order to better understand and remove the short and long term variations in sky brightness, which is currently not fully understood. Various site-dependent factors should also be taken into consideration, such as the linear dependence of sky surface brightness on geomagnetic latitude due to Aurora effects in the Van Allen belt, so that low geomagnetic latitudes have somewhat darker skies than higher latitudes. The direction of pointings towards cities can also affect the sky brightness, with Tuscon and Phoenix city lights slightly increasing the sky brightness at the VATT in that direction by 0.1 mag arcsec^{-2} in U and 0.2 mag arcsec^{-2} in BVR. However, measurements made toward

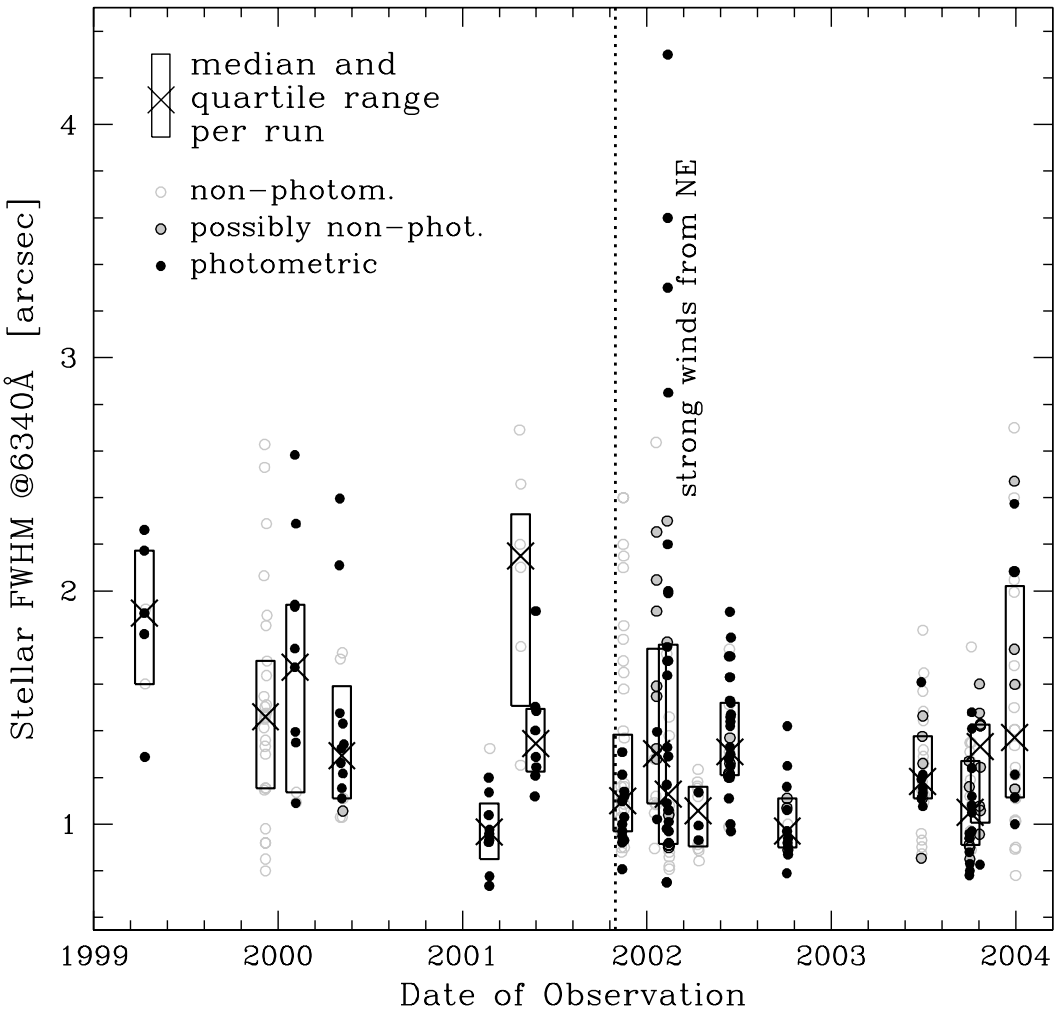

Figure 43 VATT focus exposure stellar FWHM values normalized to the R-band using the theoretical atmospheric $\lambda^{-1/5}$ dependence plus the observational median telescope contribution offsets found in Figure 42. This plot includes observing runs carried out by one of us (R. Jansen), in addition to the observing runs the rest of this chapter focuses on. The worst FWHM values were measured when strong winds were blowing from the Northeast, which always results in particularly bad seeing conditions at the VATT. Subarcsecond R-band seeing was reached on occasion throughout this time period. FWHM values are highly variable, although an overall improvement in median FWHM and scatter is apparent in the observing runs following telescope improvements made in Summer and Fall 2001. The dotted line marks the end of the implementation of these improvements.

the nearest city, Safford, are not measurably brighter than other directions (thanks to dark sky ordinances in Safford and shielding from the mountain peak at the VATT site). Nightly trends are also seen, with sky brightness values decreasing throughout at least the first half of the night by an amount that depends, at least, on the elevation of the observing site. Mt. Graham's high elevation contributes in this and many other ways to darker night skies, and the minimal effect of city lights at this location make Mt. Graham a prime dark-sky site that can easily compete with other dark sites around the world.

The FWHM of stars in images we took at the VATT have improved considerably (by $0.45''$) since maintenance operations for the Summer and Fall of 2001 corrected secondary mirror vibrations and improved the telescope pointing map. Figures 39, 40 and 43, and Table 13 show our stellar FWHM results. We were able to get sub-arcsecond seeing on occasion, especially in short (several second) focus exposures, which are less affected than long object exposures by vibrations, variable atmospheric seeing, and slipping of the telescope out of focus as the temperature changes. Because of this, the FWHM values given by focus exposures are closer to the true atmospheric seeing (by about $0.3''$) than those from faint object images.

It should also be noted that there may be a significant telescope contribution to the seeing measured at the VATT, and that the atmospheric seeing may be different at other likely locations on Mt. Graham since the presence of trees as tall as the dome around the VATT have a negative impact on the seeing at that telescope. Good seeing is not crucial to our purposes of performing surface photometry on extended galaxies, but observers who desire smaller point spread functions (PSF's) should be able to improve on our numbers by focusing more often (at least once an hour, and more often at the beginning of the night when the temperature is more unstable), and refocusing for each individual filter rather than using the focus of one filter for all filters. It should also be noted that the seeing is highly dependent on the weather, with strong northeasterly winds contributing to much worse seeing.

CHAPTER 5

CONCLUSIONS

In order to better interpret the observed rest-frame UV morphologies of high redshift galaxies, we must study the nearby late-type and peculiar/merging galaxies that resemble them in the UV. Also, comparing the properties of such nearby galaxies to those at high redshift will lead to a better understanding of the processes involved in galaxy assembly and evolution. In this work we have partially addressed these issues with studies of several galaxy structural parameters in a sample of 199 nearby, mostly late-type, irregular, and peculiar/merging galaxies, and examined their dependence on rest-frame wavelength. The parameters examined include the radial color gradients and concentration, asymmetry, and clumpiness indices of the galaxies.

In the first part of this analysis (Chapter 2) we presented images and surface brightness and color profiles for 142 mostly late-type, irregular, and peculiar galaxies observed in $UBVR$ at the VATT. Galaxies with Hubble types earlier than Sd tend to have small color gradients (if any) and become predominantly bluer outward, consistent with the conclusions of other authors (Vader et al. 1988; Franx et al. 1989; Peletier et al. 1990; de Jong 1996; Tully et al. 1996; Jansen et al. 2000; Bell & de Jong 2000; MacArthur et al. 2004). Our late-type spiral and irregular galaxies (Sd–Im), in contrast, on average tend to become significantly *redder* with increasing radius from their center. We find, however, that the scatter (range) in color gradients increases toward later Hubble type, such that one can find late-type galaxies that become somewhat bluer outward, and late-type galaxies that become much redder outward. The largest range in color gradients is found among the peculiar/interacting/merging galaxies in our sample, most of which become slightly redder outward. This particularly large scatter is consistent with the large variety of galaxy morphological types included within this class of objects, and with the complexity of the galaxy interactions.

We find that these color gradients do not have a significant dependence on the H I index, $(M_{21}–B_T^0)$, even though there is a trend of increasingly redder outer regions with fainter B_T^0 and fainter absolute H I 21 cm emission line magnitude, M_{21}. This suggests that galaxies that are faint in all bands (which tends to be true for late-type galaxies), do become on average redder with increasing radius, but these color gradients are not necessarily caused by an excess of H I. There is also a very weak trend of redder outer regions with fainter absolute far infrared magnitude, M_{FIR}. Both of these results suggest that the increasingly

strong gradients of redder colors with increasing radius in late-type galaxies may not be due to an excess of dust, but to other factors such as stellar population gradients. Other authors also conclude that these color gradients are most likely due to stellar population effects (Vader et al. 1988; de Jong 1996; Jansen et al. 2000; Bell & de Jong 2000; MacArthur et al. 2004). It would be interesting to verify this by means of a thorough study of the spatial distribution of dust in late-type galaxies.

In Chapter 2 we also presented an analysis of six galaxies observed with the Hubble Space Telescope (*HST*) with NICMOS in F160W (H) and with WFPC2 in F300W (mid-UV) and F814W (I). The F300W data and, hence, the (*F300W–F814W*) and (*F300W–F160W*) color gradients are sensitive to young stellar populations and star forming regions. We find that the two earlier-type galaxies become bluer with increasing radius in (*F300W–F814W*) and (*F300W–F160W*), while half of the four later-type galaxies become bluer with increasing radius, and half become redder with increasing radius. Even though there are small number statistics, the fact that this trend resembles the trend seen in the larger ground-based sample suggests that these conclusions are reasonable. Color gradients measured from the (*F814W–F160W*) color profile show a different trend, with all but one galaxy becoming slightly bluer with increasing radius. These small color slopes, which seem to be roughly constant with Hubble type, may be due at least in part to the fact that F814W and F160W do not sample significantly different stellar populations. This and the sensitivity of F300W on star formation may also indicate that the redder outer parts of later-type galaxies may be primarily due to recent star formation concentrated near the center of these particular galaxy types, even amongst an underlying redder, older, population that becomes more dominate toward the center of the galaxy (or the degenerate possibilities of increasing metallicity or dust toward the center of the galaxy).

We propose that these color gradient trends are consistent with the trends predicted in hierarchical galaxy formation models. The tendency of nearby irregular and peculiar/merging galaxies to become on average redder with increasing radius is similar to that of high redshift galaxies. This lends some support to the theory that high redshift galaxies are similar objects to the nearby irregular, peculiar, and merging galaxies that they resemble. A further, more detailed comparison of these nearby galaxies to high redshift galaxies is needed to more fully understand the relationship between them.

In the second part of this work (Chapter 3), we discussed concentration, asymmetry, and clumpiness (CAS) indices, which are basic structural parameters of galaxies. Because the CAS parameters are based on the light distributions of galaxies, they describe quantifiable aspects of their morphologies. A difference in these parameters as a function of rest-frame wavelength therefore contains information about how a galaxy's appearance changes with wavelength, and leads to a measure of the morphological k-correction. This is significant to high redshift studies, because at high redshift these galaxies are observed in their rest-frame UV. To quantify this, we have presented CAS parameter measurements for our sample of 199 mostly late-type and merging/peculiar galaxies observed with the VATT, HST/WFPC2, and GALEX in various combinations of filters spanning the far-UV through

the near-IR.

Our results confirm those of previous studies, but over a much wider wavelength range, that galaxies are more concentrated, less asymmetric, and less clumpy with redder color and earlier galaxy type. We find that normal and merging/peculiar galaxy type classes occupy different locations within the CAS parameter space, such that correlations between the CAS parameters can be used for statistical galaxy classification, but in a limited sense due to both intrinsic and observational scatter.

A general evolutionary trend as a merger progresses through its different stages can be drawn from these correlations, with mergers becoming significantly less concentrated, more asymmetric, and more clumpy than pre-mergers, then progressing back toward the normal galaxy parameter space, where they become merger remnants, which are more concentrated and slightly more asymmetric and less clumpy than pre-mergers.

We find no significant difference in the CAS parameters for early-type galaxies (E–S0) at rest-frame wavelengths longward of the Balmer break. We cannot measure the wavelength dependence of the CAS parameters of early-type galaxies shortward of the Balmer break, because these red galaxies have very low signal-to-noise in the GALEX and HST F255W and F300W filters. However, we find that later type galaxies (S–Im and peculiar/mergers) observed at shorter wavelengths appear to be less concentrated, more asymmetric, and more clumpy than they would appear to be at longer wavelengths. Therefore, there is little to no morphological k-correction for the CAS parameters of early type galaxies (E–S0) in the optical, but a considerable correction for all other galaxy types at all wavelengths between the far-UV and near-IR. We find a total decrease in C from the red to the far-UV of galaxies with type later than S0 of 0.38, an increase in A of 0.31, and an increase in S of 0.66.

REFERENCES

Abraham, R.G., Valdes, F., Yee, H.K.C., van den Bergh, S. 1994, ApJ, 432, 75

Abraham, R.G., Tanvir, N.R., Santiago, B.X., Ellis, R.S., Glazebrook, K., & van den Bergh, S. 1996, MNRAS, 279, 47

Balcells, M., & Peletier, R.F. 1994, AJ, 107, 135

Barnes, J., & Hernquist, L. 1996, ApJ, 471, 115

Baugh, C.M., Cole, S., Frenk, C.S., & Lacey, C.G. 1998, ApJ, 498, 504

Bell, E.F., & de Jong, R.S. 2000, MNRAS, 312, 497

Benn, C.R., and Ellison, S.L. 1998, NewAR, 42, 503

Bershady, M.A., Jangren, A., & Conselice, C.J. 2000, ApJ, 119, 2645

Bertin, E., & Arnouts, S. 1996, AJ, 117, 393

Bohlin, R.C., et al. 1991, ApJ, 368, 12

Cardiel, N., Gorgas, J., Sánchez-Blázquez, P., Cenarro, A.J., Pedraz, S., Bruzual, G., & Klement, J. 2003, A&A, 409, 511

Carlberg, R.G. 1984, ApJ, 286, 403

Cohen, S.H., Windhorst, R.A., Odewahn, S.C., Chiarenza, C.A., & Driver, S.P. 2003, AJ, 125, 1762

Cole, S., Aragon-Salamanca, A., Frenk, C.S., Navarro, J.F., & Zepf, S.E. 1994, MNRAS, 271, 781

Cole, S., Aragon-Salamanca, A., Frenk, C.S., Navarro, J.F., & Zepf, S.E. 1994, MNRAS, 271, 781

Conselice, C.J., Bershady, M.A., & Jangren, A. 2000, ApJ, 529, 886

Conselice, C.J., Bershady, M.A., Dickinson, M., & Papovich, C. 2003, AJ, 126, 1183

Conselice, C.J. 2003, ApJS, 147, 1

Corbin, M.R., Urban, A., Stobie, E., Thompson, R.I., & Schneider, G. 2001, ApJ, 551, 23

Coulman, C.E. 1985, ARA&A, 23, 19

de Grijs, R., Fritze-v. Alvensleben, U., Anders, P., Gallagher, J.S., Bastian, N., Taylor, V.A., & Windhorst, R.A. 2003, MNRAS, 342, 259

de Jong, R.S. 1996, A&A, 313, 377

Dekel, A., & Silk, J. 1986, ApJ, 303, 39

de Vaucouleurs, G., de Vaucouleurs, A., Corwin, H. G., Buta, R.J., Paturel, G., & Fouque, P. 1991, Third Reference Catalogue of Bright Galaxies (Springer, New York)

De Young, D.S. 1978, ApJ, 223, 47

Driver, S.P., Windhorst, R.A., Ostrander, E.J., Keel, W.C., Griffiths, R.E., & Ratnatunga, K.U. 1995, ApJ, 449, L23

Driver, S.P., Fernandez-Soto, A., Couch, W.J., Odewahn, S.C., Windhorst, R. A., Phillips, S., Lanzetta, K., & Yahil, A. 1998, ApJ 496, L93

Eggen, O.J., Lynden-Bell, D., & Sandage, A.R. 1962, ApJ, 136, 748

Ellis, R.S. 1997 ARA&A, 35, 389

Eskridge, P.B., et al. 2003, ApJ, 586, 923

Ferguson, H.C., et al. 2004, ApJ, 600, L107

Fried, D.L. 1965, OSAJ, 55, 1427

Friedli, D., & Benz, W. 1993, A&A, 268, 65

Friedli, D., & Benz, W. 1995, A&A, 301, 649

Franx, M., Illingworth, B., & Heckman, T., 1989, AJ, 98, 538

Garstang, R.H. 1989, PASP, 101, 306

Giavalisco, M., Steidel, C.C., & Macchetto, F.D. 1996, ApJ, 470, 189

Glazebrook, K., Ellis, R., Santiago, B., & Griffiths, R. 1995, MNRAS, 275, L19

Heckman, T.M., Armus, L., & Miley, G.K. 1990, ApJS, 74, 833

Hernquist, L., & Mihos, J. 1995, ApJ, 448, 41

Hibbard, J.E., & Vacca, W.D. 1997, AJ, 114, 1741

Hibbard, J.E., van Gorkom, J.H., Rupen, M.P., & Schiminovich, D. 2001, ASPC, 240, 657

Hill, J.K., et al. 1992, ApJ, 395, L37

Holtzman, J.A., Burrows, C.J., Casertano, S., Hester, J.J., Trauger, J.T., Watson, A.M., & Worthey, G. 1995, PASP, 107, 1065

Im, M., Griffiths, R.E., Naim, A., Ratnatunga, K.U., Roche, N., Green, R.F., & Sarajedini, V. 1999, ApJ, 510, 82

Isserstedt, J. & Schindler, R. 1986, A&A, 167, 11

Jansen, R.A., Franx, M., Fabricant, D., & Caldwell, N. 2000, ApJS, 126, 271

Kannappan, S.J., Jansen, R.A., & Barton, E.J. 2004, AJ, 127, 1371

Kauffmann, G., Nusser, A., & Steinmetz, M. 1997, MNRAS, 286, 795

Kolmogorov, A.N. 1941, in Tikhomirov, V.M., ed, Selected works of A.N. Komogorov, Mathematics and its applications (Soviet series), Klewer Academic press (1991)

Krisciunas, K., and Schaefer, B. 1991, PASP, 103, 1033

Krisciunas, K. 1997, PASP, 109, 1181

Kuchinski, L.E., et al. 2000, ApJS, 131, 441

Kuchinski L.E., Madore, B.F., Freedman, W.L., & Trewhella, M. 2001, AJ 122, 729

Landolt, A.U. 1992, AJ, 104, 340

Larson, R.B. 1974, MNRAS, 169, 229

Lotz, J.M., Primack, J., & Madau, P. 2004, AJ, 128, 163

Lowenthal, J.D., et al. 1997, ApJ, 481, 673

MacArthur, L.A., Courteau, S., Bell, E., & Holtzman, J.A. 2004, ApJS, 152, 175

Marcum, P.M., et al. 2001, ApJS, 132, 129

Massey, P., and Foltz, C.B. 2000, PASP, 112, 566

Mathews, W. 1989, AJ, 97, 42

Mihos, J., & Hernquist, L. 1994, ApJ, 425, L13

Mihos, J., & Hernquist, L. 1996, ApJ, 464, 641

Milliard, B., Donas, J., Laget, M., Armand, C., & Vuillemin, A. 1992, A&A, 257, 24

Monet, D., et al. 1996, USNO-SA2.0, (U.S. Naval Observatory, Washington DC).

Moth, P., & Elston, R.J. 2002, AJ, 124, 1886

Noguchi, M. 1988, A&A, 203, 259

Odewahn, S.C., Windhorst, R.A., Driver, S.P., & Keel, W.C. 1996, ApJ, 472, L13

Odewahn, S.C., Cohen, S.H., Windhorst, R.A., & Philip, N.S. 2002, ApJ, 568, 539

Patat, F. 2003, A&A, 400, 1183

Peletier, R.F., Davies, R.L., Illingworth, G.D., Davis, L.E., & Cawson, M., 1990, AJ, 100, 1091

Persson, S.E., Frogel, J.A., & Aaronson, M. 1979, ApJS, 39, 61

Rhoads, J.E. 2000, PASP, 112, 703

Roddier, F. 1981, in Wolf E., ed, Progress in Opt ics 19, North Holland Publ., Amsterdam

Roukema, B.F., Quinn, P.J., Peterson, B.A., & Rocca-Volmerange, B. 1997, MNRAS, 292, 835

Sandage, A. 1972, ApJ, 176, 21

Schade, D., Lilly, S.J., Crampton, D., Hammer, F., Le Fevre, O., & Tresse, L. 1995, ApJL, 451, 1

Shlosman, I., Frank, J., & Begelman, M.C. 1989, Nature, 338, 45

Shlosman, I., Begelman, M.C., & Frank, J. 1990, Nature, 345, 679

Somerville, R., Primack, J.R., & Faber, S.M. 2001, MNRAS, 320, 504

Takamiya, M. 1999, ApJS, 122, 109

Tamura, N., & Ohta, K. 2003, AJ, 126, 596

Tatarski, V.I. 1961, Wavefront Propagation in a Turbulent Medium, Dover, New York

Tinsley, B.M., & Larson, R.B. 1978, ApJ, 221, 554

Trujillo, I., et al. 2004, ApJ 604, 521

Tully, R.B., Verheijen, M.A.W., Pierce, M.J., Huang, J., & Wainscoat, R.J. 1996, AJ, 112, 2471

Vader, J.P., Vigroux, L., Lachieze-Rey, M., & Souviron, J., 1988, A&A, 203, 217

van den Bergh, S., Cohen, J.G., Hogg, D.W., & Blandford, R. 2000, AJ, 120, 2190

van Dokkum, P.G., Franx, M., Fabricant, D., Kelson, D.D., & Illingworth, G.D. 1999, ApJ, 520, L95

Walker, A. 1987, NOAO Newsletter, No. 10, 16

Walker, M. 1988, PASP, 100, 496

White, S.D.M. 1979, MNRAS, 189, 831

White, S.D., & Frenk, C.S. 1991, ApJ, 379, 52

Windhorst, R.A., et al. 2002, ApJS, 143, 113